APPLIED COMPUTATIONAL ELECTROMAGNETICS SOCIETY JOURNAL

October 2017
Vol. 32 No. 10
ISSN 1054-4887

The ACES Journal is abstracted in INSPEC, in Engineering Index, DTIC, Science Citation Index Expanded, the Research Alert, and to Current Contents/Engineering, Computing & Technology.

The illustrations on the front cover have been obtained from the research groups at the Department of Electrical Engineering, The University of Mississippi.

THE APPLIED COMPUTATIONAL ELECTROMAGNETICS SOCIETY
http://aces-society.org

EDITOR-IN-CHIEF

Atef Elsherbeni
Colorado School of Mines, EE Dept.
Golden, CO 80401, USA

ASSOCIATE EDITORS-IN-CHIEF

Sami Barmada
University of Pisa. ESE Dept.
56122 Pisa, Italy

Antonio Musolino
University of Pisa
56126 Pisa, Italy

Marco Arjona López
La Laguna Institute of Technology
Torreon, Coahuila 27266, Mexico

Mohammed Hadi
Kuwait University, EE Dept.
Safat, Kuwait

Abdul Arkadan
Marquette University, ECE Dept.
Milwaukee, WI 53201, USA

Paolo Mezzanotte
University of Perugia
I-06125 Perugia, Italy

Alistair Duffy
De Montfort University
Leicester, UK

Salvatore Campione
Sandia National Laboratories
Albuquerque, NM 87185, USA

Luca Di Rienzo
Politecnico di Milano
20133 Milano, Italy

Wenxing Li
Harbin Engineering University
Harbin 150001, China

Maokun Li
Tsinghua University
Beijing 100084, China

Rocco Rizzo
University of Pisa
56123 Pisa, Italy

EDITORIAL ASSISTANTS

Matthew J. Inman
University of Mississippi, Electrical Engineering Dept.
University, MS 38677, USA

Shanell Lopez
Colorado School of Mines, Electrical Engineering Dept.
Golden, CO 80401, USA

EMERITUS EDITORS-IN-CHIEF

Duncan C. Baker
EE Dept. U. of Pretoria
0002 Pretoria, South Africa

Robert M. Bevensee
Box 812
Alamo, CA 94507-0516, USA

Allen Glisson
University of Mississippi, EE Dept.
University, MS 38677, USA

Ahmed Kishk
Concordia University, ECS Dept.
Montreal, QC H3G 1M8, Canada

David E. Stein
USAF Scientific Advisory Board
Washington, DC 20330, USA

EMERITUS ASSOCIATE EDITORS-IN-CHIEF

Yasushi Kanai
Niigata Inst. of Technology
Kashiwazaki, Japan

Alexander Yakovlev
University of Mississippi, EE Dept.
University, MS 38677, USA

Levent Gurel
Bilkent University
Ankara, Turkey

Mohamed Abouzahra
MIT Lincoln Laboratory
Lexington, MA, USA

Ozlem Kilic
Catholic University of America
Washington, DC 20064, USA

Erdem Topsakal
Mississippi State University, EE Dept.
Mississippi State, MS 39762, USA

Fan Yang
Tsinghua University, EE Dept.
Beijing 100084, China

EMERITUS EDITORIAL ASSISTANTS

Khaled ElMaghoub
Trimble Navigation/MIT
Boston, MA 02125, USA

Christina Bonnington
University of Mississippi, EE Dept.
University, MS 38677, USA

Anne Graham
University of Mississippi, EE Dept.
University, MS 38677, USA

Mohamed Al Sharkawy
Arab Academy for Science and Technology, ECE Dept.
Alexandria, Egypt

OCTOBER 2017 REVIEWERS

Mohamed Al-Sharkaway
Ankan Bhattacharya
Muhammad Bilal
Ibrahim Elshafiey
Han Guo
Letian Guo
Yan-Jie Guo
John Ho
Bernhard Hoenders
Amir Jafargholi
Irum Jafri
Baskaran Kasi
Paulo Mendes
Donglin Meng
Andrea Morabito
Michel Ney
Andrew Peterson
Dan Shi
Yan Shi
Manuel Sierra Castañer
Manuel Sierra-Perez
Yi Sui
Hossein Torkaman
Enkuang Wang
Hao Wang
Ren Wang
Yong Wang
Wenhua Yu
Wenshen Zhou
Han Guo
Letian Guo

THE APPLIED COMPUTATIONAL ELECTROMAGNETICS SOCIETY

JOURNAL

Vol. 32 No. 10 October 2017

TABLE OF CONTENTS

© 2017, The Applied Computational Electromagnetics Society

© 2017, The Applied Computational Electromagnetics Society

A Time-Reversal FDTD Method for Image Reconstruction in the Presence of Noise

Ayed R. AlAjmi and Mohammad A. Saed

Department of Electrical Engineering
Texas Tech University, Lubbock, TX 79409, USA
ayed.alajmi@ttu.edu, mohammad.saed@ttu.edu

Abstract ─ A new method for image reconstruction using the time-reversed finite-difference time-domain method (TR-FDTD) in severely noisy environments is presented. The proposed method combines cross-correlation processing with TR-FDTD to successfully produce clear images even in the presence of large amount of noise in the captured signals. The method's capabilities are demonstrated through simulations and experiments in the x-band frequency region (8-12 GHz). Behind the wall imaging was used as a test case to validate the method. Numerical and experimental noise were added to corrupt the signals, and images were reconstructed with and without the added noise. The proposed method successfully produced clear images while the standard TR-FDTD method resulted in unrecognizable images. The efficacy and robustness of the proposed technique make it promising for applications including through-wall and buried-objects imaging in noisy environments.

Index Terms ─ Cross-correlation, FDTD, microwave imaging, time reversal.

I. INTRODUCTION

Microwave imaging techniques have attracted extensive attention because of their remarkable advantages in many applications, such as military radar, surveillance radar, and security screening [1-3]. Given their non-destructive nature on human tissues, microwave-imaging techniques are currently the subject of extensive research for medical imaging applications such as the early detection and diagnosis of breast tumors [4-6]. Microwave frequencies can also penetrate different kinds of barriers, and this feature makes them an excellent candidate for through-wall imaging [7, 8]. Significant improvements were made in the last decade in the field of microwave imaging. Some of these improvements include the confocal microwave imaging algorithm for detecting and localizing breast tumors [9]. In [10], an imaging technique based on the microwave holography was proposed for breast cancer detection. The time reversal of electromagnetic waves for imaging was introduced by Lerosey et al. [11]. The concept of time-reversal imaging algorithms relies on recording scattered signals from objects with the use of transducers and then re-emitting these signals by back-propagation into the same medium to refocus them on the source. It was first proposed in acoustics and ultrasound application [12]. In [13], a numerical study of time-reversed ultra wide-band (UWB) electromagnetic waves in continuous random media was conducted. New techniques for detecting and tracking moving targets in clutter with the use of a UWB time reversal method were investigated in [14]. Microwave breast cancer location detection using the finite difference time domain method (FDTD) with time-reversal technique was proposed in [15]. This method is based on the solutions to the time-dependent Maxwell's curl equations, which are represented as discrete formulas in time and space under a time reversal scheme to reconstruct images from previously captured data. Recently, a computationally efficient method for three-dimensional time-reversal FDTD microwave imaging technique was developed to successfully obtain detailed images of a simulated scattering object [16]. The optimum time frame to reconstruct images using this time stepping method is an important problem to which several solutions have been suggested in the literature [17-19].

Although imaging with microwave frequencies has a promising potential, the main challenge involved is the vulnerability of this range of frequencies to environmental noise that might eventually distort imaging results. In this paper, we present a novel microwave imaging technique based on the TR-FDTD method incorporating cross-correlation processing to minimize the noise effect that can corrupt the quality of the reconstructed images. Correlation is a well-known signal processing technique used in many applications in communications and radar systems in which the range or velocity of a target is determined by the correlation of the received scattered signal with a reference copy of the transmitted signal. In this study, we propose TR-FDTD microwave imaging combined with the cross-correlation processing to extract images from scattered signals in a noisy environment. This is entirely different than the use of cross-correlation

Submitted On: February 28, 2017
Accepted On: August 23, 2017

1054-4887 © ACES

in typical radar signal processing where the goal there is to enable accurate measurement of range or produce range images. In our technique, cross-correlation is used to enable accurate computation of the electric and magnetic fields in very noisy environments using the TR-FDTD method. Another important contribution this paper provides is proving that processed data through correlation can still be used in the discretized Maxwell's equations to reconstruct images successfully through the FDTD method. It is also important to note that using correlated data in a noise-free environment slightly worsens the reconstructed image compared with using the original data without correlation. However, in a noisy environment the correlation / TR-FDTD method is far superior since the reconstructed images without correlation are buried in noise, as demonstrated in the results section.

Through-wall image reconstruction in the presence of added noise is used as a test case to demonstrate the efficacy and robustness of the proposed technique. However, the proposed method is also highly promising for other microwave imaging applications.

II. ANALYSIS

A. Time-reversed FDTD

FDTD is a numerical method for solving the differential form of Maxwell's equations to obtain the electric and magnetic fields, in both the temporal and spatial domains, by implementing the Yee algorithm [20]. The latter is based on the finite difference approximation of the time and space derivatives in Maxwell's curl equations, each of which is divided into three scalar equations in the case of three-dimensional formulation, then discretized in time and space through the use of a central difference formula in a computational domain consisting of Yee cells. The future value of both the electric and magnetic fields are updated from their previous values at each point in the grid. The propagation of the fields within the computational domain is truncated by absorbing boundaries, to mimic open space [21]. Several techniques for absorbing boundaries have been proposed, one of which is the convolutional perfectly matched layers (CPML) considered to be one of the most robust and accurate methods for truncating the computational space [22]. It is capable of absorbing evanescent and propagating waves, and can be placed close the scattering objects resulting in a relatively compact computational space.

Time reversal algorithms have been used in other disciplines such as ultrasonic imaging applications. The same principle is applied in FDTD to reconstruct images from experimentally captured data by reversing all the FDTD update equations, so that the previous value of each field component is calculated using its future counterpart. As an example, for the time-reversed FDTD equations, the z component of the electric field E_z and the y-component of the magnetic field H_y in the non-CPML lossy region are given in Equations (1) and (2) respectively.

$$E_z\Big|_{i,j,k+\frac{1}{2}}^{n} = \left(\frac{1+\dfrac{\Delta t\,\sigma_z^e\big|_{i,j,k+\frac{1}{2}}}{2\varepsilon_z\big|_{i,j,k+\frac{1}{2}}}}{1-\dfrac{\Delta t\,\sigma_z^e\big|_{i,j,k+\frac{1}{2}}}{2\varepsilon_z\big|_{i,j,k+\frac{1}{2}}}}\right) \times E_z\Big|_{i,j,k+\frac{1}{2}}^{n+1}$$
$$-\left(\frac{\dfrac{\Delta t}{\varepsilon_z\big|_{i,j,k+\frac{1}{2}}}}{1-\dfrac{\Delta t\,\sigma_z^e\big|_{i,j,k+\frac{1}{2}}}{2\varepsilon_z\big|_{i,j,k+\frac{1}{2}}}}\right) \times \left[\begin{array}{l} \dfrac{1}{\Delta x}\left(H_y\Big|_{i+\frac{1}{2},j,k+\frac{1}{2}}^{n+\frac{1}{2}} - H_y\Big|_{i-\frac{1}{2},j,k+\frac{1}{2}}^{n+\frac{1}{2}}\right) \\ -\dfrac{1}{\Delta y}\left(H_x\Big|_{i,j+\frac{1}{2},k+\frac{1}{2}}^{n+\frac{1}{2}} - H_x\Big|_{i,j-\frac{1}{2},k+\frac{1}{2}}^{n+\frac{1}{2}}\right) \\ -J_{iz}\Big|_{i,j,k+\frac{1}{2}}^{n+\frac{1}{2}} \end{array}\right] \quad (1)$$

where E is electric field intensity, σ^e is electric conductivity, ε is permittivity, J is electric current density, Δt is the time step, and Δx, Δy, and Δz are the grid spacings;

$$H_y\Big|_{i+\frac{1}{2},j,k+\frac{1}{2}}^{n-\frac{1}{2}} = \left(\frac{1+\dfrac{\Delta t\,\sigma_y^m\big|_{i+\frac{1}{2},j,k+\frac{1}{2}}}{2\mu_y\big|_{i+\frac{1}{2},j,k+\frac{1}{2}}}}{1-\dfrac{\Delta t\,\sigma_y^m\big|_{i+\frac{1}{2},j,k+\frac{1}{2}}}{2\mu_y\big|_{i+\frac{1}{2},j,k+\frac{1}{2}}}}\right) \times H_y\Big|_{i+\frac{1}{2},j,k+\frac{1}{2}}^{n+\frac{1}{2}}$$
$$-\left(\frac{\dfrac{\Delta t}{\mu_y\big|_{i+\frac{1}{2},j,k+\frac{1}{2}}}}{1-\dfrac{\Delta t\,\sigma_y^m\big|_{i+\frac{1}{2},j,k+\frac{1}{2}}}{2\mu_y\big|_{i+\frac{1}{2},j,k+\frac{1}{2}}}}\right) \times \left[\begin{array}{l} \dfrac{1}{\Delta x}\left(E_z\Big|_{i+1,j,k+\frac{1}{2}}^{n} - E_z\Big|_{i,j,k+\frac{1}{2}}^{n}\right) \\ -\dfrac{1}{\Delta z}\left(E_x\Big|_{i+\frac{1}{2},j+\frac{1}{2},k+1}^{n} - E_x\Big|_{i+\frac{1}{2},j-\frac{1}{2},k}^{n}\right) \\ -M_{iy}\Big|_{i+\frac{1}{2},j,k+\frac{1}{2}}^{n} \end{array}\right] \quad (2)$$

where H is magnetic field intensity, σ^m is magnetic conductivity, μ is permeability, and M is magnetic current density.

In the simulations, the forward FDTD equations are used to record the signals scattered by objects placed in the computational domain using a plane wave as the source signal. The recorded signals can be one or more components of the electric field at a rectangular grid corresponding to receiving antenna locations. In the image reconstruction process, the recorded signals, through simulations or measurements, are used in the TR-FDTD equations to inject the time-reversed signals back into a computational domain of only vacuum. A two-dimensional image is formed in any desired plane using the magnitude of the electric field to produce a color plot in that plane. A three-dimensional image can

be formed by concatenating 2D image slices if desired.

B. Cross-correlation process

Cross-correlation [23] is a well-known signal processing technique used widely in communication systems as a measure of the similarity between two signals. It is mathematically represented for real signals by the following equation:

$$y(\tau) = \int_{-\infty}^{+\infty} x(t+\tau)g(t)dt\,, \qquad (3)$$

where x(t) and g(t) are time domain signals. In radar signal processing, x(t) represents the received signal and g(t) represents a copy of the transmitted signal.

The main idea in minimizing the effect of noise on reconstructed image quality is to apply the cross-correlation process to each captured scattered signal prior to implementing the TR-FDTD method. In other words, Equation (3) is applied to all captured signals to produce cross-correlated signals, which are then used in the TR-FDTD algorithm to produce the image. Since the correlation operation quantifies the level of similarity between two signals, the hypothesis is that desired portions of the scattered signals due to the object being imaged are preserved while the noise portions of these signals are significantly diminished. The question is then: can the signals obtained after correlation still be used in the discretized TR-FDTD algorithm to improve the quality of reconstructed images? This work clearly demonstrates that the idea works very well to produce clear images using noisy signals. The substantial improvement in the image quality is due to the fact that the cross-correlation process between the captured signals and the source signal (the stored reference signal) enhances the portions of the signals that are truly scattered by the object being imaged, and at the same time, it suppresses the uncorrelated components between them (the noise). It is worth noting that in an ideal noiseless environment, the cross-correlation operation worsens the image slightly since it enhances the stronger scattering points of the image more than the weaker scattering points. In other words, it magnifies the difference between the parts of the object that are strong scatters (e.g., corners and edges) and the parts that are not as strong. This is a small price to pay in the case of a severely noisy environment since the noise renders the image totally useless without the proposed cross-correlation processing.

In our experiment, a microwave network analyzer was used to capture scattered signal in the frequency domain, and therefore, the inverse discrete Fourier Transform was applied to obtain the time domain scattered signals prior to the cross-correlation and TR-FDTD processing. In our simulations, a time domain pulse that represents a sinc-modulated sinusoid having the same bandwidth as its experimental counterpart was used for proper comparison between simulation and experimental results.

III. SIMULATION RESULTS

To validate the method, we simulated a model for a human body behind a drywall for a near-field microwave through-wall imaging application, as depicted in Fig. 1. The human body model was illuminated by a microwave signal and the scattered signals were recorded on a uniform rectangular grid. There are several configurations that can be used in the TR-FDTD method including monostatic, bistatic, and multistatic approaches, for both reflection and transmission systems. In this simulation example, we used a multistatic configuration in which the source was a normally incident plane wave entering the computational space from the positive *x* direction. The plane wave signal was a sinc-modulated sinusoidal function with a bandwidth from 8 to 12 GHz and a center frequency of 10 GHz, as shown in Fig. 2. The scattered fields, due to reflections from the wall and human body model, were recorded by capturing the E_z component at cells on a planar grid (+ *yz* plane) separated by a uniform distance equal to 0.5λ, where λ is the wavelength at the highest frequency of the incident plane wave. The human body model had a height of 8λ and a width of 4λ, with dielectric properties of human skin (ε_r = 36 and σ_e = 4). The body was located at a distance of 1.2λ behind a drywall which had a thickness of 1.2λ, a dielectric constant ε_r = 2.19, and electrical conductivity σ_e = 0.0136 S/m, similar to what is reported in the literature for this type of wall.

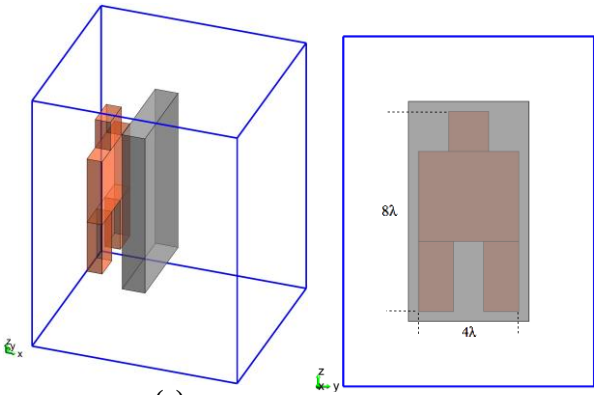

Fig. 1. (a) Perspective view and (b) front view of the original simulated object.

The reflected signals were recorded at a distance of 5λ from the wall, a sample of the recorded signals is shown in Fig. 4 (a). All the recorded signals from the forward simulation were used in the TR-FDTD algorithm to reconstruct the image of the human body, which was done successfully as shown in Fig. 3. It is worth noting

here that the TR-FDTD computational domain was assumed to be filled with air.

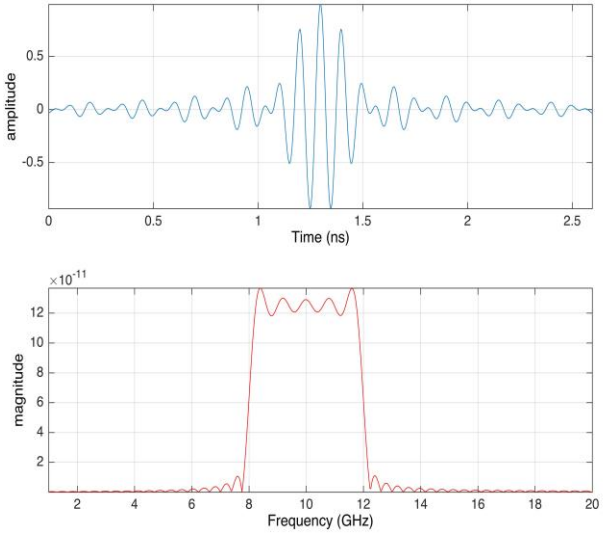

Fig. 2. Transmitted signal used in simulation and its frequency domain.

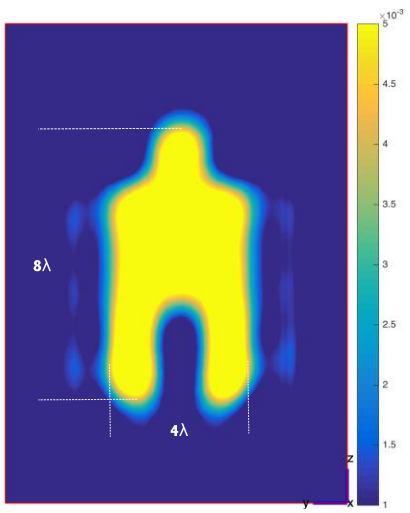

Fig. 3. Reconstructed image from the TR-FDTD algorithm.

To test the proposed technique, an interfering white Gaussian noise signal was added to the recorded signals to mimic a severe noisy environment; a sample resultant signal is shown in Fig. 4 (b). The signal-to-noise ratio (SNR), in this case, varied from −1.6 dB to −28.9 dB, due to the fact that the collected signals on the planar grid have varying strengths depending on their location with respect to the scattering object. For example, signals near the center of the planar grid have higher average signal power than those near the corners of the grid. Consequently, SNR varies since the numerically added noise power is constant regardless of the signal's location on the grid. Plugging these corrupted signals into the TR-FDTD algorithm resulted in a severely distorted image, as shown in Fig. 5 (a). To minimize the noise from the recorded signal, cross-correlation processing was applied between all the recorded signals and a copy of the transmitted signal; a sample signal after cross-correlation is shown in Fig. 4 (c). Using the cross-correlated signals as inputs to the TR-FDTD algorithm led to the successful reconstruction of the original image. Figure 5 (b) shows the reconstructed image using the cross-correlated signals. As clear from the figure, the improvement in image quality using the proposed method is remarkable.

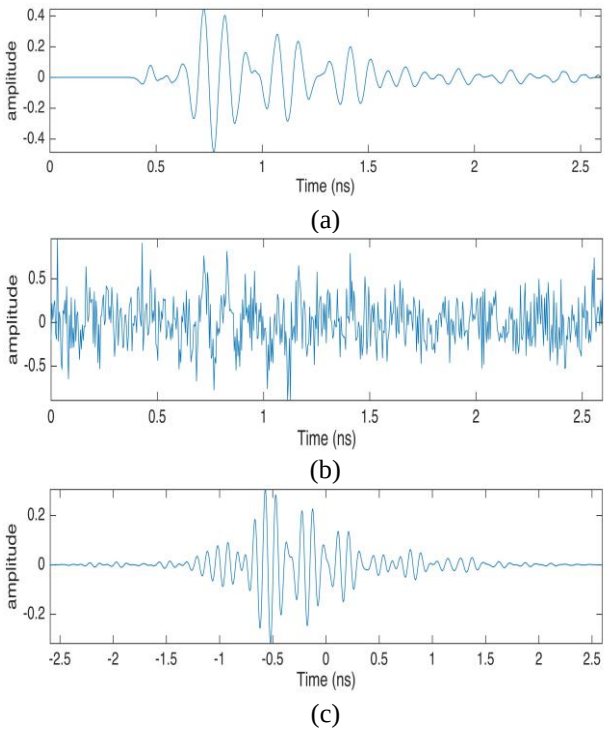

Fig. 4. Sample captured signal from the simulation: (a) in the absence of interfering noise, (b) with added noise, and (c) after cross-correlation of the corrupted signal.

IV. EXPERIMENTAL RESULTS

The proposed technique was tested experimentally using a monostatic configuration for a near-field reflection system. A single small horn antenna (aperture dimensions 4.5 × 3.0 cm) was simultaneously used as a transmitter and receiver. The antenna was moved on a uniform planar grid (20 × 30 cm) with grid spacing of 1.25 cm which corresponds to half wavelength at the highest frequency used in the measurement (12 GHz). This grid spacing resulted in 16 × 24 antenna locations for a total of 384 captured signals. A network analyzer was used as the transmitter source and receiver. The frequency domain scattering parameter S_{11} was recorded at each

antenna location using the frequency range 8-12 GHz (identical to the frequency range used in the simulations). The inverse discrete Fourier transform was then used to convert all the captured S_{11} signals to the time domain.

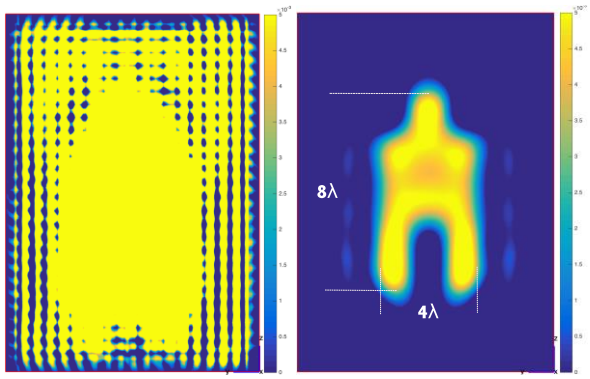

(a) (b)

Fig. 5. Reconstructed image using: (a) the corrupted signal and (b) the cross-correlated data.

A human body model, made of conducting material with exactly the same dimensions as in the simulation case, was placed behind a wall for the measurement. The wall used was made with drywall, 2 × 4 wood studs, and OSB board for a total thickness of 11cm; it was located 5 cm away from the planar grid, as shown in Fig. 6.

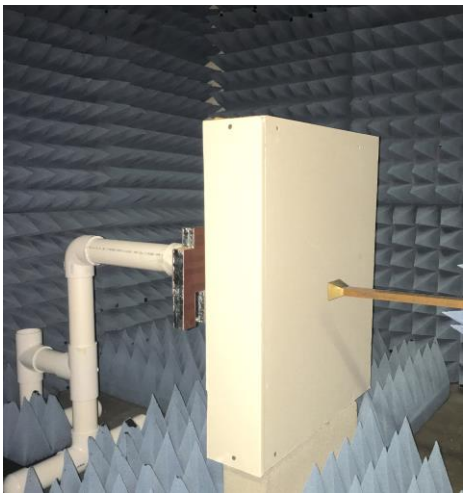

Fig. 6. Experimental setup for near-field through-wall microwave imaging of a human body model.

The time-domain transmitted (source) signal, after conversion to the time domain, is shown in Fig. 7. One sample of the scattered signals captured by the antenna is shown in Fig. 9 (a). All the signals captured by the antenna at the 384 grid locations were used in the TR-FDTD algorithm to reconstruct the image of the human body model. The image obtained resembles the original object very closely, as shown in Fig. 8.

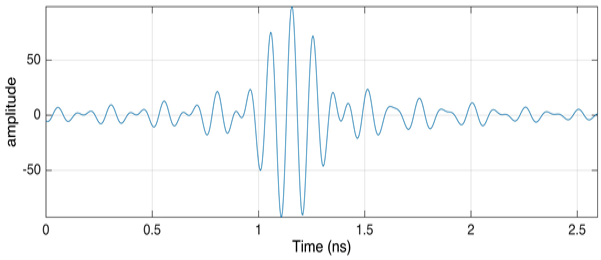

Fig. 7. Experimental transmitted signal in the time domain.

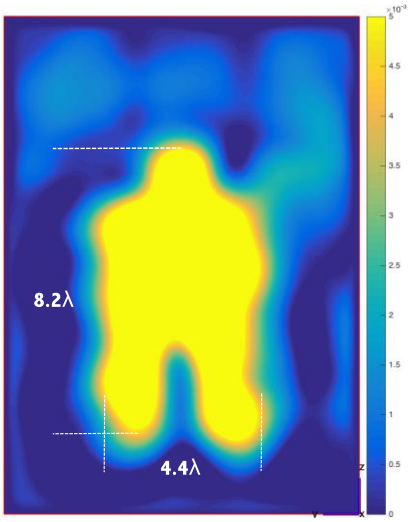

Fig. 8. Reconstructed image using experimental data.

We repeated the same scenario as in the simulation case of strong noise interference by adding an interfering noise signal to the measurements. The SNR was between –0.014dB and –6.28dB; a sample noisy signal is shown in Fig. 9 (b). It is worth noting that the noise signal used here is an experimental noise with a bandwidth limited to the bandwidth of the horn antenna, which was in the range of 8-12 GHz. The signals corrupted with noise were used in the TR-FDTD algorithm to reconstruct the image; the image obtained was unrecognizable, as shown in Fig. 10 (a).

We then applied the cross-correlation process prior to the TR-FDTD image reconstruction process. A sample signal after the cross-correlation process is shown in Fig. 9 (c). All the cross-correlated signals were then used in the TR-FDTD algorithm for image reconstruction. As shown in Fig. 10 (b), the noise was substantially minimized and the image obtained closely resembles the original object. The images shown in the figure clearly demonstrate the remarkable capability of the proposed method in minimizing the effect of noise in image reconstruction. It is worth noting that all the images are

raw images reconstructed using the proposed technique without any post-processing enhancement.

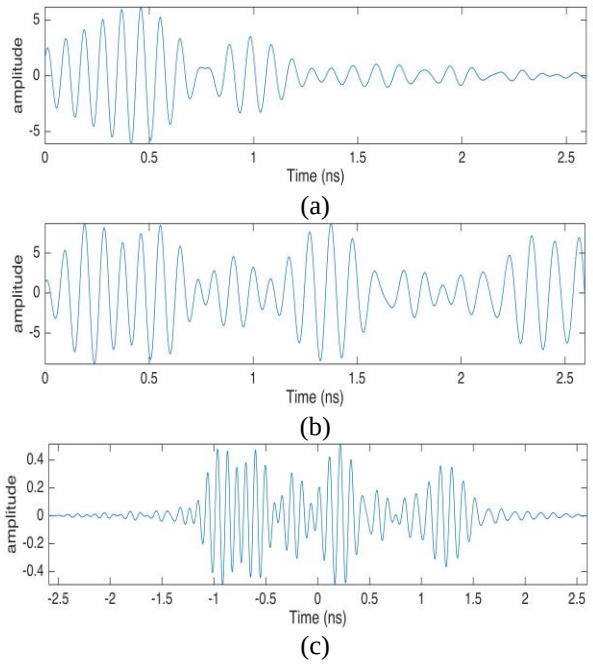

Fig. 9. Sample captured signal from the experiment: (a) in the absence of interfering noise, (b) with added noise, and (c) after cross-correlation of the corrupted signal.

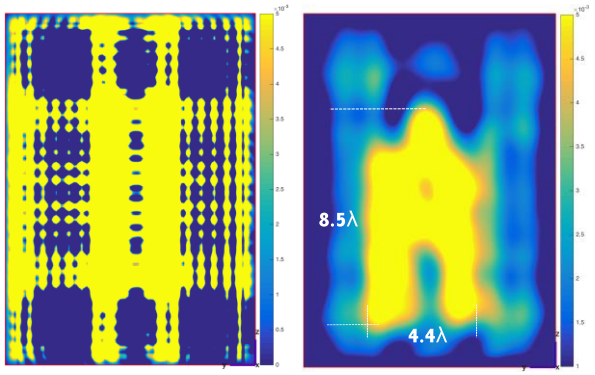

Fig. 10. Image reconstructed from: (a) the corrupted signal and (b) the cross-correlated data.

V. CONCLUSION

A new microwave imaging method combining the time-reversed finite-difference time-domain method (TR-FDTD) with cross correlation processing to minimize the effect of noise was presented. An x-band (8–12 GHz) reflection setup was used to reconstruct images using data corrupted with large amount of noise. Captured signals scattered by the object were cross-correlated with a copy of the transmitted signal prior to processing using the TR-FDTD method. Our behind the wall imaging simulations as well as experiments demonstrated the power of the proposed method. The combined TR-FDTD and cross-correlation technique successfully produced clear images, while the standard TR-FDTD method produced severely distorted images that bear no resemblance to the actual object.

REFERENCES

[1] L. Giubbolini, "A microwave imaging radar in the near field for anti-collision (MIRANDA)," *IEEE Transactions on Microwave Theory and Techniques*, vol. 47, no. 9, pp. 1891-1900, Sep .1999.

[2] Y. Wang, A. M. Abbosh, B. Henin, and P. T. Nguyen, "Synthetic bandwidth radar for ultra-wideband microwave imaging systems," *IEEE Transactions on Antennas and Propagation*, vol. 62, no. 2, pp. 698-705, Feb. 2014.

[3] M. Peichl, S. Dill, M. Jirousek, and H. Suess, "Near-field microwave imaging radiometers for security applications," *7th European Conference on Synthetic Aperture Radar (EUSAR)*, Friedrichshafen, Germany, 2008.

[4] M. Klemm, J. A. Leendertz, D. Gibbins, I. J. Craddock, A. Preece, and R. Benjamin, "Microwave radar-based breast cancer detection: Imaging in inhomogeneous breast phantoms," *IEEE Antennas and Wireless Propagation Letters*, vol. 8, pp. 1349-1352, 2009.

[5] E. C. Fear, J. Bourqui, C. Curtis, D. Mew, B. Docktor, and C. Romano, "Microwave breast imaging with a monostatic radar-based system: A study of application to patients," *IEEE Transactions on Microwave Theory and Techniques*, vol. 61, no. 5, pp. 2119-2128, May 2013.

[6] M. Klemm, J. A. Leendertz, D. Gibbins, I. J. Craddock, A. Preece, and R. Benjamin, "Microwave radar-based differential breast cancer imaging: Imaging in homogeneous breast phantoms and low contrast scenarios," *IEEE Transactions on Antennas and Propagation*, vol. 58, no. 7, pp. 2337-2344, July 2010.

[7] K. M. Yemelyanov, N. Engheta, A. Hoorfar, and J. A. McVay, "Adaptive polarization contrast techniques for through-wall microwave imaging applications," *IEEE Transactions on Geoscience and Remote Sensing*, vol. 47, no. 5, pp. 1362-1374, May 2009.

[8] F. Ahmad, M. G. Amin, and S. A. Kassam, "Synthetic aperture beamformer for imaging through a dielectric wall," *IEEE Transactions on Aerospace and Electronic Systems*, vol. 41, no. 1, pp. 271-283, Jan. 2005.

[9] E. C. Fear, X. Li, S. C. Hagness, and M. A. Stuchly, "Confocal microwave imaging for breast cancer detection: Localization of tumors in three dimensions," *IEEE Transactions on Biomedical*

Engineering, vol. 49, no. 8, pp. 812-822, Aug. 2002.

[10] M. Elsdon, M. Leach, S. Skobelev, and D. Smith, "Microwave holographic imaging of breast cancer," *International Symposium on Microwave, Antenna, Propagation and EMC Technologies for Wireless Communications*, Hangzhou, 2007.

[11] G. Lerosey, J. de Rosny, A. Tourin, A. Derode, G. Montaldo, and M. Fink "Time reversal of electromagnetic waves," *Physical Review Letters*, vol. 92, 193904, May 2004.

[12] M. Fink, D. Cassereau, A. Derode, C. Prada, P. Roux, M. Tanter, J. L. Thomas, and F. Wu, "Time-reversed acoustics," *Reports on Progress in Physics*, vol. 63, pp. 1933-1995, 2000.

[13] M. E. Yavuz and F. L. Teixeira, "A numerical study of time-reversed UWB electromagnetic waves in continuous random media," *IEEE Antennas and Wireless Propagation Letters*, vol. 4, pp. 43-46, 2005.

[14] A. E. Fouda, F. L. Teixeira, and M. E. Yavuz, "Imaging and tracking of targets in clutter using differential time-reversal," *Proceedings of the 5th European Conference on Antennas and Propagation (EUCAP)*, Rome, pp. 569-573, 2011.

[15] P. Kosmas and C. M. Rappaport, "Time reversal with the FDTD method for microwave breast cancer detection," *IEEE Transactions on Microwave Theory and Techniques*, vol. 53, no. 7, pp. 2317-2323, July 2005.

[16] C. Bardak and M. Saed, "Microwave imaging with a time-reversed finite-difference time-domain technique," *Journal of Electromagnetic Waves and Applications*, vol. 28, no. 12, 2014.

[17] W. Zheng, Z. Zhao, and Z. Nie, "Application of TRM in the UWB through wall radar," *PIER*, vol. 87, pp. 279-296, 2008.

[18] L. Li, W. Zhang, and F. Li, "A novel autofocusing approach for real-time through-wall imaging under unknown wall characteristics," *IEEE Transactions on Geoscience and Remote Sensing*, vol. 48, no. 1, pp. 423-431, Jan. 2010.

[19] A. B. Gorji and B. Zakeri, "Time-reversal through-wall microwave imaging in rich scattering environment based on target initial reflection method," *ACES Journal*, vol. 30, no. 6, June 2015.

[20] K. S. Yee, "Numerical solution of initial boundary value problems involving Maxwell's equations in isotropic media," *IEEE Transaction on Antennas and Propagation*, vol. 14, pp. 302-307, 1966.

[21] A. Z. Elsherbeni and V. Demir, *The Finite-Difference Time-domain Method for Electromagnetics with Matlab Simulations.* SciTech Publishing, 2009.

[22] J. A. Roden and S. D. Gedney, "Convolution PML (CPML): An efficient FDTD implementation of the CFS–PML for arbitrary media," *Microwave and Optical Technology Letters*, vol. 27, pp. 334-339, 2000.

[23] J. G. Proakis and D. K. Manolakis, *Digital Signal Processing*. 4th Edition, Pearson, 2007.

Ayed R. AlAjmi received the B.S. and M.S. degrees from Kuwait University, Kuwait, in 2003 and 2008, respectively, and the Ph.D. degree in Electrical Engineering from Texas Tech University, Lubbock, Texas in 2017. From 2007 to 2010, he was a Teacher at The Higher Institute of Telecommunications and Navigation, Kuwait. Since February 2010, he has been a Faculty Member in the Department of Electronics Engineering, College of Technological Studies, Public Authority for Applied Education and Training in Kuwait. His research interests include electromagnetic waves propagation, computational electromagnetics, microwave imaging and nanotechnology in electronic and communication systems.

Mohammad A. Saed received the B.S. degree in Electrical Engineering from Middle East Technical University, Ankara, Turkey in 1983, and the M.S. and Ph.D. degrees in Electrical Engineering from Virginia Tech, Blacksburg, in 1984 and 1987, respectively. From 1989 to 1990, he was a Research Associate at Virginia Tech. In 1990, he joined the faculty of the Electrical Engineering Department of State University of New York, New Paltz. In 2001, he joined the Electrical and Computer Engineering Department of Texas Tech University, Lubbock, where he is currently an Associate Professor. His research interests include applied electromagnetics with emphasis on microwave imaging and sensing, computational electromagnetics, antennas, and microwave and terahertz components and applications.

Improving the Efficiency of Computing Electromagnetic Fields from a Lossy Dielectric Cylinder due to a Line Source

Grant A. Ellis

Department of Electrical and Electronic Engineering
Nazarbayev University, Astana 010000, Kazakhstan
grant.ellis@gmail.com

Abstract ─ This paper describes analysis of electromagnetic fields from a lossy dielectric cylinder due to a line source. Series solutions for the electromagnetic fields internal and external to the cylinder are derived. Convergence is accelerated using the Watson transformation and the "*fast_callable*" function in the SageMath™ open source software. The series convergence is increased by a factor of nearly 80 using these techniques. Implementation of the Watson transform is also discussed. Applications include propagation analysis for simulating wireless body area networks and communications with wireless biosensors.

Index Terms ─ Bioelectromagnetics, creeping waves, SageMath™, Watson transform, WBAN.

I. INTRODUCTION

Wireless body area networks (WBAN) are increasingly being considered for use in wireless computing. Initially, WBAN research was for use at Wi-Fi frequencies and has been extended to UWB and is currently being studied for use in the 57-65 GHz license free band [1-4]. On-body communications can be used for medical diagnostics and monitoring patients in real-time. Applications include communications with wireless implants or bio-sensors mounted on skin or deposited inside tissue, e.g., communications with a field probe located inside a dressing [5]. Full-wave electromagnetic analysis of the human torso above 10 GHz becomes prohibitive in terms of memory.

SageMath™ is an open-source Python-based mathematics software system licensed under GPL. It is a high-level interpreted programming language for interactive use with access to several open-source packages including NumPy, SciPy, Maxima, SumPy, R, and Matplotlib [6]. It can also evaluate both symbolic and Python-type functions. It is an especially well-suited computing environment for solving analytical electromagnetics problems.

This paper is organized as follows; in Section II, analytical expressions are derived for determining the electromagnetic fields due to a line source in the presence of a lossy dielectric cylinder for TE and TM polarizations. These fields are considered for locations that are internal and external of the cylinder. In Section III, Watson series solutions are introduced to accelerate convergence. In Section IV, validation with a numerical approach is given. In Section V, results for attenuation of the fields from a dielectric cylinder used to model a human torso are given. In Section VI, computational issues such as convergence, timing, and programming are discussed. Finally, the paper is concluded.

II. THEORETICAL DEVELOPMENT

The complex dielectric properties of wet and dry skin tissue are well-known [7]. Skin conductivity (σ) increases monotonically while the relative permittivity (ε_r) decreases monotonically with increasing frequency. As a result, the penetration depth decreases with increasing frequency and is only about 2.2 cm at 2.5 GHz for dry skin. In this paper, an electric or magnetic line source located near a lossy dielectric cylinder is used to simulate the source near a human body. The configuration used for the simulations is shown in Fig. 1. The dielectric cylinder is assumed to be two-dimensional ($\partial/\partial z = 0$) with radius a, and constitutive parameters μ_r, σ, and ε_r. Cylindrical coordinates are used for the source (ρ', ϕ') and observer (ρ, ϕ) locations. The $e^{-i\omega t}$ time variation is also assumed. The line source is assumed to be external to the cylinder.

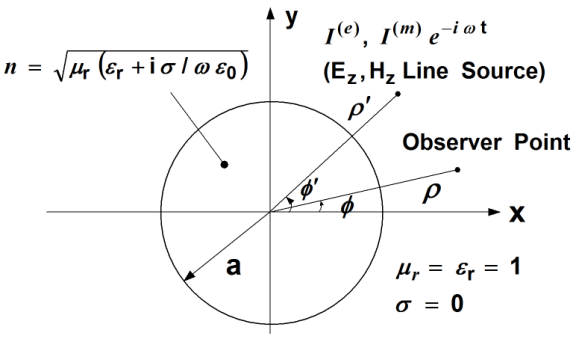

Fig. 1. Diagram of dielectric cylinder and line source.

Submitted On: October 10, 2016
Accepted On: June 14, 2017

1054-4887 © ACES

The axial components $\Pi_z^{(e)}$ and $\Pi_z^{(m)}$ of the Hertzian vectors must satisfy [8]:

$$\left(\frac{1}{\rho}\frac{\partial}{\partial\rho}\rho\frac{\partial}{\partial\rho}+\frac{1}{\rho^2}\frac{\partial^2}{\partial\varphi^2}+k_0^2\right)\Pi_z^{(e)} = \begin{cases}-\dfrac{i\,I^{(e)}}{\omega\,\varepsilon_0}\dfrac{\delta(\rho-\rho')\,\delta(\phi-\phi')}{\rho}, & \rho > a\\ 0, & \rho < a\end{cases}, \quad (1a)$$

and

$$\left(\frac{1}{\rho}\frac{\partial}{\partial\rho}\rho\frac{\partial}{\partial\rho}+\frac{1}{\rho^2}\frac{\partial^2}{\partial\varphi^2}+k_0^2\right)\Pi_z^{(m)} = \begin{cases}-\dfrac{i\,I^{(m)}}{\omega\,\mu_0}\dfrac{\delta(\rho-\rho')\,\delta(\phi-\phi')}{\rho}, & \rho > a\\ 0, & \rho < a\end{cases}. \quad (1b)$$

Solutions for $\Pi_z^{(e)}$ and $\Pi_z^{(m)}$ are both of the form:

(i) Outside the cylinder, ρ > ρ',

$$\Pi = A(\rho')\sum_{-\infty}^{\infty}\frac{i\,I}{2\,\pi\,\omega}\,exp\,\left[im(\phi-\phi')\right]H_m^{(1)}(k_0\,\rho). \quad (2a)$$

(ii) Between the cylinder and source, a < ρ < ρ',

$$\Pi = \sum_{-\infty}^{\infty}\frac{i\,I}{2\pi\omega}\,exp[im(\phi-\phi')]\times\left\{B(\rho')J_m(k_0\rho)+C(\rho')H_m^{(1)}(k_0\rho)\right\}. \quad (2b)$$

(iii) Inside the cylinder, ρ < a,

$$\Pi = D(\rho')\sum_{-\infty}^{\infty}\frac{i\,I\,n^2}{2\,\pi\,\omega}\,exp\,\left[im(\phi-\phi')\right]J_m(k\rho). \quad (2c)$$

The coefficients *A*-*D* are uniquely determined by enforcing the tangential boundary conditions for continuity of E_z and H_ϕ for the TE case (electric field perpendicular to x-y plane) and E_ϕ and H_z for the TM case (magnetic field perpendicular to x-y plane) at ρ = a. In addition, the solutions for Π above in (2a) and (2b) must be continuous due to the line source at ρ = ρ'.

After solving for these Hertz potentials, the individual *E*- and *H*-field components can then be found. For example, the axial field components outside the cylinder ρ > a are:

$$E_z = k_0^2\,\Pi_z^{(e)} \text{ and } H_z = k_0^2\,\Pi_z^{(m)}, \quad (3a)$$

and interior of the cylinder ρ < a as:

$$E_z = k_0^2\,n^2\,\Pi_z^{(e)} \text{ and } H_z = k_0^2\,n^2\Pi_z^{(m)}. \quad (3b)$$

The resulting total fields inside and outside the cylinder are [8]:

A. Fields outside of cylinder for TE or E_z polarization,

$$E_z = -I^{(e)}\frac{k_0^2}{4\,\omega\varepsilon_0}\sum_{-\infty}^{\infty}\exp\left[im(\varphi-\varphi')\right]H_m^{(1)}(k_0\rho) \times\left[J_m(k_0\rho')-\frac{J_m(k_0a)-Z^{(e)}J_m'(k_0a)}{H_m^{(1)}(k_0a)-Z^{(e)}H_m'^{(1)}(k_0a)}H_m^{(1)}(k_0\rho')\right], \quad (4a)$$

where ρ > ρ' and $Z^{(e)} = \dfrac{\mu_r\,J_m(ka)}{n\,J_m'(ka)}$.

B. Fields outside of cylinder for TM or H_z polarization,

$$H_z = -I^{(m)}\frac{k_0^2}{4\,\omega\mu_0}\sum_{-\infty}^{\infty}\exp\left[im(\varphi-\varphi')\right]H_m^{(1)}(k_0\rho) \times\left[J_m(k_0\rho')-\frac{J_m'(k_0a)-Z^{(m)}J_m(k_0a)}{H_m'^{(1)}(k_0a)-Z^{(m)}H_m^{(1)}(k_0a)}H_m^{(1)}(k_0\rho')\right], \quad (4b)$$

where ρ > ρ' and $Z^{(m)} = \dfrac{\mu_r\,J_m'(ka)}{n\,J_m(ka)}$.

The source (ρ', ϕ') and observer (ρ, ϕ) locations can be interchanged by simply interchanging the primed and unprimed coordinates. The internal fields are:

C. Fields inside of cylinder (ρ < a) for TE or Ez polarization,

$$E_z = -I^{(e)}\frac{k_0^2}{4\,\omega\varepsilon_0}\sum_{-\infty}^{\infty}\exp\left[im(\varphi-\varphi')\right]H_m^{(1)}(k_0\rho')\,J_m(k\rho) \times\left[\frac{J_m(k_0a)+R^{(e)}(m)H_m^{(1)}(k_0a)}{J_m(k\,a)}\right], \quad (5a)$$

where $R^{(e)}(m) = -\left[\dfrac{J_m(k_0a)-Z^{(e)}J_m'(k_0a)}{H_m^{(1)}(k_0a)-Z^{(e)}H_m'^{(1)}(k_0a)}\right]$.

D. Fields inside of cylinder (ρ < a) for Hz or TM polarization,

$$H_z = -I^{(m)}\frac{k_0^2}{4\,\omega\mu_0}\sum_{-\infty}^{\infty}\exp\left[im(\varphi-\varphi')\right]H_m^{(1)}(k_0\rho')\,J_m(k\rho) \times\left[\frac{J_m(k_0a)+R^{(m)}(m)H_m^{(1)}(k_0a)}{J_m(k\,a)}\right], \quad (5b)$$

where $R^{(m)}(m) = -\left[\dfrac{J_m'(k_0a)-Z^{(m)}J_m(k_0a)}{H_m'^{(1)}(k_0a)-Z^{(m)}H_m^{(1)}(k_0a)}\right]$.

III. CONVERGENCE ACCELERATION

It is well-known that the series solutions like those shown in (4a) and (4b) converge very slowly when k_0a is large. As a consequence, many terms are required to obtain reasonable accuracy. A technique known as Watson's Theorem or sometimes as Poisson's Summation

Formula can be used to accelerate the convergence of these series [8-10]. Watson's transform essentially converts (4a) and (4b) into another series by calculating the sum of the residues at their poles.

The advantage of using the Watson Transform is that a series requiring hundreds of terms or more to converge can be replaced with another series requiring only a few terms to converge. Also, the pole locations used for determining the residues are calculated only once for a particular dielectric cylinder and frequency but can be used with any source or receiver location. The disadvantage is the additional step required to compute the pole locations for computing the residues.

Equations (4a) and (4b) can be evaluated for source $\phi' = 0$ in the complex plane by using the identity [8]:

$$\sum_{-\infty}^{\infty} \exp[im\phi]\, B_m = \frac{i}{2} \int_c \frac{\exp\left[i\nu\left(\phi - \pi\right)\right] B_\nu}{\sin(\nu\pi)}\, d\nu, \qquad (6)$$

$=-2\pi i$ times the sum of the residues of $\exp\left[i\nu(\phi-\pi)\right] B_\nu / \sin(\nu\pi)$. The singularities of B_m are simple poles of the denominator of B_m and not on the real axis. Furthermore, it can be shown that the RHS of (6) is equal to:

$$i \int_{-\infty}^{\infty} \frac{\cos\left[i\nu\left(\phi - \pi\right)\right] B_\nu}{\sin(\nu\pi)}\, d\nu.$$

The resulting E_z, H_z fields for the electric line source $I^{(e)}$ then become ($\rho > \rho'$):

$$E_z = 2\pi i \cdot I^{(e)} \frac{k_0^2}{4\,\omega\,\varepsilon_0} \cdot \sum_{j=1}^{\infty} \frac{\cos\left[\nu_j\left(\phi - \pi\right)\right]}{\sin\left(\nu_j\,\pi\right)} H_{\nu_j}^{(1)}(k_0\rho)\, H_{\nu_j}^{(1)}(k_0\rho') \times \left[\frac{J_{\nu_j}(k_0 a) - Z^{(e)} J'_{\nu_j}(k_0 a)}{\frac{\partial}{\partial \nu}\left(H_\nu^{(1)}(k_0 a) - Z^{(e)} H_\nu'^{(1)}(k_0 a)\right)\Big|_{\nu=\nu_j}} \right], \qquad (7a)$$

and for the magnetic line source $I^{(m)}$:

$$H_z = 2\pi i \cdot I^{(m)} \frac{k_0^2}{4\,\omega\,\mu_0} \cdot \sum_{j=1}^{\infty} \frac{\cos\left[\nu'_j\left(\phi - \pi\right)\right]}{\sin\left(\nu'_j\pi\right)} H_{\nu'_j}^{(1)}(k_0\rho)\, H_{\nu'_j}^{(1)}(k_0\rho') \times \left[\frac{J'_{\nu'_j}(k_0 a) - Z^{(m)} J_{\nu'_j}(k_0 a)}{\frac{\partial}{\partial \nu}\left(H_\nu'^{(1)}(k_0 a) - Z^{(m)} H_\nu^{(1)}(k_0 a)\right)\Big|_{\nu=\nu'_j}} \right], \qquad (7b)$$

where ν_j, ν_j' are the singularities of B_ν and zeroes with respect to order, ν, of:

$H_\nu^{(1)}(k_0 a) - Z^{(e)} H_\nu'^{(1)}(k_0 a) = 0$ for TE and,

$H_\nu'^{(1)}(k_0 a) - Z^{(m)} H_\nu^{(1)}(k_0 a) = 0$ for TM polarization.

$\frac{\partial H_\nu^{(1)}(k_0 a)}{\partial \nu}$ and $\frac{\partial H_\nu'^{(1)}(k_0 a)}{\partial \nu}$ are computed using SageMath™ using Python-type functions from the definitions for the derivatives of Hankel functions with respect to order provided in [11, 12]. In [12], closed-from expressions are given for the first-order derivatives of Bessel ($J\nu(\,)$) and Neumann ($Y\nu(\,)$) functions with respect to order.

A. Approximations for $Z^{(e)}$ and $Z^{(m)}$

Recall the definitions for $Z^{(e)}$ and $Z^{(m)}$ in (4a) and (4b). For large argument where $z = |k_0 na| = |k\,a| >> 1$, which is typical for WBANs at microwave frequencies the following approximations for $J_\nu(z)$ can be used:

$$J_\nu(z) \approx \sqrt{\frac{2}{\pi z}} \cos\left(z - \frac{\pi\,\nu}{2} - \frac{\pi}{4}\right), \qquad (8a)$$

and

$$\frac{\partial\, J_\nu(z)}{\partial z} \approx -\sqrt{\frac{2}{\pi z}} \sin\left(z - \frac{\pi\,\nu}{2} - \frac{\pi}{4}\right) + O\left(z^{-3/2}\right). \qquad (8b)$$

Since $|ka|$ is large (>>1) then substitution of (8a) and (8b) into the definitions for $Z^{(e)}$ and $Z^{(m)}$ yield:

$$Z^{(e)} \approx -\frac{\mu_r}{n} \frac{\cos(ka - \frac{\pi\,\nu}{2} - \frac{\pi}{4})}{\sin(ka - \frac{\pi\,\nu}{2} - \frac{\pi}{4})} = -\frac{\mu_r}{n} \cot(ka - \frac{\pi\,\nu}{2} - \frac{\pi}{4}), \qquad (8c)$$

and

$$Z^{(m)} \approx -\frac{\mu_r}{n} \frac{\sin(ka - \frac{\pi\,\nu}{2} - \frac{\pi}{4})}{\cos(ka - \frac{\pi\,\nu}{2} - \frac{\pi}{4})} = -\frac{\mu_r}{n} \tan(ka - \frac{\pi\,\nu}{2} - \frac{\pi}{4}). \qquad (8d)$$

For complex $z = x + iy$, the identity:

$$\tan(z) = \frac{\sin\,(2x) + i\,\sinh\,(2y)}{\cos\,(2x) + \cosh\,(2y)},$$

can be applied to these approximations $Z^{(e)}$ and $Z^{(m)}$. For $y >> 1$ which is the case when $k_0 a$ is large, then it can be easily seen that $\tan(z) \sim i$.

From the preceding discussion for a lossy dielectric or biological material in the cylinder if imag(ka) >>1; therefore,

$$Z^{(e)} \approx i\,\frac{\mu_r}{n} \quad \text{and} \quad Z^{(m)} \approx -i\,\frac{\mu_r}{n}. \qquad (8e)$$

These approximations for $Z^{(e)}$ and $Z^{(m)}$ in (8e) can then be used in evaluating (7a) and (7b). Next, a simple procedure for determining for the simple pole locations in (7a) and (7b) can be found.

B. Procedure for determining ν_j pole locations for TE Case and ν_j' pole locations for TM Case

Using these approximations for $Z^{(e)}$ and $Z^{(m)}$, a simple procedure for determining the simple pole

locations, ν, in (7a) and (7b) is as follows: (i) for the TE polarization,

$$H_\nu^{(1)}(k_0 a) - Z^{(e)} H_\nu'^{(1)}(k_0 a) \approx H_\nu^{(1)}(k_0 a) - \frac{i\mu_r}{n} H_\nu'^{(1)}(k_0 a) = 0 , \quad (9a)$$

and, (ii) for the TM polarization,

$$H_\nu'^{(1)}(k_0 a) - Z^{(m)} H_\nu^{(1)}(k_0 a) \approx H_\nu'^{(1)}(k_0 a) + \frac{i\mu_r}{n} H_\nu^{(1)}(k_0 a) = 0 . \quad (9b)$$

In [13], the ν_j values are approximated using:

$$\nu_j = k_0 a - e^{i\pi/3}(k_0 a/2)^{1/3}\alpha_j + \frac{i\mu_r}{n}\left(1 - \frac{e^{i\pi/3}}{15(k_0 a/2)^{2/3}}\right) - \frac{e^{-i\pi/3}}{60(k_0 a/2)^{1/3}}\alpha_j^2 , \quad (10a)$$

for the TE polarization where α_j are the zero's of the Airy function and can be approximated as [14]:

$$\alpha_j \approx -\left[\frac{3\pi}{2}\left(j - \frac{1}{4}\right)\right]^{2/3} . \quad (10b)$$

For the TM polarization, the ν_j' values are approximated also using [13]:

$$\nu_j' = k_0 a - e^{i\pi/3}(k_0 a/2)^{1/3}\alpha_j' - \frac{i\mu_r}{n} e^{-i\pi/3}(k_0 a)^{2/3}\left(\frac{1}{\alpha_j'} + \frac{e^{i\pi/3}}{15(k_0 a/2)^{2/3}}\right) - \frac{e^{-i\pi/3}}{10(k_0 a/2)^{1/3}}\left(\frac{-1}{\alpha_j'} + \frac{\alpha_j'^2}{6}\right), \quad (11a)$$

where α_j' are the zero's of the derivative of the Airy function and can be approximated as [14]:

$$\alpha_j' \approx -\left[\frac{3\pi}{2}\left(j - \frac{3}{4}\right)\right]^{2/3} . \quad (11b)$$

The approximations in (8e) are used to approximate the solutions to (9a) and (9b) above and result in the approximate solutions for ν_j and ν_j' shown in (10a) and (11a). The exact values for ν_j and ν_j' can be determined using an iterative method such as Newton's method. Newton's method is implemented in SageMath™ using the approximations in (10a) and (11a) as the initial starting values. The approximations given in (9a) and (9b) are then used to approximate the derivative function with respect to order. The exact values for ν_j and ν_j' are finally used in the Watson transform formulations defined in (7a) and (7b).

IV. VALIDATION

The results in Section III were validated using simulations from CST [15]. The cylinder and line sources are approximated as a 3D dielectric ellipsoid ($\varepsilon_r = 40$, $\sigma = 2$ *S/m*) and dipole of length 10 cm and loop of radius 0.5 mm for exciting the TE and TM polarizations. The ellipsoid major axis is 1.2 m and the minor axis is 32 cm. The simulated attenuation levels normalized to the $\phi = 0$ and $\rho = 18$ *cm* value vs. ϕ-angle from CST and using the above method are shown in Table 1 for at $\rho' = 17$ *cm*, $\phi' = 0$ and f = 3 GHz. For both polarizations, the results agree to within 8 dB.

Table 1: Attenuation Watson transform (WT) vs. CST

Phi Angle	TE-WT	TE-CST	TM-WT	TM-CST
45 deg	-31.7 dB	-30 dB	-12.7 dB	-18.1 dB
90 deg	-54.6 dB	-54 dB	-24.3 dB	-32.1 dB
135 deg	-76.8 dB	-78.5 dB	-35.7 dB	-44.1 dB
180 deg	-94.1 dB	-93 dB	-41.6 dB	-49.8 dB

V. RESULTS

To illustrate the results from Sections II and III, an example is given. Here, a dielectric cylinder with radius $a = 16$ *cm* assuming the dielectric properties of wet skin are used to approximately model the human torso. Cases are considered for the source located adjacent to the body typical for a WBAN with $\rho' = 17$ *cm*, and $\phi' = 0$.

Figures 2 (a) and 2 (b) show the attenuation levels exterior to the cylinder normalized to the value at the receiver location *for* $\rho = 18$ *cm* vs. ϕ-angle for several frequencies using (4a) and (4b). For the TE polarization, the attenuation is greater than for the TM polarization at each frequency. For both polarizations and for ϕ ~ 180 degrees diffraction effects are apparent in the magnitude responses. These are due to interference caused by clockwise and counterclockwise propagating waves discussed in the next section.

Figures 3 (a) and 3 (b) show the attenuation levels interior to the cylinder normalized to the value at the surface vs. radius (ρ) at 3 GHz for several ϕ-angles using (5a) and (5b). Above this frequency, the attenuation starts to become prohibitively large where the attenuation of the fields interior to the cylinder < 90 dB than those at the surface for both polarizations.

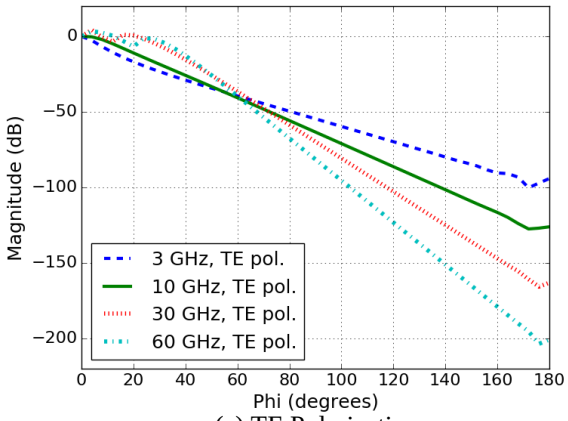

(a) TE Polarization

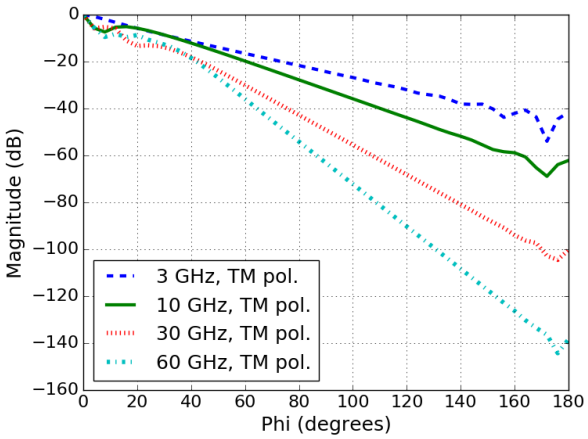

(b) TM Polarization

Fig. 2. Attenuation vs. ϕ-angle and for 3-60 GHz.

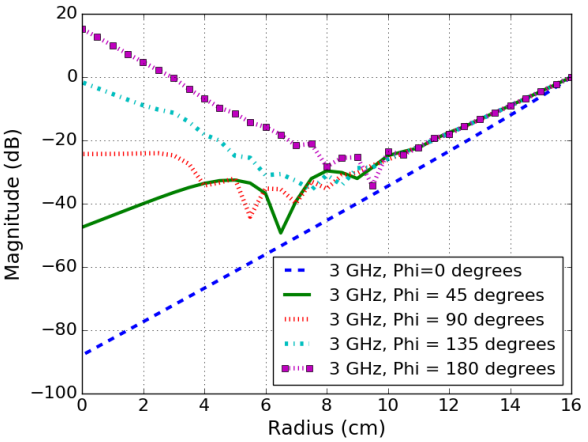

(a) TE polarization

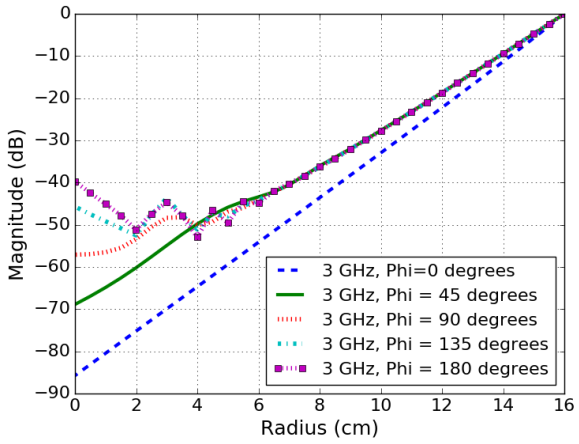

(b) TM polarization

Fig. 3. Attenuation vs. radius (ρ) for fields internal to dielectric cylinder 3 GHz for several ϕ-angle.

Table 2 shows the attenuation level at the center of the dielectric cylinder ($\rho = 0$) normalized to the level at the surface ($\phi = 0$ and $\rho = 16$ *cm*) for some frequencies reserved for biomedical telemetry and ISM applications [16]. Due to limited receiver sensitivity (> -130 dBm) and lower available power levels, the attenuation at the ISM frequencies up to 2.45 GHz is low enough to easily facilitate communications with implanted sensors. At 5.8 GHz, however, the attenuation level is nearly 176 dB for both polarizations.

Table 2: Attenuation levels interior to body for ρ = 0

Frequency	TE (dB)	TM (dB)
195 MHz	-25.8	-18.6
434 MHz	-33.2	-27.1
640 MHz	-36.9	-31.3
915 MHz	-41.2	-36.4
2.45 GHz	-67.9	-65.3
5.8 GHz	-177.2	-176.3

VI. DISCUSSION

Computational issues such as convergence, CPU time, and programming issues are considered. Because SageMath is interpreted, functions such as *fast_callable* and *fast_form* are available to speed-up computation.

A. Series convergence

The residue series solutions for the TE and TM polarizations in (7a) and (7b) both include the term $\frac{\cos \nu (\phi - \pi)}{\sin (\nu \pi)}$, which can be further expanded as:

$$\frac{\cos \nu (\phi - \pi)}{\sin (\nu \pi)} = -i \frac{\exp[i \nu \phi] + \exp[i \nu (2\pi - \varphi)]}{1 - \exp(i \nu 2\pi)}, \quad (12)$$

and can be interpreted as "creeping waves" propagating around the cylinder in the clockwise and counter-clockwise directions. Shown in Figs. 4 and 5 are the magnitudes of (12) for j = 1 to 5 (in ν_j and ν_j') versus angle, ϕ for the previous case with radius, $a = 16$ *cm* and source radius, $\rho' = 17$ *cm* and the dielectric properties for skin for 3 and 30 GHz. These parameters are assumed to be typical for body tissue. For 3 GHz, $n = 6.4 + i\,0.94$, $k_0 a = 10.1$, and $|ka| = 65$. The j = 5 term ($\nu = \nu_5$) magnitude is about 0.01 times the j = 1 ($\nu = \nu_1$) term for $\phi = 28$ *degrees* for the TE and TM cases. For 30 GHz, the j = 5 term ($\nu = \nu_5$) magnitude is about 0.01 times the j = 1 ($\nu = \nu_1$) term for ϕ = 15 degrees for TE case and $\phi = 12$ *degrees* for TM case.

It is clear from the above that the Watson series in (7a) and (7b) converge rapidly for large $k_0 a$ and angle ϕ in the shadow region of the cylinder. For ϕ > 30 degrees, less than five (5) terms are required for convergence for $f \geq 3$ GHz.

B. Use of *fast_callable* SageMath function

The SageMath™ *fast_callable* function transforms algebraic expressions into a form that can be evaluated

quickly. It is especially helpful for expressions that need to be evaluated many times.

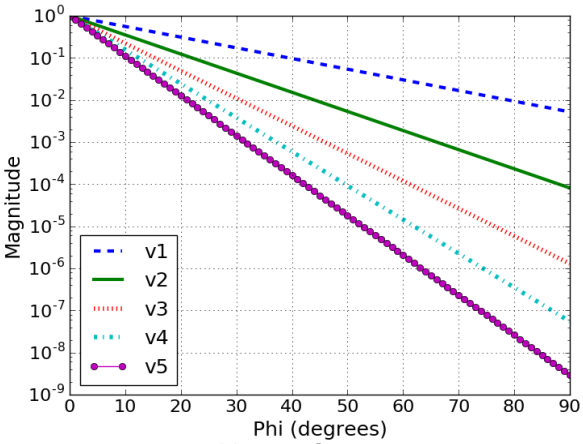

(a) TE polarization

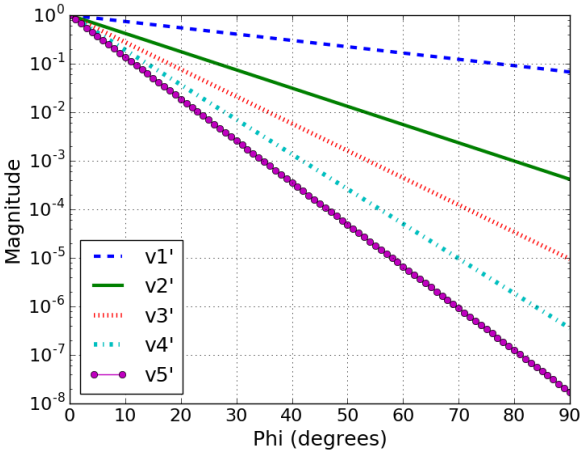

(b) TM polarization

Fig. 4. Convergence (3 GHz).

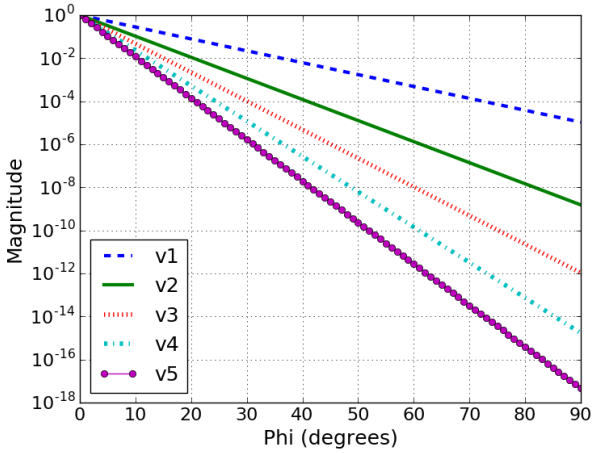

(a) TE polarization

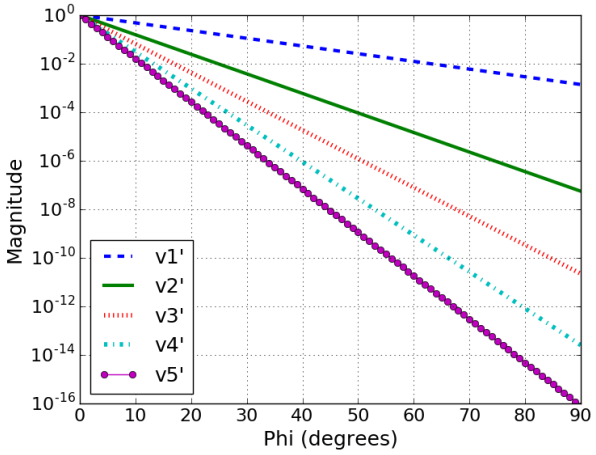

(b) TM polarization

Fig. 5. Convergence (30 GHz).

The Watson transform and the *fast-callable* function were used in calculating the fields for TE and TM polarizations. The timing results are shown below in Table 3 running SageMath^{TM} 6.9 on a Windows 8 PC with an Intel i7-377c 3.4 GHz CPU. The CPU time is reduced by more half by using *fast_callable* with Eqs. (4a) and (4b). Using the Watson transform reduces the CPU time again by nearly a factor of four. Combining the *fast_callable* function with the Watson Transform in Eqs. (7a) and (7b) reduces the CPU time by a factor of at least 77.

Table 3: Timing data for TE and TM cases

Calculation	CPU Time	Speedup
Basic Series (TE)	881.37 sec	----
Basic Series with fast_callable (TE)	369.75 sec	238%
Watson Transform (TE)	94.65 sec	931%
Watson Transform with fast_callable (TE)	11.34 sec	7772%
Basic Series (TM)	885.10 sec	----
Basic Series with fast_callable (TM)	369.05 sec	240%
Watson Transform (TM)	91.90 sec	963%
Watson Transform with fast_callable (TM)	11.09 sec	7981%

VII. CONCLUSION

In this paper, equations for computing the E_z and H_z electromagnetic fields from a lossy dielectric cylinder due to a line source are given. This analysis is

useful for quickly simulating the field penetration into and propagation around the human torso. The Watson transform and fast functions available in SageMath™ are used to significantly speed-up the computation time.

The results from the simulations show that use of frequencies less than 3 GHz result in attenuation levels that are low enough to implement buried implants. The TM polarization is also preferable over TE polarization due to lower propagation attenuation around the torso. This suggests that a preferable radiator could be a small loop or slot antenna with its axis aligned parallel to the body for WBAN applications.

ACKNOWLEDGMENT

The author wishes to thank Dr. Linus Lau of RF Station for CST simulations of the dielectric ellipsoid.

REFERENCES

[1] I. Khan, P. S. Hall, A. A. Serra, A. R. Guraliuc, and P. Nepa, "Diversity performance analysis for on-body communications channels at 2.45 GHz," *IEEE Trans. Antennas Propag*., vol. 57, pp. 956-963, April 2009.

[2] Q. B. Abbasi, M. M. Khan, and Y. Hao, "Diversity antenna techniques for enhanced ultra wideband body-centric communications," *2011 IEEE APSURSI Symp*., pp. 1323-1326, 2011.

[3] T. Mavridis, L. Petrillo, J. Sarrazin, D. Lautru, A. B. Delai, and P. De Doncker, "Creeping wave model of diffraction of an obliquely incident plane wave by a circular cylinder at 60 GHz," *IEEE Trans. Antennas Propag*., vol. 62, no. 3, pp. 1372-1377, March 2014.

[4] L. Petrillo, T. Mavridis, J. Sarrazin, D. Lautru, A. B. Delai, and P. De Doncker, "Analyical creeping wave model and measurements for 60 GHz body area networks," *IEEE Trans. Antennas Propag*., vol. 62, no. 8, pp. 4352-4356, August 2014.

[5] N. Rezaei, D. Majumdar, B. Cockburn, and C. Schlegal, "Electromagnetic energy and data transfer in biological tissues using loop antennas," *2013 International Workshop on Body Area Sensor Networks (BASNet-2013)*, pp. 908-913, 2013.

[6] Sage Math, http://www.sagemath.org/

[7] Dielectric properties of Body Tissues, http:// niremf.ifac.cnr.it/tissprop/htmlclie/htmlclie.php

[8] G. Tyras, *Radiation and Propagation of Electromagnetic Waves*. Academic Press, 1969.

[9] D. S. Jones, *Methods in Electromagnetic Wave Propagation*. 2nd ed., IEEE Press, pp. 522-530, 1995.

[10] Morse and Feshbach, *Methods of Theoretical Physics*. vol. 1, McGraw-Hill, pp. 467, 817, 1953.

[11] NIST Handbook of Mathematical Functions, Cambridge University Press, p. 227, 2010.

[12] Y. A. Brychkov, "Higher derivatives of the Bessel functions with respect to the order," *Integral Transforms and Special Functions*, April 2016.

[13] S. E. Sandstrom and C. Ackren, "Note on the complex zero's of $H'_\nu(x) + i\zeta H_\nu(x) = 0$," *Journal of Computational and Applied Mathematics*, 201, pp. 3-7, 2007.

[14] J. O. Cochran, "The zeroes of Hankel functions as functions of their order," *Numerische Mathematik*, 7, pp. 238-250, 1965.

[15] CST Microwave Studio, Darmstadt, Germany.

[16] Title 47, CFR Part 15 - Radio Frequency Devices, US Government Printing Office, 2015.

Grant Andrew Ellis received the Ph.D. degree in Electrical Engineering from the University of Washington, Seattle, in 1995. He has more than 25 years of professional experience in the areas of RF and Microwave and antenna analysis and design. Ellis has written over 40 papers and publications and holds 5 US patents. Ellis is the Founding Chairman of the IEEE MTT/ED/AP Penang Chapter. He is a registered professional engineer, a Member of ACES, and has been a Senior Member of the IEEE since 2004.

Derivation and Fast Computation of Dyadic Green's Functions of Magnetic Vector Potential for Unbounded Uniaxial Anisotropic Media

Jianliang Zhuo [1], Feng Han [1*], Na Liu [1], Longfang Ye [1], Hai Liu [1], and Qing Huo Liu [2]

[1] Institute of Electromagnetics and Acoustics, and Department of Electronic Science
Xiamen University, Xiamen, Fujian-361008, China
[*]feng.han@xmu.edu.cn

[2] Department of Electrical and Computer Engineering
Duke University, Durham, NC-27705, USA
qhliu@duke.edu

Abstract ─ The dyadic Green's function of the magnetic vector-potential **A** (DGFA) for unbounded uniaxial anisotropic media is unavailable in literature but it is needed in numerical computation. The equation of the DGFA was directly derived from the Maxwell's equations. Through the Fourier transform and the inverse Fourier transform, the triple integral form of the DGFA in the spatial domain was obtained. And it was finally simplified to Sommerfeld integrals. In order to verify these formulas, we applied the singularity subtraction technique to evaluate the Sommerfeld integrals rapidly and compared the numerical results with the analytical solutions for degenerated cases for the isotropic unbounded media, as well as the simulated results from a commercial finite element software for uniaxial anisotropic unbounded media. Finally, the effect of the singularity subtraction method was discussed.

Index Terms ─ Dyadic Green's function, magnetic vector-potential, unbounded, uniaxial anisotropic media.

I. INTRODUCTION

In the past decades, the computation of Green's functions has attracted intensive attention of many researchers. Both the scalar potential [1, 2] and vector potential methods for the computation of Green's functions are suggested. The scalar potential formulations are widely applied to the analysis of complex media [3]. The dyadic Green's functions (DGFs) of the vector potential are the kernel parts of the method of moment (MOM), which is a widely used method in electromagnetic forward and inverse problems [4-11]. So far, the DGFs have been obtained for multilayered isotropic media [12-17], unbounded anisotropic media [18-20], multilayered anisotropic media [21]-24], etc. Michalski and Mosig [17] proposed the transmission line method to calculate the electric- and magnetic-type DGFs in a multilayered medium. Waves were decomposed into transverse electric (TE) and transverse magnetic (TM) modes in the transmission line analog the multilayered medium, and DGFs were first calculated in the spectral domain and transformed back to the spatial domain later. Electric-type DGFs for general anisotropic media were obtained using the eigenvalue decomposition method by Huang and Lee [20]. The DGFs for the buried sources in stratified anisotropic media were formulated by Ali and Mahoud [24] with both complex tensor permittivities and tensor permeabilities.

However, most of the above research work regarding DGFs focused on the calculation of electric or magnetic fields excited by an infinitesimal electric or magnetic dipole, i.e., the electric- or magnetic-type DGFs. The magnetic vector potential **A** generated by an infinitesimal electric dipole, i.e., the dyadic Green's function $\overline{\overline{G}}_{\mathbf{AJ}}$ of the magnetic vector-potential **A** (DGFA), was not frequently studied for anisotropic media. But this auxiliary magnetic vector potential **A** was extensively applied to the solution of antenna radiation problems [25, 26], forward scattering [27, 28] and inverse problems [29]. Fast and precise computation of the DGFA in various media is of great demand because it establishes a direct relation between **A** and the vector current source inside the media. Researchers have proposed some computational methods for the DGFA [17, 30-32]. Moran and Gianzero [31] presented an analytical solution of the DGFA for the uniaxial anisotropic media. It was formulated in the low frequency regime and usually used in well-logging measurements in which the dielectric constant was ignored and no anisotropy of magnetic properties was considered. Abubakar and Habashy [32] provided closed-form tensor Green's functions for an unbounded homogeneous transverse isotropic (TI)-anisotropic medium. In their derivation, the permeability of the media was assumed as a scalar constant instead of the general complex form. Michalski and Mosig [17] derived DGFA from the Green's function of magnetic

Submitted On: November 30, 2016
Accepted On: September 6, 2017

1054-4887 © ACES

field **H** which is derived by transmission line analog method. The mathematical form of the DGFA was not unique and they chose a compact and convenient form.

In this paper, we presented a detailed but mathematically straightforward process for the computation of DGFA in the uniaxial anisotropic medium with both complex tensor permittivity and complex tensor permeability. Based on Maxwell's equations, the spatial domain DGFA in the triple integral was derived through the Fourier transforms and the inverse Fourier transforms. Using eigenvalue methods, Cauchy residue theorem and some mathematical identities, we finally simplified the triple integrals to Sommerfeld integrals. Because of the slow decaying and high oscillating properties, the Sommerfeld integrals can't be computed efficiently by the straightforward numerical integration methods. This process was accelerated by the singularity subtraction method [33] in which a special term was subtracted from each Sommmerfeld integrand to make the new integrand rapid decaying, where there is an analytical solution for the integration of each subtracted term. In addition, the singularity of the DGFA when the source point approaching the field point is discussed.

This paper is organized as follows. In Section 2, the DGFA is formulated with both complex tensor permittivity and tensor permeability in unbounded uniaxial anisotropic media. In Section 3, a rapid computation algorithm is applied to the evaluation of Sommerfeld integrals which are deformed from the DGFA. Furthermore, in Section 4, we verify the derived DGFAs by comparing them with the analytical solutions in the circumstance of isotropic media, and, with simulated results from a commercial software in the circumstance of uniaxial anisotropic media. And then, we show the efficiency improvements on the convergence of the Sommerfeld integrand by the singularity subtraction method. The summary and conclusions are given in Section 5.

II. FORMULATIONS AND EQUATIONS

The magnetic vector potential formulation for a homogeneous medium is described in many textbooks. In the absence of magnetic sources (where $M_i = 0$, $\rho_{mi} = 0$), Maxwell's equations (with a time variation of $e^{j\omega t}$) for an unbounded medium are given as:

$$\nabla \times \mathbf{E} = -j\omega\bar{\bar{\mu}}\mathbf{H}, \tag{1}$$

$$\nabla \times \mathbf{H} = j\omega\bar{\bar{\epsilon}}\mathbf{E} + \mathbf{J}, \tag{2}$$

$$\nabla \cdot \bar{\bar{\epsilon}}\mathbf{E} = \rho_e, \tag{3}$$

$$\nabla \cdot \bar{\bar{\mu}}\mathbf{H} = 0, \tag{4}$$

where **E** is the electric field intensity, **H** is the magnetic field intensity, **J** is the electric current densities, $\bar{\bar{\mu}}$ is the complex permeability tensor of the medium, and $\bar{\bar{\epsilon}}$ is the complex permittivity tensor, which contains information about the dielectric constant and conductivity tensor of the medium. The complex permittivity $\bar{\bar{\epsilon}}$ is defined as following:

$$\bar{\bar{\epsilon}} = \bar{\bar{\varepsilon}} + \frac{\bar{\bar{\sigma}}}{j\omega}, \tag{5}$$

where $\bar{\bar{\varepsilon}}$ is the real permittivity tensor and $\bar{\bar{\sigma}}$ is the conductivity tensor.

In this paper, we assume the optic axis of the uniaxial anisotropic medium is in the z direction. The permeability, permittivity and conductivity of the medium are written as:

$$\bar{\bar{\mu}} = \begin{bmatrix} \mu_x & 0 & 0 \\ 0 & \mu_x & 0 \\ 0 & 0 & \mu_z \end{bmatrix}, \ \bar{\bar{\varepsilon}} = \begin{bmatrix} \varepsilon_x & 0 & 0 \\ 0 & \varepsilon_x & 0 \\ 0 & 0 & \varepsilon_z \end{bmatrix},$$
$$\bar{\bar{\sigma}} = \begin{bmatrix} \sigma_x & 0 & 0 \\ 0 & \sigma_x & 0 \\ 0 & 0 & \sigma_z \end{bmatrix}. \tag{6}$$

From Equation (4), we can relate the magnetic field and the magnetic vector potential A by:

$$\mathbf{H} = \bar{\bar{\mu}}^{-1}\nabla \times \mathbf{A}. \tag{7}$$

By substituting (7) into (1) and using the vector identity that the curl of the gradient of any scalar function is zero, we can write the electric field as:

$$\boldsymbol{E} = -j\omega\boldsymbol{A} - \nabla\phi_e, \tag{8}$$

where ϕ_e is a scalar electric potential.

By substituting (7) and (8) into (2), we obtain the equation of the magnetic vector potential **A** and the scalar potential ϕ_e as:

$$\nabla \times \bar{\bar{\mu}}^{-1}\nabla \times \mathbf{A} - \omega^2\bar{\bar{\epsilon}}\mathbf{A} + j\omega\bar{\bar{\epsilon}}(\nabla\phi_e) = \mathbf{J}. \tag{9}$$

For anisotropic media, we use the gauge by Chew [34]:

$$\nabla \cdot \bar{\bar{\epsilon}}\mathbf{A} + \chi j\omega\phi_e = 0, \tag{10}$$

where χ is an arbitrary function of position $\bar{\mathbf{r}}$, and $\chi = \alpha|\bar{\bar{\epsilon}} \cdot \bar{\bar{\mu}} \cdot \bar{\bar{\epsilon}}|$. Note that α can be chosen arbitrarily. For different selection, the DGFA will be different. But the electric and magnetic field computed using DGFA will not change. In order to simplify the subsequent mathematical derivations and numerical calculation, we choose $\alpha = \frac{1}{\epsilon_x^4\mu_x^2}$, where $\epsilon_x = \varepsilon_x + \frac{\sigma_x}{j\omega}$. And then,

$$\chi = \mu_z\epsilon_z^2, \tag{11}$$

where $\epsilon_z = \varepsilon_z + \frac{\sigma_z}{j\omega}$. For this value of χ, the gauge in (10) will degenerate into the Lorentz gauge if the medium is isotropic.

Substituting (10) and (11) into (9), we obtain the equation of magnetic vector potential **A** as:

$$\nabla \times \bar{\bar{\mu}}^{-1}\nabla \times \mathbf{A} - \omega^2\bar{\bar{\epsilon}}\mathbf{A} + \frac{1}{\mu_z\epsilon_z^2}\bar{\bar{\epsilon}}\nabla(\nabla\phi_e) = \mathbf{J}. \tag{12}$$

Our choice of $\alpha = \frac{1}{\epsilon_x^4\mu_x^2}$ guarantees that the three terms in the left side of Equation (12) have the same order of coefficient magnitude. And Equation (12) can be expressed in a more compact form as:

$$\bar{\bar{Z}}_E\mathbf{A} = \mathbf{J}, \tag{13}$$

where $\bar{\bar{Z}}_E$ is a second order differential matrix, and its detailed expression is shown in the Appendix A.

If the current source is a unit point source, Equation (13) becomes the equation of the DGFA $\bar{\bar{\mathbf{G}}}_{\mathbf{AJ}}(\bar{\mathbf{r}}, \bar{\mathbf{r}}')$ in

the spatial domain as following:

$$\bar{\bar{Z}}_E\bar{\bar{\mathbf{G}}}_{\mathbf{AJ}}(\bar{\mathbf{r}},\bar{\mathbf{r}}')=\boldsymbol{\delta}(\bar{\mathbf{r}},\bar{\mathbf{r}}')\bar{\bar{\mathbf{I}}}, \quad (14)$$

where $\bar{\bar{\mathbf{I}}}$ is the unit dyadic, and the unitary point source excitation is located at $\bar{\mathbf{r}}'=\hat{\mathbf{x}}\mathrm{x}'+\hat{\mathbf{y}}\mathrm{y}'+\hat{\mathbf{z}}\mathrm{z}'$.

By applying the spatial Fourier transform to (14), we obtain the equation of DGFA $\bar{\bar{\mathbf{G}}}_{\mathbf{AJ}}(\bar{\mathbf{k}},\bar{\mathbf{r}}')$ in the spectral domain as following:

$$\bar{\bar{Z}}_A\bar{\bar{\mathbf{G}}}_{\mathbf{AJ}}(\bar{\mathbf{k}},\bar{\mathbf{r}}')=e^{j\bar{\mathbf{k}}\cdot\bar{\mathbf{r}}'}\bar{\bar{\mathbf{I}}}, \quad (15)$$

where $\bar{\mathbf{k}}$ is the wave vector, which is given as $\bar{\mathbf{r}}'=\hat{\mathbf{x}}\mathrm{k_x}+\hat{\mathbf{y}}\mathrm{k_y}+\hat{\mathbf{z}}\mathrm{k_z}$, and $\bar{\bar{Z}}_A$ is the electric wave matrix about (k_x,k_y,k_z), whose complete expression is shown in the Appendix B.

Equation (15) can be rewritten as:

$$\bar{\bar{\mathbf{G}}}_{\mathbf{AJ}}(\bar{\mathbf{k}},\bar{\mathbf{r}}')=\frac{\bar{\bar{Z}}_A^a}{|\bar{\bar{Z}}_A|}e^{j\bar{\mathbf{k}}\cdot\bar{\mathbf{r}}'}, \quad (16)$$

where $\bar{\bar{Z}}_A^a$ is the adjoint matrix of $\bar{\bar{Z}}_A$, whose determinant is $|\bar{\bar{Z}}_A|$.

Applying the spatial inverse Fourier transform, we obtain the relationship between the spatial domain DGFA $\bar{\bar{\mathbf{G}}}_{\mathbf{AJ}}(\bar{\mathbf{r}},\bar{\mathbf{r}}')$ and the spectral domain DGFA $\bar{\bar{\mathbf{G}}}_{\mathbf{AJ}}(\bar{\mathbf{k}},\bar{\mathbf{r}}')$ as:

$$\bar{\bar{\mathbf{G}}}_{\mathbf{AJ}}(\bar{\mathbf{r}},\bar{\mathbf{r}}')=\frac{1}{(2\pi)^3}\iiint_{-\infty}^{+\infty}\frac{\bar{\bar{Z}}_A^a}{|\bar{\bar{Z}}_A|}e^{-j\bar{\mathbf{k}}\cdot(\bar{\mathbf{r}}-\bar{\mathbf{r}}')}d\bar{\mathbf{k}}. \quad (17)$$

Actually, from Equations (8) and (10), we can obtain the expression of **E** in term of **A** in the spatial domain as:

$$\mathbf{E}=-j\omega\mathbf{A}-\frac{j}{\omega\mu_z\epsilon_z^2}\nabla\nabla\cdot\bar{\bar{\epsilon}}\mathbf{A}. \quad (18)$$

Therefore, if **E** and **A** in Equation (18) are excited by the same unit point source, the DGF $\bar{\bar{\mathbf{G}}}_{\mathbf{EJ}}(\bar{\mathbf{k}},\bar{\mathbf{r}}')$ of electric field and the DGFA $\bar{\bar{\mathbf{G}}}_{\mathbf{AJ}}(\bar{\mathbf{k}},\bar{\mathbf{r}}')$ in the spectral domain can be related by:

$$\bar{\bar{\mathbf{G}}}_{\mathbf{EJ}}(\bar{\mathbf{k}},\bar{\mathbf{r}}')=-j\omega(\bar{\bar{\mathbf{I}}}-\frac{\mathbf{1}}{\omega^2\mu_z\epsilon_z^2}\begin{bmatrix}k_x^2\varepsilon_x & k_xk_y\varepsilon_x & k_xk_z\varepsilon_z\\ k_xk_y\varepsilon_x & k_y^2\varepsilon_x & k_yk_z\varepsilon_z\\ k_xk_z\varepsilon_x & k_yk_z\varepsilon_x & k_z^2\varepsilon_z\end{bmatrix})\bar{\bar{\mathbf{G}}}_{\mathbf{AJ}}(\bar{\mathbf{k}},\bar{\mathbf{r}}'). \quad (19)$$

Substituting (15) into (19), we obtain the spectral domain DGF of electric field as:

$$\bar{\bar{W}}_E\bar{\bar{\mathbf{G}}}_{\mathbf{EJ}}(\bar{\mathbf{k}},\bar{\mathbf{r}}')=j\omega e^{j\bar{\mathbf{k}}\cdot\bar{\mathbf{r}}'}, \quad (20)$$

where $\bar{\bar{W}}_E$ is electric wave matrix and its detailed expression is shown in the Appendix C.

Equation (20) is in accord with the results shown in the paper [20], [24].

III. EVALUATION

The spatial DGFA $\bar{\bar{\mathbf{G}}}_{\mathbf{AJ}}$ in Equation (17) is not easy to compute due to its triple integral. It is noted, however, that $\bar{\bar{Z}}_A$ is a sixth order polynomial of k_z, and thus, has six different roots. So it can be written as:

$$|\bar{\bar{Z}}_A|=\alpha_6\prod_{i=1}^{3}(k_z-k_{z,i}^u)(k_z-k_{z,i}^d), \quad (21)$$

where the subscript $i=(1,2,3)$. The wave vectors $k_{z,i}^u$ and $k_{z,i}^d$ are couple positive and negative roots corresponding to upward and downward propagating wave, respectively. Let's define $k_\rho=\sqrt{k_x^2+k_y^2}$, so $k_{z,i}^u$ and $k_{z,i}^d$ depend only on k_ρ. The coefficient $\alpha_6=\frac{1}{\mu_x^2\mu_z}$.

Substituting (21) into (17), we obtain the spatial domain DGFA as:

$$\bar{\bar{\mathbf{G}}}_{\mathbf{AJ}}(\bar{\mathbf{r}},\bar{\mathbf{r}}')=\frac{1}{(2\pi)^3}\iiint_{-\infty}^{+\infty}\frac{\bar{\bar{Z}}_A^a(k_z)}{\alpha_6\prod_{i=1}^{3}(k_z-k_{z,i}^u)(k_z-k_{z,i}^d)}e^{-j\bar{\mathbf{k}}\cdot(\bar{\mathbf{r}}-\bar{\mathbf{r}}')}d\bar{\mathbf{k}}. \quad (22)$$

In order to avoid singularities in the evaluation of $\bar{\bar{\mathbf{G}}}_{\mathbf{AJ}}$, we apply the Cauchy residue theorem to (22). The triple integral of $\bar{\bar{\mathbf{G}}}_{\mathbf{AJ}}$ is reduced to a double integral as:

$$\bar{\bar{\mathbf{G}}}_{\mathbf{AJ}}(\bar{\mathbf{r}},\bar{\mathbf{r}}')=\frac{j}{(2\pi)^2}\sum_{i=1}^{3}\begin{cases}\iint_{-\infty}^{+\infty}\frac{\bar{\bar{Z}}_A^a(k_{z,i}^u)}{det\bar{\bar{Z}}_A(k_{z,i}^u)}e^{-j\bar{k}_i^u\cdot(\bar{\mathbf{r}}-\bar{\mathbf{r}}')}dk_xdk_y, z\geq z'\\ \iint_{-\infty}^{+\infty}\frac{\bar{\bar{Z}}_A^a(k_{z,i}^d)}{det\bar{\bar{Z}}_A(k_{z,i}^d)}e^{-j\bar{k}_i^d\cdot(\bar{\mathbf{r}}-\bar{\mathbf{r}}')}dk_xdk_y, z\leq z'\end{cases}, \quad (23)$$

where the subscript $i=(1,2,3)$ is a cyclic index with a period of 3, and $h=(u,d)$ for:

$$\bar{k}_i^h=\hat{x}k_x+\hat{y}k_y+\hat{z}k_{z,i}^h, \quad (24)$$

$$det\bar{\bar{Z}}_A(k_{z,i}^h)=2\alpha_6k_{z,i}^h\sum_{m=1}^{2}(|k_{z,i}^h|^2-|k_{z,i+m}^h|^2). \quad (25)$$

$k_{z,i}^u$ and $k_{z,i}^d$ are couple positive and negative roots, so it's easily verified that there are the same result for any two points with the symmetry of (x',y') plane in Equation (23). So here we only derive the DGFA for $z\geq z'$. Let

$$\bar{\bar{\mathbf{G}}}_{\mathrm{A}}(k_{z,i}^u)=\frac{\bar{\bar{Z}}_A^a(k_{z,i}^u)}{det\bar{\bar{Z}}_A(k_{z,i}^u)}, \quad (26)$$

and by simplifying Equation (26), we obtain $i=(1,2)$ for:

$$\bar{\bar{\mathbf{G}}}_{\mathrm{A}}(k_{z,i}^u)=\begin{bmatrix}g_{i,1}(k_\rho)k_x^2 & g_{i,2}(k_\rho)k_xk_y & g_{i,3}(k_\rho)k_x\\ g_{i,2}(k_\rho)k_xk_y & g_{i,4}(k_\rho)k_y^2 & g_{i,5}(k_\rho)k_y\\ g_{i,3}(k_\rho)k_x & g_{i,5}(k_\rho)k_y & g_{i,6}(k_\rho)\end{bmatrix}, \quad (27)$$

and $i=3$ for:

$$\bar{\bar{\mathbf{G}}}_{\mathrm{A}}(k_{z,3}^u)=\begin{bmatrix}g_{3,1}(k_\rho)k_x^2 & g_{3,2}(k_\rho)k_xk_y & 0\\ g_{3,2}(k_\rho)k_xk_y & g_{3,3}(k_\rho)k_y^2 & 0\\ 0 & 0 & 0\end{bmatrix}, \quad (28)$$

where $g_{i,j}(k_\rho)$ is the function of k_ρ, $i=(1,2,3)$, $j=(1,2,3,4,5,6)$.

Substituting (27) and (28) into (23), we can see that each term in Equation (23) for $\mathrm{z}\geq\mathrm{z}'$ is reduced to a Sommerfeld integral [33] as:

$$\mathbf{G}_{\mathbf{AJ}}^{(i,j)}=\frac{1}{2\pi}F_{i,j}(\epsilon,\mu,\rho,\varphi)\int_0^{+\infty}f_{i,j}(k_{z,i}^u|k_\rho)J_n(k_\rho\rho)k_\rho^m\,dk_\rho, \quad (29)$$

where $F_{i,j}(\epsilon,\mu,\rho,\varphi)$ is the coefficient expression of $(\epsilon,\mu,\rho,\varphi)$, $\epsilon=(\epsilon_x,\epsilon_z)$, $\mu=(\mu_x,\mu_z)$, $m=(0,1,2,3)$. (ρ,φ) are the cylindrical coordinates of the projection of the source point on the (x,y) plane, and $\rho=$

$\sqrt{(x-x')^2+(y-y')^2}$. J_n is the Bessel function of order $n=(0,1)$. $f_{i,j}\left(k_{z,i}^u|k_\rho\right)$ is the function of $k_{z,i}^u$ which is expressed by k_ρ, and it shows as (30) for $l=(-1,0,1)$:

$$f_{i,j}\left(k_{z,i}^u|k_\rho\right)=\left(k_{z,i}^u\right)^l e^{-jk_{z,i}^u(z-z\prime)}. \quad (30)$$

So the spatial domain DGFA is a symmetric matrix, and it can be written as:

$$\bar{\bar{\mathbf{G}}}_{\mathbf{AJ}}(\bar{\mathbf{r}},\bar{\mathbf{r}}')=\begin{bmatrix}G_{11}&G_{12}&G_{13}\\G_{12}&G_{22}&G_{23}\\G_{13}&G_{23}&G_{33}\end{bmatrix}, \quad (31)$$

where

$$G_{11}=\mathbf{G}_{\mathbf{AJ}}^{(1,1)}+\mathbf{G}_{\mathbf{AJ}}^{(2,1)}+\mathbf{G}_{\mathbf{AJ}}^{(3,1)}, \quad (32)$$

$$G_{12}=\mathbf{G}_{\mathbf{AJ}}^{(1,2)}+\mathbf{G}_{\mathbf{AJ}}^{(2,2)}+\mathbf{G}_{\mathbf{AJ}}^{(3,2)}, \quad (33)$$

$$G_{13}=\mathbf{G}_{\mathbf{AJ}}^{(1,3)}+\mathbf{G}_{\mathbf{AJ}}^{(2,3)}, \quad (34)$$

$$G_{22}=\mathbf{G}_{\mathbf{AJ}}^{(1,4)}+\mathbf{G}_{\mathbf{AJ}}^{(2,4)}+\mathbf{G}_{\mathbf{AJ}}^{(3,3)}, \quad (35)$$

$$G_{23}=\mathbf{G}_{\mathbf{AJ}}^{(1,5)}+\mathbf{G}_{\mathbf{AJ}}^{(2,5)}, \quad (36)$$

$$G_{33}=\mathbf{G}_{\mathbf{AJ}}^{(1,6)}+\mathbf{G}_{\mathbf{AJ}}^{(2,6)}. \quad (37)$$

Because the Sommerfeld integrands of (29) have slow decaying and intensive oscillation, straightforward numerical integration methods are not efficient. In order to reach an accurate but efficient evaluation of (29), we need to change the integrands by the singularity subtraction method [31]. In this way, an equation with the same decaying and oscillation of Equation (29) was designed as:

$$M_{(i,j)}\left(k_{\rho,i}^*\right)=\int_0^{+\infty} f_{i,j}^*\left(k_{\rho,i}^*\right)J_n(k_{\rho,i}^*\rho_i^*)k_{\rho,i}^m\,dk_{\rho,i}^*, \quad (38)$$

where $k_{\rho,i}^*$ is the asymptotic form of $k_{z,i}^u$, and

$$\lim_{k_\rho\to\infty} k_{z,i}^u\approx jQ_i(\epsilon,\mu)k_\rho=jk_{\rho,i}^*, \quad (39)$$

$$\rho_i^*=\frac{\rho}{Q_i(\epsilon,\mu)}, \quad (40)$$

$Q_i(\epsilon,\mu)$ is the coefficient expression of (ϵ,μ), $\epsilon=(\epsilon_x,\epsilon_z)$, $\mu=(\mu_x,\mu_z)$. And there is an analytical solution for $M_{i,j}(k_{\rho,i}^*)$ by the following identity [35]:

$$\int_0^{+\infty} e^{-k_\rho\alpha}J_n(k_\rho\rho)k_\rho^m\,dk_\rho=(-1)^m\rho^{-n}\frac{d^m}{d\alpha^m}\left[\frac{\left(\sqrt{\rho^2+\alpha^2}-\alpha\right)^n}{\sqrt{\rho^2+\alpha^2}}\right], \quad (41)$$

where $\rho>0, n>-m-1$.

With the subtraction $M_{i,j}(k_{\rho,i}^*)$, Equation (29) can be deformed as:

$$\mathbf{G}_{\mathbf{AJ}}^{(i,j)}=\mathbf{G}_{\mathbf{AJ}}^{(i,j)}-\widetilde{\mathbf{G}}_{\mathbf{AJ}}^{(i,j)}+\widetilde{\mathbf{G}}_{i,j}, \quad (42)$$

where $\widetilde{\mathbf{G}}_{i,j}$ is the analytical solution of $\widetilde{\mathbf{G}}_{\mathbf{AJ}}^{(i,j)}$, and

$$\widetilde{\mathbf{G}}_{\mathbf{AJ}}^{(i,j)}=\frac{1}{2\pi}F_{i,j}(\epsilon,\mu,\rho,\varphi)M_{(i,j)}\left(k_{\rho,i}^*\right). \quad (43)$$

If $\rho=0$, there are singularities in Equation (29). So here we will discuss how to deal with this problem. As ρ approaches zero, the asymptotic behaviors of the cylindrical wave functions for $k_\rho\rho\to 0$ are:

$$J_0(k_\rho\rho)\sim 1, \quad (44)$$

$$J_0(k_\rho\rho)\sim\frac{k_\rho\rho}{2}. \quad (45)$$

Substituting (44) and (45) into (29), we can easily obtain the DGFA for $\rho\to 0$ as:

$$\bar{\bar{\mathbf{G}}}_{\mathbf{AJ}}(\bar{\mathbf{r}},\bar{\mathbf{r}}')=\begin{bmatrix}G_{11}&0&G_{13}\\0&G_{22}&G_{23}\\G_{13}&G_{23}&G_{33}\end{bmatrix}, \quad (46)$$

where

$$G_{11}=G_{22}=\int_0^{+\infty}C_1k_{z,1}^ue^{-jk_{z,1}^u(z-z')}k_\rho+C_2\frac{e^{-jk_{z,2}^u(z-z')}}{k_{z,2}^u}k_\rho^3+C_3\frac{e^{-jk_{z,3}^u(z-z')}}{k_{z,3}^u}k_\rho dk_\rho, \quad (47)$$

$$G_{13}=G_{31}=C_4(x-x')\int_0^{+\infty}k_\rho^3(e^{-jk_{z,1}^u(z-z')}-e^{-jk_{z,2}^u(z-z')})dk_\rho, \quad (48)$$

$$G_{23}=G_{32}=C_5(y-y')\int_0^{+\infty}k_\rho^3(e^{-jk_{z,1}^u(z-z')}-e^{-jk_{z,2}^u(z-z')})dk_\rho, \quad (49)$$

$$G_{33}=\int_0^{+\infty}C_6\frac{e^{-jk_{z,1}^u(z-z')}}{k_{z,1}^u}k_\rho^3+C_7k_{z,2}^ue^{-jk_{z,2}^u(z-z')}k_\rho dk_\rho, \quad (50)$$

C_i, $i=[1,2,3,4,5,6,7]$, is the coefficient expression of (ϵ,μ), $\epsilon=(\epsilon_x,\epsilon_z)$, $\mu=(\mu_x,\mu_z)$.

When $z=z'$, it is easily verified that $G_{11}=G_{22}=\infty$, $G_{33}=\infty$, $G_{13}=G_{31}=0$ and $G_{23}=G_{32}=0$. In this way, the DGFA becomes a diagonal dyad.

IV. NUMERICAL VALIDATION

The aforementioned derivations indicate the solution process of DGFA. However, it is difficult to verify the solutions because most commercial numerical simulation software computes field intensity **E** and **H** instead of magnetic vector potential **A**. Therefore, in this work, we verified our derivations for the DGFA in three steps. First, we calculated the $\bar{\bar{\mathbf{G}}}_{\mathbf{AJ}}$ for a degenerated case, i.e., for the unbounded isotropic medium since there was an analytical solution for $\bar{\bar{\mathbf{G}}}_{\mathbf{AJ}}$ in the isotropic media. In the second step, by using (18), also in the circumstance of an isotropic medium, we computed **E** from **A** which is assumed to be generated by an infinitesimal electric dipole source. We compared these calculated **E** field values to the results simulated by the commercial software COMSOL. Finally, following the similar procedure, we compared **E** field values computed from $\bar{\bar{\mathbf{G}}}_{\mathbf{AJ}}$ and those from COMSOL simulations but for uniaxial anisotropic media.

In the unbounded homogeneous isotropic space, the DGFA becomes an analytical scalar instead of a dyad. And it is expressed as:

$$\mathrm{g}(\bar{\mathbf{r}},\bar{\mathbf{r}}')=\mu\frac{e^{-jk|\bar{\mathbf{r}}-\bar{\mathbf{r}}'|}}{4\pi|\bar{\mathbf{r}}-\bar{\mathbf{r}}'|}. \quad (51)$$

In the computation, for case 1, we set that the permeability $\mu=10\mu_0$, the permittivity $\varepsilon=10\varepsilon_0$, and electric conductivity $\sigma=0.0001$S/m, where μ_0 and ε_0 are the permeability and permittivity in the free space. We choose a computation domain of 6 m × 6 m × 6 m, where 216 observation points are uniformly distributed. The electric dipole source is located in the center of the region, and the the operation frequency is 1 GHz. The $\bar{\bar{\mathbf{G}}}_{\mathbf{AJ}}$ dyadics of those 216 points evaluated by the Sommerfeld integrals in Equation (42) only show non-

zero diagonal values while having zero values in all the off-diagonal elements. Figure 1 shows the good agreements between DGFA computation and the analytical solutions for those non-zero diagonal elements. Only 72 of 216 points (sampled uniformly per three points) are shown to make the comparisons more discernable.

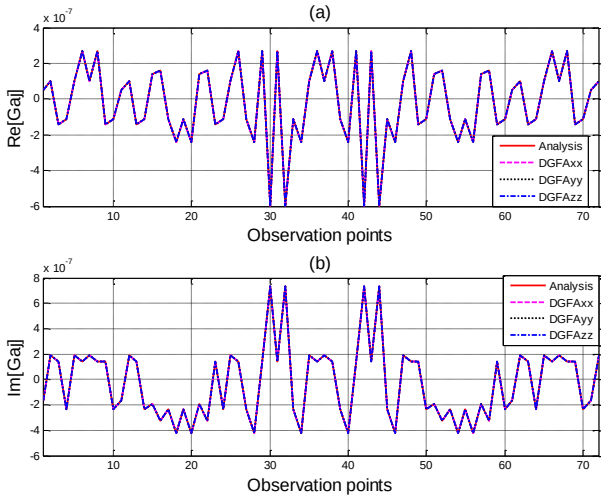

Fig. 1. Comparisons of the diagonal values of $\overline{\overline{\mathbf{G}}}_{\mathbf{AJ}}$ and the analytical solutions: (a) depicts the real part, and (b) depicts the imaginary part.

We define the relative error as:

$$Err_{ii} = \sqrt{\frac{\left\| \mathrm{g} - [\overline{\overline{\mathbf{G}}}_{\mathbf{AJ}}]_{ii} \right\|^2}{\|\mathrm{g}\|^2}}, \tag{52}$$

where $\| \|$ is L2 norm and $ii = (xx, yy, zz)$. Using this definition, we calculated the relative numerical error for the evaluation of $\overline{\overline{\mathbf{G}}}_{\mathbf{AJ}}$ and found that $Err_{xx} = 3.0772 \times 10^{-7}$, $Err_{yy} = 3.0772 \times 10^{-7}$, and $Err_{zz} = 3.0650 \times 10^{-7}$.

In order to save computation of resource for COMSOL simulation of electromagnetic wave propagating inside a homogeneous isotropic medium, we decreased the computation domain to $0.3\ \mathrm{m} \times 0.3\ \mathrm{m} \times 0.3\ \mathrm{m}$. We performed the simulations for two cases. In case 2, we set $\mu = \mu_0$, $\varepsilon = \varepsilon_0$ and $\sigma = 0.0001$ S/m. In case 3, we set $\mu = 0.1\mu_0$, $\varepsilon = 0.1\varepsilon_0$ and $\sigma = 0.0001$ S/m. The 216 observation points are also uniformly distributed within the domain. The electric dipole polarized by (1,1,1) is located in the center of the region and radiates 1 GHz electromagnetic waves. In the COMSOL simulation models, the source location as well as its polarization and the electrical parameters such as μ, ε and σ are the same as those used in the DGFA computation. The mesh sizes are set to be 'EXTRA FINE' and the thickness of the perfect match layers (PML) is set as 0.15 m which are located outside the computation domain. The mesh sizes and PML thickness are the same for all the COMOSL simulations presented in this paper. When we computed **E** from **A** using (18), numerical central differential method was applied to gradient and divergence operation.

The comparisons for the electric fields among analytic solutions, calculations from DGFA $\overline{\overline{\mathbf{G}}}_{\mathbf{AJ}}$ and simulations by COMSOL are shown in Fig. 2. Here, only 54 (sampled uniformly per four points) representative points of 216 are chosen to make the comparisons more discernable. Moreover, we only show the *x*-component comparisons for case 2 while *y*-component comparisons for case 3. Comparisons for other components are not presented since they are similar as those for the *x*-component or the *y*-component. In order to evaluate the computation error, we give an error definition similar as (52):

$$Err_i = \sqrt{\frac{\|E_{ana} - E_i\|^2}{\|E_{ana}\|^2}}, \tag{53}$$

where $i = (COMSOL, DGFA)$ and E_{ana} is the analytical solution calculated using (51).

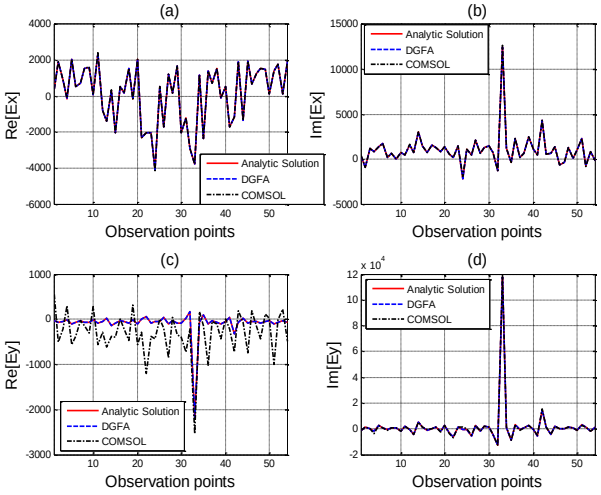

Fig. 2. Comparisons of electric fields computed by analytical methods, using DGFA and from COMSOL simulations in an isotropic medium: (a) and (b) are for case 2; (c) and (d) are for case 3; (a) and (c) depict the real parts while (b) and (d) depict the imaginary parts.

Figures 2 (a) and (b) show the comparisons of E_x in case 2. The relative error between calculations using DGFA and the analytical solutions is 9.441×10^{-8}. The relative error between COMSOL simulations and the analytical solutions is 9.9×10^{-3}. We can see that the x-components of **E** computed in three ways show good agreements. Figures 2 (c) and (d) show the comparisons of E_y in case 3. The relative error between calculations using DGFA and the analytical solutions is 1.2608×10^{-7}. The relative error between COMSOL simulations and the analytical solutions is 3.14×10^{-2}. There is an obvious mismatch between COMSOL simulations and

analytical solutions in Fig. 2 (c). Actually, not only the E_y real part has this mismatch, but also the real part of E_x and E_z which are not shown here. This mismatch may be due to that the imaginary part is around 50 times larger than the real part and thus the numerical iteration precision cannot be maintained for the real parts which have much smaller values.

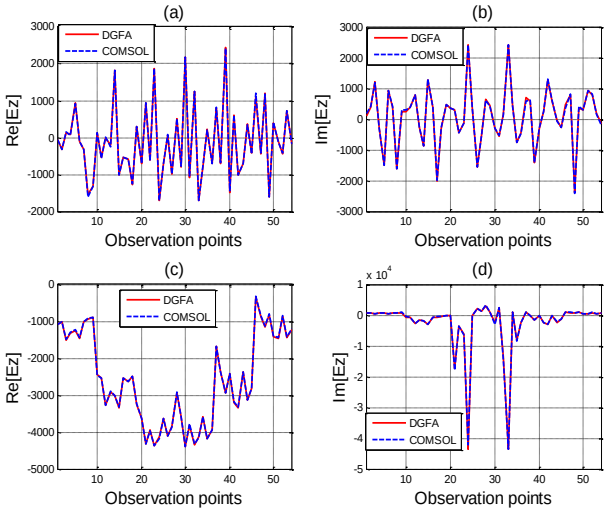

Fig. 3. Comparisons of electric fields computed using DGFA and from COMSOL simulations in an uniaxial anisotropic medium: (a) and (b) are for case 4; (c) and (d) are for case 5; (a) and (c) depict the real parts while (b) and (d) depict the imaginary parts.

In aforementioned two steps, we verified the derivation of $\bar{\bar{\mathbf{G}}}_{\mathbf{AJ}}$ in the circumstance of isotropic media. Now let us check its correctness inside a uniaxial anisotropic media. Since there is no analytical solution for the **E** field in uniaxial anisotropic media, we only compare the electric fields computed using $\bar{\bar{\mathbf{G}}}_{\mathbf{AJ}}$ and simulated by COMSOL. The simulation domain, observation points, the source dipole position as well as its polarization are the same as in previous case 2 and case 3. However, we use following dielectric parameters in case 4:

$$\bar{\bar{\mu}} = \mu_0 \begin{bmatrix} 1 & 0 & 0 \\ 0 & 1 & 0 \\ 0 & 0 & 5 \end{bmatrix}, \ \bar{\bar{\varepsilon}} = \varepsilon_0 \begin{bmatrix} 1 & 0 & 0 \\ 0 & 1 & 0 \\ 0 & 0 & 5 \end{bmatrix},$$
$$\bar{\bar{\sigma}} = \begin{bmatrix} 0.001 & 0 & 0 \\ 0 & 0.001 & 0 \\ 0 & 0 & 0.005 \end{bmatrix} \text{S/m}. \quad (54)$$

And we use following dielectric parameters in case 5:

$$\bar{\bar{\mu}} = \mu_0 \begin{bmatrix} 1 & 0 & 0 \\ 0 & 1 & 0 \\ 0 & 0 & 0.1 \end{bmatrix}, \ \bar{\bar{\varepsilon}} = \varepsilon_0 \begin{bmatrix} 1 & 0 & 0 \\ 0 & 1 & 0 \\ 0 & 0 & 0.1 \end{bmatrix},$$
$$\bar{\bar{\sigma}} = \begin{bmatrix} 0.001 & 0 & 0 \\ 0 & 0.001 & 0 \\ 0 & 0 & 0.0001 \end{bmatrix} \text{S/m}. \quad (55)$$

Figure 3 shows the comparisons of z-component of E between calculations using DGFA and simulations by COMSOL. Here, we also choose 54 representative points. We can see that E_z values are highly consistent for two computation methods for both real parts and imaginary parts in two cases. If the relative error between these two results is defined as:

$$Err_{CD} = \sqrt{\frac{\|E_{DGFA} - E_{COMSOL}\|^2}{\|E_{DGFA}\|^2}}. \quad (56)$$

The error for case 4 is 2.32×10^{-2}, and, 3.33×10^{-2} for case 5.

In our work, we use the singularity subtraction method [31] to accelerate the integral process of Equation (29), which is calculated segment by segment on the Sommerfeld integral path until the desired accuracy is obtained [31]. If the efficiency improvement is defined as:

$$Effi = \frac{ISN_{wo} - ISN_w}{ISN_{wo}}, \quad (57)$$

where *ISN* is the number of the segments for the Sommerfeld integrals, and subscript *wo/w* means without/with subtraction.

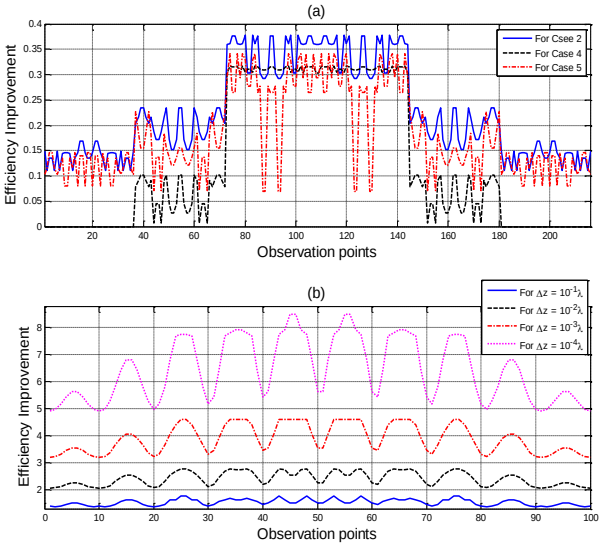

Fig. 4. Efficiency improvements for different cases through the singularity subtraction method: (a) is for case 2, case 4 and case 5; (b) is for extreme cases in which observation points get closer to the z' plane.

Figure 4 shows the efficiency improvements by the subtraction method. Figure 4 (a) displays the results for case 2, case 4 and case 5. It is clear that the efficiency improvements are different for different observation points. When the observation points are far from the source point in the z direction, i.e., when $|z - z'|$ values are large, the efficiency improvements are not obvious. However, when $|z - z'|$ becomes smaller, efficiency improvements become obvious, and reach about 30%

in case 2, case 4 and case 5. We further decrease the distance in the *z* direction between the source point and field points to verify the efficiency improvement. Figure 4 (b) shows the results for $\Delta z = |z - z'|$ of $10^{-1}\lambda$, $10^{-2}\lambda$, $10^{-3}\lambda$ and $10^{-4}\lambda$. All the computation is performed in the same background medium with dielectric parameter shown in (54). And 100 observation points are uniformly distributed in the computation domain. Clearly, after the subtraction, the smaller is Δz, the larger is the efficiency improvement. If the observation points are placed in the source plane, i.e., $|z - z'| = 0$, it is easy to verify that Equation (29) can't converge, but Equation (42) can converge with very few number of the integral segments under the desired accuracy. Therefore, the efficiency improvement by the singularity subtraction method becomes more significant when the observation points get closer to the source point in the *z* direction.

V. SUMMARY AND CONCLUSIONS

In this paper, the DGFA formula for the unbounded uniaxial anisotropic media were derived. Starting from Maxwell's equations and through the forward and inverse spatial Fourier transforms, DGFA formula in the integral forms were obtained for three-dimensional cases. Based upon Cauchy residue theorem, the closed form of DGFA formula were finally simplified to one-dimensional Sommerfeld integrals. By applying the singularity subtraction method and Gaussian quadrature, we can efficiently and accurately evaluate these Sommerfeld integrals. The numerical accuracy was only restricted by the Gaussian quadrature. In an effort to verify our derivations for those formula, we compared our results with analytical and simulated results in the circumstance of isotropic and uniaxial anisotropic media respectively. These comparisons showed that the results obtained from the DGFA and those by analytical methods and numerical simulations agreed well. The effect of the singularity subtraction was validated by several numerical experiments. Hence, the derivation and evaluation of DGFA presented in this paper are reliable and efficient.

ACKNOWLEDGMENT

This work was supported by the National Natural Science Foundation of China under Grant No. 41504120, and the Education Department of Fujian Province, China under Grant No. JA14005.

APPENDIX A. EXPRESSIONS OF $\bar{\bar{Z}}_E$

$$\bar{\bar{Z}}_E = \begin{bmatrix} Z_{E,11} & Z_{E,12} & Z_{E,13} \\ Z_{E,21} & Z_{E,22} & Z_{E,23} \\ Z_{E,31} & Z_{E,32} & Z_{E,33} \end{bmatrix}, \quad \text{(A1)}$$

where:

$$Z_{E,11} = \frac{\varepsilon_x^2}{\mu_z\varepsilon_z^2}\frac{\partial^2}{\partial x^2} + \frac{1}{\mu_z}\frac{\partial^2}{\partial y^2} + \frac{1}{\mu_x}\frac{\partial^2}{\partial z^2} + \omega^2\varepsilon_x, \quad \text{(A2)}$$

$$Z_{E,12} = -\frac{1}{\mu_z}\frac{\partial^2}{\partial x \partial y} + \frac{\varepsilon_x^2}{\mu_z\varepsilon_z^2}\frac{\partial^2}{\partial x \partial y}, \quad \text{(A3)}$$

$$Z_{E,13} = -\frac{1}{\mu_x}\frac{\partial^2}{\partial x \partial z} + \frac{\varepsilon_x}{\mu_z\varepsilon_z}\frac{\partial^2}{\partial x \partial z}, \quad \text{(A4)}$$

$$Z_{E,21} = Z_{E,12}, \quad \text{(A5)}$$

$$Z_{E,22} = \frac{1}{\mu_z}\frac{\partial^2}{\partial x^2} + \frac{\varepsilon_x^2}{\mu_z\varepsilon_z^2}\frac{\partial^2}{\partial y^2} + \frac{1}{\mu_x}\frac{\partial^2}{\partial z^2} + \omega^2\varepsilon_x, \quad \text{(A6)}$$

$$Z_{E,23} = -\frac{1}{\mu_x}\frac{\partial^2}{\partial y \partial z} + \frac{\varepsilon_x}{\mu_z\varepsilon_z}\frac{\partial^2}{\partial y \partial z}, \quad \text{(A7)}$$

$$Z_{E,31} = Z_{E,13}, \quad \text{(A8)}$$

$$Z_{E,32} = Z_{E,23}, \quad \text{(A9)}$$

$$Z_{E,33} = \frac{1}{\mu_x}\left(\frac{\partial^2}{\partial x^2} + \frac{\partial^2}{\partial y^2}\right) + \frac{1}{\mu_z}\frac{\partial^2}{\partial z^2} + \omega^2\varepsilon_z. \quad \text{(A10)}$$

APPENDIX B. EXPRESSIONS OF $\bar{\bar{Z}}_A$

$$\bar{\bar{Z}}_A = \begin{bmatrix} Z_{A,11} & Z_{A,12} & Z_{A,13} \\ Z_{A,21} & Z_{A,22} & Z_{A,23} \\ Z_{A,31} & Z_{A,32} & Z_{A,33} \end{bmatrix}, \quad \text{(B1)}$$

where:

$$Z_{A,11} = \omega^2\varepsilon_x - \frac{k_x^2\varepsilon_x^2}{\mu_z\varepsilon_z^2} - \frac{k_y^2}{\mu_z} - \frac{k_z^2}{\mu_x}, \quad \text{(B2)}$$

$$Z_{A,12} = \left(\frac{1}{\mu_z} - \frac{\varepsilon_x^2}{\mu_z\varepsilon_z^2}\right)k_x k_y, \quad \text{(B3)}$$

$$Z_{A,13} = \left(\frac{1}{\mu_x} - \frac{\varepsilon_x}{\mu_z\varepsilon_z}\right)k_x k_z, \quad \text{(B4)}$$

$$Z_{A,21} = Z_{A,12}, \quad \text{(B5)}$$

$$Z_{A,22} = \omega^2\varepsilon_x - \frac{k_x^2}{\mu_z} - \frac{k_y^2\varepsilon_x^2}{\varepsilon_z^2\mu_z} - \frac{k_z^2}{\mu_x}, \quad \text{(B6)}$$

$$Z_{A,23} = \left(\frac{1}{\mu_x} - \frac{\varepsilon_x}{\mu_z\varepsilon_z}\right)k_y k_z, \quad \text{(B7)}$$

$$Z_{A,31} = Z_{A,13}, \quad \text{(B8)}$$

$$Z_{A,32} = Z_{A,23}, \quad \text{(B9)}$$

$$Z_{A,33} = \omega^2\varepsilon_z - \frac{k_x^2}{\mu_x} - \frac{k_y^2}{\mu_x} - \frac{k_z^2}{\mu_z}. \quad \text{(B10)}$$

APPENDIX C. EXPRESSIONS OF $\bar{\bar{Z}}_A$

$$\bar{\bar{W}}_E = \begin{bmatrix} W_{E,11} & W_{E,12} & W_{E,13} \\ W_{E,21} & W_{E,22} & W_{E,23} \\ W_{E,31} & W_{E,32} & W_{E,33} \end{bmatrix}, \quad \text{(C1)}$$

where:

$$W_{E,11} = \omega^2\varepsilon_x - \frac{k_y^2}{\mu_z} - \frac{k_z^2}{\mu_x}, \quad \text{(C2)}$$

$$W_{E,12} = \frac{k_x k_y}{\mu_z}, \quad \text{(C3)}$$

$$W_{E,13} = \frac{k_x k_z}{\mu_x}, \quad \text{(C4)}$$

$$W_{E,21} = W_{E,12}, \quad \text{(C5)}$$

$$W_{E,22} = \omega^2\varepsilon_x - \frac{k_x^2}{\mu_z} - \frac{k_z^2}{\mu_x}, \quad \text{(C6)}$$

$$W_{E,23} = \frac{k_y k_z}{\mu_x}, \quad \text{(C7)}$$

$$W_{E,31} = W_{E,13}, \quad \text{(C8)}$$

$$W_{E,32} = W_{E,23}, \quad \text{(C9)}$$

$$W_{E,33} = \omega^2\varepsilon_z - \frac{k_x^2}{\mu_x} - \frac{k_y^2}{\mu_x}. \quad \text{(C10)}$$

REFERENCES

[1] M. J. Havrilla, "Scalar potential depolarizing dyad

artifact for a uniaxial medium," *Progress In Electromagnetics Research*, vol. 134, no. 1, pp. 151-168, 2013.

[2] M. J. Havrilla, "Scalar potential formulation for a uniaxial inhomogeneous medium," *Radio Science Meeting (USNC-URSI NRSM)*, 2014.

[3] W. S. Weiglhofer and S. O. Hansen, "Faraday chiral media revisited. I. Fields and sources," *IEEE Transactions on Antennas and Propagation*, vol. 47, no. 5, pp. 807-814, 1999.

[4] A. Y. Qing, "Electromagnetic inverse scattering of multiple perfectly conducting cylinders by differential evolution strategy with individuals in groups (GDES)," *IEEE Transactions on Antennas and Propagation*, vol. 52, no. 5, pp. 1223-1229, 2004.

[5] L. P. Zha, R. S. Chen, and T. Su, "Fast EM scattering analysis for the hard targets in a layered medium by using the hierarchical vector basis functions," *Applied Computational Electromagnetics Society Journal*, vol. 30, no. 11, pp. 1154-1160, 2015.

[6] J. L. Hu, Z. P. Wu, H. Mccann, L. E. Davis, and C. G. Xie, "Sequential quadratic programming method for solution of electromagnetic inverse problems," *IEEE Transactions on Antennas and Propagation*, vol. 53, no. 8, pp. 2680-2687, 2005.

[7] D. W. Winters, B. D. Van Veen, and S. C. Hagness, "A sparsity regularization approach to the electromagnetic inverse scattering problem," *IEEE Transactions on Antennas and Propagation*, vol. 58, no. 1, pp. 145-154, 2010.

[8] X. M. Xu and Q. H. Liu, "The BCGS-FFT method for electromagnetic scattering from inhomogeneous objects in a planarly layered medium," *IEEE Antennas and Wireless Propagation Letters*, vol. 1, no. 1, pp. 77-80, 2002.

[9] F. H. Li, L. P. Song, and Q. H. Liu, "Three-dimensional reconstruction of objects buried in layered media using born and distorted born iterative methods," *IEEE Antennas and Wireless Propagation Letters*, vol. 1, no. 2, pp. 107-111, 2004.

[10] M. Pastorino, M. Raffetto, and A. Randazzo, "Electromagnetic inverse scattering of axially moving cylindrical targets," *IEEE Transactions on Geoscience and Remote Sensing*, vol. 53, no. 3, pp. 1452-1462, 2015.

[11] J. G. Wang, Z. Q. Zhao, Z. P. Nie, and Q. H. Liu, "Electromagnetic inverse scattering series method for positioning three-dimensional targets in near-surface two-layer medium with unknown dielectric properties," *IEEE Geoscience and Remote Sensing Letters*, vol. 12, no. 2, pp. 299-303, 2015.

[12] J. L. Xiong and W. C. Chew, "A newly developed formulation suitable for matrix manipulation of layered medium Green's functions," *IEEE Transactions on Antennas and Propagation*, vol. 58, no. 3, pp. 868-875, 2010.

[13] A. Yakovlev, S. Ortiz, et al., "Electric dyadic Green's functions for modeling resonance and coupling effects in waveguide-based aperture-coupled patch arrays," *Applied Computational Electromagnetics Society Journal*, vol. 17, no. 2, pp. 123-133, 2002.

[14] P. M. Smith, "Dyadic Green's functions for multi-layer SAW substrates," *IEEE Transactions on Ultrasonics, Ferroelectrics, and Frequency Control*, vol. 48, no. 1, pp. 171-179, 1999.

[15] G. W. Hanson, "Dyadic Green's function for a multilayered planar medium-A dyadic eigen-function approach," *IEEE Transactions on Antennas and Propagation*, vol. 52, no. 12, pp. 3350-3356, 2004.

[16] E. Simsek and Q. H. Liu, "Fast computation of dyadic Green's function for layered media and its application in interconnect simulations," *IEEE Transactions on Antennas and Propagation*, vol. 3, no. 3, pp. 2783, 2004.

[17] K. A. Michalski and J. R. Mosig, "Multilayered media Green's functions in integral equation formulations," *IEEE Transactions on Antennas and Propagation*, vol. 45, no. 3, pp. 508-519, 1997.

[18] P. G. Cottis, C. N. Vazouras, and C. Spyrou, "Green's function for an unbounded biaxial medium in cylindrical coordinates," *IEEE Transactions on Antennas and Propagation*, vol. 47, no. 1, pp. 195-276 199, 1999.

[19] P. G. Cottis and G. D. Kondylis, "Properties of the dyadic Green's function for an unbounded anisotropic medium," *IEEE Transactions on Antennas and Propagation*, vol. 43, no. 2, pp. 154-279 161, 1995.

[20] Y. Huang and J. K. Lee, "Dyadic green's functions for unbounded and two-layered general anisotropic media," *Progress In Electromagnetics Research B*, vol. 30, no. 30, pp. 27-46, 2011.

[21] F. L. Mesa, R. Marques, and M. Horno, "A general algorithm for computing the bidimensional spectral Green's dyad in multilayered complex bian-isotropic media: The equivalent boundary method," *IEEE Transactions on Microwave Theory and Techniques*, vol. 39, no. 9, pp. 1640-1649, 1991.

[22] A. Eroglu, Y. H. Lee, and J. K. Lee, "Dyadic Green's functions for multi-layered uniaxially anisotropic media with arbitrarily oriented optic axes," *IET Microwaves, Antennas, Propagation*, vol. 5, no. 15, pp. 1779-1788, 2011.

[23] P. P. Ding, C. W. Qiu, Z. Sad, and S. P. Yeo, "Rigorous derivation and fast solution of spatial domain Green's functions for uniaxial anisotropic multilayers using modified fast Hankel transform

method," *IEEE Transactions on Microwave Theory and Techniques*, vol. 60, no. 2, pp. 205-217, 2012.
[24] S. M. Ali and S. F. Mahoud, "Electromagnetic fields of buried sources in stratified anisotropic media," *IEEE Transactions on Antennas and Propagation*, vol. 27, no. 5, pp. 671-678, 1979.
[25] D. H. Werner, "An exact integration procedure for vector potentials of thin circular loop antennas," *IEEE Transactions on Antennas and Propagation*, vol. 44, no. 8, pp. 157-165, 1996.
[26] N. Georgieva, Z. Z. Chen, and P. Bhartia, "Analysis of transient electromagnetic fields based on the vector potential function," *IEEE Transactions on Magnetics*, vol. 35, no. 3, pp. 1410-1413, 1999.
[27] F. De. Flaviis, M. G. Noro, R. E. Diaz, G. Franceschetti, and N. G. Alexopoulos, "A time-domain vector potential formulation for the solution of electromagnetic problems," *IEEE Microwave and Guided Wave Letters*, vol. 8, no. 9, pp. 310-312, 1998.
[28] Z. R. Yu, W. J. Zhang, and Q. H. Liu, "A mixed-order stabilized bi-conjugate gradient FFT method for magnetodielectric objects," *IEEE Transactions on Antennas and Propagation*, vol. 62, no. 11, pp. 5647-5655, 2014.
[29] Z. R. Yu, W. J. Zhang, and Q. H. Liu, "The mixed-order BCGS-FFT method for the scattering of three-dimensional inhomogeneous anisotropic magneto-dielectric objects," *IEEE Transactions on Antennas and Propagation*, vol. 63, no. 12, pp. 5709-5717, 2015.
[30] R. D. Nevels and J. Jeong, "Time domain coupled field dyadic Green function solution for Maxwell's equations," *IEEE Transactions on Antennas and Propagation*, vol. 56, no. 8, pp. 2761-2764, 2008.
[31] J. H. Moran and S. Gianzero, "Effects of formation anisotropy on resistivity-logging measurements," *Geophysics*, vol. 44, no. 7, pp. 1266-1286, 1979.
[32] A. Abubakar and T. M. Habashy, "A closed-form expression of the electromagnetic tensor Green's functions for a homogeneous TI-anisotropic medium," *IEEE Geoscience and Remote Sensing Letters*, vol. 3, no. 4, pp. 447-451, 2006.
[33] E. Simsek, Q. H. Liu, and B. J. Wei, "Singularity subtraction for evaluation of Green's functions for multilayer media," *IEEE Transactions on Microwave Theory and Techniques*, vol. 54, no. 1, pp. 216-225, 2006.
[34] W. C. Chew, "Vector potential electromagnetics with generalized gauge for inhomogeneous media: Formulation," *Progress in Electromagnetics Research*, vol. 149, pp. 69-84, 2014.
[35] A. Jeffrey and D. Zwillinger, *Table of Integrals, Series, and Products*. Elsevier, Burlington, 2007.

Jianliang Zhuo received the B.S. degree in Communication Engineering and Business Administration, and the M.S. degree in Communication and Information System from the University of Electronic Science and Technology of China, Chengdu, China, in 2007 and 2011. He is currently pursuing the Ph.D. degree at Xiamen University, Xiamen, China. His research interests include fast forward solvers in electromagnetics and inverse scattering methods for microelectronics and RF system

Feng Han received his B.S. degree in Electronic Science from Beijing Normal University and M.S. degree in Geophysics from Peking University, China, in 2003 and 2006, respectively. He received his Ph.D. in Electrical Engineering from Duke University, USA, in 2011. He is currently working as an Assistant Professor with the Institute of Electromagnetics and Acoustics, Xiamen University, China. His current research interests include ionosphere remote sensing by radio atmospherics, electromagnetic full wave inversion by integral equations, reverse time migration image, and the design of electromagnetic detection system.

Na Liu received the Ph.D. degree in Computational Mathematics from University of Chinese Academy of Sciences, Beijing, China, in 2013. From April 2012 to April 2013, she was a visiting student in the Department of Electrical and Computer Engineering, Duke University, Durham, NC. From November 2013 to January 2017, she was a Post-doctoral with Xiamen University where she is now an Associate Professor in Institute of Electromagnetics and Acoustics, Xiamen University, China. Her research is on computational electromagnetics, especially the fast and efficient methods for complex media and their applications in cavities, optical waveguide problems.

Longfang Ye received the Ph.D. degree in Electromagnetic Field and Microwave Technology from the University of Electronic Science and Technology of China, Chengdu, China, in 2013. From Oct. 2011 to Jan. 2013, he was a visiting student at Massachusetts Institute of Tech-

nology, Cambridge, MA, USA. Since July 2013, he has been an Assistant Professor with the Institute of Electromagnetics and Acoustics and Department of Electronic Science, Xiamen University, Xiamen, China. His current research interests include microwave circuits and antennas, terahertz waveguides and graphene-based devices.

Hai Liu received his B.E. and M.E. degrees in Civil Engineering from Tongji University, Shanghai, China, in 2007 and 2009, respectively. He received his Ph.D. in Environmental Studies from Tohoku University, Sendai, Japan in 2013. He is currently working as an Assistant Professor with the Institute of Electromagnetics and Acoustics, Xiamen University, Xiamen, China. He was with the Center for Northeast Asian Studies at Tohoku University, Sendai, Japan as a Research Fellow from April 2013 to March 2014. His current research interests include the development of ground-penetrating radar systems and algorithms for a wide variety of applications, such as non-destructive testing in civil engineering, environmental monitoring, archeological investigation and lunar exploration.

Qing Huo Liu received his B.S. and M.S. degrees in Physics from Xiamen University, China in 1983 and 1986, and Ph.D. degree in Electrical Engineering from the University of Illinois at Urbana-Champaign in 1989. His research interests include computational electromagnetics and acoustics, inverse problems, and their applications in nanophotonics, geophysics, biomedical imaging, and electronic packaging. He has published over 400 papers in refereed journals and 500 papers in conference proceedings. He was with the Electromagnetics Laboratory at the University of Illinois at Urbana-Champaign as a Research Assistant from September 1986 to December 1988, and as a Postdoctoral Research Associate from January 1989 to February 1990. He was a Research Scientist and Program Leader with Schlumberger-Doll Research, Ridgefield, CT from 1990 to 1995. From 1996 to May 1999 he was an Associate Professor with New Mexico State University. Since June 1999 he has been with Duke University where he is now a Professor of Electrical and Computer Engineering. He received the 2017 ACES Technical Achievement Award.

Performance of a Massively Parallel Method of Moment Solver and Its Application

Yan Chen, Zhongchao Lin*, Daniel Garcia-Donoro, Xunwang Zhao, and Yu Zhang

School of Electronic Engineering
Xidian University, Xi'an, Shaanxi 710071, China
zclin@xidian.edu.cn

Abstract ─ A massively parallel Method of Moment (MoM) solver able to run on 200,000 CPU cores and solve matrices larger than 1.3 million unknowns is presented. The solver implements a novel LU decomposition algorithm based on the Communication Avoiding LU (CALU) scheme. By using a new pivoting policy, the communication between processes is improved enhancing the parallel speed up of the algorithm. Solver effectiveness and performance are demonstrated comparing the results with two of the most important math libraries used by direct dense solvers: the commercial MKL and the open source ScaLapack. Results show how simulation time is reduced significantly thanks to this novel LU decomposition algorithm making possible the simulation of incredibility electrically large problems using MoM.

Index Terms ─ Communication avoiding, high performance, LU decomposition, massively parallel, method of moments.

I. INTRODUCTION

Nowadays the analysis of extremely large structures is of crucial interest in military (and also civil) electromagnetic applications. The use of higher working frequencies makes the analysis of these structures, despite the constant enhancement in computer power, a challenge.

Among the pure numerical techniques employed in these analyses such as Finite Element Method (FEM) [1], Finite Difference Time Domain (FDTD) [2] or Method of Moments (MoM) [3], is the latter one that can provide the most accurate results for a wide variety of complex electromagnetic problems. However, the memory requirement and the computing complexity of MoM grow rapidly with $O(N^2)$ and $O(N^3)$, respectively, where N is the number of unknowns [4]. Thus, subject to these constraints, the applications of MoM for the simulation of extremely large structures are seriously limited.

In order to breaks these restriction, researchers have been employing several types of eclectic approaches; hybrid algorithms, as for example, the hybridization of MoM with high frequency methods [5, 6] or fast algorithms such as the fast multiple method (FMM) [7, 8]. These approaches reduce the memory requirement and the computation complexity; however, hybrid algorithms pay the price of losing accuracy, and the fast algorithms may be confronted with slow convergence or even divergence issues in applications involving complex structures and various materials.

It is worth noting that another approach must be considered without the needed of changing MoM as main numerical method keeping, in this way, the accuracy on the results. Along with the latest developments on computer technology, the use of parallel High Performance Computing (HPC) techniques on supercomputer platforms, with thousands of terabytes (TB) of memory available for simulation, can expand massively the application of MoM for extremely large analyses.

Working on the latter approach, authors have been developing during the last years their own numerical tools, being able to solve electromagnetic problem up to 1.0 million unknowns [9] by using a direct dense LU out-of-core solver [10]. Some of the previous work done by authors [4, 11] was focused on the use of LU factorization algorithms provided by the Intel Math Kernel Library (MKL) [12]. However, MKL does not always perform efficiently on some homemade platforms, especially when the communication components are based on Message Passing Interface (MPI) [13] techniques. Contrarily, if OpenMP [14] or other shared-memory parallel technique as the Basic Linear Algebra Subroutines (BLAS) [12] is used, MKL always performs well on Intel's CPU. Thus, one straightforward idea can be the use of open source parallel math libraries based on MPI techniques that help MKL to deal with its problems with MPI. One of the most important open source libraries of this kind is the well-known ScaLapack library [14]. This combination can not only make full use of the high-speed network, but also the full performance of the CPU cores, improving the simulation speed. With this point of view in mind, the already mentioned direct dense LU out-of-core solver was developed and expanded to 4096 CPU

Submitted On: December 29, 2016
Accepted On: August 12, 2017

1054-4887 © ACES

cores with a parallel efficiency higher than 60% in [16].

However, it is worth to mention that the framework of ScaLapack is not the best scheme for parallelization. The computation and communication model of this framework were analyzed in detail in [16], concluding that the block of columns involved on each step of the factorization process (called panel factorization) is located in a critical position. The factorization process based on classic algorithm as Gaussian elimination with partial pivoting (GEPP) is not able to minimize the number of message exchange because of its pivoting strategy, which requires to permute the element of maximum magnitude to the diagonal position at each step in the panel factorization leading to a poor parallel performance. Then, better LU decomposition algorithms are required to break this poor parallel performance and improve the simulation time on supercomputer platforms with hundred thousand of CPU cores available. Under this scenario, authors have implemented a novel LU decomposition algorithm that drastically enhances the parallel performance of traditional LU decomposition algorithms enabling the possibility of running electrically large simulation on supercomputer efficiently. This novel LU decomposition algorithm takes, as starting point on its development, the Communication Avoiding LU (CALU) algorithm proposed and studied in [17] and [18]. However, mayor changes on the commutation scheme and the pivoting strategy help us to reduce the number and volume of the message exchanged between processes.

The paper presents the performance of a massively parallel MoM solver where the mentioned novel LU decomposition algorithm is included. Thanks to this technique the solver is able to run on more than 200,000 CPU cores and solve problems larger than 1.5 million unknowns. In order to demonstrate its effectiveness, the numerical results of three different benchmarks are compared with two of the most important math libraries used by direct dense solvers: the commercial MKL and the open source library ScaLapack.

II. ELECTROMAGNETIC THEORY

A briefly review about the integral equation form and the basis functions employed by the solver to approximate the solution are given in this Section.

The solver is based on the solution of surface integral equations in frequency domain for the equivalent electric and magnetic currents over the dielectric boundary surfaces and electric currents only over perfect electric conductors (PECs). The set of integral equations obtained are solved by using MoM, and specifically using the Galerkin's method. The solver is able to handle inhomogeneous dielectrics categorized by a combination of various homogeneous dielectrics. Therefore, any composite metallic and dielectric electromagnetic structure can be represented by a finite number of linear, homogeneous and isotropic regions radiating in an unbounded linear, homogeneous and isotropic environment.

The integral equation employed is a general form of the Poggio-Miller-Chang-Harrington-Wu (PMCHW) formulation [4]. When one of the boundary surfaces between the two different regions is PEC, the magnetic currents are equal to zero at the boundary surface and that equation degenerates into the electric field integral equation (EFIE).

Flexible geometric modeling is achieved by using bilinear quadrilateral patches to characterize surfaces, as shown in Fig. 1 (a). Efficient approximation for the unknown currents is obtained by using the higher-order basis functions (HOBs) consisting of combinations of polynomials, which are of the following form:

$$\boldsymbol{F}_{ij}(p,s) = \frac{\boldsymbol{\alpha}_s}{\left|\boldsymbol{\alpha}_p \times \boldsymbol{\alpha}_s\right|} p^i s^j, \quad -1 \le p \le 1, \quad -1 \le s \le 1 \tag{1}$$

where, p and s are the local coordinates, i and j are the orders of basis functions, and $\boldsymbol{\alpha}_p$ and $\boldsymbol{\alpha}_s$ are covariant unitary vectors [4]. The polynomials can also be used as the basis functions for wire structures. In this case, truncated cones are used for geometric modeling, as shown in Fig. 1 (b). In the thin-wire model, the circumferential variation of the currents on the wires is neglected, and in addition the length of the wire should be at least 10 times larger than its radius.

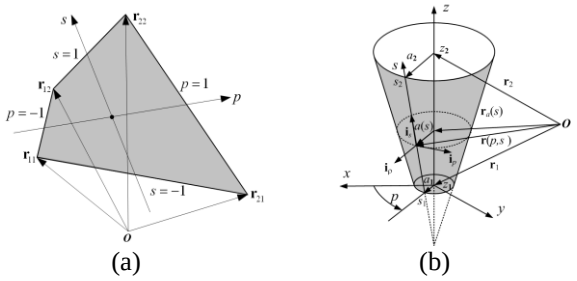

(a) (b)

Fig. 1. Geometric modeling for higher-order basis functions: (a) a bilinear quadrilateral patch defined by four vertices with the position vectors of $\boldsymbol{r}_{11}$, $\boldsymbol{r}_{21}$, $\boldsymbol{r}_{12}$ and $\boldsymbol{r}_{22}$, and (b) a truncated cone defined by position vectors and radii of its beginning and end, characterized by $\boldsymbol{r}_1$, a_1, and $\boldsymbol{r}_2$, a_2, respectively.

The orders can be adjusted according to the electrical size of a geometric element. The orders increase as the element becomes larger. The electrical size of a geometric element can be as large as two wavelengths. Typically, the number of unknowns for HOBs is reduced by a factor of 5–10 compared with that for traditional piecewise basis functions, e.g., the RWGs, and thus the use of HOBs drastically reduces the computation and saves memory requirement.

There are also some other advantages in using the polynomial basis functions. For example, the intermediate results obtained in evaluating the elements of the impedance matrix for lower-order can be used in the computation of the elements of the impedance matrix when using higher-order polynomials. In addition, the Green's function for each pair of integration points belonging to two patches is needed to be evaluated only once. These advantages improve the efficiency of the matrix filling of the solver and help when the filling is performed using thousands of CPU cores.

III. PARALLEL LU DECOMPOSITION

As it was commented previously, better LU decomposition algorithms are required to break the poor parallel performance given by traditional LU decomposition schemes. In this section details about the novel LU decomposition algorithm included in our parallel MoM solver are given. In order to provide a better understanding about how this new LU algorithm (refers as NLU from now) enhances the parallel performance of the traditional LU decomposition algorithm, the latter is also detailed in this section. The algorithm described here (refers as ScaLapack LU from now) is the one given in [15].

A. ScaLapack LU algorithm

Let us consider an N×N dense complex matrix divided in blocks of size $n_b \times n_b$ and distributed across a $P_r \times P_c$ process grid. Choosing a value of P_c approximately equal to P_r, the communication volume is minimized, and in consequent, the high parallel efficiency is improved. Also, the communication complexity regarding column panel is higher than the complexity involved in the row panel. Therefore, it is better to set P_c slightly larger than P_r [16]. Figure 2 shows the main steps involved on the ScaLapack LU decomposition and it will be used as additional help when describing the algorithm.

After distributing the matrix on the processes grid, the LU decomposition algorithm starts with k=1 in Fig. 2 (a) where k is the number of the block of columns that are involved on the factorization step. This block of columns is called column panel. The size of this panel is $[N-(k-1)\times n_b]$ rows by n_b columns where the row size decreases when the factorization process advances. The panel is marked in green in Fig. 2 (a) and labeled as $\mathbf{Z}_{kk} + \mathbf{L}_{(k)}$. The operation performed during this step can be written as:

$$\mathbf{P}\begin{bmatrix}\mathbf{Z}_{kk}\\ \mathbf{L}_{(k)}\end{bmatrix} = \mathbf{P}\begin{bmatrix}\mathbf{L}_{kk}\\ \mathbf{L}^{(k)}\end{bmatrix}\mathbf{U}_{kk}\,, \tag{2}$$

where $\mathbf{P}$ is the permutation matrix corresponding to the partial pivoting scheme, $\mathbf{Z}_{kk} + \mathbf{L}_{(k)}$ is the column panel previously mentioned and $\mathbf{L}_{kk}$, $\mathbf{U}_{kk}$, and $\mathbf{L}^{(k)}$ are the result of the factorization process. In order to save computational resources, $\mathbf{Z}_{kk}$ is generally overwritten by the lower triangular matrix $\mathbf{L}_{kk}$ and the unit upper triangular matrix $\mathbf{U}_{kk}$. Figure 2 (b) shows the row exchange process where the element of maximum magnitude is permuted to the diagonal position in the panel factorization (this movement is given by matrix $\mathbf{P}$). It is worth to remind that this row exchange process requires a large volume of message communication leading on poor parallel performance. Submatrices $\mathbf{L}_{kk}$, $\mathbf{U}_{kk}$, and $\mathbf{L}^{(k)}$ are also displayed on the figure.

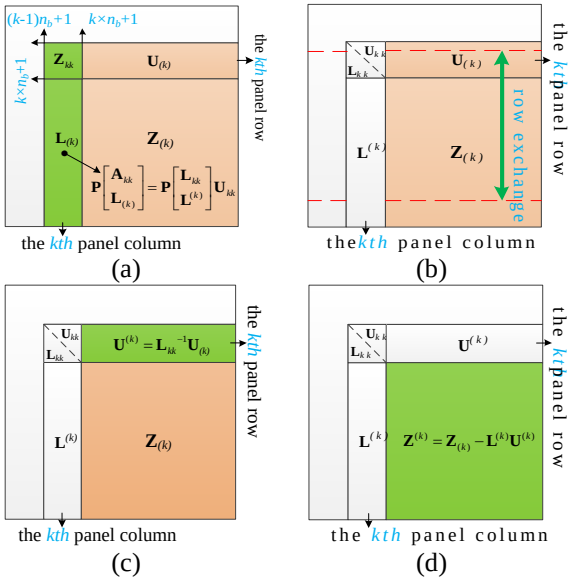

Fig. 2. ScaLapack LU decomposition: (a) panel factorization, (b) row exchange, (c) broadcast L_{kk} and panel row update, and (d) broadcast $L^{(k)}$ and $U^{(k)}$ and trailing update. *Note that the subscript* (*k*) *changing to the superscript* (*k*) *indicates that the current operation is complete.*

The next step corresponds to the row panel update process (see green submatrix marked in Fig. 2(c)) using the submatrices obtained previously. The update is given by:

$$\mathbf{U}^{(k)} = \mathbf{L}_{kk}^{-1}\mathbf{U}_{(k)}\,, \tag{3}$$

where $\mathbf{U}_{(k)}$ is the original row panel and $\mathbf{L}_{kk}$ is the lower triangular matrix of the column panel. Once the unknown $\mathbf{U}^{(k)}$ is obtained, the original row panel $\mathbf{U}_{(k)}$ is overwritten saving computational resources as the previous case.

The last step performs the update of the trailing submatrix $\mathbf{Z}_{(k)}$, marked in orange in Fig. 2 (c). This update uses the results of both panel factorization and row panel update. The resulting $\mathbf{Z}^{(k)}$ submatrix is given by:

$$\mathbf{Z}^{(k)} = \mathbf{Z}_{(k)} - \mathbf{L}^{(k)}\mathbf{U}^{(k)}\,. \tag{4}$$

Once the new $\mathbf{Z}^{(k)}$ submatrix is obtained, k is incremented and a new block of columns is factorized

continuing this process until the original matrix is decomposed completely.

B. Novel LU algorithm

The main different between the ScaLapack LU algorithm and our NLU resides on the way that the column panel is decomposed. This decomposition is located on a critical position on the LU algorithm being, in the case of the ScaLapack, unable to minimize the number of message exchanged due to the partial pivoting scheme. However NLU, adopting a different pivoting strategy, is able to reduce the number and amount of communication during this process enhancing the parallel performance.

It is worth mentioning that there are no differences between the ScaLapack LU algorithm and NLU for the others steps on the factorization process. Once the decomposition of the column panel is done, the algorithms follow the same scheme regarding the row update and the trailing submatrix update. For this reason, and in order to give a better description of our algorithm, only the decomposition of the column panel is detailed here.

Let us consider the same N×N dense complex matrix than the previous case. The column panel shown in Fig. 2 (a) (remember green columns on the left) is extracted and redisplayed in Fig. 3 as **A**. The distribution of the matrix on the process grid is performed as the previous case. However, for simplicity, we assume that the total number of processes is P=24. According to the criteria of choosing P_r and P_c aforementioned, the best choice is P_r = 4 and P_c = 6 obtaining four pieces of **A**:

$$\mathbf{A} = \begin{bmatrix} \mathbf{A}_0^T & \mathbf{A}_1^T & \mathbf{A}_2^T & \mathbf{A}_3^T \end{bmatrix}^T, \tag{5}$$

where the matrix **A** is of size [N-(k-1)×n_b] by n_b and $\mathbf{A}_0$, $\mathbf{A}_1$, $\mathbf{A}_2$ and $\mathbf{A}_3$ are distributed on processes P_0, P_1, P_2, and P_3, respectively. Without loss of generality, we assume the size of $\mathbf{A}_i$ is m_i×n_b with i=0, 1, 2, 3 and m_i about [N-(k-1)×n_b]/4. Generally, these four submatrices are referenced as *local panels*.

The decomposition of the column panel **A** is divided in three steps. The first step performs the decomposition of each of the submatrices $\mathbf{A}_0$, $\mathbf{A}_1$, $\mathbf{A}_2$ and $\mathbf{A}_3$ using *partial pivoting*. This decomposition process is done independently in each MPI processes without any interaction between them. Thus, this step is called *local decomposition step* where no communication between processes is required. Equation 6 shows the decomposition of each submatrix of the column panel **A**:

$$\begin{aligned} \mathbf{A_0} &= \mathbf{P}_0^{(1)}\mathbf{L}_0^{(1)}\mathbf{U}_0^{(1)} \\ \mathbf{A_1} &= \mathbf{P}_1^{(1)}\mathbf{L}_1^{(1)}\mathbf{U}_1^{(1)} \\ \mathbf{A_2} &= \mathbf{P}_2^{(1)}\mathbf{L}_2^{(1)}\mathbf{U}_2^{(1)} \\ \mathbf{A_3} &= \mathbf{P}_3^{(1)}\mathbf{L}_3^{(1)}\mathbf{U}_3^{(1)} \end{aligned}, \tag{6}$$

where $\mathbf{P}_i^{(1)}$ is the permutation matrix with the information of the pivoting and $\mathbf{L}_i^{(1)}$ and $\mathbf{U}_i^{(1)}$ are the corresponding submatrices result of the factorization process. Then, a set of *local pivoting rows* is obtained and permuted to the first n_b rows of each submatrix using the permutation matrix $\mathbf{P}_i^{(1)}$. Figure 3 shows this process under the label step 1 where the small matrices on the right contains the rows selected for pivoting during the *local decomposition step*.

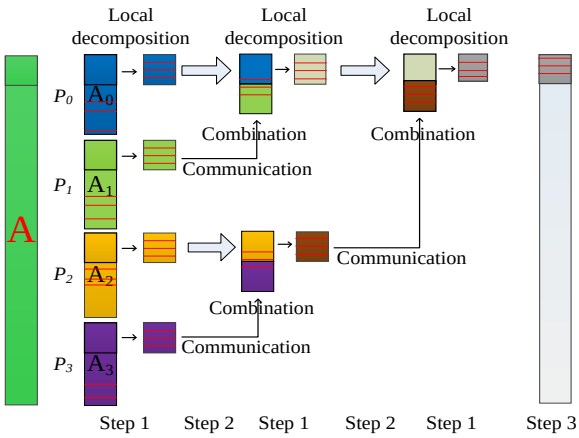

Fig. 3. Illustration of column factorization in our parallel MoM LU decomposition algorithm.

The second step combines the *local pivoting rows* pair to pair using a recursive scheme. For example, the local pivoting rows of $\mathbf{A}_0^{(1)}$ and $\mathbf{A}_1^{(1)}$ are combined in one pair while the rows of $\mathbf{A}_2^{(1)}$ and $\mathbf{A}_3^{(1)}$ are combined to form another pair (see the label step 2 on the left in Fig. 3). These new pairs are called new l*ocal column panels* which are treated as new panels for decomposition. Equation 7 shows the decomposition of this new *local column panels*:

$$\begin{aligned} \begin{bmatrix} \mathbf{A}_0^{(1)} \\ \mathbf{A}_1^{(1)} \end{bmatrix} &= \mathbf{P}_0^{(2)}\mathbf{L}_0^{(2)}\mathbf{U}_0^{(2)} \\ \begin{bmatrix} \mathbf{A}_2^{(1)} \\ \mathbf{A}_3^{(1)} \end{bmatrix} &= \mathbf{P}_1^{(2)}\mathbf{L}_1^{(2)}\mathbf{U}_1^{(2)} \end{aligned}. \tag{7}$$

Once this new local decomposition step is carried out, a new set of *local pivoting rows* is obtained and permuted to the first n_b rows of the column panel (submatrices marked in brown and gray in Fig. 3). Both *local decomposition* and *combination step* are called iteratively until only one block of *pivoting rows* is obtained. The total number of operations needed to obtain the final pivoting block is equal to $\log_2 P_r$. Continuing with the decomposition of **A**, the final local decomposition step is given by:

$$\begin{bmatrix} \mathbf{A}_0^{(2)} \\ \mathbf{A}_1^{(2)} \end{bmatrix} = \mathbf{P}_0^{(3)}\mathbf{L}_0^{(3)}\mathbf{U}_0^{(3)}. \tag{8}$$

Once this local decomposition is done, the final

pivoting rows are obtained. These *pivoting rows* are similar to the one used to form the permutation matrix **P** employed in (2). However, if one permutes these pivoting rows to the first n_b rows of **A**, then the LU decomposition without pivoting could be performed. In practice, even the LU decomposition is unnecessary because the latest *local decomposition* gives the upper triangular matrix **U** which is the same as the ultimately **U** we expect to obtain such as $\mathbf{U}_0^{(3)}$ in (8). So the only operation needed after executing this pivoting technique is a multiplication of an upper triangular matrix $\mathbf{U}_0^{(3)}$ by a block of column of **A** as shown in (9):

$$\mathbf{A}(n_b:m,1:n_b)=\mathbf{A}(n_b:m,1:n_b)\mathbf{U}_0^{(3)\ -1}, \qquad (9)$$

where **A** is the permuted column panel with the *pivoting rows* already located in the first n_b rows of the matrix. It is obviously that the communication appears only in the step of the combination of the *local pivot rows*, as implied by the arrows labeled with "communication" in Fig. 3.

The above description was simplified for the case of P_r = 4 but, actually this procedure can be easily extended to a situation with P_r = 8, 16, 32 and so on. With some additional but easy work, P_r could be an arbitrary quantity, rather than just power of 2. Of course, the extension from binary tree to quad tree or octree is not a big deal.

It is worth to mention that the *combination step* between *local pivoting rows* is not straightforward. In a first stage, it is necessary to determine which two *pivoting blocks* are combined. Then, as these two associated *pivoting blocks* are located at two different MPI processes, one also needs to define the communication pattern between them. Finally, after the combination, one needs to know which MPI process will perform the new *local decompositions*. In this work, the binary tree reduction method [17] is employed to guide the combination step. More specifically, two pivoting blocks located on adjacent MPI processes are the one chosen to be combined. After a combination, only half of the current MPI processes will perform the new *local decomposition step*. This reduction in the number of the working processes is continuously done until only one process performs the last *local decomposition step*, meanwhile the other processes will be waiting for the final permutation matrix.

Compared with the original CALU algorithm studied in [16, 17] the major difference with NLU resides in the communication pattern involved in the combination step. As shown in Fig. 3 all the processes are paired up to get a new *pivoting block*. In the original CALU algorithm each process exchanges their own *pivoting blocks* with its partner and then both the processes perform the same *local decomposition*, while in NLU only a unidirectional communication is performed and only the receiver-process performs the *local decomposition*. After several tests, we concluded that this variation provides a better implementation and makes the algorithm easier to achieve when using supercomputer platforms. Also, the extension from binary tree to quad tree or octree is much straightforward using the unidirectional communication version than the omnidirectional scheme.

C. Analysis of algorithm complexity

Before going to the numerical results section, the analysis of the computation complexity and the communication pattern of NLU algorithm is carried out. In order to perform a complete analysis, a comparison with the computation complexity of the ScaLapack LU algorithm is also done. As it was commented previously, the main different between the ScaLapack algorithm and NLU resides on the way that the column panel is decomposed. Therefore, the communication during the panel factorization is discussed in detail here.

Let us take, for example, the *k*'th step of LU decomposition shown in Fig. 2. Assuming that the size of $\mathbf{L}^{(k)}$ is $m \times n_b$ and the size of $\mathbf{L}_{kk}$ is $n_b \times n_b$, the amount of multiplication and addition operations can be calculated as it is shown later. We ignore the division operation because there are only few of those during the algorithms. Furthermore, let us assume that the communication latency is α and the communication bandwidth is 1/β. Thus, the communication time *T* taken to send a message of size *L* is:

$$T = \alpha + \beta L. \qquad (10)$$

Now, let us consider the ScaLapack LU algorithm first. For every column in the panel, a binary-exchange of size 2 n_b data items is performed [19], being n_b the number of columns in the panel. The communication complexity of this binary-exchange is $log_2 P_r$ given a total communication time of:

$$\begin{aligned} T_{comm,s} &= n_b \times (\alpha + 2 \times n_b \beta) \times \log_2 P_r \\ &= n_b \alpha \log_2 P_r + 2\beta n_b^2 \log_2 P_r \end{aligned}. \qquad (11)$$

In order to calculate the computation time taken by ScaLapack, we can consider that the panel factorization is a LU decomposition of a non-square matrix. Thus, the computation time can be evaluated according to the standard LU decomposition time that is:

$$T_{fact,s} = (m - \frac{n_b}{3}) n_b^{\ 2} \gamma, \qquad (12)$$

where γ is the time for each multiplication or addition operation, *m* is the number of row in the column panel and n_b is the number of columns.

In the case of NLU, one can see from Fig. 3 that the number of point-to-point communications performed by the busiest MPI process (P_0) is $log_2 P_r$. A final broadcast operation is also necessary at the end of the preprocess step, so the communication complexity of this broadcast operation (also $log_2 P_r$) has to be added to the total communication time. Assuming that the number of element to be broadcasted is $n_b^2 / 2$, the total communication time is given by:

$$T_{comm,c} = (\alpha + \beta n_b^2) \times \log_2 P_r + (\alpha + \beta \times \frac{n_b^2}{2}) \times \log_2 P_r \\ = 2\alpha \log_2 P_r + 1.5\beta n_b^2 \log_2 P_r \quad (13)$$

Generally, m is much greater than n_b, so it is clear that the operations described by (6) and (9) contribute the most amount of calculation in this case. Both operations have almost the same times of multiplication and addition as ScaLapack. So the computation time in NLU is about 2 times more than in ScaLapack:

$$T_{fact,c} = 2(m - \frac{n_b}{3}) n_b{}^2 \gamma \, . \quad (14)$$

Comparing the communication time given by (11) and (13), it can be concluded that NLU requires less communication time than ScaLapack. In the other hand, comparing the computation time given by (12) and (14) one can see how NLU pays a double price during the calculation. However, we have to take into account the order of magnitude of the variables involved on the calculation each time. The γ time employed by the computer to perform a multiplication or addition is much smaller than the latency time α and the inverse of the communication bandwidth β. Furthermore, NLU can utilize many excellent sequential factorization algorithms directly in the *local decomposition step*, such as recursive sequential LU, performing the floating point operation at machine peak performance, which means that the operation time γ in (14) is generally smaller than the time employed in (12). Thus, even employing a larger computational time, the NLU provides a shorter global time for matrix factorization. In order to demonstrate this affirmation, the next section presents the numerical results where the computational time of different benchmarks is compared.

IV. NUMERICAL RESULTS AND DISCUSSION

This section shows the comparison of the computational times for three different benchmarks between NLU and two of the most important math libraries used by direct dense solvers: the commercial MKL and the open source ScaLapack. The benchmarks considered here have consisted of the use of different matrix sizes, the use of different number of CPU cores and a comparison on the parallel efficiency of the algorithms. These benchmarks have been run on three different high performance computing (HPC) platforms that are described next.

A. Description of the computational resources

The first platform is the HPC cluster of Xidian University (XDHPC), which is equipped with 100 compute nodes connected by 56 Gbps InfiniBand network. Each node has two twelve-core Intel Xeon 2690 V2 2.2 GHz CPUs. The second platform is the MilkyWay-2 (Tianhe-2), which has 16,000 compute nodes. Each compute node is equipped with two Intel Xeon E5-2600 processors and three Intel Xeon Phi accelerators. All compute nodes are connected by a homemade 150 Gbps network. The third platform is the Sunway BlueLight MPP, a Chinese petaflop homegrown supercomputer. Sunway BlueLight uses ShenWei SW-3 1600, a 16-core 64-bit MIPS-compatible CPU. The total number of compute nodes on the system is 8704 connected by InfiniBand QDR network.

B. Numerical results for different matrix size

This benchmark has consisted of two tests using different matrix size and checking the factorization time of the algorithms. The first test employs a matrix size of 20,000~100,000 using 240 CPU cores in a process grid of 15x16, while the second test makes use of a matrix size of 80,000~180,000 in 720 CPU cores with a process grid of 24x30. The computing time obtained using the Intel MKL, ScaLapack and NLU are listed in Table 1. The improvement in percentage regarding the computing time using our solver versus MKL and ScaLapack is listed in the last two columns of the table. For example, the percentage corresponding with the improvement against MKL was calculated by using the following expression: $(T_{MKL}-T_{NLU}) / T_{MKL} \times 100\%$. The percentage corresponding to ScaLapack was calculated in a similar way. According to Table 1, the performances of our solver are clearly better than both MKL and ScaLapack for all the cases.

C. Numerical results for different CPU cores

The second benchmark has consisted of the simulation of two real world applications using different number of CPU cores. The first simulation analyzes the radar cross section (RCS) of an airplane. The second test calculates the radiation pattern of an airborne wire array antenna. XDHPC platform was used to run this benchmark.

Testing-I: The RCS of the airplane shown in Fig. 4 is calculated in this test. The size of the airplane is 18.92 m by 13.56 m by 5.05 m and the simulation frequency is 500 MHz, given a total number of unknowns of 203,436. The computing time consumed by NLU and MKL using 240~2048 CPU cores is listed in Table 2. The last row of data indicates the improvement in the computing time with respect to MKL. According to this table, the performance of our solver gets better when the number of CPU cores increases (in consequence more communication message are required) improving between 5.5%-8% the computational time given by MKL. The comparison between the RCS values obtained using our LU decomposition algorithm and the MKL library for the azimuth cut are shown in Fig. 5 where a very good agreement is appreciated. This behavior is expected as both decomposition algorithms are solving the same

matrix although, as aforementioned, NLU improves the computational time around 8% in the best case.

Table 1: Computing time for NLU, MKL and ScaLapack

CPU Cores	Size of Matrix	Time of LU Decomposition (Unit: s)			NLU VS MKL	NLU VS ScaL
		NLU	MKL	ScaL		
240	20,000	12.20	15.35	13.10	20.52%	6.83%
	40,000	61.41	70.86	68.17	13.34%	9.91%
	60,000	175.01	194.71	196.61	10.12%	10.99%
	80,000	397.96	417.31	449.60	4.64%	11.48%
	100,000	714.77	758.18	796.24	5.72%	10.23%
720	80,000	173.04	200.01	192.38	13.49%	11.18%
	100,000	316.15	351.01	346.82	9.93%	9.70%
	120,000	506.72	556.97	578.68	9.02%	14.20%
	140,000	781.27	822.87	851.76	5.06%	9.02%
	160,000	1093.43	1180.17	1264.40	7.35%	15.64%
	180,000	1490.39	1607.81	1693.76	7.30%	13.65%

Table 2: Computing time for NLU and MKL

CPU Cores	240	720	960	1200	2048
NLU Time	20091.5	2127.08	1588.10	1274.39	858.88
MKL Time	19257.7	2131.75	1650.88	1386.33	909.58
Time Saved	-4.33%	0.22%	3.80%	8.07%	5.57%

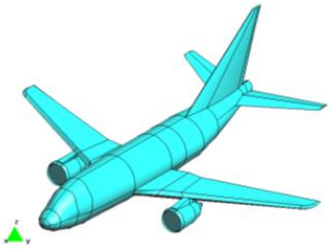

Fig. 4. Airplane model for RCS calculation using RWG.

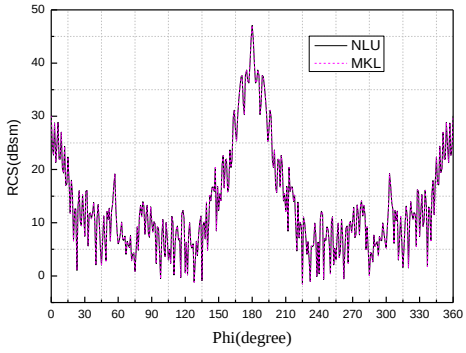

Fig. 5. RCS comparison using NLU and MKL.

Testing-II: The analysis of an airborne wire array antenna with 72 × 14 elements is performed in this test. The simulation model is shown in Fig. 6. The dimensions of the full array are 10 m × 2.5 m × 0.018 m. Each element of the array is fed by a short pin, and the amplitude at the feed of the array is designed by a –35 dB Taylor distribution both along length and width. The operation frequency of the array is 1.0 GHz given a total number of unknowns of 259,128.

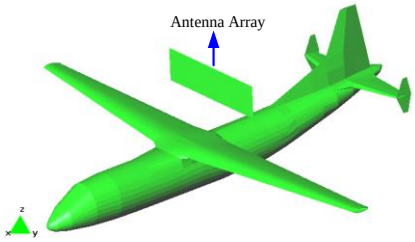

Fig. 6. Simulation model of the wire antenna array.

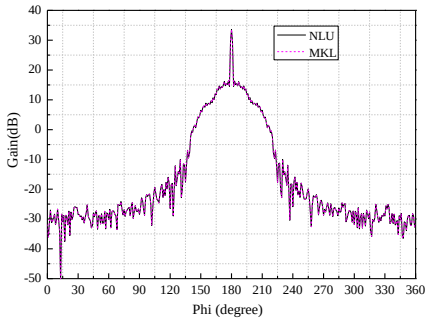

Fig. 7. Gain comparison in dB for NLU and MKL.

Table 3: Computing time for NLU and MKL

CPU Cores	240	720	960	1200	2048
NLU Time	11033.6	4407.73	3295.77	2743.26	1673.46
MKL Time	11174.0	4472.85	3501.06	2909.09	1788.27
Time Saved	1.26%	1.46%	5.86%	5.70%	6.42%

The computing time consumed by our LU decomposition algorithm and MKL using 240~2048 CPU cores is shown in Table 3, where the improvements in the time are listed in the last row as the previous test. The comparison between the 2D gain patterns are given in Fig. 7 where a very good agreement is appreciated. It is worth mention that according to Table 3, as the number of CPU cores increases the improvement in the computing time given by our solver is greater.

D. Numerical results for parallel efficiency

The last benchmark has consisted of the simulation of two massively parallel simulations used to measure the parallel efficiency of the algorithms. The parallel efficiency can be defined as:

$$\eta = T \big/ pT_p \times 100\% , \tag{15}$$

where T is the total time taken by a single process and T_p is the total time taken by p processes. In practice, if the problem cannot fit into a single computing node, the time for the smallest number of processes is taken as reference.

The calculation of the radiation pattern of a rectangular microstrip patch antenna array formed by 37 × 9 elements mounted on an aircraft is considered first. The simulation model of the array and the airplane are shown in Figs. 8 and 9. The dimensions of each patch element of the array are 205.6 mm × 154.8 mm providing a total dimension for the full array of 10 m × 2.5 m × 0.018 m. The material parameters of the substrate are $\varepsilon_r = 4.2$ and $\mu_r = 1.0$ and the operation frequency of the array is 440 MHz. The dimensions of the airplane were 55 m long by 47.6 m wide and 15.8 m high obtaining a total number of unknowns for the simulation of 308,371.

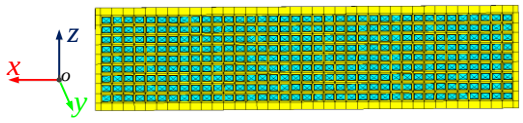

Fig. 8. Model of the microstrip patch array antenna.

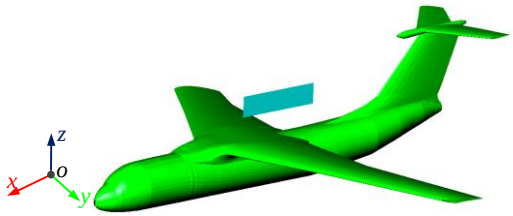

Fig. 9. Computational model with the aircraft and array.

The solving time taken by NLU using 600~12000 CPU cores is shown in Table 4, where the last two columns give the memory required in the form of value and percentage. Milkyway-2 platform was used to run this benchmark. Setting the solving time given by the 600 CPU cores simulation as the reference, the speed up listed in the fourth column is calculated by $S_P = 7504.08/T_P$, and the parallel efficiency listed in fifth column is calculated by $S_P/(P/600)$, where P is the number of the CPU cores and T_P and S_P is the corresponding solving time and speedup. Figure 10 shows the variation of speedup and parallel efficiency on CPU cores. According to the figure, efficiency higher than 65% can still be achieved when the parallel scale extends by 20, from 600 to 12000 CPU cores. Although more CPU cores usually mean shorter simulation time, the efficiency may deteriorate rapidly when the memory ratio is less than 2%. It should be pointed out that the maximum memory ratio should better less than 80% because of the operating system's requirement. Therefore, in order to avoid an extreme degradation on the parallel performance, the number of CPU cores should be choose carefully. Figure 11 shows the simulation results for this benchmark, where a -25 dB side lobe level in both *yoz* and *xoy* planes is appreciated fitting in the design specifications.

Table 4: Parallel efficiency and memory ratio for NLU

0	CPU Cores	Solving Time (s)	Speed-up	Parallel Efficiency (%)	Memory (GB)	Memory Ratio (%)
308,371	600	7504.08	1	100	1417	70.90
	1200	3799.00	1.97	98.76		35.45
	2400	2112.25	3.55	88.81		17.73
	3600	1471.84	5.09	84.97		11.82
	4800	1158.78	6.47	80.94		8.86
	7200	858.42	8.74	72.84		5.91
	9600	650.32	11.53	72.11		4.43
	12000	551.97	13.59	67.97		3.55

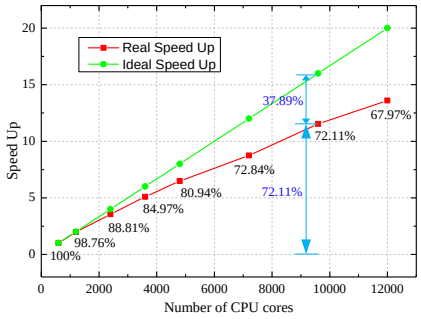

Fig. 10. Parallel efficiency for microstrip.

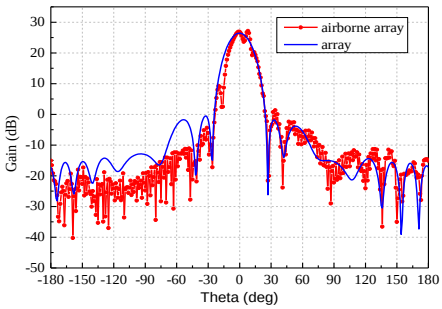

(a)

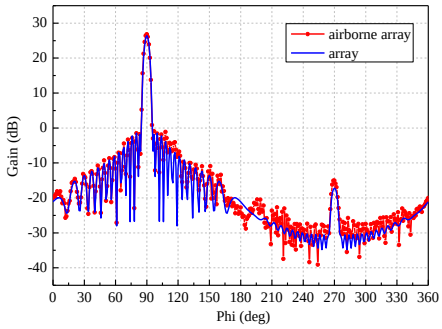

(b)

Fig. 11. 2D gain patterns for: (a) yoz plane and (b) xoy plane.

The parallel efficiency of NLU is further tested by the simulation of the bistatic RCS of the airplane shown in Fig. 12 at frequencies of 1.5 GHz and 2.5 GHz. Milkyway-2 platform was also used to run this simulation.

The dimensions of the airplane are 18.92 m × 14.56 m × 5.05 m, given a number of unknowns of 273,808 for the first frequency and 671,777 for the second one. The excitation is a z-axis polarized plane wave propagating along the negative x-axis direction.

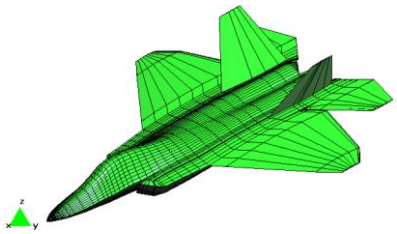

Fig. 12. Airplane model for efficiency test II.

The computing time consumed by NLU in the simulation is shown in Table 5. The number of processes used at 1.5 GHz ranges between 1536 and 25920 CPU cores while this number ranges from 25920~107520 CPU cores at 2.5 GHz. According the table, it can be seen how the efficiency is still higher than 50% even when using more than 100,000 CPU cores, as long as the memory ratio is larger than 2% approximately. The results of the RCS are listed in Fig. 13.

E. Numerical results for practical engineering

The RCS of the airplane shown in Fig. 12 is now calculated at a higher frequency to demonstrate the ability of the solver to calculate electric super-lager targets. The working frequency in this case is 3.2 GHz given a total number of unknowns of 1,270,200, which requires 23.4 TB of memory. A total number of 201,600 CPU cores are employed to solve the problem. The computing time and simulation result are listed in Table 6 and Fig. 14, respectively.

Table 5: Parallel efficiency for test II

Unknowns	CPU Cores	Solving Time (s)	Parallel Efficiency	Memory (GB)	Memory Ratio
273,808	1,536	2376.71	100%	1117.32	27.28%
	12,960	437.88	80.41%		3.23%
	25,920	246.81	45.51%		1.62%
671,777	25,920	2388.10	100%	6724.66	9.73%
	76,800	1629.09	83.43%		3.28%
	107,520	1264.98	57.06%		2.35%

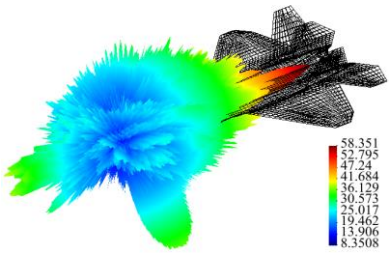

(a)

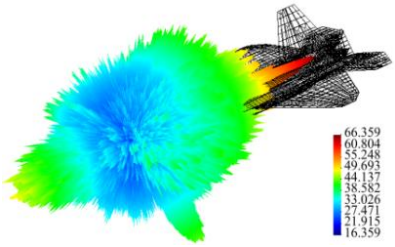

(b)

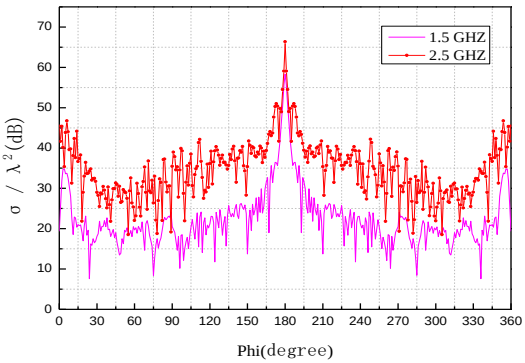

(c)

Fig. 13. Bistatic RCS results for: (a) 3D-RCS at 1.5 GHz, (b) 3D-RCS at 2.5 GHz, and (c) 2D-RCS on xoy at 1.5 GHz and 2.5 GHz.

Table 6: Solving matrix equation using 200,000 CPU cores

CPU Cores	Unknowns	Process Grid	Block Size	Filling Time (s)	Solving Time (s)
201,600	1,270,200	400×504	128	23.10	3021.05

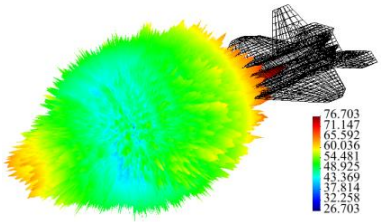

(a)

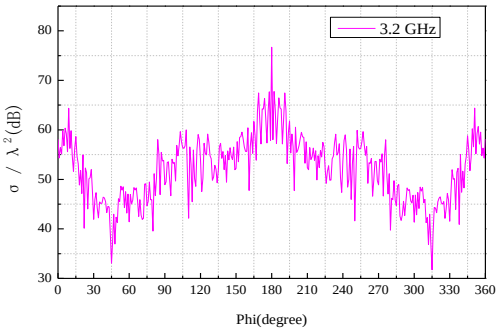

(b)

Fig. 14. Bistatic RCS results at 3.2 GHz for: (a) 3D-RCS and (b) 2D-RCS for azimuth cut.

V. CONCLUSION

A massively parallel MoM solver able to run on 200,000 CPU cores and solve matrices larger than 1.3 million unknowns has been presented. Details about a novel LU decomposition algorithm have been given demonstrating its improvements in the simulation time in comparison with commercial Intel MKL and open source ScaLapack Libraries. The new algorithm is about 10~20 percent faster than the open source ScaLapack framework. Also, compared with the commercial Intel MKL on InfiniBand interconnected platform when thousands of CPU cores are used, it still has 5~10 percent advantage in performance. Furthermore, one can see how the algorithm can still achieve a high parallel efficiency even when 200,000 CPU cores are used presenting a new powerful tool for solving very challenging electromagnetic problems in reasonable time.

ACKNOWLEDGMENT

This work was supported in part by the National Key Research and Development Program of China under Grant 2017YFB0202102, in part by the National High Technology Research and Development Program of China (863 Program) under Grant 2014AA01A302, in part by the China Postdoctoral Science Foundation funded project under Grant 2017M613068, in part by the Key Research and Development Program of Shandong Province under Grant 2015GGX101028, and in part by the Special Program for Applied Research on Super Computation of the NSFC-Guangdong Joint Fund (the second phase) under Grant No. U1501501.

REFERENCES

[1] J. M. Jin, *The Finite Element Method in Electromagnetics*. John Wiley & Sons, Inc., 1993.

[2] A. Taflove, *Computational Electrodynamics: The Finite-Difference Time-Domain Method*. Artech House, Norwood, Mass, USA, 2000.

[3] R. F. Harrington, *Field Computation by Moment Methods in IEEE Series on Electromagnetic Waves*. IEEE, New York, NY, USA, 1993.

[4] Y. Zhang and T. K. Sarkar, *Parallel Solution of Integral Equation Based EM Problems in the Frequency Domain*. Hoboken, NJ: John Wiley, 2009.

[5] J. Chen, M. Zhu, M. Wang, S. Li, and X. Li, "A hybrid MoM-PO method combining ACA technique for electromagnetic scattering from target above a rough surface," *ACES Journal*, vol. 29, no. 4, pp. 301-306, 2014.

[6] Y. Kim, H. Kim, K. Bae, J. Park, and N. Myung, "A hybrid UTD-ACGF technique for DOA finding of receiving antenna array on complex environment," *IEEE Trans. Antennas Propag.*, vol. 63, no. 11, pp. 5045-5055, 2015.

[7] J. M. Song, C. C. Lu, and W. C. Chew, "Multilevel fast multipole algorithm for electromagnetic scattering by large complex object," *IEEE Trans. Antennas Propag.*, vol. 45, no. 10, pp. 1488-1493, 1997.

[8] H. Fangjing, N. Zaiping, and H. Jun, "An efficient parallel multilevel fast multipole algorithm for large-scale scattering problems," *ACES Journal*, vol. 25, no. 4, pp. 381-387, 2010.

[9] Y. Zhang, T. K. Sarkar, M. C. Taylor, and H. Moon, "Solving MoM problems with million level unknowns using a parallel out-of-core solver on a high performance cluster," *in IEEE Antennas and Propagation Soc. Int. Symp*., Charleston, SC, USA, pp. 1-4, 2009.

[10] Y. Zhang, R. A. van ce Geijn, M. C. Taylor, and T. K. Sarkar, "Parallel MoM using higher-order basis functions and PLAPACK in-core and out-of-core solvers for challenging EM simulations," *IEEE Trans. Antennas Propag.*, vol. 51, no. 5, pp. 42-60, 2009.

[11] Y. Zhang, T. K. Sarkar, X. Zhao, D. Garcia-Donoro, W. Zhao, M. Salazar, and S. Ting, *Higher Order Basis Based Integral Equation Solver (HOBBIES)*. Hoboken, NJ: John Wiley, 2012.

[12] Intel Copyright (2015) Intel Math Kernel Library for Linux OS User's Guide, Intel Corporation. available: https://software.intel.com/sites/default/files/managed/df/1e/mkl_11.3_lnx_userguide.pdf.

[13] W. Gropp, T. Hoefler, and R. Thakur, *Using Advanced MPI: Modern Features of the Message-Passing Interface*. Cambridge, MA: The MIT Press, 2014.

[14] B. Chapman, G. Jost, R. van der Pas, and D. J. Kuck, (foreword), *Using OpenMP: Portable Shared Memory Parallel Programming*. The MIT Press, Cambridge, MA, 2007.

[15] L. S. Blackford, J. Choi, A. Cleary, et al., "ScaLAPACK: A portable linear algebra library for distributed memory computers - Design issues and performance," *Proceedings of the 1996 ACM/IEEE Conference on Supercomputing, IEEE*, pp. 1-20, 1996.

[16] Y. Zhang, Z. Lin, X. Zhao, et al., "Performance of a massively parallel higher-order method of moments code using thousands of CPUs and its applications," *IEEE Trans. Antennas Propag*., vol. 62, no. 12, pp. 6317-6324, 2014.

[17] L. Grigori, J. W. Demmel, and H. Xiang, "CALU: A communication optimal LU factorization algorithm," *SIAM Journal on Matrix Analysis and Applications*, vol. 32, no. 4, pp. 1317-1350, 2008.

[18] A. Khabou, J. W. Demmel, L. Grigori, and M. Gu, "LU factorization with panel rank revealing pivoting and its communication avoiding version," *eprint arXiv:1208.2451*, 2012.

[19] http://www.netlib.org/benchmark/hpl/scalability.html

Hybrid Sparse Reconstruction-Method of Moments for Diagnosis of Wire Antenna Arrays

Huapeng Zhao, Ying Zhang, Jun Hu, and Zhizhang Chen

School of Electronic Engineering
University of Electronic Science and Technology of China, Chengdu, 611731, P. R. China
huapengzhao@uestc.edu.cn

Abstract ─ In this work, sparse reconstruction is hybridized with method of moments (MoM) for diagnosis of wire antenna arrays. In the hybrid method, excitation voltages of array under diagnosis are related to near field observations through integral equations (IEs), and IEs are transformed into matrix equations by MoM. Sparse reconstruction is then used to solve excitation voltages of array under diagnosis. Finally, locations of failing elements are found by the solved excitation voltages. The hybrid method models mutual coupling effect by MoM, and it achieves higher diagnosis reliability than sparse reconstruction without mutual coupling consideration. Simulation results are presented to show the validity and advantages of the hybrid method.

Index Terms ─ Array diagnosis, integral equation, method of moments, sparse reconstruction.

I. INTRODUCTION

Large scale antenna arrays are widely used in radar systems and radio telescopes. If some elements of an array are not working properly, the array radiation pattern can be significantly affected. In order to repair a failing array, it is essential to develop fast and reliable array diagnosis methods. Recently, array diagnosis based on sparse reconstruction attracted much interest. The key advantage of sparse reconstruction is the reduction of required observations. This was first demonstrated by numerical simulations using planar arrays [1]. Theoretical proof was later derived for uniform linear arrays [2]. Besides, estimation of diagnosis reliability was developed in [3].

In practice, diagnosis reliability is affected by various factors, including element positioning error, measurement noise, mutual coupling between array elements, etc. Effects of element positioning error and Gaussian noise were discussed in [1], and non-Gaussian noise was studied in [4]. Toeplitz property of the mutual coupling matrix was utilized to model the mutual coupling of uniform linear array [5]. However, mutual coupling of arbitrarily shaped arrays has not been considered in existing work.

In order to model the effect of mutual coupling, this work combines sparse reconstruction with method of moments (MoM). Using MoM, a matrix equation linking excitation voltages and near field observations is first derived from integral equations. Excitation voltages are then solved by sparse reconstruction to locate failing elements. The main advantage of the proposed method is the inclusion of mutual coupling effect of arbitrarily shaped arrays, which is shown to significantly improve diagnosis reliability.

It should be noted that there have been MoM-based source reconstruction methods for solving inverse problems [6, 7]. Unknowns in these methods are equivalent currents which are usually not sparse. On the other hand, unknowns in the proposed method are excitation voltages, which can be made sparse and solved by sparse reconstruction. Furthermore, the support vector machine (SVM) based-source identification method was proposed in [8]. The SVM based-source identification requires a training process. It is able to detect the radiation source efficiently once the training process is completed. For the large scale arrays considered in this work, the training process may be tedious.

II. THE PROPOSED METHOD

Consider the wire antenna array shown in Fig. 1. Fields are observed on an observation plane and they are used to reconstruct the excitation voltages.

A. Relating excitation voltages and observed fields

Assuming the wire antenna is thin (the radius of the wire is less than one hundredth of the wavelength), electromagnetic behavior of the array is described using the thin wire integral equation [9]. Using MoM, the thin wire integral equation is discretized and the following matrix equation is derived:

$$\mathbf{Zc}=\mathbf{f}, \tag{1}$$

where $\mathbf{Z}$ is the interaction matrix, $\mathbf{c}$ is an unknown vector constituted by current expansion coefficients, and $\mathbf{f}$ is the excitation vector arising from excitation voltages. The dimension of $\mathbf{Z}$ is $BN_J \times BN_J$, and the dimension of $\mathbf{c}$ and $\mathbf{f}$ is $BN_J \times 1$, where N_J is the number of basis functions

Submitted On: January 27, 2017
Accepted On: August 12, 2017

1054-4887 © ACES

for one antenna element and B is the total number of antenna elements. Definitions of **Z** and **f** are given in Equations (4.68) and (4.69) of [9], and they are omitted here. It should be mentioned that the mutual coupling effect is automatically included in the interaction matrix **Z**.

At the q-th observation point $\vec{r}_q$ (q=1,2,...,Q, where Q is the total number of observations), electric field is calculated using the thin wire integral equation. Substituting current expansion into the thin wire integral equation, the following matrix equation is obtained:

$$\mathbf{E} = \mathbf{U}\mathbf{c}, \tag{2}$$

where **E** is a vector constituted by E_q and E_q is electric field at the q-th observation point. **U** is a complex-valued matrix arising from point matching of the thin wire integral equation, and its dimension is $Q \times BN_J$. The excitation vector **f** is written as:

$$\mathbf{f} = \mathbf{T}\mathbf{v}, \tag{3}$$

where **v** is a column vector constituted by V_b (b = 1, 2, ..., B) and V_b is the excitation voltage at the b-th feed port. **T** is a $BN_J \times B$ complex-valued matrix defined as:

$$T_{m,b} = \frac{-j}{\omega\mu\delta_b}\int_{P_b} s_m(\vec{r})d\vec{r}\,, \tag{4}$$

where P_b is the line segment where the b-th feed port is located, δ_b is the length of P_b, and s_m is the m-th triangular basis function. Substituting (3) into (1), we have:

$$\mathbf{Z}\mathbf{c} = \mathbf{T}\mathbf{v}. \tag{5}$$

From (5) and (2), it is observed that matrix **Z** needs inverting in order to obtain an explicit linear relationship between excitation voltages **v** and observed fields **E**. When the size of **Z** is large, it is difficult to directly invert **Z**. In that case, fast integral equation methods should be used to accelerate the computation of **Z** and its inversion [10]. In this work, we assume that the inversion of **Z** can be computed directly. Equation (5) is then rewritten as:

$$\mathbf{c} = \mathbf{Z}^{-1}\mathbf{T}\mathbf{v}, \tag{6}$$

where $\mathbf{Z}^{-1}$ is the inversion of **Z**. Substituting (6) into (2), excitation voltages are related to observed fields as:

$$\mathbf{E} = \mathbf{Y}\mathbf{v}, \tag{7}$$

with $\mathbf{Y} = \mathbf{U}\mathbf{Z}^{-1}\mathbf{T}$.

B. Finding excitation from observation

In order to utilize advantages of sparse solution, this work adopts the differential formulation proposed in [1] for small failing rate. According to the differential formulation [1], the following equation is derived from (7):

$$\mathbf{E}_\delta = \mathbf{Y}\mathbf{v}_\delta, \tag{8}$$

where $\mathbf{E}_\delta = \mathbf{E} - \mathbf{E}_{ref}$ and $\mathbf{v}_\delta = \mathbf{v} - \mathbf{v}_{ref}$. $\mathbf{E}_{ref}$ and $\mathbf{v}_{ref}$ are observed fields and voltage sources of the normal array, and they are assumed known in advance. $\mathbf{v}_\delta$ is sparse when the failing rate is small. Therefore, $\mathbf{v}_\delta$ can be estimated using ℓ_1-norm solver. Once $\mathbf{v}_\delta$ is obtained, **v** is recovered as $\mathbf{v}_{ref} + \mathbf{v}_\delta$. In practice, the failing rate is unknown. Hence, one may reconstruct the voltage excitation source using both (7) and (8) and choose the one whose radiating fields are closer to the observed fields. Taking Equation (7) as an example, **v** is obtained by solving the following optimization problem:

$$\min_{\mathbf{v}} \left(\|\mathbf{v}\|_p \right)^p, \tag{9a}$$

$$\text{subject to } |E_m - \mathbf{Y}_m\mathbf{v}| \le \epsilon, \ \forall m, \tag{9b}$$

where $||\mathbf{v}||_p$ is the ℓ_p-norm of **v**, E_m is the m-th element of **E**, $\mathbf{Y}_m$ is the m-th row of **Y**, and ϵ is the tolerance. When p = 2, ℓ_2-norm solution is obtained, which results in the minimum root mean square error solution. If p = 1, a sparse solution will be derived. When the solution is sparse, ℓ_1-norm solver renders better accuracy than ℓ_2-norm solver. The solution of (9) is detailed in [4], and it is omitted here.

The computational complexity of solving the optimization problem in (9) is the same as the array diagnosis method presented in [4]. Because the mutual coupling effect is considered in the proposed method, the matrix filling requires longer CPU time. In order to save the CPU time, matrix **Y** in (8) can be pre-stored and reused.

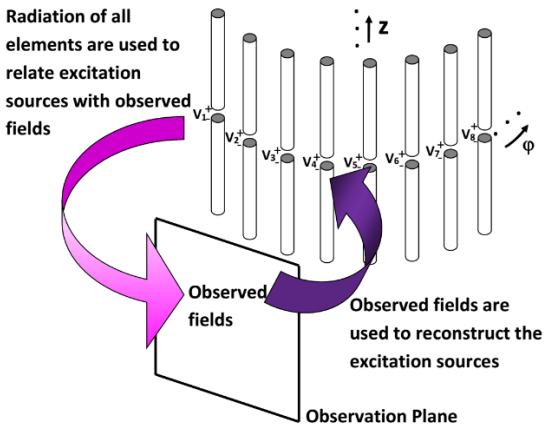

Fig. 1. Diagnosis of a dipole array. The excitation voltage at the m^{th} feed port is denoted by V_m.

III. SIMULATION RESULTS

A. Accuracy study

This section presents simulation results to study the accuracy of our proposed method and to demonstrate the accuracy improvement by considering mutual coupling.

1) Simulation Setup

The array under consideration is a 10 × 10 cylindrical array consisting of half-wavelength dipole antennas. The array elements are distributed on a z-directed cylinder of radius 5λ with $z \in [0, 9.5\lambda]$ and $\phi \in [-0.45, 0.45]$, where λ denotes the wavelength. The elemental spacings in z- and ϕ-directions are 1.0λ and 0.1 radian, respectively.

Radiated fields are observed on a rectangular plane defined as $x = 6\lambda$, $y \in [-2.25\lambda, 2.25\lambda]$, and $z \in [0, 9.5\lambda]$. For validation purpose, radiated near fields of the array are first calculated with uniform voltage excitation of 1 *V*. Results from our code agree well with those from commercial software FEKO. This validates the calculation of matrices **Z**, **T**, and **U**. Our code is then used to generate observed fields with the voltage excitation following Gaussian distribution. *z*-component of the electric field is used for failure diagnosis. Furthermore, Gaussian noise is added to the synthetic data in order to simulate the measurement uncertainty in experiment. To enhance the robustness against Gaussian noise, the quadratic loss function is adopted in the unsupervised support vector regression [4]. The relative root mean square error (RMSE) is used to measure the accuracy of the reconstructed source. In order to consider the effect of location of failing elements, RMSE is obtained by 50 independent simulations, each with random locations of failing elements.

2) Accuracy for Sparse Solution

Figure 2 presents RMSE against the number of observations for sparsity of 92% and 96%. The signal to noise ratio (SNR) is fixed to 40 dB. It is seen that RMSE reduces as the number of observations increases, with the reduction rate becoming slow after certain number of observations. This indicates that there is a critical point Q_c, after which adding extra observation data provides insignificant accuracy improvement. Figure 2 shows that the value of Q_c is smaller for the case of 96% solution sparsity. Hence, sparser solution requires smaller *Qc*. For practical application, Q_c may be determined by gradually adding observation data until the convergence of the solution vector [11]. Figure 2 also compares RMSE with and without mutual coupling consideration. It is seen that the accuracy is improved by one order of magnitude when mutual coupling is considered. Meanwhile, the accuracy improvement is higher for the case of 96% solution sparsity. This is because higher solution sparsity results in a larger number of passive radiating elements, which makes the role of mutual coupling more important.

Figure 3 shows RMSE versus SNR, where the number of observations is fixed to 100. It is seen that RMSE with and without mutual coupling consideration is large when SNR is below 20 dB. However, RMSE is lower when mutual coupling is considered. Meanwhile, RMSE is reduced by one order of magnitude via considering mutual coupling when SNR is larger than 20 dB. Furthermore, RMSE reduction is larger when solution sparsity is 96%. This agrees with the observation from Fig. 2.

3) Accuracy Against Sparsity of the Solution

In the case of Figs. 2 and 3, the solution sparsity is high. It is interesting to see how the accuracy is affected by the solution sparsity. Figure 4 presents RMSE with solution sparsity dropping from 95% to 50%. As the solution sparsity drops, RMSE gradually rises. In the case of SNR=40 dB, the accuracy improvement by considering mutual coupling is one order of magnitude for all solution sparsity. When SNR is 20 dB, RMSE is high for both with and without mutual coupling consideration. Figure 5 shows the rate of correct detection using the detection criterion presented in [4]. For both values of SNR, considering mutual coupling increases the rate of correct detection. When SNR is 40 dB, the proposed method provides 100% rate of correct detection for all solution sparsity. When SNR is 20 dB, the rate of correct detection is 98% for sparsity of 95%. However, as the sparsity decreases, the rate of correct detection drops. For low sparsity, the rate of correct detection may be improved by increasing the number of observations [4].

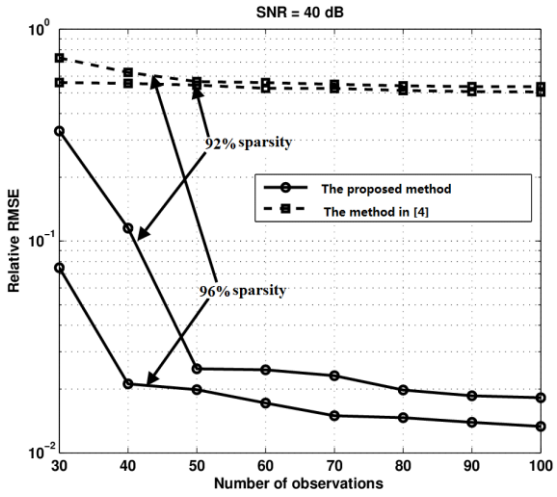

Fig. 2. RMSE versus the number of observations.

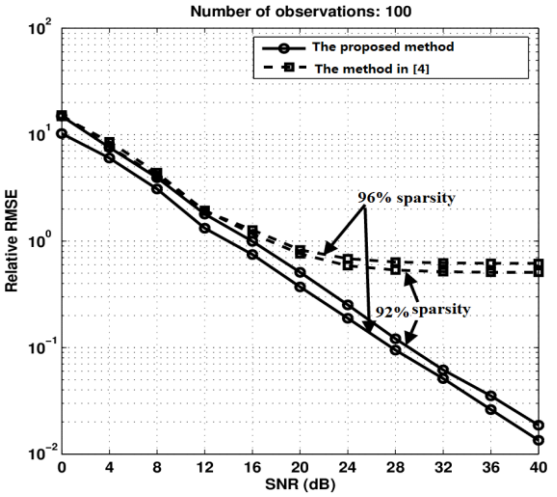

Fig. 3. RMSE versus SNR.

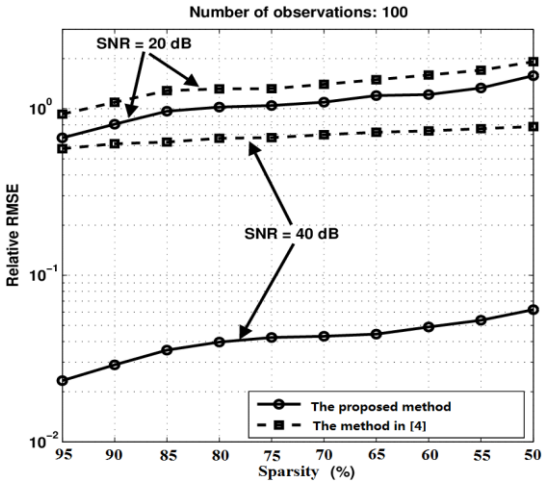

Fig. 4. RMSE versus solution sparsity.

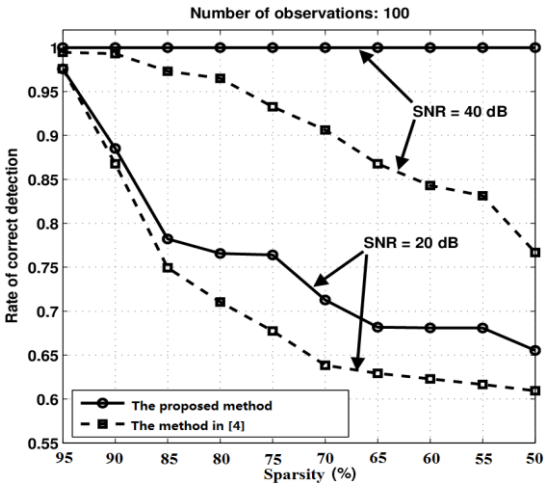

Fig. 5. Rate of correct detection versus solution sparsity.

B. Application to a 40 × 30 cylindrical dipole array

The proposed method is applied to diagnose a 40 × 30 cylindrical array constituted by half-wavelength dipole antennas. The array is located on a *z*-directed cylinder with radius of 5λ, $\phi \in [-0.975, 0.975]$ and $z \in [0, 21.75\lambda]$. The elemental spacings in ϕ- and *z*-directions are 0.05 radian and 0.75λ, respectively. The voltage excitation of the array is shown in Fig. 6 (a), with failing elements forming an 'E'-shape. The *z*-component of radiated electric field is observed on a plane defined as $x = 6\lambda$, $y \in [-5\lambda, 5\lambda]$ and $z \in [-0.25\lambda, 22\lambda]$, with 41 and 31 field points in *y*- and *z*-directions, respectively. SNR is set to 20 dB. It is assumed that the failing rate is unknown, and the voltage excitation source is reconstructed using both (7) and (8). The reconstructed voltage source with smaller approximation error is chosen. Figure 6 (b) presents the reconstructed voltage excitation with mutual coupling consideration. It is seen that the failing elements are correctly detected when mutual coupling is considered.

Figure 6 (c) shows the reconstructed voltage source without mutual coupling consideration, where locations of failing elements are obscure.

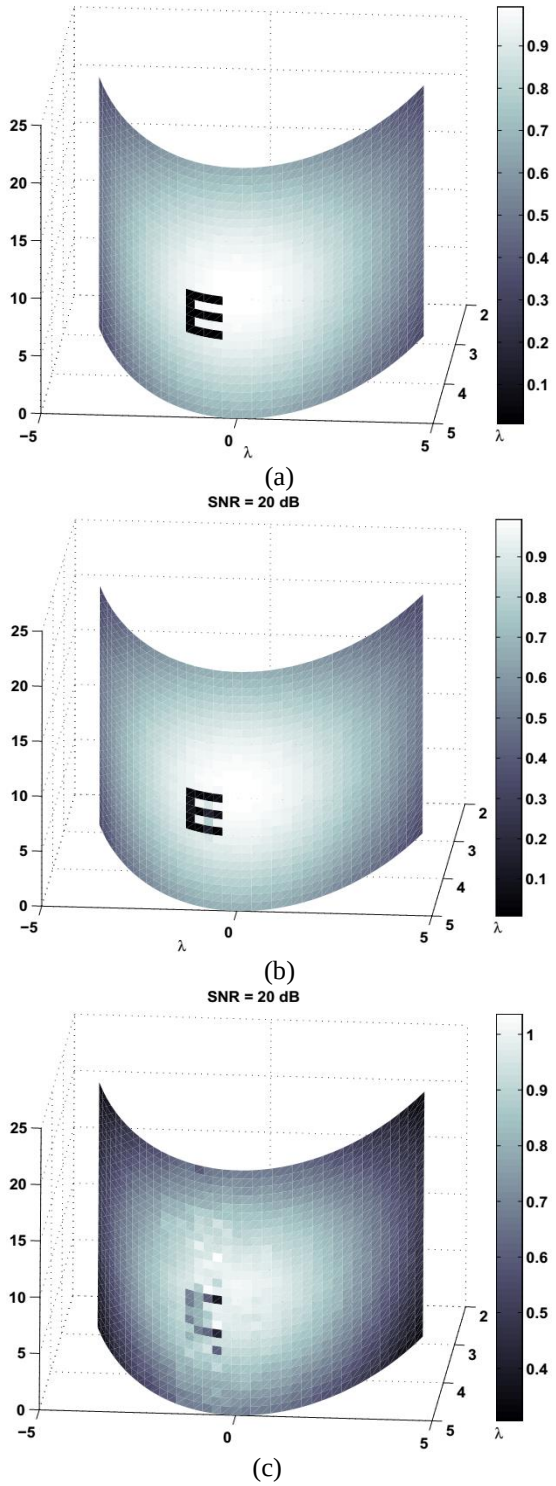

Fig. 6. Excitation source of the large cylindrical dipole array: (a) original, (b) reconstructed by the proposed method, and (c) reconstructed by the method in [4].

IV. CONCLUSION

This paper presented diagnosis of wire antenna arrays by hybrid sparse reconstruction-MoM. Mutual coupling between array elements has been taken into account by MoM. Simulations have been conducted to study the accuracy of the proposed method. It has been observed that the accuracy can be improved by one order of magnitude when taking mutual coupling into consideration. Furthermore, application to a large array has been demonstrated. It has been found that failing elements are correctly located when mutual coupling is considered. On the other hand, ignoring mutual coupling results in obscure locations of failing elements. Although the array elements considered here are half-wavelength dipole antennas, the proposed method can deal with other type of elements because of the flexibility of MoM.

ACKNOWLEDGMENT

This work is supported by the National Science Foundation of China under Grants No. 61471107, No. 61425010, No. 61271033, No. 61671121, and by the UESTC Research Start-up funding under Grant No. ZYGX2016KYQD106.

REFERENCES

[1] M. D. Migliore, "A compressed sensing approach for array diagnosis from a small set of near-field measurements," *IEEE Trans. Antennas Propagat.*, vol. 59, no. 6, pp. 2127-2133, June 2011.

[2] ——, "Array diagnosis from far-field data using the theory of random partial Fourier matrices," *IEEE Antennas Wireless Propagat. Lett.*, vol. 12, pp. 153-166, 2013.

[3] G. Oliveri, P. Rocca, and A. Massa, "Reliable diagnosis of large linear arrays-A Bayesian compressive sensing approach," *IEEE Trans. Antennas Propagat.*, vol. 60, no. 10, pp. 4627-4636, Oct. 2012.

[4] H. Zhao, Y. Zhang, E.-P. Li, A. Buonanno, and M. D'Urso, "Diagnosis of array failure in impulsive noise environment using unsupervised support vector regression method," *IEEE Trans. Antennas Propagat.*, vol. 61, no. 11, pp. 5508-5516, Nov. 2013.

[5] Y. Zhang and H. Zhao, "Failure diagnosis of a uniform linear array in the presence of mutual coupling," *IEEE Antennas Wireless Propagat. Lett.*, vol. 14, pp. 1010-1013, 2015.

[6] P. Li, Y. Li, L. Jiang, and J. Hu, "A wide band equivalent source reconstruction method exploiting the Stoer-Bulirsch algorithm with the adaptive frequency sampling," *IEEE Trans. Antennas Propagat.*, vol. 61, no. 10, pp. 5338-5343, Oct. 2013.

[7] M. Bod, R. Sarraf-Shirazi, GH. Moradi, and A. Jafargholi, "A regularized source current reconstruction method for reactive near field to far field transformation," *Applied Computational Electromagnetics Society Journal*, vol. 32, no. 2, pp. 113-119, 2017.

[8] D. Shi and Y. Gao, "Electromagnetic radiation source identification based on spatial characteristics by using support vector machines," *Applied Computational Electromagnetics Society Journal*, vol. 32, no. 2, pp. 120-127, 2017.

[9] W. Gibson, *The Method of Moments in Electromagnetics*. New York: Chapman and Hall, 2008.

[10] J. M. Tamayo, A. Heldring, and J. M. Rius, "Multilevel adaptive cross approximation (MLACA)," *IEEE Trans. Antennas Propagat.*, vol. 59, no. 12, pp. 4600-4608, Dec. 2011.

[11] H. Zhao and Y. Zhang, "Extrapolation of wideband electromagnetic response using sparse representation," *IEEE Trans. Antennas Propagat.*, vol. 60, no. 2, pp. 1026-1034, Feb. 2012.

Huapeng Zhao received the Ph.D. degree from the Nanyang Technological University, Singapore, in June 2012. He was a Scientist with the A*STAR Institute of High Performance Computing from August 2011 to December 2015. Since December 2015, he has been an Associate Professor with the School of Electronic Engineering at the University of Electronic Science and Technology of China, Chengdu, P. R. China.

Ying Zhang received the Ph.D. degree from the Nanyang Technological University, Singapore, in June 2011. She was a Post-Doctoral researcher with the Nanyang Technological University from July 2010 to July 2011. In July 2011, she joined the University of Electronic Science and Technology of China as an Associate Professor.

Jun Hu received the B.S., M.S., and Ph.D. degrees in Electromagnetic Field and Microwave Technique from the University of Electronic Science and Technology of China (UESTC), Chengdu, P. R. China, in 1995, 1998, and 2000, respectively. Currently, he is a Full Professor with the School of Electronic Engineering, UESTC. During 2001, he was with the Center of Wireless Communication in the City University of Hong Kong, Kowloon, Hong Kong, as a Research Assistant. From March to August of 2010, he was a Visiting Scholar in the ESL of the Electrical and Computer Engineering Department, Ohio

State University. He was a Visiting Professor of the City University of Hong Kong from February to March in 2011. His current research interests include integral equation methods in computational electromagnetics, electromagnetic scattering and radiation.

Hu is a Member of the Applied Computational Electromagnetics Society. He served as the Chairman for the IEEE Chengdu Joint AP/EMC Chapter during 2014-2016. He was a recipient of the 2004 Best Young Scholar Paper Award from the Chinese Radio Propagation Society and was selected into 'Who's Who in the World' (Marquis, 31 Edition).

Zhizhang Chen received the M.S. degree in Radio Engineering from Southeast University, Nanjing, China, and the Ph.D. degree in Electrical Engineering from the University of Ottawa, Ottawa, ON, Canada. He was an NSERC Postdoctoral Fellow with McGill University, Montreal, QC, Canada. He is currently a Professor at Dalhousie University, Halifax, NS, Canada, where he has served as the Head of the Department of Electrical and Computer Engineering. He has been an Adjunct or Visiting Professor at the University of Nottingham, U.K., Ecole Nationale Superieure des Telecommunications de Bretagne of France, Shanghai Jiaotong University, Beihang University, Fuzhou University, and the University of Electronic Science and Technology of China. He has authored and coauthored more than 300 journal and conference papers in computational electromagnetics, RF/microwave electronics, antennas, and wireless technologies. His current research interests are in unconditionally stable electromagnetic modeling techniques, ultrawideband wireless communication systems and wireless power transfer.

Chen is a Fellow of the IEEE, the Canadian Academy of Engineering and the Engineering Institute of Canada. He was one of the originators of the unconditionally stable methods that have been highly cited and used. He received the 2005 Nova Scotia Engineering Award, a 2006 Dalhousie Graduate Teaching Award, the 2007 & 2015 Dalhousie Faculty of Engineering Research Award, and the 2013 IEEE Canada Fessenden Medal.

Real-Coded Genetic Algorithm with Differential Evolution Operator for Terahertz Quasi-Optical Power Divider/Combiner Design

Fan Zhang, Kaijun Song, and Yong Fan

EHF Key Laboratory of Science, School of Electronic Engineering
University of Electronic Science and Technology of China, Chengdu, Sichuan, 611731, P. R. China
ksong@uestc.edu.cn

Abstract ─ This paper describes a modified real-coded genetic algorithm with a differential evolution operator (RGA-DE) for a shaped reflector of terahertz (THz) quasi-optical power divider/combiner. The real-coded genetic algorithm (RGA) is more convenient to define the reflector surfaces as compared to other coding methods. Interpolation method is applied to smooth the sophisticated surfaces. A better searching ability is obtained in a small number of individuals by using the differential evolution operator instead of the conventional crossover operator. So a bionics algorithm combining real-coded genetic algorithm and differential evolution (DE) algorithm has been presented to design the THz quasi-optical multiple-way holographic power-combining circuits. The RGA-DE has been utilized to optimize the coupling coefficient κ of the field distribution to get close to 1. Two real-world examples operating at 380 GHz and 450 GHz respectively are described. The computed results are verified by using the commercial software FEKO Suite.

Index Terms ─Differential evolution operator, quasi-optical power divider/combiner, real-coded genetic algorithm, terahertz technology.

I. INTRODUCTION

Shape optimization is one of the key techniques in the design of a quasi-optical power-combining circuit, which entails optimizing the shape of the metallic reflector [1-5]. The design of large shaped reflector for quasi-optical power-combining circuits has remained a challenge. The shape of the reflector surface is adjusted via a synthesis technique until the pre-defined field distribution is achieved within some acceptable level of accuracy. Numerous synthesis methods based on principles of geometrical optics (GO) [1-2] or physical optics (PO) [3-5] have been developed to compute the electromagnetic wave propagation. In order to get the desired field distribution, the Broyden–Fletcher–Goldfarb–Shanno (LBFGS) algorithm was applied in the past research. But as a gradient optimizer, to get the variation of the target function is a very complicated process. Even if gradient information of a practical problem is available, it can be unreliable or difficult to compute. Thus, non-gradient methods are incredibly useful optimization tools [6].

In this paper, we developed a bionics algorithm combining the real-coded genetic algorithm with a differential evolution operator (RGA-DE) to solve the problem of shaping the reflector surface without gradient information. The conventional genetic algorithm (GA) based on swarm intelligence is easy to be realized and already applied to many fields [7-8]. GA based on real-coding (RGA) can improve the precision of the optimization and the convergence rate [9-10]. But the traditional RGA don't perform well in a small number of individuals and they makes it fall into a local optimum due to the population losing its genetic diversity. Therefore, a differential evolution operator, which is borrowed from the differential evolution algorithm (DE) [11-13], is introduced to, instead of the crossover operator, obtain better searching ability in a small number of individuals.

The remainder of this paper is organized as follows. In Section 2, we introduce the design of the THz quasi-optical power-combining circuits. Subsequently in Section 3, we present RGA-DE to optimize the shape of the metallic reflector. The results achieved, discussed in Section 4, include the verified data by using the commercial software FEKO Suite. Finally, the findings of this paper are summarized in the conclusion.

II. ANALYSIS OF THZ QUASI-OPTICAL POWER-COMBINING CIRCUITS

Power-combining circuits in planar or waveguide structure are more suitable at microwave frequency due to large substrate, ohmic and radiation losses at millimeter- and submillimeter-wave frequencies [14-16]. Therefore, several quasi-optical and spatial holographic power combining techniques performed in free space to avoid these losses attract more and more attention [1-5]. There are two common quasi-optical circuit topology models indicated in Fig. 1. Pyramidal horn antenna and reflector are included in both topology models. But the

Submitted On: July 8, 2017
Accepted On: August 31, 2017

1054-4887 © ACES

receiving efficiency of such a setup will be strongly decreased if there is mismatch of radiation pattern between the transmitting and receiving radiation patterns. The popular method to solve this problem is to use holography. Figure 1 (a) shows the periodic hologram with a simple stepped surface profile and one shaped reflector. In the other topology, the two shaped reflectors are regarded as computer-generated phase holograms. Both of them are used to shape the electromagnetic wavefront for the field matching.

The surfaces of interest are labeled with P_i, i = 1, 2, 3, 4 in Fig. 1. $\boldsymbol{H}_i$ denotes the field distribution on the surface P_i. The reflectors were assigned parabolic surface to focus the power into the receiving plane P_4 on the antenna array placement. The field on surface P_2 and P_3 in Fig. 1 (a) and on surface P_2 in Fig. 1 (b) can be computed by using the Huygens-Fresnel principle [4]:

$$\boldsymbol{H}_{i+1}(\boldsymbol{r}) = \frac{j}{\lambda_0}\int_{P_i} \boldsymbol{H}_i(\boldsymbol{r}')\frac{e^{-jk_0|\boldsymbol{r}-\boldsymbol{r}'|}}{|\boldsymbol{r}-\boldsymbol{r}'|}\cos(\hat{\boldsymbol{n}}_0, \boldsymbol{r}-\boldsymbol{r}')dp', \quad (1)$$

where $\hat{\boldsymbol{n}}_0$ is the aperture surface's unit normal vector, k_0 is the free space wave number, and λ_0 is the free space wavelength. The computation of the diffraction of each reflector is based on the PO [4, 17]. In the PO for a perfect electric conductor surface, the observation point at r can be computed as:

$$\boldsymbol{H}_{i+1}(\boldsymbol{r}) = \int_{P_i} \boldsymbol{h}(\boldsymbol{r},\boldsymbol{r}')\frac{e^{-jk_0|\boldsymbol{r}-\boldsymbol{r}'|}}{|\boldsymbol{r}-\boldsymbol{r}'|}dp', \quad (2)$$

where

$$\boldsymbol{h}(\boldsymbol{r},\boldsymbol{r}') = -\frac{jk}{2\pi}\hat{\boldsymbol{r}}'\times(\hat{\boldsymbol{n}}'\times\boldsymbol{H}_i(\boldsymbol{r}'))\left(1+\frac{1}{jk_0|\boldsymbol{r}-\boldsymbol{r}'|}\right), \quad (3)$$

where $\hat{\boldsymbol{r}}' = (\boldsymbol{r}-\boldsymbol{r}')/|\boldsymbol{r}-\boldsymbol{r}'|$, $\boldsymbol{H}(\boldsymbol{r}')$ and $\hat{\boldsymbol{n}}'$ denote the magnetic field and the unit normal vector at the integration point $\boldsymbol{r}'$, respectively. When $|\boldsymbol{r}-\boldsymbol{r}'| >> \lambda$, the formula can be written as:

$$\boldsymbol{h}(\boldsymbol{r},\boldsymbol{r}') \approx -\frac{jk}{2\pi}\hat{\boldsymbol{r}}'\times(\hat{\boldsymbol{n}}'\times\boldsymbol{H}_i(\boldsymbol{r}')). \quad (4)$$

In Fig. 1 (b), $\boldsymbol{H}_3$ is calculated by $\boldsymbol{H}_2$ based on PO approximation, and in the same way, $\boldsymbol{H}_4$ in the receiving plane can be obtained by $\boldsymbol{H}_3$. Due to the large electrical dimensions of the reflectors, the computation time is dominated by the integration time. To speed up the computation of the integral, the fast far-field approximation method (FAFFA) is used [18]. In the FAFFA, if $r_{l'l} >> r_{jl'}$ and $r_{l'l} >> r_{li}$, then we have:

$$\frac{e^{-jk_0|\boldsymbol{r}_i-\boldsymbol{r}_j|}}{|\boldsymbol{r}_i-\boldsymbol{r}_j|} \approx \frac{e^{-jk_0(r_{l'l}+\hat{\boldsymbol{r}}_{l'l}\cdot\boldsymbol{r}_{li}+\hat{\boldsymbol{r}}_{l'l}\cdot\boldsymbol{r}_{jl'})}}{r_{l'l}}. \quad (5)$$

Substituting Equation (5) into integral Equations (1) and (2), after three steps of aggregation, translation and disaggregation, the operation count will be reduced from N^2 to $N^{1.5}$. Although the reflector which is one of the most important parts of the quasi-optical power-combining circuit is used to focus the energy on the receiving plane P_4, one reflector with periodic hologram or two simple reflectors cannot get a desired field distribution. Only a small amount of energy in plane P_4 is fed into the receiving antenna array because of the field mismatching. Therefore, a reflector with shaped surface relief is an inevitable choice to get an ideal field distribution.

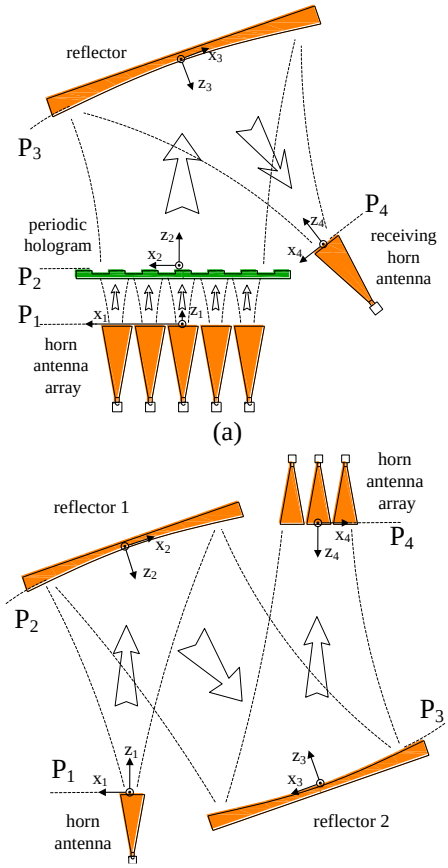

Fig. 1. (a) Power combiner with linear oscillator array, and (b) 2-D quasi-optical power divider consisting of two shaped reflectors.

III. SHAPE OPTIMIZATION VIA RGA-DE

The RGA-DE combines the real genetic algorithm and differential evolution so that a smooth convergence to a more global minimum can be achieved in a small number of individuals. It is noted that the conventional GA may converge slow and to a local minimum. The RGA-DE tends to avoid the aforementioned problem, and is thus, particularly useful for the shaped reflector design.

We first give a detailed coding method for the algorithm. The initial shape of the reflector is parabolic

and this parabolic surface can be expressed in the form:

$$z = \frac{1}{2}\left(\frac{x^2}{R_1} + \frac{y^2}{R_2}\right), \tag{6}$$

where x and y are along the local principal surface directions with R_1 and R_2 being their associated principal surface radii of curvatures.

We discretized the reflector surface into small squares with same periods along the x and y coordinates. The z coordinate of all nodes of the surface can be expressed as a matrix:

$$Z_{parab} = \begin{bmatrix} z_{11} & z_{12} & \cdots & z_{1n} \\ z_{21} & z_{22} & \cdots & z_{2n} \\ \vdots & \vdots & \ddots & \vdots \\ z_{m1} & z_{m2} & \cdots & z_{mn} \end{bmatrix}. \tag{7}$$

In general, $\lambda/3$ gird's width is sufficiently accurate in a practical case. But each grid is variable, meaning, the surface is not smooth after the optimization is completed. Smooth procedures such as low-pass filtering [4] or moving average procedure [5] should be used. Here, an interpolation method is applied to smooth the reflector surface in the real coding.

A certain amount of nodes that are as the optimal variables is enough to interpolate all rest points. *Linear*, *spline* and *cubic* are several common interpolation methods in MATLAB. Interpolation method is a simple and efficient way to yield a smooth surface reflector. The surface correction ΔZ_{interp} interpolates from all interpolating nodes ΔZ. The number of ΔZ_{interp} is about 64 times the number of ΔZ in the following examples. The actual surface relief is:

$$Z_{shaped} = Z_{parab} + \Delta Z_{interp}. \tag{8}$$

The Z_{shaped} will be used in the field calculation. Individuals ΔZ using real-coding can be expressed as below:

$$Z^i(t) = \begin{bmatrix} z_{11}^{ti} & z_{12}^{ti} & \cdots & z_{1q}^{ti} \\ z_{21}^{ti} & z_{22}^{ti} & \cdots & z_{2q}^{ti} \\ \vdots & \vdots & \ddots & \vdots \\ z_{p1}^{ti} & z_{p2}^{ti} & \cdots & z_{pq}^{ti} \end{bmatrix}, \tag{9}$$

where $z_{uv}^{ti} \in [z_{\max}, z_{\min}]$, $u \in [1, p]$, $v \in [1, q]$, $i \in [1, NP]$. NP is the number of individuals in a population. i and t donate the ith individual and the tth generation, respectively. z_{uv}^{ti} which is the interpolation node is as one of the variables pq on the optimization and it is a real number. The variation range of the interpolation node z_{uv}^{ti} is from $z_{\min}$ to $z_{\max}$.

The process of RGA-DE can be represented by the flowchart form as shown in Fig. 2. The loop runs for a number for predefined generations and is composed mainly of evaluate fitness, selection, differential evolution and, mutation steps.

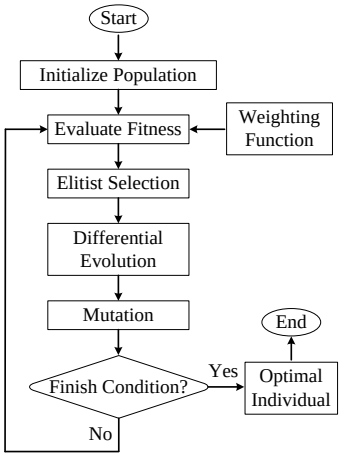

Fig. 2. Flow chart of the proposed RGA-DE.

A. Selection

A selection operator picks individuals based on their fitness function values from a current population and then reproduces these individuals into a differential evolution pool. The individuals that take part in the reproduction step are determined using the roulette wheel method. It means that the individuals are assigned a probability of being selected based on their fitness.

After evolution differential and mutation the new population is generated based on their fitness. With the help of elitism we can store the best found individual. The remaining individual is delivered for the next generation. In this way we cannot lose the best genetics.

B. Differential evolution

Differential evolution operator is to produce new offspring while exploring the solution space. For each individual $Z^i(t)$, a perturbed individual $Z^i(t+1)$ is generated according to scheme DE/best/1 [11], the DE operator is expressed as below:

$$Z^i(t+1) = Z^{best}(t) + F_{DE} \cdot (Z^j(t) - Z^k(t)), \tag{10}$$

with $i, j, k \in [1, NP]$ integer. j and k are picked randomly from 1 to NP for each individual $Z^i(t+1)$, and F_{DE} is a real constant factor, $F_{DE} \in [0, 2]$.

The best performing individual of the current generation $Z^{best}(t)$ will be the perturbed by the differential variation $Z^j(t) - Z^k(t)$, whose amplification is controlled by the constant factor F_{DE}. The DE operator has the advantage of strong local search capability, which is shown in Fig. 3. It is logical to assume that the solution may lie near the parent that has a better fitness.

For a practical problem, if $z_{uv}^{(t+1)i} > z_{\max}$, then let $z_{uv}^{(t+1)i} = z_{\max}$, or if $z_{uv}^{(t+1)i} < z_{\min}$, then let $z_{uv}^{(t+1)i} = z_{\min}$.

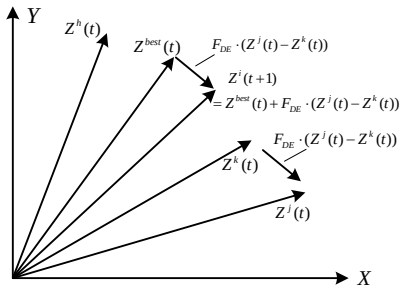

Fig. 3. The process for generating next generation in scheme DE/best/1 showing strong local search capability.

C. Mutation

In DE algorithm, crossover operator is implied to increase the diversity of individuals, but in GA it is realized by mutation. Here, we used a random variation to exploit the solution space.

for n=1 to Q (Mutation number)

Rondomly generate index $u \in [1, p]$ and $v \in [1, q]$.

$z_{uv}^{(t+1)i} = z_{uv}^{ti} + F_m \cdot (z_{random} - z_{uv}^{ti})$;

if $z_{uv}^{(t+1)i} < z_{\min} \,||\, z_{uv}^{(t+1)i} > z_{\max}$

$z_{uv}^{(t+1)i} = z_{\min} + r \cdot (z_{\max} - z_{\min})$;

end

end

where Q is the mutation number, $z_{random} \in [z_{\max}, z_{\min}]$ and r is generated from the interval [0, 1]. The best performing individual in the (t+1)th will not involve in the mutation and it will be preserved in the next generation in the selection operator.

D. Fitness

To quantify the performance of the reflector, we usually use coupling coefficient κ to characterize a potential solution as follows [4]:

$$\kappa = \frac{< H_{cal}, H_{ideal} >_P}{\sqrt{< H_{cal}, H_{cal} >_P < H_{ideal}, H_{ideal} >_P}}, \qquad (11)$$

where H_{cal} and H_{ideal} are the calculated field and ideal field, respectively. The scalar products for two complex-valued vector functions f and g are defined as:

$$< f, g >_P = \int_P f^*(y) g(y) dP(y). \qquad (12)$$

The fitness function of the problem is defined as:

$$fitness = \text{Re}\{\kappa\}. \qquad (13)$$

Sometimes, a weighting function can be applied to guide the evolution in some ways in (11). Using $\tilde{H}_{cal} = H_{cal}.*W_1$ and $\tilde{H}_{ideal} = H_{ideal}.*W_2$ instead of H_{cal} and H_{ideal}, respectively. '.*' denotes element-by-element multiplication. The element of the weighting matrices W_1 and W_2 is usually chosen $\in [0.7, 1.4]$:

$$\tilde{\kappa} = \frac{< \tilde{H}_{cal}, \tilde{H}_{ideal} >_P}{\sqrt{< \tilde{H}_{cal}, \tilde{H}_{cal} >_P < \tilde{H}_{ideal}, \tilde{H}_{ideal} >_P}}. \qquad (14)$$

In the loop runs, $fitness = \text{Re}\{\tilde{\kappa}\}$ can be a candidate to characterize the solution. But when the loop is finished, κ is used to quantify the optimal solution.

IV. NUMERICAL VALIDATION AND DISCUSSION

In order to demonstrate RGA-DE's applicability to real-world problems, two THz quasi-optical holographic power-combining circuits have been designed with RGA-DE. The two circuits are both designed and optimized by MATLAB programming.

The topology model of the first example operating at 380 GHz is shown in Fig. 1 (a), which is a five-way holographic power combiner. The binary phase grating is as a thin lens introducing a phase delay only, which consists of Teflon. The wavefront radiated by the line source consisting of five horn antennas is transformed by the phase grating and is focused to the receiving horn antenna by the shaped reflector. The reflector has a size of about 69λ×48λ. It is discretized to matrices of size 207×144 corresponding to approximately 3 points per wavelength. The optimization result is that κ is approximately 0.88-*j*0.00 at the observation plane 24λ×24λ after two thousand generations, whereas κ is about 0.68+*j*0.13 for the initial shape of the reflector surfaces. The shaped surface obtained for the power divider is illustrated in Fig. 4. Figures 5 (a) and (b) shows the calculated field distribution in the receiving plane P_4.

The parallel computing for each generation of four individuals consumes 15s using a 3.3 GHz quad-core CPU E3-1230v3. Figure 6 shows the progress of both RGA-DE optimization and conventional RGA as the function of the number of generations with different F_{DE}, F_m and NP. In the conventional RGA, the uniform crossover operator is expressed as below:

$$Z^i(t+1) = \alpha \cdot Z^{best}(t) + (1-\alpha) \cdot Z^i(t), \qquad (15)$$

with a constant factor $\alpha = 0.6$ in this paper. It takes about 6.3 hours to complete a single trail with a number of individuals NP = 4 and a fixed mutation number Q = 2. It is obviously that the RGA-DE has a faster convergence speed. The RGA-DE takes only 900 generations to reach the optimal value while the conventional RGA needs 1500 generations. The convergences of different NP are also displayed. In Fig. 6, the numerical results demonstrate that the RGA-DE runs well with high efficiency and stability. It shows that design method based on RGA-DE reached the almost same goal through different routes.

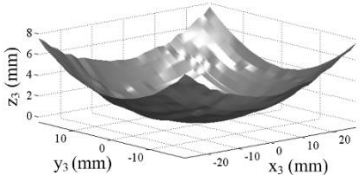

Fig. 4. The surface relief of the reflector.

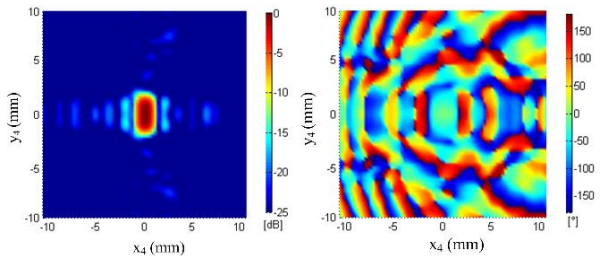

Fig. 5. Optimization results from the presented RGA-DE: (a) magnitude and (b) phase of electric field E_y.

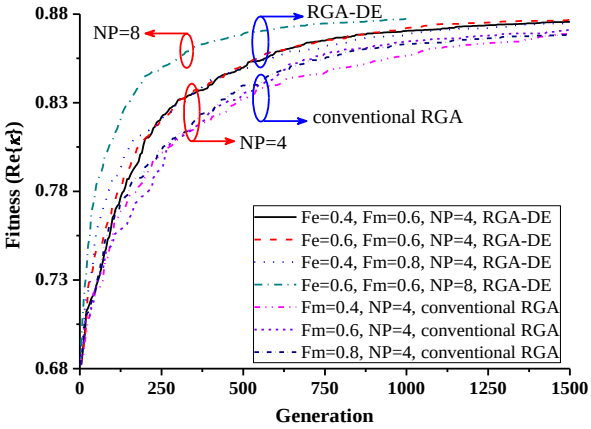

Fig. 6. Convergence characteristics of both RGA-DE and conventional RGA.

The topology model of the second example operating at 450 GHz is shown in Fig. 1 (b), which is a 2-D nine-way (3*3) holographic power combiner. The reflectors both have a size of about 74λ×78λ, which is 42% of the surface area for wavelength scale in [4-5]. The two reflectors are discretized to matrices of size 221×234 corresponding to approximately 3 points per wavelength. The computer-generated holograms, in other words, the shaped surfaces obtained for the power divider are illustrated in Fig. 7.

The optimization result is that κ is approximately 0.89+*j*0.01 at the observation plane 40λ×42λ, whereas κ is about 0.36+*j*0.08 for the initial shape of the reflector surfaces. 64% of the overall radiated power can be received in P_4. Figures 8 (a) and (b) shows the calculated magnetic field distribution in the receiving plane P_4. The correctness of the calculating method and calculated result are verified by using the commercial software FEKO Suite. Figures 8 (c) and (d) shows the verified results. The computation method is MLFMM in FEKO Suite and its calculated field data is imported to MATLAB to draw Figs. 8 (c) and (d). It is noted that the verified results agree closely with the one by PO in MATLAB programming.

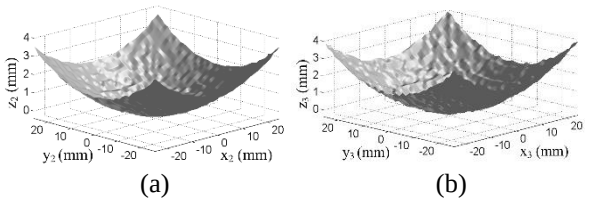

Fig. 7. (a) Surface relief of the first reflector and (b) the second one.

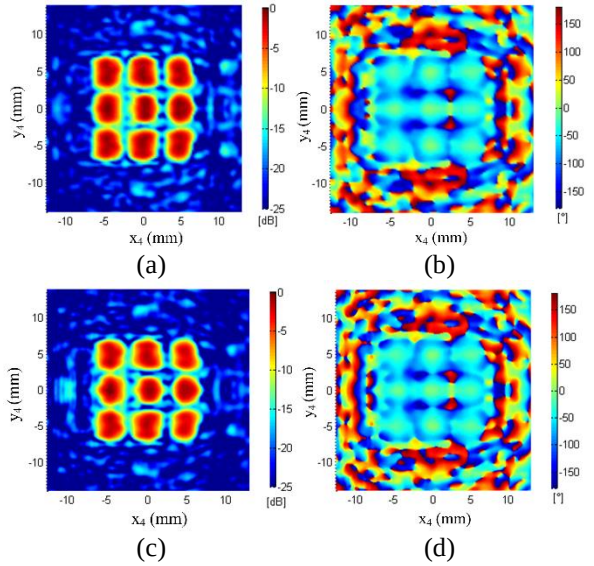

Fig. 8. Optimization results: (a) magnitude, (b) phase of electric field E_y from the presented RGA-DE, (c) magnitude, and (d) phase from the FEKO Suite.

V. CONCLUSION

A bionics algorithm using a differential evolution operator to realize crossover effects in a real-coded genetic algorithm to design the quasi-optical holographic power-combining circuits is investigated at THz frequencies. Real coding with interpolation method is applied to yield a smooth shaped surface. This proposed swarm intelligence optimization algorithm provides a new way to find a solution of complex problems without the gradient information and has good searching ability. It is easy to be realized using parallel computing to improve the computational efficiency. To verify the design and analysis of the THz quasi-optical holographic power-combining circuits, two examples operating at 380 GHz and 450 GHz respectively have been provided. The FEKO Suite's results agree with the optimization ones, which proves that the proposed RGA-DE algorithm is useful in the design of a THz quasi-optical holographic power divider/combiner.

ACKNOWLEDGMENT

The work was supported in part by National Natural Science Foundation of China (Grant No: 61271026) and by the Research Fund of Shanghai Academy of Spaceflight Technology (Grant No: SAST2016094).

REFERENCES

[1] M. Hoft, "Spatial power/combiner in D-band," *IEEE Trans. Microw. Theory Tech*., vol. 52, no. 10, pp. 2379-2384, 2004.

[2] R. Judaschke, M. Hoft, and K. Schunemann, "Quasi-optical 150-GHz power combining oscillator," *IEEE Microw. Wireless Compon. Lett.*, vol. 15, no. 5, pp. 300-302, 2005.

[3] T. Magath, M. Hoft, and R. Judaschke, "A two-dimensional quasi-optical power combining oscillator array with external injection locking," *IEEE Trans. Microw. Theory Tech*., vol. 52, no. 2, pp. 567-572, 2004.

[4] T. Magath, "Diffraction synthesis and experimental verification of a quasi-optical power splitter at 150 GHz," *IEEE Trans. Microw. Theory Tech.*, vol. 52, no. 10, pp. 2385-2389, 2004.

[5] T. Magath, R. Judaschke, and K. Schunemann, "2-D quasi-optical power combining oscillator array at D-band," *Microwave Symposium Diqest, IEEE MTT-S International 2006*, pp. 634-637, 2006.

[6] W. Hare, J. Nutini, and S. Tesfamariam. "A survey of non-gradient optimization methods in structural engineering," *Advances in Engineering Software*, no. 59, pp. 19-28, 2013.

[7] J. H. Holland, *Adaptation in Natural and Artificial Systems: An Introductory Analysis with Applications to Biology, Control, and Artificial Intelligence*. 2nd ed., Cambridge: MIT Press, 1992.

[8] T. Back, U. Hammel, and H. P. Schwefel, "Evolutionary computation: Comments on the history and current state," *IEEE Trans. Evol. Comput.*, vol. 1, no. 1, pp. 3-17, 1997.

[9] K. Chen, X. Yun, Z. He, and C. Han, "Synthesis of sparse planar arrays using modified real genetic algorithm," *IEEE Trans. Antennas and Propagat.*, vol. 55, no. 4, pp. 1067-1073, 2007.

[10] S. R. Rengarajan, "Genetic algorithm optimization of a planar slot array using full wave method-of-moments analysis," *Int. J. Comput. Aid RF Microw. Eng.*, vol. 23, no. 4, pp. 430-436, 2013.

[11] R. Storn, "On the usage of differential evolution for function optimization," *Fuzzy Information Processing Society, NAFIPS, 1996 Biennial Conference of the North American, IEEE*, 1996.

[12] R. Storn, "System design by constraint adaptation and differential evolution," *IEEE Trans. Evol. Comput.*, vol. 3, no. 1, pp. 22-34, 1999.

[13] M. Maddahali, A. Tavakoli, and M. Dehmollaian, "Shape reconstruction of three dimensional conducting objects using opposition-based differential evolution," *Applied Computational Electromagnetics Society Journal*, vol. 32, no. 1, pp. 93-98, Jan. 2017.

[14] K. Song, S. Hu, F. Zhang, and Y. Zhu, "Four-way chained quasi-planar power divider using rectangular coaxial waveguide," *IEEE Microw. Wireless Compon. Lett.*, vol. 25, no. 6, pp. 373-375, 2015.

[15] A. Mahan, S. H. Sedighy, and M. Khalaj-Amirhosseini, "A compact dual-band planar 4-way power divider," *Applied Computational Electromagnetics Society Journal*, vol. 32, no. 3, pp. 243-248, Mar. 2017.

[16] K. Song, F. Zhang, S. Hu, and Y. Fan, "Ku-band 200-W pulsed power amplifier based on waveguide spatially power-combining technique for industrial applications," *IEEE Trans. Ind. Electron.*, vol. 61, no. 8, pp. 4274-4280, 2014.

[17] G. Franceschetti and A. Mohsen, "Recent developments in the analysis of reflector antennas: A review," *IET Microwaves Antennas and Propagation IEE Proceedings H*, vol. 133, no. 1, pp. 65-76, 1986.

[18] C. C. Lu and W. C. Chew, "Fast far-field approximation for calculating the RCS of large objects," *Microwave Opt. Technol. Lett.*, vol. 8, no. 5, pp. 238-241, 1995.

Fan Zhang was born in Hunan, China, in 1989. He received the B.S. degree from the Hefei University of Technology, Hefei, China, in 2012. He is currently working toward the Ph.D. degree in the School of Electronic Engineering, University of Electronic Science and Technology of China, Chengdu, China. He is interested in the investigation of quasi-optical beam-shaping techniques.

Kaijun Song (M'09-SM'12) received the M.S. degree in Radio Physics and the Ph.D. degree in Electromagnetic Field and Microwave Technology from the University of Electronic Science and Technology of China (UESTC), Chengdu, China, in 2005 and 2007, respectively. Since 2007, he has been with the EHF Key Laboratory of Science, School of Electronic Engineering, UESTC, where he is currently a full Professor. He has published more than 80 internationally refereed journal papers. His current research fields include microwave and millimeter-wave/THz power-combining technology;

UWB circuits and technologies; and microwave remote sensing technologies.

Yong Fan received a B.E. degree from Nanjing University of Science and Technology, Nanjing, Jiangsu, China, in 1985, and a M.S. degree from University of Electronic Science and Technology of China, Chengdu, Sichuan, China, in 1992. He is a Senior Member of Chinese Institute of Electronics. From 1985 to 1989, he was interested in microwave integrated circuits. Since 1989, his research interests include millimeter-wave communication, electro-magnetic theory, millimeter-wave technology and millimeter-systems. He has authored or coauthored over 90 papers, 30 of which are searched by SCI and EI.

Design of a Novel Miniaturized Vivaldi Antenna with Loading Resistance for Ultra Wideband (UWB) Applications

Yongzhong Zhu [*1], Daoyi Su [2], Wenxuan Xie [1], Zihao Liu [1], and Kaiwei Zuo [1]

[1] Department of Information Engineering
Engineering University of PAP, Xi'an, Shanxi, 710086, P. R. China
*bsbs1980@sina.com, 184753211@qq.com, 33591232@qq.com, zkwcapf@163.com

[2] Guangdong Mikwave Communication Tech. LTD
Guangzhou, Guangdong, 510700, P. R. China
510727155@qq.com

Abstract ─ A compact improved Vivaldi antenna working on 0.8-3.8 GHz was designed by using resistance-loaded and slotting technology. Resistance-loaded can reduce the plane size of antenna and three symmetrical unequal rectangular slots in the antenna radiation part can increase the gain. The improved Vivaldi antenna size is 150×150×0.508 mm^3, which can be used in ground penetrating radar. The simulation results and experimental results are presented to validate the performance of the proposed improved structure of Vivaldi antenna.

Index Terms ─ ETSA, loading resistance, UWB antenna, Vivaldi antenna.

I. INTRODUCTION

An exponentially tapered slot antenna (ETSA), which was firstly described by Gibson in 1979 [1], has been widely studied and applied due to its simple structure, light weight, wideband, high efficiency and high gain. It has been utilized in many ultra wideband (UWB) applications such as ground penetrating radar, UWB communication systems, UWB imaging system, etc. Theoretical and experimental analysis of various Vivaldi antenna characteristics can be found in [2]–[16].

In the tapered slot-line antenna, Vivaldi antenna has infinite bandwidth in theory [2], and therefore it gets wide application and research. However, the actual prepared Vivaldi antenna always has limited bandwidth. There are two main reasons: one is its feed structure limits that it can only achieve resonance in a limited bandwidth; the other is the maximum exponential type slot width of Vivaldi antenna determines the maximum electric length of antenna, and limits the lowest working frequency. Therefore, currently a lot of studies focus on the design of Vivaldi antenna above 3 GHz.

According to the structure of the radiating element, Vivaldi antenna can be divided into three categories: Vivaldi antenna [3, 4], antipodal Vivaldi antenna [6], and balance antipodal Vivaldi antenna [7]. In [3], it adopted coplanar waveguide feed to improve the VSWR of low frequency. In [4], in order to make miniaturization, it also improved the feeding part. It increased the area of feeding part and adopted feed with stepped structure. In [5] and [6], they made improvement on radiation part. The antenna in [5] opened unequal semicircle slots while that in [6] opened multiple rectangular slots on the edge of the radiation part, so as to improve antenna gain. The antenna in [7] adopted the method of increasing the length of the dielectric substrate to improve the directivity, and so on. Compared with several antennas, the antennas in [3] and [4] do better in miniaturization, but somewhat lacking in direction and gain, the antennas in [5-7] have higher antenna gain, while make some sacrifices in miniaturization.

In order to further reduce the size of the Vivaldi antenna, some scholars have put forward many new ways to improve the miniaturization of these structures. A tapered slot edge with resonant cavity (TSERC) structure is adopted to improve the design of a planar printed conventional Vivaldi antenna in [8], the low-end cutoff frequency of the TSERC structure is further reduced with the same antenna size. In [9], the gain and the impedance bandwidth are significantly improved by using two pairs of eye-shaped slots, especially at the low frequencies. In [10], structural modifications in the radiating fins of the antipodal Vivaldi antenna can reduce the lower operating frequency from 5.2 GHz to 3.7 GHz and achieve 28.8% size reduction without altering the dimensions. In [11], an UWB miniaturized antipodal Vivaldi antenna (AVA) with two pairs of tapered slot and two circularly shaped conductor is presented, its feed structure adopts the transition from broadside parallel stripline to CPW which makes it easily being integrated with RF circuit. The antenna in [12] adopts the method of modifying corrugated balanced antipodal Vivaldi structure with director to improve the directivity and

Submitted On: June 12, 2017
Accepted On: August 12, 2017

1054-4887 © ACES

impedance matching of low frequency.

This paper proposes an improved structure of Vivaldi antenna, which loads resistance at the bottom of exponential type antenna to improve voltage standing wave ratio (VSWR) at low frequency, and opens three symmetrical unequal rectangular slots in the antenna radiation part to increase the gain. The proposed antenna has the impedance bandwidth of 0.8-3.8 GHz and is proper for UWB applications. Also, the improvement of antenna gain at 0.8-1.5 GHz band is very obvious. The maximum gain at 3.8 GHz is 8.1 dB. The simulation and analysis of the proposed antenna is performed by using HFSS. The simulated and measured results are in good agreement and validate the design approach.

II. ANTENNA DESIGN

Traditional Vivaldi antenna can be divided into three parts: feeding part, transition part and radiation part. Figure 1 (a) shows the structure of traditional Vivaldi antenna.

Based on the traditional Vivaldi antenna, Fig. 1 (b) shows a Vivaldi antenna with loading resistor. A chip resistor is loaded on the new antenna, and a short circuit pin is utilized at the one end of the feeding line. The Vivaldi antenna in this paper loads resistance at the bottom of the exponential-type slot in the feeding part, and opens three unequal rectangular slots on both sides in the radiation part. Among them, loading resistance is to improve the feeding structure, so that the antenna can better match in low frequency band and increase the degree of miniaturization. Slotting is to improve the low frequency gain and to strengthen the directionality. Figure 1 (c) shows the structure of resistive loaded and three unequal rectangular slotted Vivaldi antenna. The dielectric substrate used in the designed antenna is FR-4, whose relative dielectric constant is 4.4 and thickness is 0.508 mm. The size of the substrate is 150×150 mm^2 (L×B). Feeding mode adopts microstrip line feed, which is located under the substrate.

The equivalent circuit model of the proposed new antenna is given in Fig. 2, where jX_m denotes the equivalent inductance of the pin; jX expresses the equivalent reactance brought by the discontinuity of the slotline. All of the circuit elements are transformed to the input of the microstrip, and the following equations can be deduced:

$$R_S = n^2 \frac{R^2 + Z_{Ant}R + X^2}{(R+Z_{Ant})^2 + X^2} Z_{Ant}, \quad (1)$$

$$X_S = n \frac{Z_{Ant}^2 X}{(R+Z_{Ant})^2 + X^2}. \quad (2)$$

It is indicated by (2) that the value of X_S can be greatly reduced if $R \gg Z_{Ant}$. On the other hand, the inductance of the short circuit pin is so small that it can be neglected. Therefore, the reflection coefficient can be expressed as:

$$\Gamma_{in} \approx \frac{R_s - Z_{om}}{R_s + Z_{om}}. \quad (3)$$

At the aspect of energy distribution, the power consumed by the chip resistor is little while it is far higher than radiation impedance, for the resistance is parallel with the antenna radiation part.

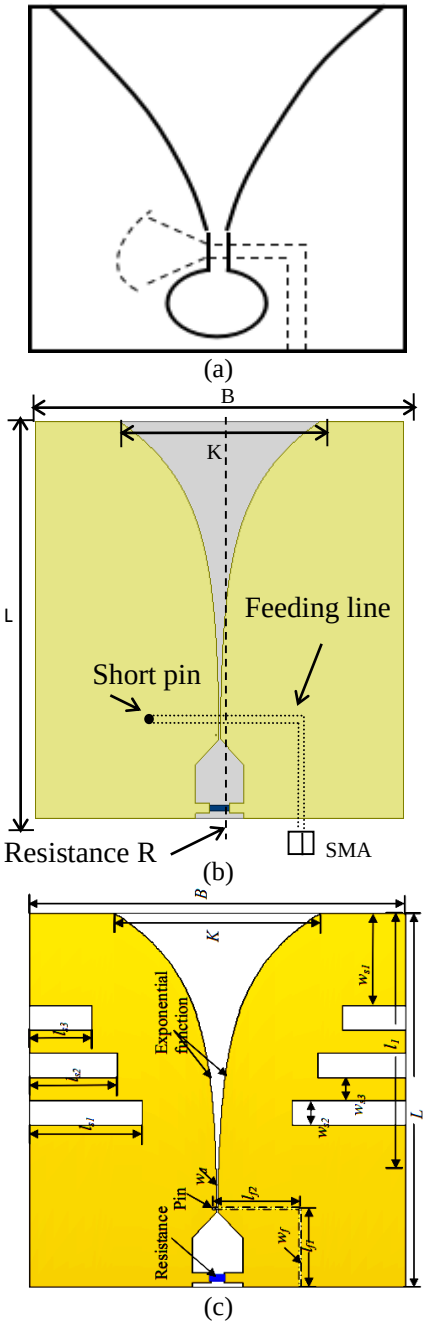

Fig. 1. Modification process of designed antennas: (a) traditional Vivaldi antenna (Ant.0); (b) a Vivaldi antenna with a chip resistor (Ant.I); (c) a novel Vivaldi antenna with a chip resistor and three unequal rectangular slots (Ant.II).

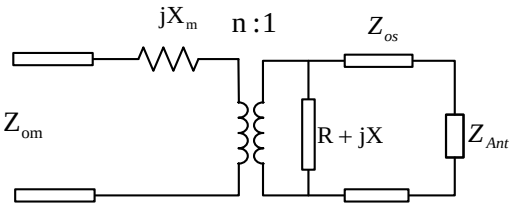

Fig. 2. Equivalent transmission line model of Fig. 1.

III. SIMULATION AND TEST OF ANTENNA

Ansoft HFSS15 is used to simulate, analyze and optimize the parameters of the antenna. When other parameters are constant, the effects of a single parameter on antenna performance are observed.

A. The influence of dielectric substrate thickness h on antenna performance

The change of substrate thickness *h* will directly affect the radiation conductance of antenna and the quality factor Q changes accordingly. The greater of the *h*, the smaller of Q value it is, the wider of frequency band is, but at the same time the surface wave will be more intensified. So only choosing appropriate thickness can ensure the comprehensive performance of the antenna.

Figure 3 is the influence of substrate thickness *h* on antenna return loss (S_{11}). It can be known from Fig. 3 that, when the thickness of *h* increases, the lowest frequency will be decreased. Therefore, the optimal value h = 0.5 mm is obtained.

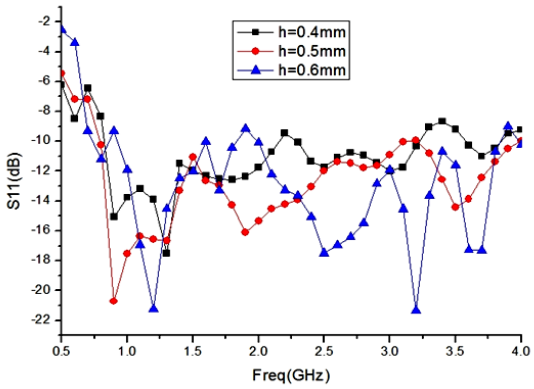

Fig. 3. The influence of substrate thickness h on S_{11}.

B. The influence of loading resistance R on antenna performance

Figure 4 shows the influence of the loading resistance value *R* on S_{11}, when Resistance value *R* respectively is 200 Ω, 300 Ω and 400 Ω. It can be known from the figure that, the lowest frequency basically remains unchanged when the resistance of the loading resistance changes. When R = 200 Ω, the performance will be worsen sharply at around 1.5 GHz and 2.7 GHz, this is caused by impedance mismatching at the higher frequency due to the small resistance. When R = 300 Ω or 400 Ω, the performances are very similar. However, when the bottom resistance value is greater, the antenna current will be decreased and the radiation efficiency is lower. Moreover, this paper selects SMD resistor with specifications of 2512, resistance of 331 Ω.

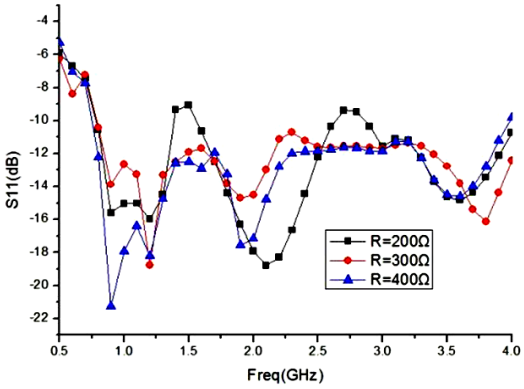

Fig. 4. The influence of resistance R on S_{11}.

C. The influence of the position of rectangular slots in radiative part on antenna performance

There are many parameters of rectangular slots. This paper is focused on its location. In Fig. 5 it shows that when the slot position is closer to the top of the exponential-type slot, the bandwidth of the antenna is more quickly decreased. If the slot position reaches a certain distance, the performance of the antenna will not change much. But with the continuing increase in distance, the performance of antenna working on about 3.2 GHz will decline. Therefore, the optimal value w_{s1} = 37 mm is obtained.

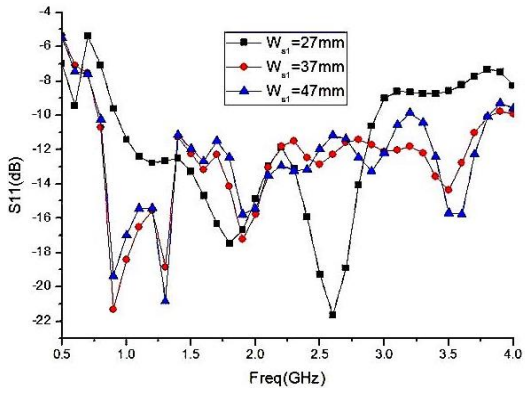

Fig. 5. The influence of slot position w_{s1} on S_{11}.

In addition to the above parameters optimized in the process of simulation experiment, other parameters also make further optimization such as feeding line width w_f, three rectangular slot lengths l_{s1}, l_{s2}, l_{s3}, three rectangular slot width w_{s2} and spacing distance w_{s3} between the

rectangular slots. The final optimization results of the various parameters of antenna are shown in Table 1.

Antenna I is a Vivaldi antenna that only loads resistance at the bottom and antenna II is a Vivaldi antenna that both loads resistance and rectangular slots. After improvement, the antenna II improves the current distribution. First, the structure suppresses the edge current of the antenna, resulting in an increase in the current density of the antenna, and the current is more concentrated in the vicinity of the exponential-type slot. Second, reducing the current through the resistor in the low frequency band of the antenna, the performance has been improved. Thirdly, near the open gradient slot line, the original surface current is changed to be distributed along the trough line, so that the equivalent size of the antenna is relatively increased; thereby these methods result in declining the low frequency cutoff frequency and playing a miniaturization effect.

Table 1: Final optimization results of the parameters of antenna (Unit: mm)

L	150	w_f	0.8	l_{s1}	45	w_{s1}	37
B	150	l_{f1}	32	l_{s2}	35	w_{s2}	10
K	82	l_{f2}	30	l_{s3}	25	w_{s3}	9
l_1	103	w_d	0.8	h	0.5	R (Ω)	331

Figure 6 shows a comparison of the simulated radiation efficiency of antenna 0, antenna I and antenna II. Antenna II optimizes the antenna's low frequency band (0.8 to 1.5 GHz) performance by using the method of slotting. Especially at the frequency of 0.8 GHz, the radiation efficiency improves from the original 48% to 59%.

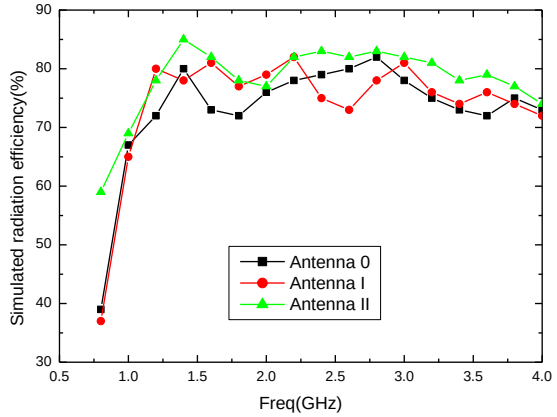

Fig. 6. The comparison of the simulated radiation efficiency of antenna I and antenna II.

In order to further verify the working performance of antenna, it prepares material object through accurate processing according to the optimal data. Figure 7 shows the picture of the antenna. The curves of the measured and simulated results are shown in Fig. 8 and Fig. 9.

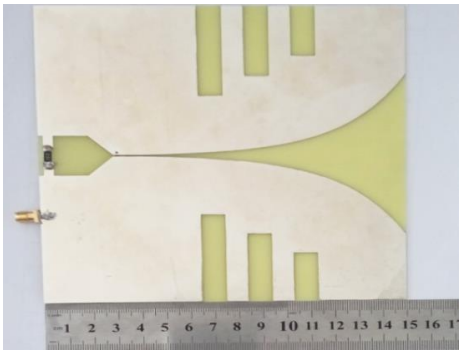

Fig. 7. Picture of the antenna.

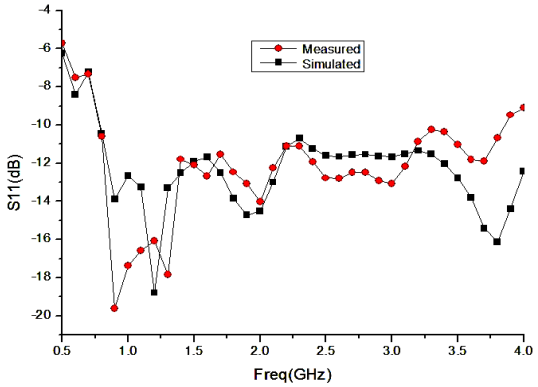

Fig. 8. Measured and simulated results for S_{11} of the antenna.

Table 2: The size and performance of the Vivaldi antennas

Ref.	Dimensions (mm^3)	O.W.B. (GHz)	Length/ λ_L	Width/ λ_L	Freq. (GHz)/ Gain (dB)
4	41×48×0.8	3-15.1	0.41	0.48	3.5/5 14/5.5
5	52×145×0.508	3.1-10.6	0.52	1.45	3/3.5 11/12.5
6	50×66.4×1	4-30	0.67	0.89	4/5 30/5
7	50×166×3.15	3-18	0.50	1.66	3.5/2 18/12
This work	150×150×0.508	0.8-3.8	0.40	0.40	0.8/2.4 2.8/6.1 3.8/8.1

Note: "O.B.W." states the operating bandwidth; "λ_L" is the wave length of minimum frequency in bandwidth.

It can be known from Fig. 8 that, the measured antenna impedance bandwidth is 0.8-3.8 GHz. The measured and simulated curves are almost identical. Compared with the simulation results, the measured curve will be slightly up at high frequencies around 3.5 GHz. Figure 9 shows the simulated and measured antenna pattern. It can be known from figure that the simulation results are consistent with the measured

results, so the antenna has stronger directivity within the scope of the bandwidth. Because of the inevitable effects of factors such as process error and test environment, measured results are not as ideal as simulation results, but on the whole, error is within the allowed range. The proposed novel Vivaldi antenna maintains realized gain between 2.4 dB to 8.1 dB. The parameters performance of the Vivaldi antennas in [4-7] and the designed antenna in this work parameters performance is roughly summarized in Table 2. Implementation of this method does not require any additional layers and simple structural modifications are used to achieve better performance.

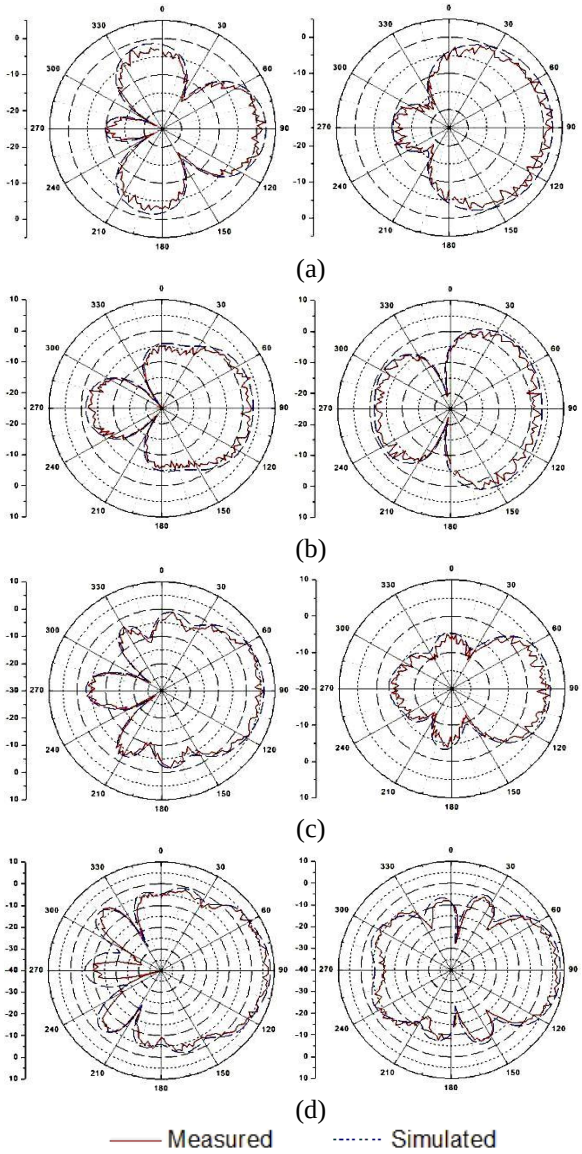

Fig. 9. The radiation patterns of the antenna at E-plane (left) and H-plane (right) at: (a) 0.8, (b) 1.8, (c) 2.8, and (d) 3.8 GHz.

IV. CONCLUSION

This paper designs and prepares a new type of Vivaldi antenna with the dimensions of 150×150×0.508 mm^3. The antenna adopts the loading resistance and opening unequal rectangular slots to optimize traditional Vivaldi antenna, which realizes the design objective of ultra-wideband, good directionality, and low frequency. In addition, it can be known from simulation and measure that the impedance bandwidth of the antenna is 0.8-3.8 GHz. Moreover, the measured results show that the antenna has good work performance and certain practical values.

ACKNOWLEDGMENT

This work was supported by the National Natural Science Foundation of China (No. 61302051 and No. 61771490), the Basic Research Program of ENGG University of the Chinese People Armed Police Force (No. WJY201606).

REFERENCES

[1] L. Lewis, M. Fassett, and J. Hunt, "A broadband stripline array element," *IEEE Antennas and Propagation Society International Symposium*, pp. 335-337, June 1974.

[2] M. Chiappe and G. L. Gragnani, "Vivaldi antennas for microwave imaging: Theoretical analysis and design considerations," *IEEE Transactions on Instrumentation and Measurement*, vol. 55, no. 6, pp. 1885-1891, Nov. 2006.

[3] J. Shao, G. Fang, Y. Ji, K. Tan, and H. Yin, "A novel compact tapered-slot antenna for GPR applications," *IEEE Antennas and Wireless Propagation Letters*, vol. 12, no. 1, pp. 972-975, Aug. 2013.

[4] J. Wu, Z. Zhao, Z. Nie, and Q. H. Liu, "A printed UWB Vivaldi antenna using stepped connection structure between slotline and tapered patches," *IEEE Antennas and Wireless Propagation Letters*, vol. 13, no. 1,pp. 698-701, Apr. 2014.

[5] D. M. In, S. Pyo, H. S. Lee, M. J. Lee, and Y. S. Kim, "Antipodal linearly tapered slot antenna using unequal half-circular slotted sides for gain improvements," *Microwave Conference Proceedings (APMC), 2010 Asia-Pacific*, Yokohama, pp. 2036-2039, Mar. 2010.

[6] G. Teni, N. Zhang, J. Qiu, and P. Zhang, "Research on a novel miniaturized antipodal Vivaldi antenna with improved radiation," *IEEE Antennas and Wireless Propagation Letters*, vol. 12, no. 2, pp. 417-420, Mar. 2013.

[7] A. Molaei, M. Kaboli, S. A. Mirtaheri, and M. S. Abrishamian, "Dielectric lens balanced antipodal Vivaldi antenna with low cross-polarisation for ultra-wideband applications," *IEEE Microwaves*,

Antennas & Propagation, vol. 8, no. 14, pp. 1137-1142, Nov. 2014.

[8] M. OstadRahimi, L. Shafai, and J. LoVetri, "Analysis of a double-layered Vivaldi antenna inside a metallic enclosure," *Progress In Electromagnetics Research*, vol. 143, pp. 503-518, 2013.

[9] K. Ma, Z. Zhao, J. Wu, S. M. Ellis, and Z.-P. Nie, "A printed Vivaldi antenna with improved radiation patterns by using two pairs of eye-shaped slots for UWB applications," *Progress In Electromagnetics Research*, vol. 148, pp. 63-71, 2014.

[10] Y. Zhang, E. Li, C. Wang, et al., "Radiation enhanced Vivaldi antenna with double-antipodal structure," *IEEE Antennas & Wireless Propagation Letters*, vol. 16, no. 7, pp. 561-564, July 2017.

[11] D. Wu, X. Wang, Y. Xie, et al., "A novel hybrid loaded Vivaldi antenna with broadened relative bandwidth," *Microwave & Optical Technology Letters*, vol. 58, no. 9, pp. 2037-2041, June 2016.

[12] M. Moosazadeh and S. Kharkovsky, "A compact high-gain and front-to-back ratio elliptically tapered antipodal Vivaldi antenna with trapezoid-shaped dielectric lens," *IEEE Antennas & Wireless Propagation Letters*, vol. 15, no. 7, pp. 552-555, July 2016.

[13] M. Abbak, M. N. Akinci, M. Cayoren, et al., "Experimental microwave imaging with a novel corrugated Vivaldi antenna," *IEEE Transactions on Antennas and Propagation*, vol. 65, no. 6, pp. 3302-3307, June 2017.

[14] J. Wu, Z. Zhao, and Q. Liu, "A novel Vivaldi antenna with extended ground plane stubs for ultra-wideband applications," *Microwave & Optical Technology Letters*, vol. 57, no. 4, pp. 983-987, Feb. 2015.

[15] G. K. Pandey, H. Verma, and M. K. Meshram, "Compact antipodal Vivaldi antenna for UWB applications," *Electronics Letters*, vol. 51, no. 4, pp. 308-310, Feb. 2015.

[16] R. Natarajan, J. V. George, M. Kanagasabai, et al., "A compact antipodal Vivaldi antenna for UWB applications," *IEEE Antennas & Wireless Propagation Letters*, vol. 14, no. 3, pp. 1557-1560, Mar. 2015.

Double Lens Antennas in Millimeter-Wave Automotive Radar Sensors

Nurdan Sönmez, Fikret Tokan, and Nurhan Türker Tokan

Department of Electronics and Communications Engineering
Yıldız Technical University, 34220, Istanbul, Turkey
nurdansonmez.ytu@gmail.com, ftokan@yildiz.edu.tr, nturker@yildiz.edu.tr

Abstract ─ In the near future, all newly introduced cars will be equipped with radar based systems enabling safer and more convenient driving. The performance of such systems is directly related with the performance of the antenna front end. Recently, double lens focusing system is proposed. With its high broadside directivity and low scan loss over a wide angular range, it can be considered as a good candidate for future long range radars. In this paper, effects of materials on beam scanning performance of double lens antennas are investigated for millimeter wave radars.

Index Terms ─ Automotive radar, double lens, millimeter-wave antennas, millimeter-wave radar, multiple-lens antennas.

I. INTRODUCTION

The majority of road accidents occur due to human errors. To reduce the human responsibility in accidents driver assistance systems are introduced. In automotive radar systems, the radar antennas placed to the front and/ or sides of the vehicle detects the objects surrounding the vehicle and decision on motion of the vehicle is activated. Automotive radar applications such as adaptive cruise control (ACC) and collision avoidance require highly directional antennas capable of distinguishing targets in the field of view. The choice of the radar antenna is determined by the requirements such as high gain and low loss combined with compact size and low cost. With lens antennas, radar sensors with different field of views can be easily build by simply changing the lens of the sensor. Lens antennas are well suited for automotive radar sensors and have been using as automotive radar antennas for over 10 years. The main advantage of this type of antenna is that they typically exhibit very low feed loss, thus yielding a high amount of gain for a given surface area [1]. The volume of this lens antenna is the major disadvantage since they require a non-negligible depth of few centimeters.

Recently, for automotive radars millimeter-wave range is forced by the regulatory agencies to eliminate the problem of the world-wide frequency allocation. The 77/79 GHz frequency band is the future choice for long-, mid- and short-range automotive radar [2-3]. Since almost all long or mid-range antennas will operate in the 76-81 GHz range in the near future, lens and reflector antennas are the first choice at millimeter-waves [4].

At millimeter waves, the most advanced antenna solutions available today are for ACC applications at 77 GHz. Some solutions are based on standard dielectric lens antennas (Bosch Gmbh and TRW/Autocruise) with a detection range up to 250 m and a field of view up to 30° [5]. With increasing requirements towards a much more detailed observation of the scenery in front or around the vehicle, the design of novel antenna concepts in combination with modified overall sensor arrangements became more important. These include multibeam antennas, scanning antennas, switched antenna concepts, and beam forming approaches with multiple transmit and receive antennas [6-11]. In practice, the standard lens antenna solutions proposed to scan the antenna beam use a unique lens illuminated by offset feeds. The feed offset dictates the beam pointing direction, as in optics. Nevertheless, large offset values lead to very poor antenna performance with increased scan loss and beam deterioration which is not acceptable for automotive sensors. In one of recent preliminary studies, the usage of double lens configuration to circumvent these limitations is demonstrated [12]. In literature, multiple lenses are mostly used in physics (e.g., microscope, telescope and camera). In [13], a double lens configuration operating at 30 GHz is proposed for single beam applications, whereas it was constructed and studied for the purpose of irradiation of biological objects in the range of 75-110 GHz in [14]. Compared with a single substrate lens antenna, the two lens antenna system can achieve up to 75% reduction of the lens material while maintaining about the same length and on-axis characteristics. In [12], it is proved that an integrated lens antenna with a double lens focusing system consisting of a hemispherical substrate lens and a plano-convex objective lens can provide simultaneously a high broadside directivity and low scan loss over a wide angular range. In the lens system, a material with low relative permittivity (ultem, $\varepsilon_r = 3.01$) is used in

Submitted On: March 11, 2017
Accepted On: August 12, 2017

1054-4887 © ACES

both lenses. The lens material has a strong impact on the radiation properties of the lens antennas. As the lens material changes, illumination angle provided by the primary feed would change and stronger impacts of internal reflections would be observed for the lens with high index of refraction. To minimize deteriorating effect of internal reflections, anti-reflective coatings are offered for dense lenses [15-16]. Dielectric lens antennas fabricated with a dense dielectric material allow good power transfer efficiency through the lens and enable fabrication of low-cost and compact-size lens antennas. Although, this is an important subject to be investigated, there is no work in literature that observes the effects of materials on radiation properties of double lenses.

In this work, double lens approach has been applied to millimeter-wave automotive radar antennas and its radiation characteristics are observed for antennas with low/high permittivity lenses. The scanning characteristics are observed. The structures are analyzed by means of a full wave simulator (Computer Simulation Technology (CST) software) based on finite integration technique. Due to ray principles of lenses, with a double lens antenna designed for the automotive radar antennas, better field of view (about 60º) is observed.

This paper is organized as follows: The configuration of the double lens antenna with its feed and circular corrugation is explained in Section II. The radiation characteristics and performance comparison results are reported in Section III. Conclusions are drawn in the last section.

II. CONFIGURATION OF THE ANTENNA

The motivation to use double lens systems is to combine the pattern characteristics of hemispherical and planospherical lenses. The planospherical lens alone can scan a beam with low loss, however it has a limit due to its high scanning loss. Hemispherical lens antennas show higher scanning capability, but lower gain characteristics. In the double lens configuration, the radiation characteristics of the hemispherical lens compensate for the losses of the planospherical lens. When a hemispherical lens is placed on the feed antenna and a planospherical lens is used at some distance, much better scanning and gain can be obtained. This is the basic motivation for double lens configurations. By using the double lens system, 30º scanning, resulting as 60º field of view is achieved with lower than 3 dB loss in gain.

A. Double lens geometry

The considered double lens antenna geometry can be seen in Fig. 1. It consists of an extended hemispherical lens as the immersion lens and a planospherical lens as the objective lens. *E* is the thickness of the objective lens, *F* is the distance between the antenna feeding plane and objective lens, ϕ_1 and ϕ_2 are the radii of the hemispherical and objective lens, respectively. In some cases, an additional cylindrical dielectric extension is added to obtain elliptical lens profile which enhances the antenna pattern. *L* is the extension length of the hemispherical lens. ε_{r1} and ε_{r2} are the relative permittivity of the immersion and objective lens, respectively. The effects of these design parameters on the radiation characteristics are investigated with the full-wave simulator. Thus, all multiple internal reflection are accounted for dense materials.

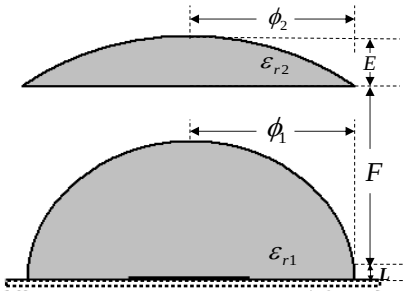

Fig. 1. Cut view of the double lens antenna geometry.

As the thickness of the planospherical lens (*E*) becomes larger, the focus distance, *F* gets smaller. Equations for obtaining the focus distance of a lens are available in literature; however these equations, which are functions of ϕ_2, ε_{r2} and *E*, don't give exact values, especially for thick lenses. To determine the exact location of the double lens focus, ray tracing code written in receiving mode is utilized. The path of the waves is calculated considering the varying propagation velocity, absorption characteristics, and reflecting surfaces. The point where all collimated rays are focused is found as the focus of the lens system. This is validated by the plane wave analysis of double lenses in receiving mode in CST. The plane of the focus point horizontal to the planar feed antenna is set as the feeding plane. Then, the radiation properties of the lens system illuminated by on- and off-axis feedings are investigated. As it is well-known, the lens system should be fed from the focus if the lens is aimed to radiate only to broadside direction. If it would be used for scanning purposes, it should scan the desired field of view with minimum scanning loss. In order to analyze the scanning performance, the feed antenna is shifted to a distance in *x*-axis. With the movement of the feed from on-axis to off-axis, the direction of the main beam rotates from 0° to larger scan angles. The decrease in maximum level of the pattern gives the scanning loss at that scan angle.

B. Feeding of the double lens antenna

Beam scanning performance of the proposed antennas is demonstrated by shifting a single feed antenna on *x*-axis and comparing the radiation

performance with that of on-axis feed. The primary source is an aperture coupled microstrip patch antenna printed on a RT/Duroid 5880 substrate ($\varepsilon_{r,subs} = 2.23$) given in Fig. 2. It gives almost symmetric radiation patterns in E- and H-planes and is well suited to be realized in integrated or printed circuit board (PCB) technology. Two primary feeds have been designed at 77 GHz. First is designed to radiate into low permittivity material, namely ultem ($\varepsilon_r = 3.01, \tan\delta = 3\times10^{-3}$ at 77 GHz) [12], second is designed to radiate into high permittivity material, alumina ($\varepsilon_r = 9, \tan\delta = 1\times10^{-3}$ at 77 GHz). The patch whose dimensions are given in Table 1 has a nearly-symmetrical radiation pattern with a half power beam width (HPBW) of about 60°. The feed displacement with respect to the lens axis is denoted as *x*.

Table 1: Dimensions of the primary feed designed to radiate into ultem and alumina (all units are in mm)

	L_{patch}	L_{slot}	L_{stub}	W_{line}	W_{slot}	$h_{substrate}$
Ultem	0.9	0.58	0.5	0.3	0.26	0.127
Alumina	0.6	0.58	0.45	0.3	0.26	0.1

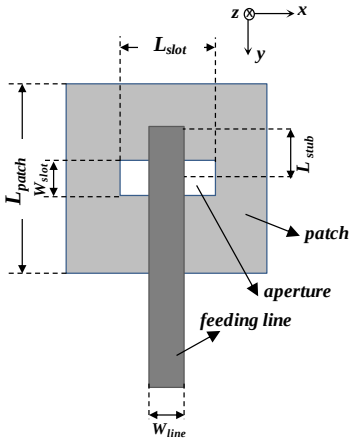

Fig. 2. Geometry of the primary feed (bottom view).

C. Matching layers for lenses with dense materials

Lens antennas made with high dielectric materials are desirable to favor power transfer from the feed to the lens. However, the impedance and radiation characteristics of such lenses are significantly distorted due to the excitation of multiple internal reflections [15]. These limitations can be moderately overcome by reducing the dielectric contrasts at the lens interface, using either conventional matching layers [15-16] or optimized ones [17-18]. Solution of adding a matching layer is difficult to realize since there may remain a gap of air between two layers. The existence of an air gap can expand the main lobe and raise the sidelobes. In automotive radar antenna design, low side lobe levels are crucial as high side lobes may lead to a false alarm in a collision avoidance system. An alternative solution is proposed in [19] by replacing an anti-reflection layer with the corrugated layer. This solution is realized by rectangular corrugations of alumina and was manufactured by stereolithography technique. Stereolithography is an additive layer-by-layer process that allows forming locally solid parts by selectively illuminating polymer photoresists or photoreactive ceramic suspensions. Consequently it becomes possible to construct all-dielectric 3-D devices with arbitrary complex geometries and/or adjustable refractive index by controlling the volumetric proportions of the composite materials. These concepts have been applied to design non-homogeneous monolithic lens antennas in Ka-band [20-21]. The corrugations are integrated directly on the surface of the lens. However, the weak point of using rectangular corrugations is that the results for the TE and TM modes are not identical which means it cannot be used for applications requiring bi-polarization or circular polarization. Thus, circular corrugation is proposed as the anti-reflective coating of the dense material lenses as shown in Fig. 3. The dimensions of each corrugation are calculated so that the relative permittivity is equal to that of the anti-reflection layer. *P* is the width and length of each unit cell. *D* is the diameter of each circular corrugation and is set to 0.8 mm. The thickness of the corrugations has no impact on the calculation of relative permittivity. Thus, it is set as the thickness of the quarter-wave transformer (0.56 mm at 77 GHz).

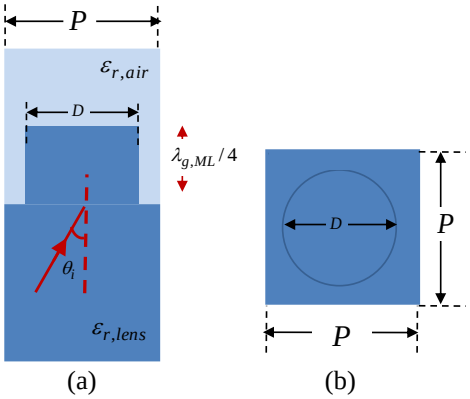

Fig. 3. Unit cell of a circular corrugation designed at 77 GHz: (a) cross-section view and (b) top view.

III. RESULTS

A. Analysis results

First attempt for the double lens antenna design is with a low permittivity, low cost dielectric, ultem. With the relative permittivity of $\varepsilon_r = 3.01$ and tangent loss $\tan\delta = 3\times10^{-3}$ at 77 GHz, this material can be considered as a good candidate for automotive radar applications. The diameter of the lenses is set to 64 mm (16.4 λ_o) in

order to obtain approximately 30 dB gain at 77 GHz. The scanning performance of the system is observed for thick and thin planospherical lenses. Numerical analysis based on double lens dimensions (skipped for brevity) gives the lowest beam scanning loss when its parameters are set to L=0, E=10 mm, F=54 mm. The overall volume of the double lens is 64 mm x 64 mm x 64 mm (width x length x height) without boxing. Normalized E-plane radiation patterns of double lens with aperture coupled microstrip feed are given in Fig. 4 (a). Only E-plane patterns are demonstrated due to nearly-symmetrical radiation pattern of the feed antenna. The family of the curves refers to different feed positions. The directivity is obtained as 30.8 dB when fed by on-axis feed. It scans 30° with approximately 3 dB loss. 30° scanning is achieved by feeding the double lens 18 mm away from the focus point. When the size for the patch of the feed antenna (0.9 mm x 0.9 mm) and the distance between the feedings are considered, it is clear that more feed antennas can be added to the array to have better resolution. The scanning loss gets higher when the double lens is fed further than 18 mm, thus patterns up to 30° main beam direction are plotted.

Lens with a dense dielectric material allow good power transfer efficiency through the lens and enable fabrication of low-cost and compact-size lens antenna. Thus, effects of using high permittivity material on double lens antenna radiation are investigated. Firstly, only the material of the objective lens is changed. Alumina with relative permittivity $\varepsilon_{r2} = 9$ is used in the objective lens. Using dense dielectric material causes strong multiple internal reflection behavior inside the lens. These multiple reflections deteriorate not only the return loss but also the radiation characteristics. Wide angle scanning performance is limited due to off-axis aberrations. To avoid the reflections that occur between air-alumina and alumina-air interface, the anti-reflective coating, namely circular corrugation described in the previous section is added to the upper and lower sides of the planospherical lens. After numerical analysis of the double lens, the results with highest directivity and lowest scanning loss is obtained with dimensions L=0, E=5 mm, F=39 mm. The directivity of the double lens fed by on-axis feed is 32.4 dB and the size of the structure is 64 mm x 64 mm x 44 mm (width x length x height) without boxing. Although the height of the double lens is reduced by 20 mm with this design, its beam scanning performance is not as good as the previous case. This can be observed with the normalized E-plane patterns shown in Fig. 4 (b).

Afterwards, the case with immersion lens having high permittivity material (alumina) and objective lens having low permittivity material (ultem) is analyzed. The best configuration with 30.1 dB directivity and 1.5 dB loss in 20° scanning has dimensions: L=4 mm, E=10 mm, F=42 mm. Its normalized radiation patterns are given in Fig. 4 (c). It is found that 4 mm extension to the hemispherical lens enhances the beam scanning performance of the double lens. The aperture coupled microstrip antenna radiating to alumina is used as the feed antenna. The corrugations are added to half-sphere of the extended hemispherical lens. The antireflective coating is not added to the extension part due to the lack of radiation from that region. For scanning up to 30°, the feed patch should be placed 8 mm away from the focus, however the patterns are deteriorated after 5 mm displacement of the feed. This is due to smaller critical angle for alumina ($\theta_i \cong 19.5^o$) compared to the critical angle of ultem ($\theta_i \cong 35^o$); total internal reflection occurs. Besides, when the size of the feed patch (0.6 mm x 0.6 mm) is considered, it is clear that it would be a challenging task to design feed array for this double lens antenna. Besides, the scanning losses of the antenna are greater compared to previous two designs.

The last numerical analysis is performed for both immersion and objective lenses having dense material, alumina. With L=2 mm, E=4 mm, F=43 mm, this double lens has 49 cm total height. The matching is applied to both sides of planospherical lens and to the upper half-sphere of the extended hemispherical lens. The usage of matching layers has reduced the sidelobes; however they are still significant, especially for off-axis feedings (Fig. 4 (d)).

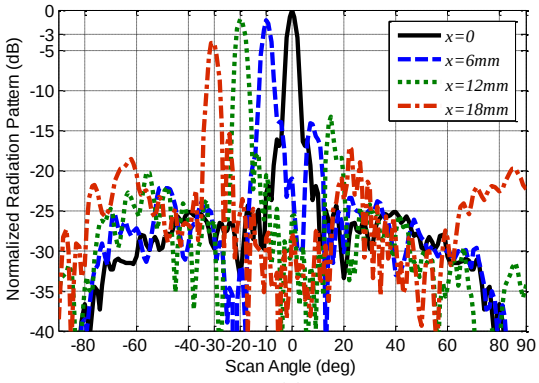

(a)

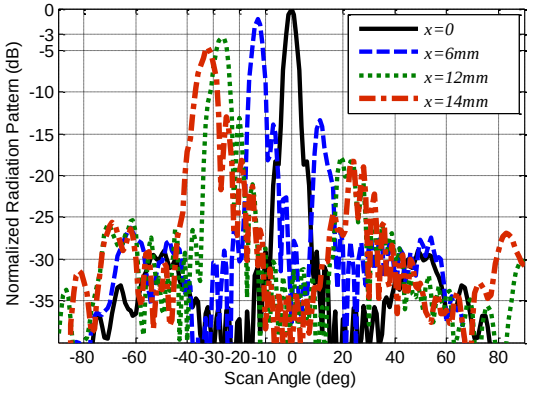

(b)

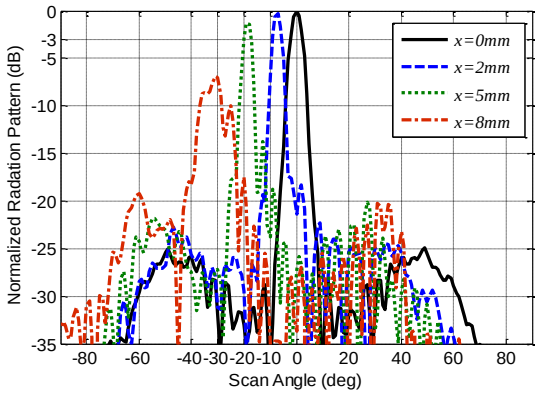

(c)

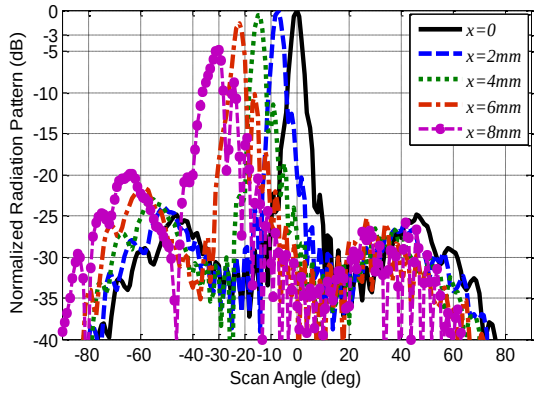

(d)

Fig. 4. The normalized E-plane radiation pattern of the double lens antenna with: (a) $\varepsilon_{r1}=\varepsilon_{r2}=3.01$; (b) $\varepsilon_{r1}=3.01$, $\varepsilon_{r2}=9$; (c) $\varepsilon_{r1}=9$, $\varepsilon_{r2}=3.01$; (d) $\varepsilon_{r1}=\varepsilon_{r2}=9$.

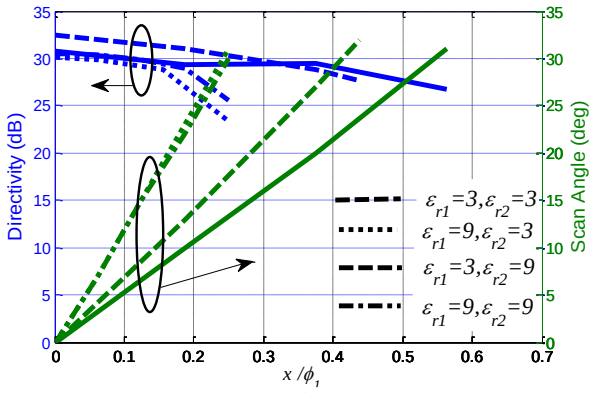

(a)

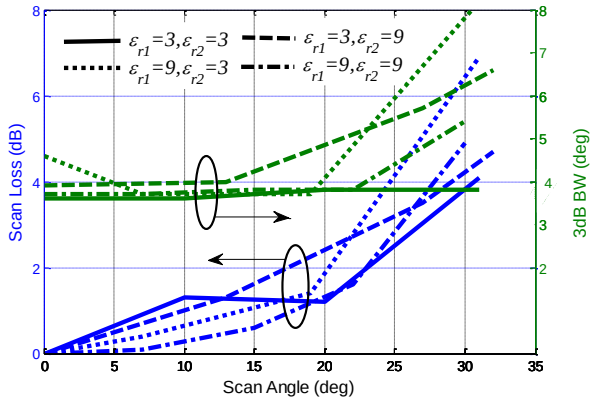

(b)

Fig. 5. Performance comparison of double lenses: (a) directivity and scan angle vs. feed position; (b) scan loss and 3 dB beamwidth vs. scan angle.

B. Comparison

In the previous section, radiation patterns of four final designs are demonstrated. They are all fed by the same feed which is aperture coupled microstrip antenna designed to radiate into the dielectric material of the immersion lens. Comparison of the results is summarized in Fig. 5. In Fig. 5 (a), left axis belongs to simulated directivity as the function of the feed position for the double lens antenna in E-plane. The main beam direction is shown at the right axis. The scan angle is the same for both planes. It can be observed that when the immersion lens is made of dense dielectric material its feed has to be closer to the focus point to scan the same angle. The directivity of the configurations with low permittivity immersion lens is more stable compared to ones with immersion lens having high permittivity. In Fig. 5 (b), scan loss and 3 dB beamwidth vs. scan angle is given. When these figures are investigated, the double configurations having low permittivity material in immersion lens is found to have the most promising results for the millimeter-wave long-range radar.

IV. CONCLUSIONS

Lens antennas are well suited for automotive radar sensors. Automotive radars consisting of planospherical lenses are in use to detect complex traffic scenarios. As an alternative to this lens, double lens that combines the pattern characteristics of a planospherical and hemispherical lens is proposed in [12] which is manufactured with a low permittivity material. However, it is well-known that the lens material has a strong impact on the radiation characteristics of the antenna. Thus, in this paper, the effects of materials on scanning performance of double lens antennas are investigated. The performance of the double lens system has been successfully verified via full-wave analysis. The results obtained with a double lens system consisting of extended hemispherical lens made of low-permittivity material demonstrate the excellent scanning performance that could be achieved with such systems. The presented analysis results of the double lens demonstrate its good performance in terms of beam scanning performance and gain. With its wider field of view and high directivity, double lenses can be a strong candidate for millimeter-wave automotive radar sensors.

ACKNOWLEDGMENT

This work was supported with a joint project by the French National Center for Scientific Research (CNRS) and The Scientific and Technological Research Council of Turkey (TUBITAK) under contract113E089.

REFERENCES

[1] W. Menzel, *Antennas in Automobile Radar, in Handbook of Antenna Technologies*. Springer Sci. Business Med., pp. 2475-2500, 2016.

[2] H. L. Blöecher, M. Andres, C. Fischer, A. Sailer, M. Goppelt, and J. Dickmann, "Impact of system parameter selection on radar sensor performance in automotive applications,"*Adv. Radio Sci.*, vol. 10, pp. 33-37, 2012.

[3] C. Sturm, G. Li, G. Heinrich, and U. Lübbert, "79 GHz wideband fast chirp automotive radar sensor with agile bandwidth," *IEEE MTT-S Int. Conf. on Microwaves for Int. Mobility (ICMIM)*, San Diego, CA, pp. 1-3, May 2016.

[4] W. Menzel and A. Moebius, "Antenna concepts for millimeter-wave automotive radar sensors," *Proc. of the IEEE*, vol. 100, no. 7, pp. 2372-2379, July 2012.

[5] J. Hasch, E. Topak, R. Schnabel, T. Zwick, R. Weigel, and C. Waldschmidt, "Millimeter-wave technology for automotive radar sensors in the 77 GHz frequency band," *IEEE Trans. on Microwave Theory and Tech.*, vol. 60, no. 3, pp. 845-860, Mar. 2012.

[6] T. Binzer, M. Klar, and V. Gross, "Development of 77 GHz radar lens antennas for automotive applications based on given requirements," *Proc. Int. Conf. Antennas*, Munich, Germany, pp. 205-209, Mar. 2007.

[7] M. Kishida, K. Ohguchi, and M. Shono, "79 GHz band high resolution milimeter wave radar," *Fujitsu Sci. Tech.*, vol. 51, no. 4, pp. 55-59, Oct. 2015.

[8] M. Steinhauer, H. O. Ruo, H. Irion, and W. Menzel, "Millimeter-wave radar sensor based on a transceiver array for automotive applications," *IEEE Trans. Microw. Theory Tech.*, vol. 56, no. 2, pp. 261-269, Feb. 2008.

[9] C. Lievers, W. van Rossum, A. Maas, and A. Huizing, "Digital beam forming on transmit and receive with an AESA FMCW radar," *Proc. Eur. Radar Conf.*, Munich, Germany, pp. 47-50, Oct. 2007.

[10] I. Sarkas, M. Khanpour, A. Tomkins, P. Chevalier, P. Garcia, and S. Voinigescu, "W-band 65-nm CMOS and SiGeBiCMOS transmitter and receiver with lumped I-Q phase shifters," *Proc. IEEE Radio Freq. Integr. Circuits (RFIC) Symp.*, Boston, MA, pp. 441-444, June 2009.

[11] C. Wagner, M. Hartmann, A. Stelzer, and H. Jaeger, "A fully differential 77 GHz active IQ modulator in a silicon-germanium technology," *IEEE Microw. Wireless Compon. Lett.*, vol. 18, pp. 362-364, May 2008.

[12] N. T. Nguyen, A. Boriskin, L. Le Coq, and R. Sauleau, "Improvement of the scanning performance of the extended hemispherical integrated lens antenna using a double lens focusing system," *IEEE Trans. on Ant. Propag.*, vol. 64, pp. 3698-3702, May 2016.

[13] X. Wu and G. V. Eleftheriades, "Two-lens and lens-fed reflector antenna systems for mm-wave wireless communications," *Int. Symp. Ant. and Propag. Soc.*, Toronto, Canada, pp. 660-663, July 2000.

[14] K. Komoshvili, B. Kapilevich, B. Litvak, and Y. Nagar, "Two lens-antenna system for mm-wave biological experiments systems," *IEEE Int. Conf. on Microwaves, Comm., Ant. and Electronics Sys.*, Ariel, Israel, pp. 1-4, Dec. 2011.

[15] N. T. Sönmez and N. T. Tokan, "Effects of antireflective coatings on scanning performance of millimetre-wave lenses," *IET Microw. Antennas Propag.*, vol. 10, no. 14, pp. 1-7, Oct. 2016.

[16] Y. Tajima and Y. Yamada, "Simulations of a shaped dielectric lens antenna by FEKO," *Applied Computational Society Journal*, vol. 24, no. 4, pp. 419-426, Aug. 2009.

[17] J. R. Costa, C. A. Fernandes, G. Godi, R. Sauleau, L. Le Coq, and H. Legay, "Compact Ka-band lens antennas for LEO satellites," *IEEE Trans. Antennas Propag.*, vol. 56, no. 51, pp. 1251-1258, May 2008.

[18] F. Tokan, "Optimization-based matching layer design for broadband dielectric lens antennas," *Applied Computational Society Journal*, vol. 29, no. 6, pp. 499-507, 2014.

[19] N. T. Nguyen, N. Delhote, M. Ettorre, D. Baillargeat, L. Le Coq, and R. Sauleau, "Design and characterization of 60-GHz integrated lens antennas fabricated through ceramic stereolithography," *IEEE Trans. Antennas Propag.*, vol. 58, no. 8, pp. 2757- 2762, Aug. 2010.

[20] K. F. Brakora, J. Halloran, and K. Sarabandi, "Design of 3-D monolithic MMW antennas using ceramic stereolithography," *IEEE Trans. Antennas Propag.*, vol. 55, no. 3, pp. 790-797, Mar. 2007.

[21] J. S. Silva, M. G. Vigueras, T. Debogovic´, J. R. Costa, C. A. Fernandes, and J. R. Mosig, "Stereolithography based antennas for satellite communications in Ka-band," *Proceedings of the IEEE*, vol. 105, no. 4, Apr. 2017.

Nurdan Sönmez was born in Istanbul, Turkey. She received her B.Sc. and M.Sc. degree in Electronics and Communication Engineering from the Yıldız Technical University, in 2012 and 2014, respectively. She is currently working on her Ph.D. in Communication Engineering at the same university. Her research interests include dielectric lens antennas, and automotive radars.

Fikret Tokan received his Ph.D. degree from Yıldız Technical University, Istanbul, in Communication Engineering in 2010. From October 2011 to October 2012, he was Postdoctoral Researcher in the EEMCS Department of Delft University of Technology. From October 2012 to May 2013, he was a Postdoctoral Fellow at the Institute of Electronics and Telecomm. (IETR), University of Rennes 1, France. He has been currently working as an Assoc. Prof. in the Electronics and Communications Engineering Department of YTU, Istanbul. His current research interests are UWB antenna design, dielectric lens antennas, electromagnetic waves, propagation, antenna arrays, scattering and numerical methods.

Nurhan Türker Tokan received her B.Sc. degree in Electronics and Communications Engineering from Kocaeli University in 2002 and her M.Sc. and Ph.D. degree in Communication Engineering from Yıldız Technical University (YTU), Istanbul, Turkey, in 2004 and 2009, respectively. From May 2003 to May 2009, she worked as a Research Assistant in the Electromagnetic Fields and Microwave Technique Section of the Electronics and Commun-ications Engineering Department of YTU, Istanbul, Turkey. Between May 2009 and April 2015, she worked as an Assistant Professor in the Electronics and Communications Engineering Department of YTU. Since April 2015, she has been working as an Associate Professor at the same department. From October 2011 to October 2012, she was Postdoctoral Researcher in the EEMCS Department of Delft University of Technology, Delft, Netherlands. From October 2012 to May 2013, she was a Postdoctoral Fellow supported by European Science Foundation at the Institute of Electronics and Telecommunications (IETR), University of Rennes 1, Rennes, France. She is the author or coauthor of more than 30 papers published in peer-reviewed international journals and conference proceedings. Her current research interests are analysis and design of antennas with emphasis on dielectric lens antennas and wideband antennas, microwave circuits and intelligent systems.

Position Optimization of Measuring Points in Voltage Non-contact Measurement of AC Overhead Transmission Lines

Dongping Xiao, Yutong Xie, Huaitong Liu, Qichao Ma, Qi Zheng, and Zhanlong Zhan

State Key Laboratory of Power Transmission Equipment & and System Security
Chongqing University, Chongqing 400044, China
xiaodongping@cqu.edu.cn, 20151102059t@cqu.edu.cn, 20141102032@cqu.edu.cn, 20151113002t@cqu.edu.cn, 20161113031t@cqu.edu.cn, zhangzl@cqu.edu.cn

Abstract ─ In this paper, an innovative idea is proposed to realize the voltage non-contact measurement of AC overhead transmission lines (OTLs), which is to reversely calculate the voltage characteristic parameters by using the measured AC electric field data under OTLs. The main challenge to realize the goal is the serious ill-posedness of the inverse problem. The condition number of the observation matrix $\boldsymbol{K}$ is the main index to reflect the ill-posedness of the inverse problem. Because the matrix $\boldsymbol{K}$ is determined by the positions of OTLs and the measuring points of electric field, it is an effective but often overlooked solution to search the optimal positions of measuring points. In this paper, an improved particle swarm optimization algorithm with the adaptive adjustment of inertia weight is developed to search the optimal measuring positions. The presented examples indicate that the selection of optimal positions for the measuring points significantly improves the accuracy and stability of the inverse solution. Meanwhile, the strong searching ability, fast convergence rate, and high stability of the proposed optimal algorithm are demonstrated as well.

Index Terms ─ AC overhead transmission lines (OTLs), electric field, ill-posed problem, inverse calculation, position optimization, voltage.

I. INTRODUCTION

The amplitude and phase of the sinusoidal voltage directly reflect the running status and health level of the AC overhead transmission lines (OTLs). Measuring the voltage of OTLs is the basis to evaluate power quality, and to diagnose and locate faults. The voltage is traditionally measured by potential transformer in the substation located at the beginning and end of OTLs. At present, the development of smart grids has increased the demand for the real-time monitoring of the OTLs' voltage to realize intelligent warning and automatic control [1, 2]. In view of the operating principle and electrical characteristics of potential transformer [3, 4], adding new potential transformers in existing lines will be confronted with many difficulties, and even it is not feasible. Therefore, some new methods of monitoring the voltage of OTLs, at the same time to meet the demands of safety and convenience, are of great value to be developed.

Numerous studies on the electromagnetic environment of high-voltage AC OTLs reveal that the power-frequency voltages of OTLs generate power-frequency electric fields in the surrounding space, which means that the sources and the fields are significantly correlated [5-8]. Thus, we propose the innovative idea to reversely calculate the voltage characteristic parameters of AC OTLs on the basis of the electric field data measured by the sensors placed under OTLs. In this way, the voltage non-contact measurement of AC OTLs can be realized.

However, the inverse calculation is a serious ill-posed problem. Specifically, the mathematical relation between the voltage matrix $\boldsymbol{U}$ and the electric field matrix $\boldsymbol{E}$ can be expressed as the following equations:

$$\boldsymbol{E} = \boldsymbol{K}\boldsymbol{U}, \tag{1}$$

where $\boldsymbol{K}$ is the observation matrix determined by the position of OTLs and the position of electric field measuring points.

Errors and noises inevitably exist in the actual measurement. We can only obtain $\boldsymbol{E}^{\delta}$ ($||\boldsymbol{E} - \boldsymbol{E}^{\delta}||<\delta$). If the positions of the measuring points are selected randomly, the condition number of the matrix $\boldsymbol{K}$ (i.e., cond($\boldsymbol{K}$)) may be much large. Consequently, a small noise in $\boldsymbol{E}$ may cause the inverse solution $\boldsymbol{U}^{\delta}$ to severely deviate from the true value $\boldsymbol{U}$.

Various processing methods have been proposed to address the ill-posed problem of inverse solution [9-12]. Based on our studies, we find that choosing the optimal positions of the electric field measuring points can greatly reduce cond($\boldsymbol{K}$) and the sensitivity of the inverse calculation to measuring noise.

In this paper, the optimal positions of the measuring points are searched by using cond($\boldsymbol{K}$) as the fitness function. An improved particle swarm optimization algorithm with the adaptive adjustment of inertia weight

Submitted On: December 14, 2016
Accepted On: August 12, 2017

1054-4887 © ACES

is developed to search optimal positions. Simulation examples with different search scopes are set up and the results are compared to verify the effectiveness of the proposed method in improving the ill-posed problem. And other favorable performances of the improved particle swarm optimization algorithm are discussed.

II. MATHEMATICAL MODEL OF POWER-FREQUENCY VOLTAGES AND ELECTRIC FIELDS OF OTLS

Under the power-frequency condition, the electric field around the high-voltage OTLs can be regarded as quasi-static field and being generated only by the voltages of OTLs. The length of OTLs is far greater than the distances between the measuring points and the conductors, so two-dimensional calculation can be adopted.

The analog line charges are set in the equivalent conductors based on the Charge Simulation Method [13, 14]. The relationship between the voltage matrix $\boldsymbol{U}$ and the analog charge matrix $\boldsymbol{\tau}$ is formulated as follows:

$$\boldsymbol{U} = \boldsymbol{P}\boldsymbol{\tau}, \tag{2}$$

where $\boldsymbol{P}$ is a N dimensional potential coefficient matrix and its elements can be calculated based on the principle of mirror image:

$$\begin{cases} p_{ii} = \dfrac{1}{2\pi\varepsilon_0}\ln\dfrac{2y_i}{R_{eq}} \\ p_{ij} = \dfrac{1}{2\pi\varepsilon_0}\ln\dfrac{L_{ij}^{'}}{L_{ij}} \quad (i \neq j) \end{cases}, \tag{3}$$

where ε_0 is the dielectric constant of air, L_{ij} is the distance between the i^{th} and j^{th} conductors, $L_{ij}^{'}$ is the distance between the i^{th} mirror conductor and the j^{th} conductor, i.e.,

$$L_{ij} = \sqrt{(x_i - x_j)^2 + (y_i - y_j)^2},$$
$$L_{ij}^{'} = \sqrt{(x_i - x_j)^2 + (y_i + y_j)^2},$$

where (x_i, y_i) and (x_j, y_j) are the coordinate positions of i^{th} and j^{th} conductors, respectively.

The electric field components $E_{x\text{-}o}$ and $E_{y\text{-}o}$ at the measuring points $o(x_o, y_o)$ are represented as:

$$\begin{cases} E_{x\_o} = \boldsymbol{G}_{x-o}\boldsymbol{\tau} \\ E_{y\_o} = \boldsymbol{G}_{y-o}\boldsymbol{\tau} \end{cases}, \tag{4}$$

where $\boldsymbol{G}_{x\text{-}o}$ and $\boldsymbol{G}_{y\text{-}o}$ are N dimensional row vectors, and their i^{th} elements are given by:

$$\begin{cases} g_{x\_oi} = \dfrac{1}{2\pi\varepsilon_0}\left(\dfrac{x_o - x_i}{L_{oi}^2} - \dfrac{x_o - x_i}{L_{oi}^{'2}}\right) \\ g_{y\_oi} = \dfrac{1}{2\pi\varepsilon_0}\left(\dfrac{y_o - y_i}{L_{oi}^2} - \dfrac{y_o + y_i}{L_{oi}^{'2}}\right) \end{cases}, \tag{5}$$

where L_{oi} is the distance between the measuring points and i^{th} conductor, $L_{oi}^{'}$ is the distance between the measuring points and the i^{th} mirror conductor.

The positions of conductors, mirror conductors and measuring points, as well as the distances between them, are shown in Fig. 1.

Finally, the equations can be formed as Eq. (1). The matrix $\boldsymbol{K}$ equals:

$$\boldsymbol{K} = \boldsymbol{G}\boldsymbol{P}^{-1}. \tag{6}$$

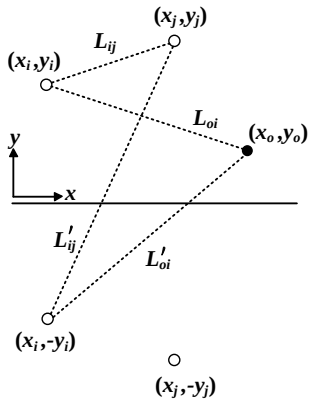

Fig. 1. Positions of the conductors, mirror conductors, measuring points and the distances between them.

III. POSITION OPTIMIZATION BASED ON IMPROVED PARTICAL SWARM OPTIMIZATION ALGORITHM

The particle swarm optimization algorithm is a global random search algorithm based on swarm intelligence. It has strong global search ability for complex problems, such as nonlinear, multi-peak, and so on. For these reasons, the particle swarm optimization algorithm has been widely applied in scientific research and engineering practice [15-18].

In the algorithm, a group of random particles should first be initialized to solve the fitness function value. Then, the location of the particle swarm should be updated, and the optimal solution is found during the successive iterations. The particle swarm updates its velocity and position by tracking the individual and global optimal positions in each iteration.

In our study, the fitness function is defined as the condition number of the matrix $\boldsymbol{K}$:

$$FitFun = \mathrm{cond}(\boldsymbol{K}). \tag{7}$$

According to Section II, each element in $\boldsymbol{K}$ is a function with the positions of the measuring points as variables. The variables are the coordinate positions of measuring points in the x and y axes:

$$\boldsymbol{X}_m = [x_{m1}, \cdots, x_{mn}, \cdots, x_{mN}],$$
$$\boldsymbol{Y}_m = [y_{m1}, \cdots, y_{mn}, \cdots, y_{mN}],$$

where n is the order number of the measuring points, N is the number of measuring points and the dimension of the objective search space in the optimization algorithm, m is the order number of the particle, and M is the number of particles.

The goal of the optimization is to minimize *FitFun* under certain boundary conditions. That is,

$$\text{Minimize } \{FitFun\}, \tag{8}$$

subject to,

(i) $x_{\min} \le x_{mn} \le x_{\max}$ for m=1,…., M and n=1,…., N;

(ii) $y_{\min} \le y_{mn} \le y_{\max}$ for m=1,…., M and n=1,…., N.

The flight velocities of the m^{th} particle along the directions of x and y axes are, respectively,

$$\boldsymbol{V}_{x,m} = [v_{x,m1}, \cdots, v_{x,mn}, \cdots, v_{x,mN}],$$
$$\boldsymbol{V}_{y,m} = [v_{y,m1}, \cdots, v_{y,mn}, \cdots, v_{y,mN}].$$

The flight velocities of the particles affect the algorithm's searching ability. A high velocity may cause the particles to miss the optimal positions. By contrast, a slow velocity will lead to a large time cost.

During the iterative process of searching for the optimal solution, the fitness function values of each particle must be calculated and compared. Then, the historical optimal solution location of each particle $\boldsymbol{X}_{Hbest,m}$, $\boldsymbol{Y}_{Hbest,m}$ and the global history optimal solution location of the particle swarm $\boldsymbol{X}_{Gbest}$, $\boldsymbol{Y}_{Gbest}$ are dynamically updated. Finally, the particle swarm converges to the global optimal position. According to the algorithm proposed by [19], the iteration formula for the velocity and position of the particle swarm in the $(t+1)^{\text{th}}$ generation are as follows:

$$\begin{aligned}\boldsymbol{V}_{x,m}^{t+1} &= \omega \boldsymbol{V}_{x,m}^{t} + c_1 r_{x1}^{t+1}(X_{Hbest,m} - \boldsymbol{X}_m^t) \\ &\quad + c_2 r_{x2}^{t+1}(X_{Gbest} - \boldsymbol{X}_m^t),\end{aligned} \tag{9a}$$

$$\begin{aligned}\boldsymbol{V}_{y,m}^{t+1} &= \omega \boldsymbol{V}_{y,m}^{t} + c_1 r_{y1}^{t+1}(Y_{Hbest,m} - \boldsymbol{Y}_m^t) \\ &\quad + c_2 r_{y2}^{t+1}(Y_{Gbest} - \boldsymbol{Y}_m^t),\end{aligned} \tag{9b}$$

$$\boldsymbol{X}_m^{t+1} = \boldsymbol{X}_m^t + \boldsymbol{V}_{x,m}^{t+1}, \tag{10a}$$

$$\boldsymbol{Y}_m^{t+1} = \boldsymbol{Y}_m^t + \boldsymbol{V}_{y,m}^{t+1}, \tag{10b}$$

where ω is the inertia weight; c_1 and c_2 are the learning factors; r_{x1}^{t+1}, r_{x2}^{t+1}, r_{y1}^{t+1}, and r_{y2}^{t+1} are random numbers of the (0, 1) distribution.

The iterative termination conditions are set as reaching the maximum number of iterations and the preset fitness threshold value. Then, the optimal value of the global fitness G_{best} and its corresponding optimal positions $\boldsymbol{X}_{Gbest}$, $\boldsymbol{Y}_{Gbest}$ are output.

The inertia weight ω is one of the important parameters in the particle swarm optimization algorithm. A large ω improves the global search capability of the algorithm, whereas a small ω enhances the local search capability of the algorithm. Selecting a suitable value can balance the convergence speed and the accuracy of the algorithm. To ensure the high probability that the particles are close to the global optimal solution in the early search and are close to local optimal solution in the late search, an adaptive adjustment strategy to set the inertia weight is used to control the search process in this paper. The inertia weight ω^t used in the t^{th} iteration is determined by the following equation:

$$\omega^t = (\omega^{\text{ini}} - \omega^{\text{end}}) \times \left(\frac{t^{\text{end}} - t}{t^{\text{end}}} \right)^2 + \omega^{\text{end}}, \tag{11}$$

where ω^{ini} and ω^{end} are the initial and final values of the inertia weight, respectively; t^{end} is the total number of iterations; and t is the current iteration number.

The algorithm flow chart is shown in Fig. 2.

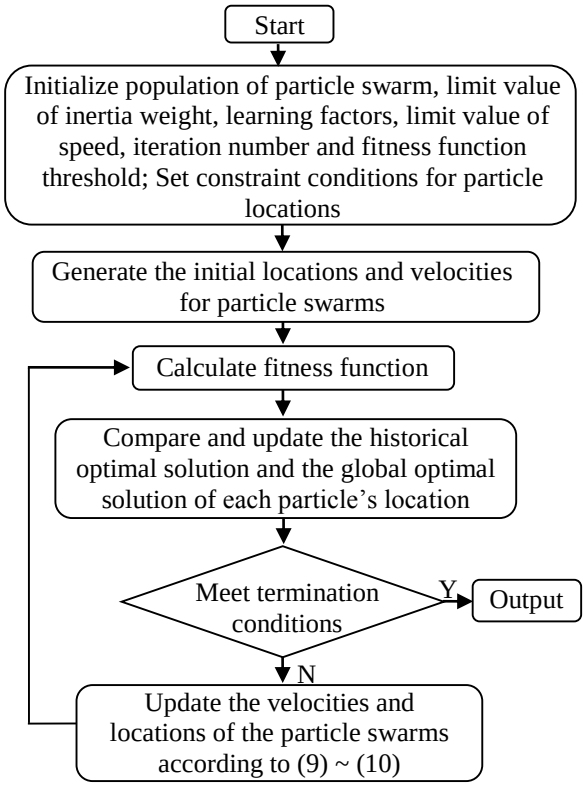

Fig. 2. Flow chart of improved particle swarm optimization algorithm.

IV. SIMULATION DETAILS AND RESULTS

A. OTLs layout and analysis condition setting

Figure 3 shows the layout of the three-phase conductors in a 220 kV OTLs system. The type of the phase conductor is 2×LGJ-400/35. The radius of the sub-conductor is 13.41 mm. The radius of the bundled circle is 0.35 m.

The analysis conditions are set as follows:

(i) The three-phase voltages of OTLs are symmetrical, i.e.,

$$\boldsymbol{U} = \begin{bmatrix} U_A \\ U_B \\ U_C \end{bmatrix} = \begin{bmatrix} 127.02\angle 0° \\ 127.02\angle -120° \\ 127.02\angle 120° \end{bmatrix} \text{kV}.$$

(ii) Only three measuring points are set so that the electric field measurement can be easily operated in practical engineering application. The three measuring

points are symmetrically placed corresponding to the symmetrical structure of the three-phase conductors.

(iii) The accurate values of the electric fields can be calculated based on (2)~(5). Given that the actual measurement may be severely disturbed, a signal-to-noise ratio of 15 dB is set and a random Gauss white noise is added in the calculated electric fields. Then the analog electric field measurement data are generated.

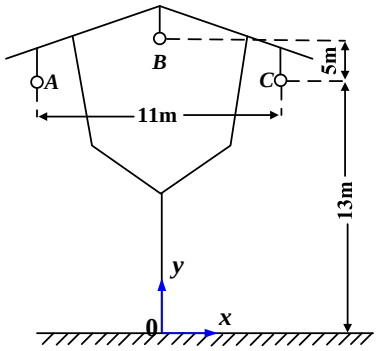

Fig. 3. Space layout of the three-phase conductors in a 220 kV OTLs system.

B. Results and analysis under the condition of randomly selecting measuring points

Three sets of measuring points are randomly selected and the corresponding cond(***K***) are calculated. The solution of voltages can be obtained by direct matrix inversion of Equation (1).

Each set of the voltages' inverse solution $\boldsymbol{U}^{\delta}$ are different because of the addition of random noise in the analog electric field measurement data. The mean and variance of $\boldsymbol{U}^{\delta}$ are calculated after running the program 10 times for each set of measuring points. The statistics are shown in Table 1.

As shown in Table 1, cond(***K***) and $\boldsymbol{U}^{\delta}$ have significant difference respectively for the three sets of measuring points that are randomly selected. The greater cond(***K***) is, the farther the inverse solution $\boldsymbol{U}^{\delta}$ deviate from the true solution ***U***. Consequently, the variances of the amplitude and angle of the calculated $\boldsymbol{U}^{\delta}$ are very large that means the stability of the inverse calculation is very poor.

C. Results and analysis under the condition of position optimization in a large space

Supposing that the optimal positions of measuring points can be searched in a large space, such as:

$$\begin{cases} -50\ \text{m} \le x_k \le 50\ \text{m} \\ 1\ \text{m} \le y_k \le 17.5\ \text{m} \end{cases}.$$

The optimal parameters are set as M=10, $\omega^{\text{ini}} = 0.9$, $\omega^{\text{end}} = 0.6$. The adaptive particle swarm optimization algorithm is used to search for the optimal positions of the measuring points with the minimum fitness function value.

Different solutions would be obtained by running program repeatedly because of the addition of random noise. Taking three sets cond(***K***) and $\boldsymbol{U}^{\delta}$ are shown in Table 2.

As shown in Table 2, although the obtained optimal positions in three optimization processes are different, the values of cond(***K***) in the three cases are approximate, which are all in the range of [1, 1.5]. Because cond(***K***) is very small, the three-phase voltages' inverse solution is close to the true value. The variance of $\boldsymbol{U}^{\delta}$ is evidently smaller than that in Table 1, which implies the computational stability is greatly improved.

Figures 4 (a)~(c) show the evolution of the global optimal solution G_{best} (i.e., the minimum of cond(***K***)) during the process of searching for the optimal positions as shown in Table 2, respectively. The three optimization processes reveal that the global optimal solution G_{best} tends to stabilize after 5~6 iterations.

Table 1: Results under the condition of randomly selecting measuring points

Measuring Points $(x_k\ y_k)$ / m	Cond(***K***)	Inverse Solution $\boldsymbol{U}^{\delta}$	
		Mean Value / kV	Variance (Amplitude Angle)
(−5.5 1.5) (0 1.5) (5.5 1.5)	98.90	199.50∠-5.8° 420.97∠−71.2° 114.77∠40.7°	(2953 1118) (19303 14603) (4998 11453)
(−7 1.5) (0 3) (7 1.5)	68.75	166.72∠5.8° 350.11∠-84.7° 146.68∠104.5°	(4335 703) (42436 14030) (3811 2309)
(−10 5) (0 5) (10 5)	20.87	128.28∠-3.5° 156.41∠-96.8° 123.18∠121.3°	(647 125) (2828 11781) (954 177)

Table 2: Results under the condition of position optimization in a large space

Measuring Points $(x_k\ y_k)$ / m	Cond($\boldsymbol{K}$)	Inverse Solution $\boldsymbol{U}^{\delta}$	
		Mean Value / kV	Variance (Amplitude Angle)
(−6.6 17.5) (0 6.8) (6.6 17.5)	1.09	$\begin{bmatrix}128.80\angle 0.5^\circ\\125.11\angle -119.9^\circ\\131.74\angle 119.3^\circ\end{bmatrix}$	(97.05 26.28) (232.67 17.32) (46.67 11.63)
(−6.1 8.4) (0 14.4) (6.1 8.4)	1.34	$\begin{bmatrix}130.41\angle 1.1^\circ\\128.72\angle -121.2^\circ\\127.21\angle 120.7^\circ\end{bmatrix}$	(102.12 39.16) (173.71 17.56) (239.56 13.92)
(−8.2 10.6) (0 14.6) (8.2 10.6)	1.36	$\begin{bmatrix}123.67\angle -2.1^\circ\\124.97\angle -117.6^\circ\\130.38\angle 120.6^\circ\end{bmatrix}$	(123.66 34.29) (124.97 19.79) (130.38 15.13)

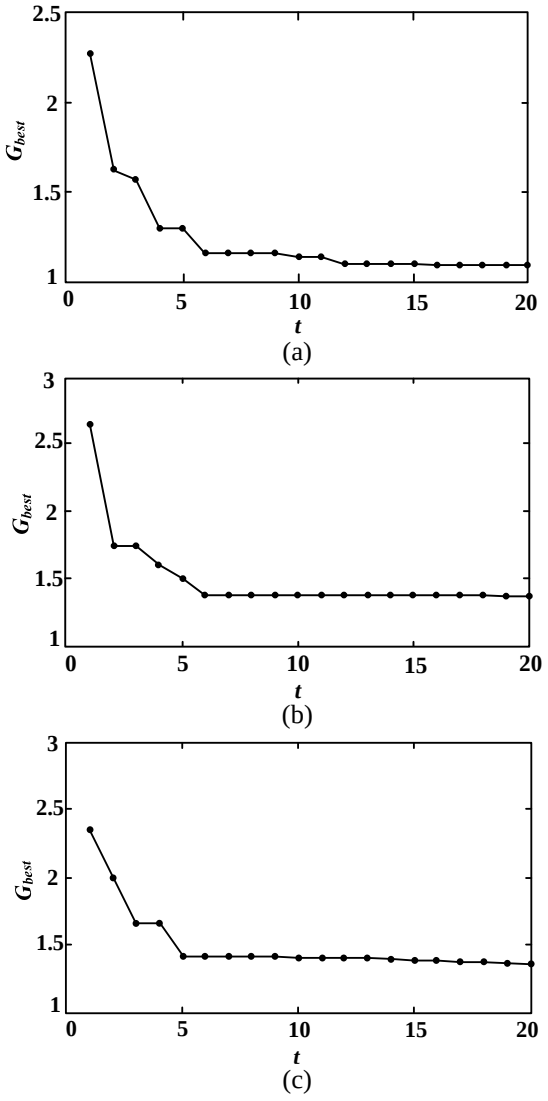

Fig. 4. Evolution of the global optimal solution G_{best} during the iterative process with adaptive adjustment ω algorithm.

D. Results and analysis under the condition of position optimization in a small space

In view of the limitations of the actual measurement conditions, the position of the measuring points can only be selected within a small space. Basing on our previous study, we propose two measurement schemes: (i) setting the measurement near the ground; (ii) setting the measurement near the conductors.

In the first measurement scheme, the search scope is set as:

$$\begin{cases}-15\ \text{m} \le x_k \le 15\ \text{m}\\ 1\ \text{m} \le y_k \le 4\ \text{m}\end{cases}.$$

The global optimal solutions obtained by separately running ten optimization processes are identical and they are (-15 4), (0 1) and (15 4). Then, cond($\boldsymbol{K}$)=21.89, and the voltage inverse solutions are:

$$\boldsymbol{U}^{\delta T} = \begin{bmatrix}143.02\angle -2.2^\circ\\148.25\angle -139.6^\circ\\114.01\angle 115.7^\circ\end{bmatrix}\text{kV}.$$

The maximum variances of the calculated amplitude and angle of the three-phase voltages are 1054 and 437, respectively.

In the second measurement scheme, the search scope is set as:

$$\begin{cases}-10\ \text{m} \le x_k \le 10\ \text{m}\\ 12\ \text{m} \le y_k \le 14\ \text{m}\end{cases}.$$

The global optimal solutions obtained by separately running ten optimization processes are also identical and they are (-9 12), (0 14) and (9 12). Then, cond($\boldsymbol{K}$)=1.46, and,

$$\boldsymbol{U}^{\delta T} = \begin{bmatrix}126.88\angle 2.2^\circ\\123.17\angle -117.2^\circ\\132.75\angle 117.4^\circ\end{bmatrix}\text{kV}.$$

The maximum variances of the calculated amplitude and angle of the three-phase voltages are 279 and 32, respectively.

The results of the position optimization process in the two measurement schemes demonstrate that the proposed algorithm can accurately search for the unique global optimal solution when the search scope is set properly.

Figures 5 (a) and 5 (b) show the comparison of the three-phase voltage waveforms in time domain between the inverse solution and the true value in the two measurement schemes, respectively.

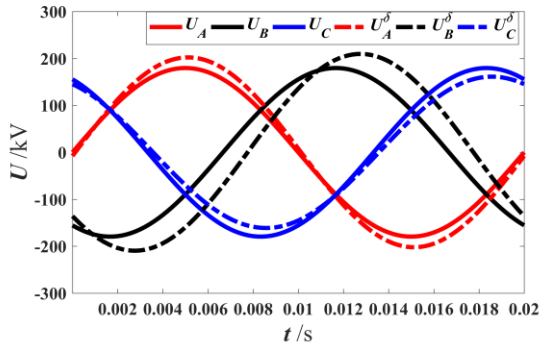

(a) In measurement scheme (i)

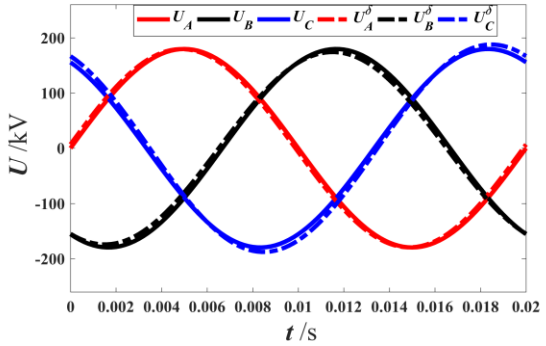

(b) In measurement scheme (ii)

Fig. 5. Comparison of the three-phase voltage waveforms in time domain between the inverse solution and the true value.

The inverse solutions obtained from the measurements near the conductors are superior to those obtained from the measurements near the ground. The error between the inverse solutions and true values is insignificant. However, measuring near the ground has the advantages of simple operation, flexibility, and safety, which is more able to reflect the superiority of the non-contact measurement approach. So further study is necessary.

V. CONCLUSION

The mathematical model between the power-frequency electric field and the voltages of OTLs is established in this paper, which reveals that it is feasible to reversely calculate the characteristic parameters of three-phase voltages by using the measured electric field data under OTLs. In view of the serious ill-posedness of the inverse solution, an improved particle swarm optimization algorithm based on adaptive adjustment of inertia weight is proposed to search for the optimal positions of the measuring points where the condition number of the observed matrix $\boldsymbol{K}$ in mathematical model is minimum. The simulation examples verify that the inverse solutions are more accurate and stable when the electric field data measured at optimal positions are used to calculate. The proposed optimization algorithm has the advantages of strong searching ability, fast convergence rate, and high stability.

Position optimization of measuring points is an effective and feasible method to weaken the ill-posedness of the specific inverse problem in this paper. It is greatly beneficial in improving the accuracy and speed of the inverse calculation. For the case that measurements are set near the ground, the regularized treatment or other inverse algorithms can be adopted further.

ACKNOWLEDGMENT

This work was supported in part by National Natural Science Foundation of China under Grant NSFC 51407016 and 51577017.

REFERENCES

[1] A. Sendin, R. Guerrero, and Pablo Angueira, "Signal injection strategies for smart metering network deployment in multitransformer secondary sub-stations," *IEEE Trans. Power Del.*, vol. 26, no. 4, pp. 2855-2861, Oct. 2011.

[2] V. M. Catterson, J. Castellon, J. A. Pilgrim, T. K. Saha, H. Ma, M. Vakilian, A. Moradnouri, M. Gholami, and B. D. Sparling, "The impact of smart grid technology on dielectrics and electrical insulation," *IEEE Trans. Dielect. El. In.*, vol. 22, no. 6, pp. 3505-3512, Jan. 2015.

[3] X. N. Lin, P. Liu, and S. M. Liu, "Ultra saturation state during transformer switch-in with load and its influence to transformer differential protection," *Proceedings of the CSEE*, vol. 22, no. 3, pp. 6-11, Mar. 2002 (in Chinese).

[4] L. X. Zhou, Z. D.Yin, and L. Zheng, "Research on principle of PT resonance in distribution power system and its suppression," *Trans. of ECS*, vol. 22, no. 5, pp. 153-158, May 2007 (in Chinese).

[5] R. G. Olsen and P. S. Wong, "Characteristics of low frequency electric and magnetic fields in the vicinity of electric power lines," *IEEE Trans. Power Del.*, vol. 7, no. 4, pp. 2046-2055, Oct. 1992.

[6] B. Florkowska, A. J. Korczynski, and M. Timler, "Analysis of electric field distribution around the high-voltage overhead transmission lines with an ADSS fiber-optic cable," *IEEE Trans. Power Del.*, vol. 19, no. 3, pp. 1183-1189, July 2004.

[7] J. H. Beggs, D. L. Marcum, and S. L. Chan, "Numerical method of characteristics for electro-

magnetics," *ACES Journal*, vol. 14, no. 2, pp. 25-36, July 1999.

[8] J. C. Salari, A. Mpalantinos, and J. I. Silva, "Comparative analysis of 2- and 3-D methods for computing electric and magnetic fields generated by overhead transmission lines," *IEEE Trans. Power Del.*, vol. 24, no. 1, pp. 338-344, Jan. 2009.

[9] A. N. Tikhonov and V. Y. Arsenin, *Solution of Ill-Posed Problems*. *Wiley*, New York, 1977.

[10] U. Hämarik and T. Raus, "On the choice of the regularization parameter in ill-posed problems with approximately given noise level of data," *J. Inv. Ill-Posed Problems*, vol. 14, no. 3, pp. 251-266, 2006.

[11] V. V. Vasin, "Relationship of several variational methods for the approximate solution of ill-posed problems," *Math. Notes. Acad. Sci. USSR*, vol. 7, no. 3, pp. 161-165, Mar. 1970.

[12] F. Yang, H. Wu, and W. He, "Investigation on the electric field inverse problem of HV transmission lines and discussion on its application," *ACES Journal*, vol. 25, no. 2, pp. 129-136, Feb. 2010.

[13] N. H. Malik, "A review of the charge simulation method and its application," *IEEE Trans. Elect. Insul.*, vol. 24, no. 1, pp. 3-20, Feb. 1989.

[14] H. Singer, H. Steinbigler, and P. Weiss, "A charge simulation method for the calculation of high voltage fields," *IEEE Trans. Power App. Syst.*, vol. 93, no. 5, pp. 1660-1668, Sep.-Oct. 1974.

[15] J. Kennedy and R. C. Eberhart, "Particle swarm optimization," *Proc. IEEE. Int. Conf. Neur. Net*., Houston, Texas, USA, pp. 1942-1948, 1995.

[16] W. C. Weng, "Optimal design of an ultra-wideband antenna with the irregular shape on radiator using particle swarm optimization," *ACES Journal*, vol. 27, no. 5, pp. 427-434, May 2012.

[17] K. E. Parsopoulos and M. N. Vrahatis, "Recent approaches to global optimization problems through particle swarm optimization," *NAT. COMPUT*, vol. 1, no. 2, pp. 235-306, June 2002.

[18] C. L. Li, C. H. Sun, C. C. Chiu, and L. F. Tuen, "Solving inverse scattering for a partially immersed metallic cylinder using steady-state genetic algorithm and asynchronous particle swarm optimization by TE waves," *ACES Journal*, vol. 28, no. 8, pp. 663-671, Aug. 2013.

[19] Y. H. Shi and R. Eberhart, "A modified particle swarm optimizer," *Proc. IEEE. Int. Conf. Evol. Comp*., Anchorage, Alaska, USA, pp. 69-73, 1998.

Dongping Xiao received the B.Sc. degree in Industrial Automation from Chongqing University, Chongqing, China, in 1999, and the M.Sc. and Ph.D. degrees in Electrical Engineering from Chongqing University, in 2004 and 2009, respectively. From 2012 to 2013, she was a Visiting Scholar with Washington State University, USA. Currently, she is an Associate Professor at the College of Electrical Engineering, Chongqing University, China. Her main fields of interests include calculation and simulation of electromagnetic field, electromagnetic measurement and running state monitoring of power transmission equipment.

Yutong Xie received the B.Eng. (Electrical Engineering) degree from Chongqing University, China, in 2015. Currently, she is studying for her master's degree (Electrical Engineering) at Chongqing University, China. Her research interest is electro-magnetic field calculation.

Huaitong Liu received the B.Eng. (Electrical Engineering) degree from Tianjin Chengjian University, China, in 2010. Currently, he is studying for his master's degree (Electrical Engineering) at Chongqing University, China. His research interests are electromagnetic field calculation and electromagnetic measurement.

Optimization of Permanent Magnet Synchronous Motors Using Conformal Mappings

Behrooz Rezaeealam* and Farhad Rezaee-Alam

Department of Electrical Engineering, Lorestan University, Khorramabad, Lorestan, 68137-17133, Iran
*rezaeealam@gmail.com

Abstract ─ An optimal permanent magnet synchronous motor (PMSM) should be a low cogging torque and a sinusoidal back-EMF. In this paper, different magnetizations and shaping models of permanent magnets (PMs) are investigated for achieving an optimal performance. The technique of slot opening shift is simultaneously implemented on the stator slots for more reducing of the cogging torque. To this end, the conformal mapping (CM) method as an accurate and fast technique is used to calculate the motor performance under each condition. In final, the optimal results obtained through the CM method are verified by comparing with the corresponding results obtained from the finite element method (FEM).

Index Terms ─ Cogging torque, conformal mapping (CM), magnetization, permanent magnet (PM), sinusoidal shaping (sin-shaping), slot opening shift.

I. INTRODUCTION

Due to high power density and high efficiency, the permanent magnet synchronous motors (PMSMs) are increasingly used in different industrial applications from automotive to aerospace. For this reason, the performance of PMSMs should be optimal as far as possible. To optimize the performance of PMSMs, it is necessary to shape the air gap magnetic field distribution in sinusoidal and to reduce the cogging torque.

So far, different techniques have been introduced for shaping the air gap magnetic field distribution. These techniques are divided into three groups: (a) the techniques based on the magnetization of PMs [1], (b) the techniques based on the shaping of PMs [2-4], and (c) the hybrid techniques based on the magnetization and the magnet shaping, simultaneously [5].

There are three types of PM magnetization, radial, parallel, and Halbach magnetization. The radial magnetization is usually suitable for PM BLDC machines, whereas the parallel and Halbach magnetizations are usually used in PM BLAC machines. The shaping techniques, including the sinusoidal shaping (sin-shaping) [5], the inverse cosine air gap shaping [5], and the loaf shape [6] are used to sinusoidally shape the air gap flux density and to save the magnet material, simultaneously. These techniques are nearly efficient for cogging torque reduction too.

There are also various techniques for cogging torque reduction more efficiently, such as PM or slot skewing [7-8], magnet segmentation [9], fractional slot winding [10], asymmetrical distribution of magnet poles [11] or stator tooth width [12] and so on. However, the motor performance drops by using the majority of these methods in addition to the cogging torque reduction. For this reason, the slot opening shift method is also used in this paper to more reduce the cogging torque, without reduction in the motor performance. So far, different modeling techniques have been used to calculate the cogging torque and the magnetic field distribution due to shaping and magnetization of permanent magnets, such as FEM and subdomain model [5]. The subdomain model acts based on the solving of governing equations in all subdomains, including air gap, PMs, slots, and slot openings [13-14].

In this paper, the CM method is used to calculate the air gap magnetic field, back-EMF, and cogging torque. The CM method acts based on the complex analysis. Carter used the CMs to calculate the suitable coefficients (Carter's coefficients) for considering the slotting effect. Zhu introduced a relative permeance function to consider the slotting effect in air gap magnetic field distribution [15]. However, this relative permeance function cannot consider the tangential component of air gap flux density. To remove this defect, zarko introduced the complex permeance model which can consider the radial and the tangential components of air gap flux density, simultaneously [16]. The complex permeance model assumes that the slot opening is infinitely deep, and it also cannot consider the interaction effect between adjacent slots. To resolve these problems, the SC Toolbox was used in [17-18]. In [17-18], the SC mapping was solved numerically by using the SC Toolbox. In real, the CM method presented in [17-18] is a semi-analytical method. In this paper, this semi-analytical method is used for investigating the influence of PM magnetization, PM shaping, and the slot opening shift on the performance of two typical PMSMs with integral and fractional slot

Submitted On: August 6, 2016
Accepted On: August 12, 2017

1054-4887 © ACES

winding.

This paper is organized as follows: Section II introduces the CM method. The calculation of air gap magnetic field, and back-EMF are presented in Sections III-IV, respectively. Section V shows the cogging torque calculation and reduction for different configurations of PMs, and by using the slot opening shift method. Section VI gives conclusions.

II. CM METHOD

The CM method is an analytical and numerical tool for analysis of different 2-D fields, such as electrostatic, magnetostatic, and so on. The main parameters of two typical PMSM analyzed in this paper are presented in Table 1. In this paper, three CMs, including two logarithmic complex functions and the SC mapping, are used to reach the canonical domain.

Table 1: Main parameters of analyzed PMSMs

Parameter	Value and Unit
Number of pole pairs, p	2
Number of slots, Q_s	12 / 6
Winding type	Single layer / Double layer
Magnet remanence, B_r	0.96 T
Relative recoil permeability, μ_r	1.07
Rated frequency, f	50 Hz
Motor topology	Internal rotor
Magnetization	Radial
Stator outer diameter	130 mm
Stator inner diameter	75 mm
Active length, L	65 mm
Air gap length, g	1 mm
Magnet thickness	3.5 mm
Pole arc to pole pitch ratio, α_p	0.9 (radial and parallel magnetization) 1 (segmented Halbach magnetization, and sin-shaping)
Winding turns per coil, N_c	200
Rated voltage (V_{RMS})	170 (volts)

A. First logarithmic CM

The first CM is a logarithmic complex function as:

$$z = log(s). \quad (1)$$

The motor geometry in s-plane (physical domain) is transformed to z-plane using (1), as shown in Figs. 1 (a-b) for one typical PMSM with 6 slots and 4 poles.

B. Schwartz-Christoffel (SC) mapping

SC mapping is defined as follows:

$$z = f(w) = A\int \prod_{k=1}^{n-1}(w - w_k)^{-\frac{\alpha_k}{\pi}-1}\, dw + C, \quad (2)$$

where A and C are the integration constants, n is the number of polygon corners in z-plane, $w_k's$ are the points on the boundary in w-plane corresponding to the polygon corners, $\alpha_k's$ are the interior angles in polygon corners.

SC transformation $z = f(w)$ maps the canonical domain in w-plane to the interior or exterior of respective polygon in z-plane. The canonical domain in w-plane may be a rectangle, disk, bi-infinite strip, and upper or lower half-plane. In this paper, the canonical domain in w-plane is one rectangle.

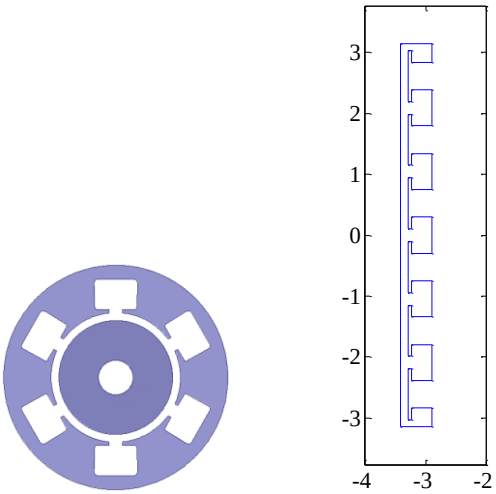

(a) s-plane (b) z-plane

Fig. 1. The motor geometry (6 slots/4 poles).

C. Second logarithmic CM

The third CM is also a logarithmic complex function, as follows:

$$w = j\left(log(\psi)\frac{\Delta x}{2\pi} + \frac{\Delta y}{2} - j\frac{\Delta x}{2}\right),$$
$$\Delta x = w(2) - w(1)\,,\ \Delta y = w(3) - w(2). \quad (3)$$

The canonical rectangle in w-plane is mapped to an annulus in ψ-plane by using (3). Figure 2 shows the main canonical domain in ψ-plane.

The selection of annulus as the main canonical domain has two main advantages. First, the boundary condition is applied automatically in ψ-plane. Second, the hague solution is known for an annular domain.

D. Hague's solution

Figure 2 shows an annulus including a line current located at $\psi = ce^{j\theta_1}$. The radii of stator and rotor in the main canonical domain (annular domain) are "a" and "b", respectively. The magnetic permeability of the stator core, air gap, and the rotor core are also μ_1, μ_2, and μ_3, respectively. Hague presents a solution for scalar magnetic potential in this annular domain as a function of r and θ, as [19]:

$$\Omega_\psi = \begin{cases} \frac{\mathrm{I}}{2} + \sum_{n=1}^{\infty}\left(\left(A_n - \frac{I}{2n\pi c^n}\right)r^n + B_n r^{-n}\right)\sin\left(n(\Delta\theta)\right), r < c \\ \frac{I(\Delta\theta+\pi)}{4\pi} + \sum_{n=1}^{\infty}\left(A_n r^n + B_n r^{-n}\right)\sin\left(n(\Delta\theta)\right), r = c \\ \frac{I\Delta\theta}{2\pi} + \sum_{n=1}^{\infty}\left(A_n r^n + \left(\frac{Ic^n}{2n\pi} + B_n\right)r^{-n}\right)\sin\left(n(\Delta\theta)\right), r > c \end{cases} \quad (4)$$

where

$$\begin{cases} A_n = \frac{-I(\mu_1-\mu_2)\{b^{2n}(\mu_3-\mu_2)+c^{2n}(\mu_3+\mu_2)\}}{c^n 2n\pi\left(b^{2n}(\mu_1-\mu_2)(\mu_2-\mu_3)+a^{2n}(\mu_1+\mu_2)(\mu_2+\mu_3)\right)}, \\ B_n = \frac{b^{2n}I(\mu_3-\mu_2)\{c^{2n}(\mu_1-\mu_2)+a^{2n}(\mu_1+\mu_2)\}}{c^n 2n\pi\left(b^{2n}(\mu_1-\mu_2)(\mu_2-\mu_3)+a^{2n}(\mu_1+\mu_2)(\mu_2+\mu_3)\right)}. \\ \Delta\theta = \theta - \theta_I \end{cases}$$

The air gap flux density in the main canonical domain is then calculated as:

$$B_\psi = -\mu_0 \nabla\Omega_\psi = -\mu_0\left[\frac{\partial\Omega_\psi}{\partial r}\overrightarrow{a_r} + \frac{1}{r}\frac{\partial\Omega_\psi}{\partial\theta}\overrightarrow{a_\theta}\right]. \quad (5)$$

The air gap flux density is similarly calculated for all line currents due to the armature winding and PMs.

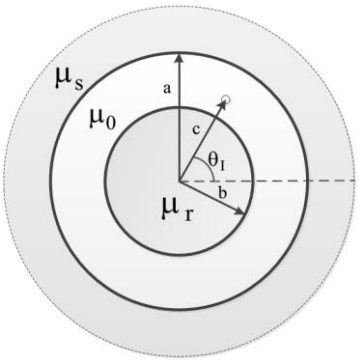

Fig. 2. The main canonical domain in ψ-plane.

E. Air gap complex permeance

The air gap flux density in the physical domain (s-plane) is calculated as [17]:

$$B_s = B_\psi\left(\frac{\partial\psi}{\partial s}\right)^* = \frac{B_\psi}{\left(\frac{\partial s}{\partial\psi}\right)^*} = B_\psi\left(\frac{1}{\frac{\partial w}{\partial\psi}}\right)^*\left(\frac{1}{\frac{\partial z}{\partial w}}\right)^*\left(\frac{\partial z}{\partial s}\right)^*, \quad (6)$$

$$B_s = B_r + jB_t$$

where

$$\frac{\partial w}{\partial\psi} = j\frac{\Delta x}{2\pi\psi}, \quad (7)$$

$$\frac{\partial z}{\partial w} = evaldiff(f, w), \quad (8)$$

$$\frac{\partial z}{\partial s} = \frac{1}{s}. \quad (9)$$

The complex permeance for the slotted air gap is defined as:

$$\lambda = \left(\frac{1}{\frac{\partial w}{\partial\psi}}\right)\left(\frac{1}{\frac{\partial z}{\partial w}}\right)\left(\frac{\partial z}{\partial s}\right), \quad (10)$$

$$\lambda = \lambda_r + j\lambda_t, \quad (11)$$

where λ_r and λ_t are respectively the radial and tangential components of slotted air gap complex permeance, and evaldiff (f, w) calculates the derivative of function "f" with respect to "w".

Figure 3 shows the radial and tangential components of air gap complex permeance for one typical PMSM with 6 slots and 4 poles. This figure shows the slotting effect with the period of one slot pitch.

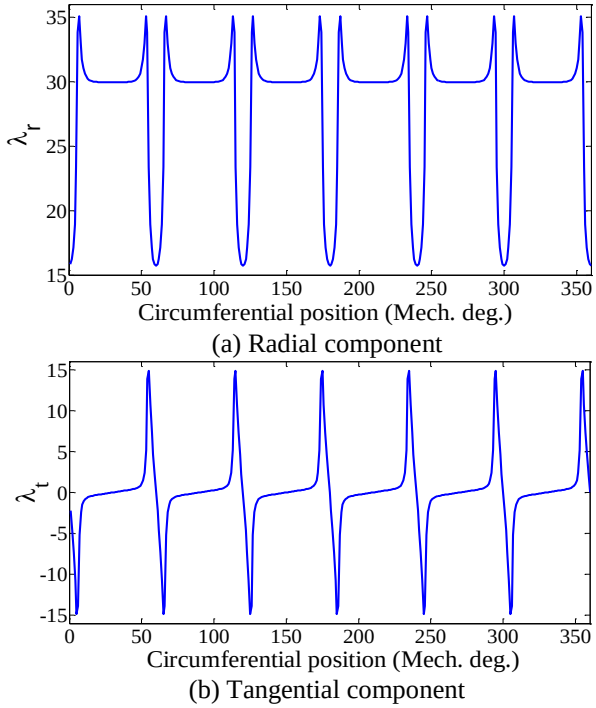

(a) Radial component

(b) Tangential component

Fig. 3. The components of air gap complex permeance.

F. Excitation modeling

All excitation, including PM and armature winding, are modeled by using equivalent line currents. For modeling the armature reaction, each coil side is easily replaced by using at least one equivalent line current. However, the PM equivalent line currents have to be calculated while considering the magnetization type.

The magnetization characteristic for each PM is usually written as:

$$\vec{M} = \frac{B_R}{\mu_0} + \left(\mu_r - 1\right)\vec{H} = M_r\overrightarrow{a_r} + M_t\overrightarrow{a_t}, \quad (12)$$

where B_R is the magnet remanence, μ_0 is the magnetic permeability of air, μ_r is the relative permeability of PM, and H is the magnetic field intensity inside PM due to the armature reaction.

The PM equivalent line currents are divided into two groups: the equivalent surface and volume currents. The densities of these PM equivalent currents are defined as:

$$J_s = \vec{M} \times \overrightarrow{a_n}\ \left(A/m\right), \quad (13)$$

$$J_v = \vec{\nabla} \times \vec{M}\left(A/m^2\right), \quad (14)$$

where $\overrightarrow{a_n}$ is the unit vector perpendicular to the PM surface.

Since the relative permeability of PMs is very close to one, therefore the PM magnetization distribution can assumed to be a uniform distribution. Consequently, the equivalent volume currents can be ignored in PM modeling.

For one PM with radial magnetization and radial sides, the equivalent surface currents exist only on lateral sides (Fig. 4). The magnitude of these equivalent surface currents are calculated as:

$$I_s = \frac{B_R}{\mu_0} \times \frac{l_m}{n_1}, \tag{15}$$

$$M = \frac{B_R}{\mu_0}, \tag{16}$$

where l_m is the magnet thickness, and n_1 is the number of equivalent currents on each lateral side of PMs.

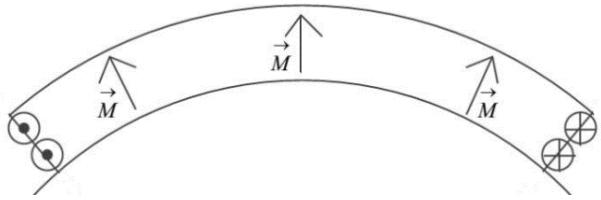

Fig. 4. The PM equivalent currents for radial magnetization.

For one PM with parallel magnetization, the equivalent surface currents also exist on the inner and outer arcs (Fig. 5). These equivalent surface currents are defined as:

$$J_s = \begin{cases} M \times \cos\left(\frac{\alpha_p \pi}{2p}\right) & \theta = \frac{\alpha_p \pi}{2p} \\ -M \times \cos\left(\frac{\alpha_p \pi}{2p}\right) & \theta = -\frac{\alpha_p \pi}{2p} \\ M \times \sin\theta & -\frac{\alpha_p \pi}{2p} \le \theta \le \frac{\alpha_p \pi}{2p}\ ,\ r = R_m \\ -M \times \sin\theta & -\frac{\alpha_p \pi}{2p} \le \theta \le \frac{\alpha_p \pi}{2p}\ ,\ r = R_r \end{cases} \tag{17}$$

$$I_s = J_s \times r \times d\theta,$$

where α_p is the pole arc coefficient, p is the number of pole pair, R_r is the inner radius of PM, R_m is the outer radius of PM, θ is the angular position of each surface element relative to the symmetrical axis of PM, and $d\theta$ is the arc length of each surface element in radian.

For one PM with segmented Halbach magnetization (Fig. 6), the equivalent surface currents exist on all sides of all PM segments. The radial and tangential components of magnetization vector $(\vec{M})$ for each PM segment are calculated as:

$$\begin{aligned} M_r &= M \times \sin\left(\alpha_i + (\theta - \theta_i)\right), \\ M_\theta &= M \times \cos\left(\alpha_i + (\theta - \theta_i)\right), \end{aligned} \tag{18}$$

where θ is the circumferential position on the surface of PM.

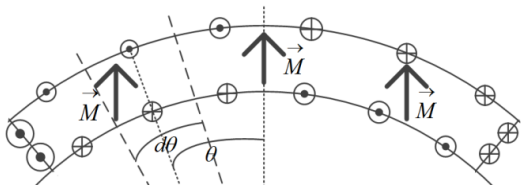

Fig. 5. The PM equivalent currents for parallel magnetization.

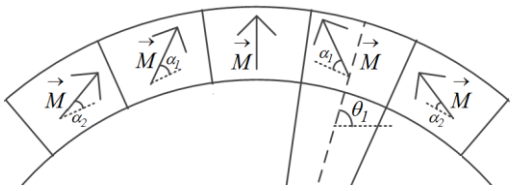

Fig. 6. PM with segmented Halbach magnetization.

For each PM segment with Halbach magnetization, the equivalent surface currents can be calculated while having the radial and tangential components of magnetization vector.

III. MAGNETIC FIELD CALCULATION

The radial and tangential components of air gap magnetic field are calculated by using (6). For radial and parallel magnetization, Fig. 7 shows the components of air gap magnetic field due to PMs (for PMSM with 12 slot/4 pole). As shown, the air gap field obtained through the parallel magnetized PMs is more sinusoidal than it obtained from the radial magnetized PM. However, it is still far from a suitable sinusoidal air gap field.

For creating a more sinusoidal air gap field, the Hat-type configuration and the sin-shaping are considered for PM poles with full pitch. As shown in Fig. 8, the segmented-Halbach magnetization is selected for each PM pole in Hat-type configuration. Figure 9 also shows one typical PM pole with sin-shaping and parallel magnetization. In Fig. 9, ξ shows the eccentricity value of outer arc of PM pole relative to the rotor center, R_m is radius of outer arc, h_{min} and h_{max} are respectively the minimum and maximum thickness of PM poles. To reduce the harmonic content of air gap magnetic field, the optimal configurations of Hat-type and sin-shaped magnet poles are obtained as shown in Tables 2-3.

Table 2: Optimal parameters of Hat-type poles

Optimal Widths	Optimal Orientations	Optimal Thickness
$w_1 = 40^\circ$	$\alpha_1 = 90^\circ$	$l_1 = 3.5\ (mm)$
$w_2 = 15^\circ$	$\alpha_2 = 75^\circ$	$l_2 = 2.6\ (mm)$
$w_3 = 10^\circ$	$\alpha_3 = 37.5^\circ$	$l_3 = 1.56\ (mm)$

Table 3: Optimal parameter of sin-shaped poles

ξ	R_m	h_{min}	h_{max}
8.2 (mm)	28.3 (mm)	0.5 (mm)	3.5 (mm)

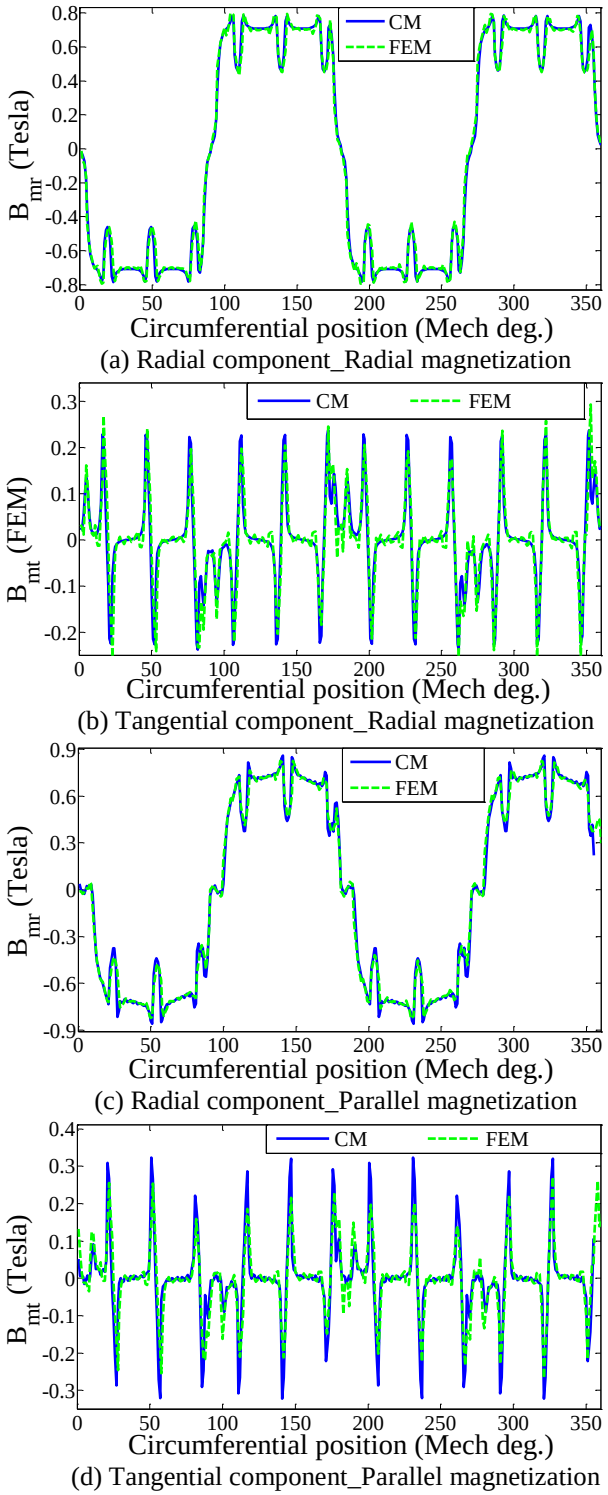

Fig. 7. The components of air gap magnetic field.

For these optimal configurations, Fig. 10 shows the radial components of air gap magnetic field due to PMs (for PMSM with 12 slot/4 pole).

Table 4 compares the total harmonic distortion (THD) of B_{mr} obtained through the analyzed PMSM (12 slot/ 4 pole) while considering the radial magnetization, parallel magnetization, optimal Hat-type configuration, and optimal sin-shaped pole. As shown, the air gap magnetic field obtained through sin-shaped configuration is more sinusoidal than others.

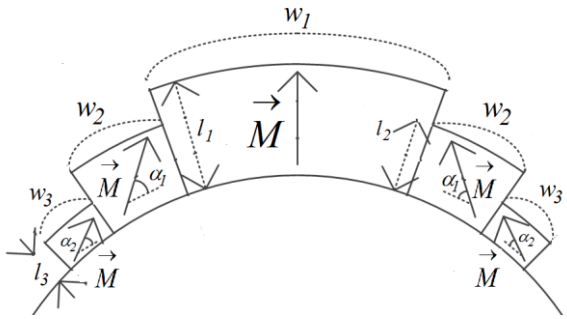

Fig. 8. Hat-type configuration with segmented Halbach magnetization.

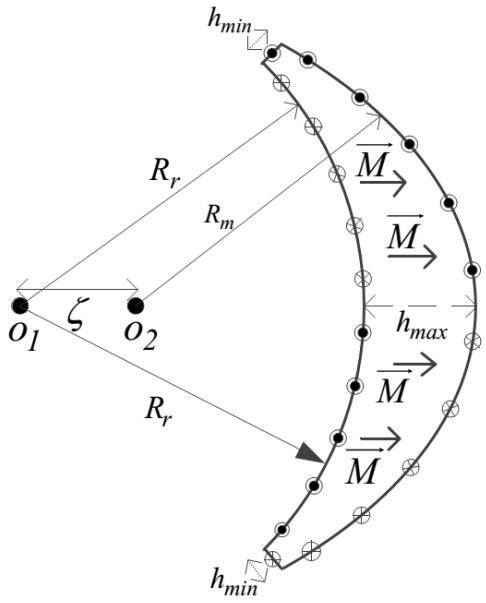

Fig. 9. Sin-shaped PM pole with parallel magnetization.

Table 4: THD comparison of B_{mr}

	Radial Magnetization	Parallel Magnetization	Optimal Hat-type	Optimal Sin-shape
THD	40.5%	27.37%	15.6%	10.8%

IV. BACK-EMF CALCULATION

The PM flux-linkage and back-EMF can be calculated

for each phase while having the distribution of air gap magnetic field and phase windings

$$\lambda_m = R_g.L\int_0^{2\pi} n_A(\varphi).B_{mr}(\varphi)\,d\varphi, \quad (19)$$

$$E_m = \frac{d\lambda_m}{dt}, \quad (20)$$

where R_g is the radius of integration contour in the middle of air gap, L is the axial length of the core, n_A is the turn function of phase A, B_{mr} is the radial component of air gap field, λ_m is the PM flux-linkage of phase A, and E_m is the PM back-emf of phase A.

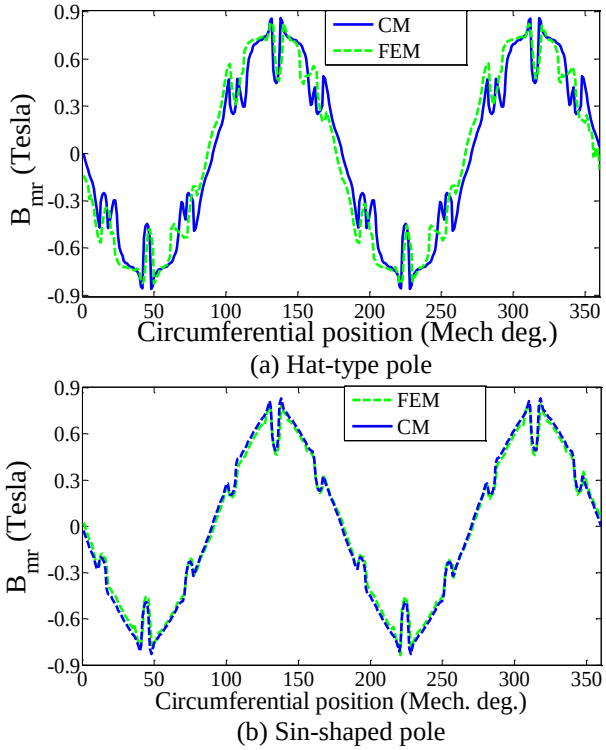

Fig. 10. Radial components of air gap field obtained through optimal Hat-type and sin-shaped configurations.

Figure 11 shows the PM back-EMF for an analyzed PMSM with 12 slots and 4 poles while considering different magnetizations and shaping for PMs. As shown, the back-EMF waveform is more sinusoidal for sin-shaped PM poles than others.

Figure 12 shows the optimal PM back-EMF obtained through two analyzed PMSMs (12s/4p, and 6s/4p). Table 5 compares these optimal results in terms of THD. As shown, the optimal PM back-EMF obtained through PMSM 6s/4p is more sinusoidal than the other.

Table 5: THD comparison of optimal back-EMFs

	12 slot / 4 pole	6 slot / 4 pole
THD	5.2%	1.8%

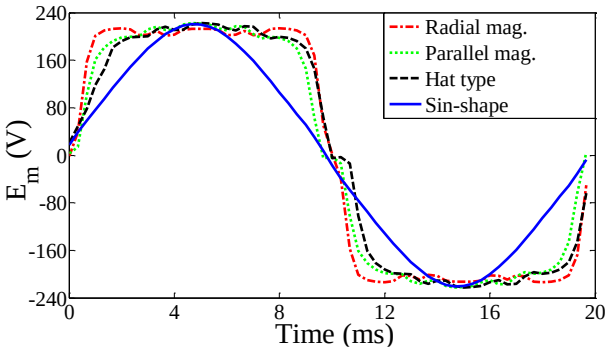

Fig. 11. Back-EMF comparison.

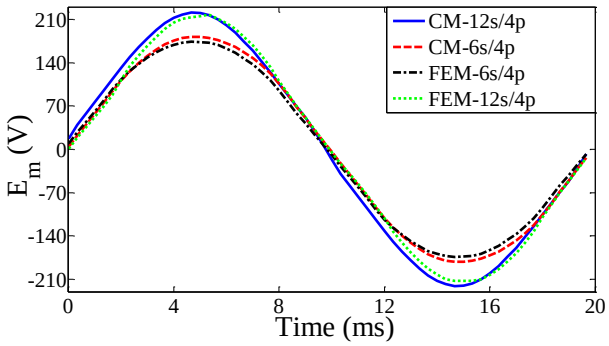

Fig. 12. Optimal PM back-EMFs.

V. COGGING TORQUE

A. Cogging torque calculation

One of the main drawbacks of PM machines, particularly in integral slot PM motor, is the cogging torque. Cogging torque is the main cause of torque pulsation and results in the shaft vibration and acoustic noise. In real, cogging torque is due to the interaction effect between the rotor PMs and the stator teeth. In this paper, Maxwell Stress Tensor (MST) method is used to calculate the cogging torque as follows:

$$T_c = \frac{L.R_g^2}{\mu_0}\int_0^{2\pi} B_{mr}.B_{mt}\,d\theta, \quad (21)$$

where B_{mt} is the tangential component of air gap field due to PMs.

Figure 13 shows the cogging torque waveforms for different configurations of analyzed PMSMs. For clarity in comparison, the cogging torque waveforms are shown in Fig. 13 (a) except for sin-shaped configuration. The comparison between Figs. 13 (a & b) shows the extreme influence of sin-shaped PM poles on the cogging torque reduction. In real, by using the sin-shaped PM poles, the peak to peak value of cogging torque waveforms for PMSMs 12s/4p and 6s/4p are respectively reduced about 95% and 97% in comparison to the configuration with radial magnetized PMs. Figure 13 (b) also shows that the PMSM 6s/4p is more effective than the PMSM 12s/4p

for cogging torque reduction, so that the ratio of peak to peak value of T_c $(T_{c,p-p})$ for analyzed PMSMs is as follows:

$$\frac{T_{c,p-p,6s/4p}}{T_{c,p-p,12s/4p}} \cong 0.36.$$

B. Slot opening shift method

The design technique for cogging torque reduction can be divided into two general groups, as follows:

- ✓ Rotor design techniques;
- ✓ Stator design techniques.

The magnet shaping technique is in the first category. In this paper, the technique of slot opening shift is also implemented on the stator simultaneous with using of sin-shaped PMs on the rotor. The technique of slot opening shift is in the second category, and it has no side effect on the motor performance such as the air gap field, back-EMF, and average torque.

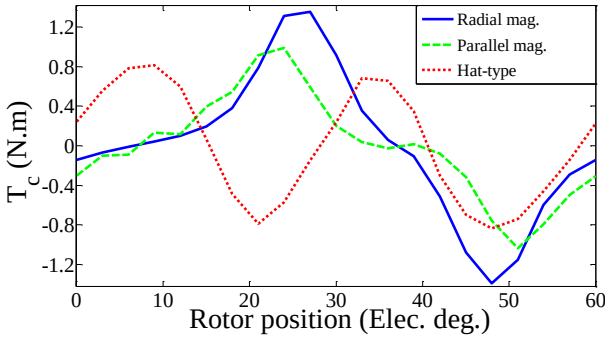

(a) PMSM 12s/4p

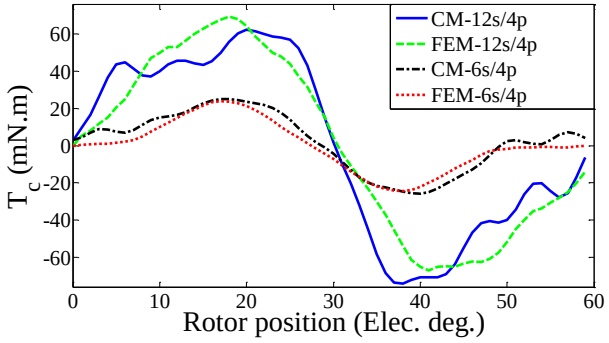

(b) Sin-shaping of PMs

Fig. 13. Cogging torque comparison.

In the slot opening shift method, the γ adjacent slots take as a group. It is obvious that γ should be equal to the number of cogging torque periods per pole, as follows:

$$\gamma = \frac{N_c}{2p}, \tag{22}$$

where N_c equals to the least common multiple of the number of stator slots N_s and the rotor poles $2p$. γ equals to 3 slots for both analyzed PMSMs. Therefore, all stator slots are divided into 4 groups for PMSM 12s/4p and 2 groups for PMSM 6s/4p. The optimization variables (angular shift of the slot opening position for each slot group) are defined.

For PMSM 12s/4p:

$$\begin{cases} -5^\circ \le \theta_1 \le 0^\circ \\ 0^\circ \le \theta_2 \le 5^\circ \end{cases} \rightarrow \begin{cases} \theta_{1,optimal} = -4.25^\circ \\ \theta_{2,optimal} = 5^\circ \end{cases}.$$

For PMSM 6s/4p:

$$\begin{cases} -11^\circ \le \theta_1 \le 0^\circ \\ 0^\circ \le \theta_2 \le 11^\circ \end{cases} \rightarrow \begin{cases} \theta_{1,optimal} = -4^\circ \\ \theta_{2,optimal} = 10.5^\circ \end{cases}.$$

These optimal results are obtained by using the genetic algorithm. Figure 14 shows the final optimal model for PMSMs 12s/4p and 6s/4p while considering the shifted slot openings on the stator and the sin-shaped PMs on the rotor, simultaneously.

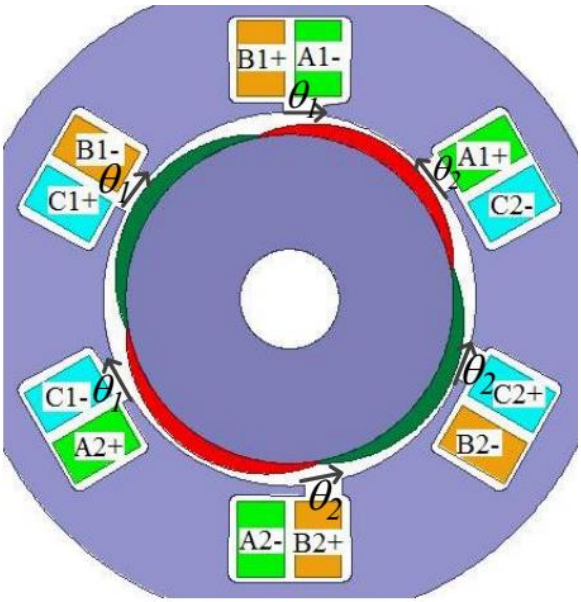

(a) PMSM 6s/4p

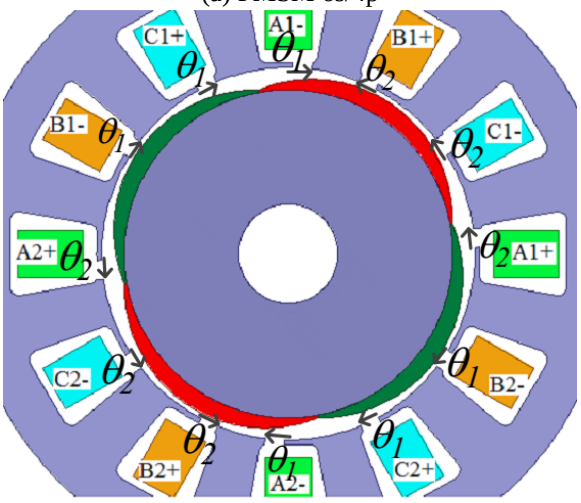

(b) PMSM 12s/4p

Fig. 14. Final optimal models.

Figures 15-16 show the waveforms of cogging torque and PM back-EMF obtained through optimal PMSMs. As seen from Fig. 15, the peak to peak value of cogging torque is extremely reduced (about 98.8%) in comparison to the PMSMs with radial magnetized PMs.

Figure 16 also shows that the technique of slot opening shift has no side effect on the sinusoidal back-EMF obtained through PMSMs with sin-shaped PMs.

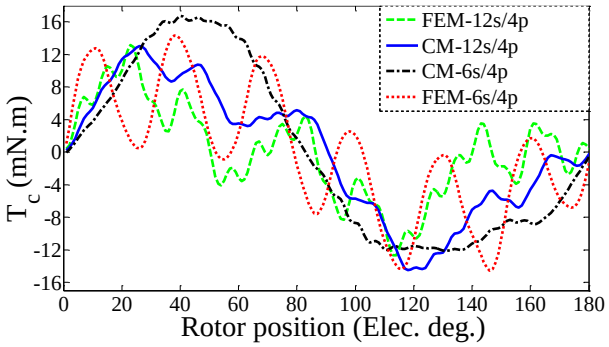

Fig. 15. Optimal waveforms of cogging torque.

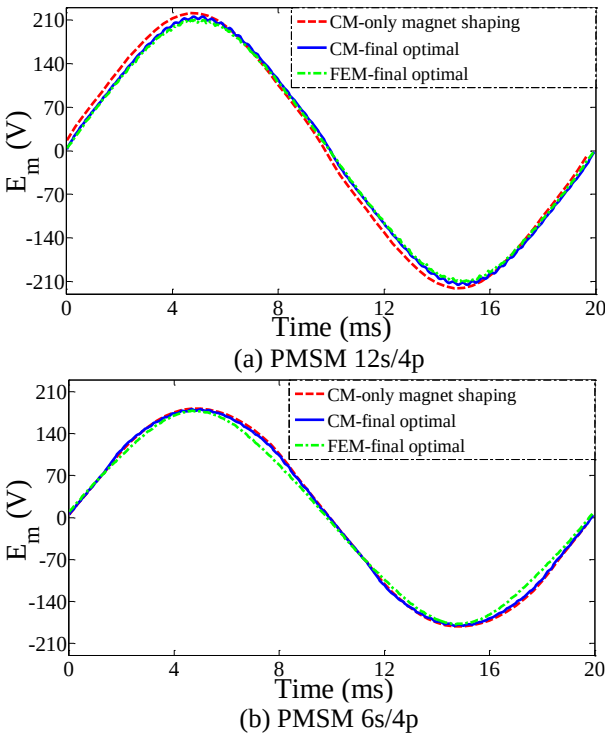

Fig. 16. Optimal waveforms of PM back-EMF.

VI. CONCLUSION

In this paper, by using the CM method as an accurate and fast method, a new optimal design was presented for PMSMs (either integral or fractional slot), which can include different design considerations. This new optimal configuration included the sin-shaped magnet poles on the rotor with shifted slot openings on the stator. The air gap magnetic field is sinusoidal by using this technique of magnet shaping. This hybrid technique simultaneously leads to an ideal PM back-EMF and the extreme reduction in the cogging torque without any destructive effect on the motor performance. This important feature distinguishes this new optimal design from other techniques which have been presented so far. Without using the technique of slot opening shift, the results show that the fractional slot PMSMs are more optimal than the integral slot PMSMs. However, by using the shifted slot opening on the stator in simultaneous with the magnet shaping technique, the obtained results are fairly similar for both fractional and integral slot PMSMs. The using of slot opening shift method has no side effect on the motor performance.

REFERENCES

[1] J. Wang and D. Howe, "Tubular modular permanent-magnet machines equipped with quasi-Halbach magnetized magnets--Part I: Magnetic field distribution, EMF, and thrust force," *IEEE Trans. Magn.*, vol. 39, no. 3, pp. 1793-1799, 2003.

[2] P. Zheng, J. Zhao, J. Han, J. Wang, Z. Yao, and R. Liu, "Optimization of the magnetic pole shape of a permanent-magnet synchronous motor," *IEEE Trans. Magn.*, vol. 43, no. 6, pp. 2531-2533, 2007.

[3] K. Wang, Z. Q. Zhu, and G. Ombach, "Torque improvement of five-phase surface-mounted permanent magnet machine using third-order harmonic," *IEEE Trans. Energy Convers.*, vol. 29, no. 3, pp. 735-747, 2014.

[4] Y. Li, J. Xing, T. Wang, and Y. Lu, "Programmable design of magnet shape for permanent-magnet synchronous motors with sinusoidal back EMF waveforms," *IEEE Trans. Magn.*, vol. 44, no. 9, pp. 2163-2167, 2009.

[5] Y. Shen and Z. Q. Zhu, "Investigation of permanent magnet brushless machines having unequal-magnet height pole," *IEEE Trans. Magn.*, vol. 48, no. 12, pp. 4815-4830, 2012.

[6] S. M. Jang, H. Park, J. Y. Choi, K. J. Ko, and S. H. Lee, "Magnet pole shape design of permanent magnet machine for minimization of torque ripple based on electromagnetic field theory," *IEEE Trans. Magn.*, vol. 47, no. 10, pp. 3586-3589, 2011.

[7] W. Fei and Z. Q. Zhu, "Comparison of cogging torque reduction in permanent magnet brushless machines by conventional and herringbone skewing techniques," *IEEE Trans. Energy Convers.*, vol. 28, no. 3, pp. 664-674, 2013.

[8] C. Xia, Z. Zhang, and Q. Geng, "Analytical modeling and analysis of surface mounted permanent magnet machines with skewed slots," *IEEE Trans. Magn.*, vol. 51, no. 5, Article#: 8104508, 2015.

[9] K. Abbaszadeh, F. Rezaee Alam, and S. A. Saied, "Cogging torque optimization in surface-mounted permanent-magnet motors by using design of experiment," *Energy Convers. Manage*., vol. 52, no. 10, pp. 3075-3082, 2011.

[10] Z. Q. Zhu and D. Howe, "Influence of design parameters on cogging torque in permanent magnet motors," *IEEE Trans. Energy Convers.*, vol. 15, no. 4, pp. 407-412, 2000.

[11] M. Gulec and M. Aydin, "Magnet asymmetry in reduction of cogging torque for integer slot axial flux permanent magnet motors." *IET Electr. Power Appl*., vol. 8, no. 5, pp. 189-198, 2014.

[12] C. Liu, J. Zhu, Y. Wang, G. Lei, and Y. Guo, "Cogging torque minimization of SMC PM transverse flux machines using shifted and unequal-width stator teeth," *IEEE Trans. Appl. Supercond.*, vol. 26, no. 4, Article#: 5204704, 2016.

[13] Z. Q. Zhu, L. J. Wu, and Z. P. Xia, "An accurate subdomain model for magnetic field computation in slotted surface-mounted permanent-magnet machines," *IEEE Trans. Magn.*, vol. 46, no. 4, pp. 1100-1115, 2010.

[14] Z. J. Liu and J. T. Li, "Accurate prediction of magnetic field and magnetic forces in permanent magnet motors using an analytical solution." *IEEE Trans. Energy Conversion*, vol. 23, no. 3, pp. 717-726, Sep. 2008.

[15] Z. Q. Zhu and D. Howe, "Instantaneous magnetic field distribution in brushless permanent magnet dc motors. Part III: Effect of stator slotting," *IEEE Trans. Magn.*, vol. 29, no. 1, pp. 143-151, 1993.

[16] D. Zarko, D. Ban, and T. A. Lipo, "Analytical calculation of magnetic field distribution in the slotted air gap of a surface permanent-magnet motor using complex relative air-gap permeance," *IEEE Trans. Magn.*, vol. 42, no. 7, pp. 1828-1837, 2006.

[17] T. C. O'Connell and P. T. Krein, "A Schwarz-Christoffel-based analytical method for electric machine field analysis," *IEEE Trans. Energy Convers*., vol. 24, no. 3, pp. 565-577, 2009.

[18] F. Rezaee Alam and K. Abbaszadeh, "Magnetic field analysis in eccentric surface-mounted permanent-magnet motors using an improved conformal mapping method," *IEEE Trans. Energy Convers*., vol. 31, no. 1, pp. 333-344, Nov. 2015.

[19] B. Hague, *Electromagnetic Problems in Electrical Engineering*. London, U.K.: Oxford Univ. Press, 1929.

Wideband Filtering Crossover Based on Ring Resonator with Sharp Rejection

Wanchen Yang [1,2], Wenjie Feng [1,2*], and Wenquan Che [1]

[1] Department of Communication Engineering, Nanjing University of Science & Technology, Nanjing, China

[2] State Key Laboratory of Millimeter Waves, Southeast University, Nanjing, China
fengwenjie1985@163.com

Abstract — A wideband filtering crossover based on ring resonators with sharp rejection is proposed in this paper. Four transmission zeros near the crossover passband can be adjusted conveniently by the even/odd-mode characteristic impedance of the coupled lines. A high selectivity wideband filtering crossover located at 3.0 GHz is designed and fabricated for verification. Good filtering performance and high selectivity for the crossover are realized and experimentally verified.

Index Terms — Coupled lines, even/odd-mode, filtering crossover, transmission zero, wideband.

I. INTRODUCTION

Crossover is a very important component and can be integrated in Butler matrix, which exhibits two signal paths crossing over each other with perfect isolation and all ports matched. Air-bridge and bond-wire are always used to transport signals in different layers for conventional crossovers [1]-[2], resulting in complex structures and relatively high fabrication cost. Cascaded rings and branch-lines couplers are used to overcome these drawbacks [3]-[5]; however, multi-section rings and couplers enlarge the circuit size and the transmission insertion loss. The conductor-backed coupling lines can be used to realize wideband crossovers [6], which can avoid using cascaded structures. Moreover, microwave passive components including crossovers, filters, and couplers are always single elements, integrating two functions in one component is an effective method for size reduction, such as filtering balanced circuits [7] and filtering crossovers [8].

In this paper, a wideband filtering crossover with sharp rejection is proposed. Four transmission zeros for the crossover passband with good isolation performance over a very wide frequency range can be realized [9]-[10]. Using coupled lines and open stubs with different electrical wavelength, fifth-order passband can be easily achieved for the planar crossover. The desired crossover configuration can be obtained using even/odd-mode characteristic impedance of the coupled lines and characteristic impedance of the open stubs. A wideband filtering crossover located at 3.0 GHz with 3-dB bandwidth 26.3% (2.58-3.37 GHz) is designed and fabricated for verification. All the circuits and structures are simulated with Ansoft Designer v3.0 and Ansoft HFSS v13.0, and constructed on the dielectric substrate with ε_r = 2.65, h = 1.0 mm, and $tan\delta$ = 0.003.

II. DESIGN OF PROPOSED WIDEBAND CROSSOVER

Figure 1 shows an improved crossover based on dual-mode ring resonator [6], four quarter-wavelength side-coupled lines (electrical length θ, even/odd-mode characteristic impedance Z_{e1}, Z_{o1}) are attached to the four input/output ports. Four microstrip lines with characteristic impedance $Z_0 = 50\ \Omega$ are connected to Ports 1 to 4. Due to the symmetry of the single-band crossover, the even-odd-mode analysis is employed to simplify the analysis and to derive the impedance values [1]-[6], which are required to meet the following properties:

$$|S_{11}| = |S_{22}| = |S_{33}| = |S_{44}| = 0,$$
$$|S_{21}| = |S_{23}| = |S_{41}| = 0\ ,\ |S_{31}| = |S_{24}| = 1. \qquad (1)$$

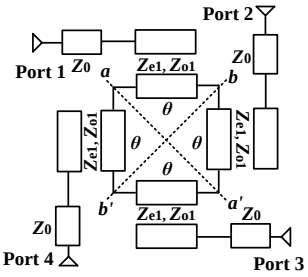

Fig. 1. Ideal circuit of the improved crossover based on ring resonator [6].

By placing electric wall (*E*-wall) and *E*-wall, magnetic wall (*H*-wall) and *H*-wall, *E*-wall and *H*-wall, *H*-wall, and *E*-wall along the symmetry lines *a*-*a*′ and *b*-*b*′, respectively, as shown in Figs. 2 (a)-(d); four even/odd eigen-admittances Y_{ee}, Y_{eo}, Y_{oe}, Y_{oo} can be required [6]:

Submitted On: February 18, 2017
Accepted On: August 13, 2017

1054-4887 © ACES

$$Y_{ee} = j\frac{2\tan\theta}{Z_{e1}+Z_{o1}},\ Y_{eo} = -j\frac{2(Z_{e1}+Z_{o1})\tan\theta}{(Z_{e1}-Z_{o1})^2\tan^2\theta - 4Z_{e1}Z_{o1}}, \quad (2)$$

$$Y_{oe} = j\frac{2(Z_{e1}+Z_{o1})\tan\theta}{Z_{e1}Z_{o1}},\ Y_{oo} = j\frac{2(Z_{e1}+Z_{o1})\tan\theta}{Z_{e1}Z_{o1}}. \quad (3)$$

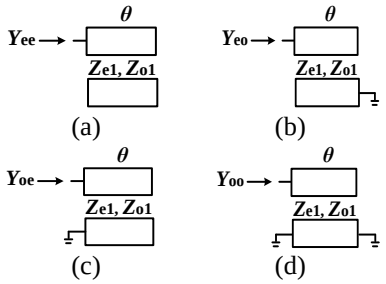

Fig. 2. Decomposed equivalent circuits of the crossover based on ring resonator: (a) even–even-mode circuit; (b) even–odd-mode circuit; (c) odd–even-mode circuit; (d) odd–odd-mode circuit.

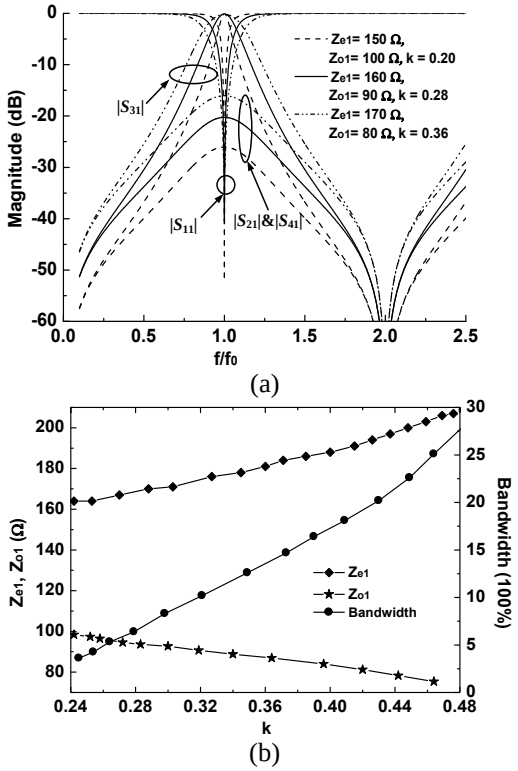

Fig. 3. (a) Simulated results of the crossover based on ring resonator, and (b) bandwidth versus coupling coefficient *k*.

After further calculation, we find that different combinations of design values that can be used to realize a broadband performance for the crossover. Figures 3 (a)-(b) show the simulated results of the crossover based on ring resonator versus Z_{e1}, Z_{o1}, and the bandwidth of the crossover increases with the coupling coefficient *k* increases (k = (Z_{e1}-Z_{o1})/(Z_{e1}+Z_{o1})), and the isolation between Ports 1 to 2, and 4 become worse as *k* increases. Due to the PCB fabrication precisions, the width for the transmission lines and coupled lines are always greater than 0.20 mm, so the maximum coupling coefficient *k* of the coupling lines in this work is nearly 0.45 (ε_r = 2.65, h = 1.0 mm), and the characteristic impedance of the transmission lines is always less than 130 Ω, so the bandwidth of the crossover cannot increase infinitely.

The ideal circuit of the proposed wideband filtering crossover is shown in Fig. 4, a two-stage coupling line is used to increase the bandwidth for Fig. 1, and four half-wavelength open stubs (electrical length 2θ, characteristic impedance Z_1) are attached in the input coupled lines, and four open/shorted coupled lines (Z_{e2}, Z_{o2}, θ) are shunted connected in the input/output Ports 1 to 4. As discussed in [7], [9], four transmission zeros realized by the half-wavelength open stubs and open/shorted coupled lines can be obtained as:

$$\theta_{tz1} = \pi/4, \qquad \theta_{tz2} = 3\pi/4, \quad (4)$$

$$\theta_{tz3} = \arccos\frac{Z_{e2}-Z_{o2}}{Z_{e2}+Z_{o2}}, \quad \theta_{tz4} = \pi - \theta_{tz3}. \quad (5)$$

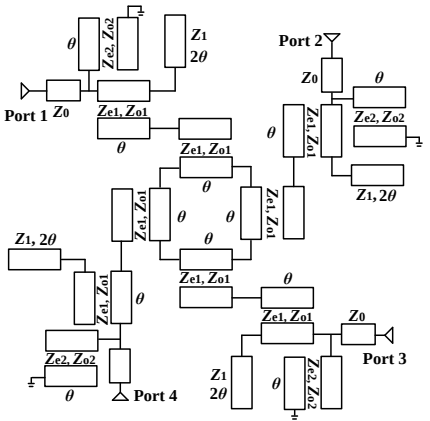

Fig. 4. Proposed wideband filtering crossover based on ring resonator.

The half-wavelength open stubs are all wide passband structures [11], they can be seen as an ideal open circuit in the center frequency of the crossover. In addition, we can find that two transmission zeros f_{tz3}, f_{tz4} don't change with Z_1, Z_{e1}, and Z_{o1}, so when the even/odd-mode characteristic impedance Z_{e1}, Z_{o1} are fixed, the bandwidth of the wideband crossover can be adjusted by the characteristic impedance of the open stubs Z_1, and the out-of-band performance of the crossover can be further improved by the two transmission zeros f_{tz3}, f_{tz4}. The simulated results of the wideband filtering crossover with/without four transmission zeros are shown in Figs.

5 (a)-(c). The passband order can be increased from third to fifth, and four transmission zeros can be used to realize a wide passband for the crossover with sharp rejection, the two transmission zeros f_{tz3}, f_{tz4} nearly do not change the bandwidth of the wideband filtering crossover, and the in-band performance can be also adjusted by the characteristic impedance Z_1 of the four half-wavelength open stubs.

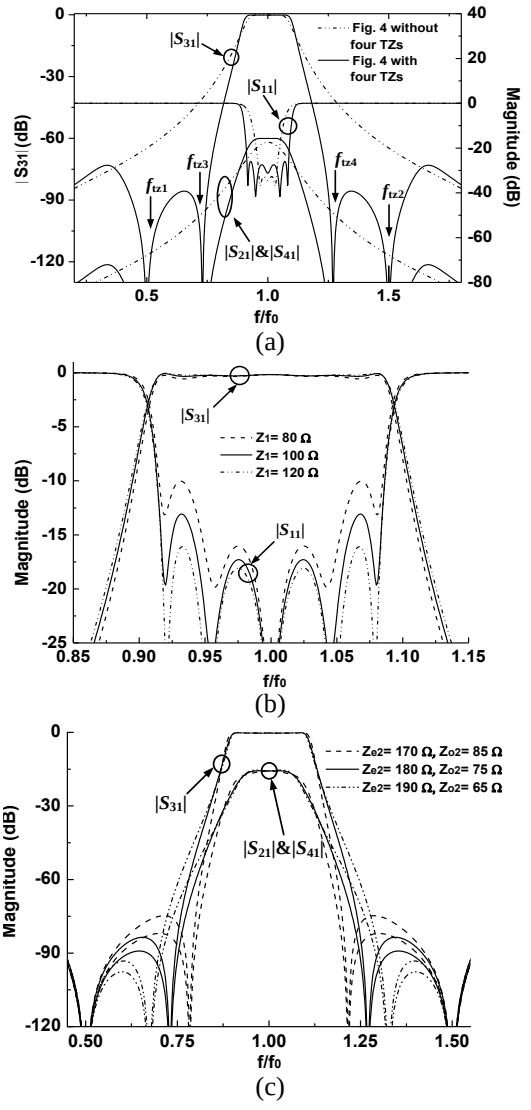

Fig. 5. Simulated results of the wideband filtering crossover. (a) With/without transmission zeros, (b) $|S_{31}|$, $|S_{11}|$ versus Z_1, and (c) $|S_{31}|$, $|S_{21}|$ versus Z_{e2}, Z_{o2}. ($Z_0 = 50\ \Omega$, $Z_1 = 120\ \Omega$, $Z_{e1} = 170\ \Omega$, $Z_{o1} = 108\ \Omega$, $Z_{e2} = 180\ \Omega$, $Z_{o2} = 75\ \Omega$).

Referring to the discussions and the simulated results, the 3-dB bandwidth of the filtering crossover is chosen as 26%, and the final parameters for Fig. 4 are $Z_0 = 50\ \Omega$, $Z_{e1} = 175\ \Omega$, $Z_{o1} = 112\ \Omega$, $Z_1 = 125\ \Omega$. The simulated results of Fig. 6 are illustrated in Fig. 7, and five transmission zeros are located at 1.5, 2.0, 2.2, 3.6 and 4.5 GHz, the passband $|S_{31}|$ is greater than -1.2 dB, the isolation $|S_{21}|$ and $|S_{41}|$ are less than -18 dB for 0~10.0 GHz.

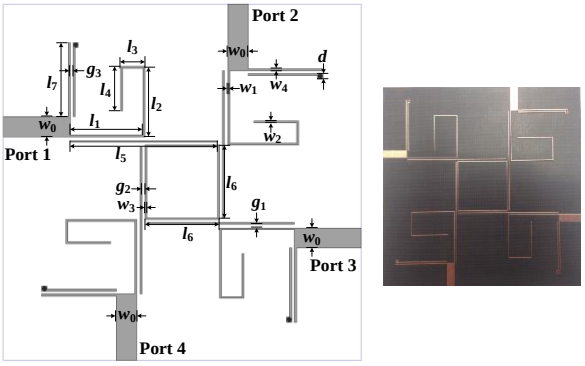

Fig. 6. Geometry of the wideband filtering crossover. (l_1 =18.0, l_2 = 15.5, l_3 = 8.45, l_4 = 13.0, l_5 = 36.3, l_6 = 18.25, l_7 = 18.25, w_0 = 2.7, w_1 = 0.24, w_2 = 0.27, w_3 = 0.23, w_4 = 0.3, $g_1 = g_2 = 0.45$, $g_2 = 0.35$, $d = 0.6$, all in *mm*).

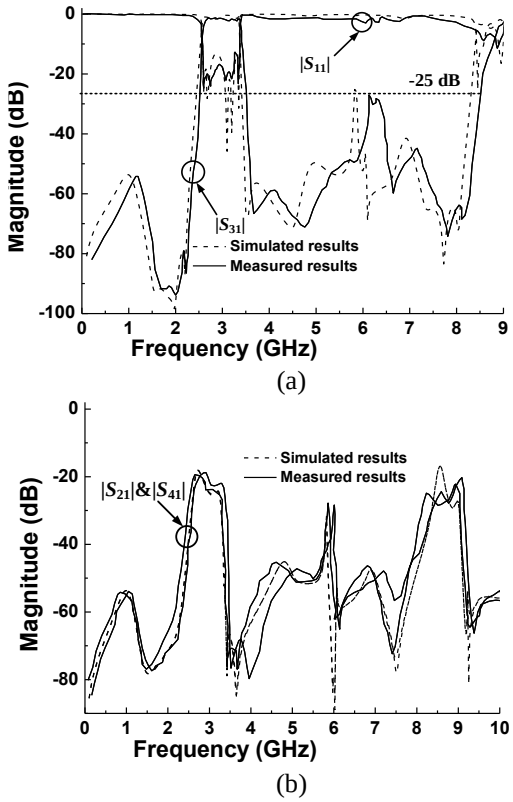

Fig. 7. Simulated and measured results of the crossover. (a) $|S_{31}|$, $|S_{11}|$, and (b) $|S_{21}|$, $|S_{41}|$.

III. EXPERIMENT AND RESULTS

The photograph, measured results of the wideband crossovers are also shown in Figs. 6-7. For the wideband

crossover, five measured transmission zeros are located at 1.6, 2.0, 2.3, 3.5 and 4.7 GHz, the 3-dB bandwidth is 26.3% (2.58-3.37), the in-band $|S_{31}|$ is greater than -2.3 dB, the isolation $|S_{21}|$ and $|S_{41}|$ are less than -18.5 dB for 0~10.0 GHz ($3.3f_0$).

For the purpose of comparison, Table 1 illustrates the measured results for some crossovers with proposed wideband filtering crossover. It can be seen that, the proposed filtering crossover has wideband isolation for $|S_{21}|$ and $|S_{41}|$, and the upper stopband for $|S_{31}|$ can be extended up to $2.8f_0$ ($|S_{31}|$< -25 dB), and further circuit size reduction can be also realized by using folded lines in multi-layer circuits.

Table 1: Comparisons of measured results for some crossovers

Crossover Structures	TZs, $\|S_{31}\|$ 0-2f_0,	Isolation $\|S_{21}\|/\|S_{41}\|$, dB	Stopband $\|S_{31}\|$, dB	Filtering Response
Ref. [3]	0 (1.0 GHz)	25%, <-20	<-10, 1.50f_0	No
Ref. [4]	0 (2.5 GHz)	14.0%, <-20	---	No
Ref. [6]	0 (2.5 GHz)	200%, <-12	---	No
Ref. [8]	4 (2.0 GHz)	100%, <-20	<-25, 2.50f_0	Yes
This work	5 (3.0 GHz)	330%, <-19	<-25, 2.80f0	Yes

IV. CONCLUSIONS

In this paper, a wideband filtering crossover with sharp rejection based on ring resonator is proposed, four transmission zeros can be easily realized by the adding open stubs and open/shorted coupled lines. The proposed wideband filtering crossover has advantages of high selectivity, wide stopband and wideband. Good agreements between simulated and measured responses of the structures are demonstrated.

ACKONWLEGEMENT

This work was supported by the Natural Science Foundation of China (61601224) and Jiangsu Province (BK20160844), and in part by the Fundamental Research Funds for the Central Universities of China under Grant 30916011318, and the Open Funding of State Key Laboratory of Millimeter Waves (K201721, K201804) and "Qing Lan Project" of Jiangsu Province (2017-2020).

REFERENCES

[1] T. Becks and I. Wolff, "Analysis of 3-D metallization structures by a full-wave spectral domain technique," *IEEE Trans. Microw. Theory Techn*., vol. 40, no. 12, pp. 2219-2227, Dec. 1992.

[2] W. Feng, T. Zhang, W. Che, and Q. Xue, "Compact single/dual-band planar crossovers based on coupled lines loaded with open stubs," *IEEE Trans. Compon. Packag. Manuf. Technol*., vol. 60, no. 6, pp. 854-862, June 2016.

[3] Y. C. Chiou, J. T. Kuo, and H. R. Lee, "Design of compact symmetric four-port crossover junction," *IEEE Microw. Wireless Compon. Lett*., vol. 19, no. 9, pp. 545-547, Sep. 2009.

[4] J. J. Yao, C. Lee, and S. P. Yeo, "Microstrip branch-line couplers for crossover application," *IEEE Trans. Microw. Theory Techn*., vol. 59, no. 1, pp. 87-92, Jan. 2011.

[5] Y. L. Wu, L. X. Jiao, Z. Zhuang, and Y. Liu, "The art of power dividing: a review for state-of-the-art planar power dividers," *China Communications*, vol. 14, no. 5, pp. 1-16, May 2017.

[6] H. Zhu, Y. Wang, and A. M. Abbosh, "Broadband microwave crossover using parallel coupled microstrip lines and short-ended stubs," *IET Microw. Antennas Propag.*, vol. 9, no. 1, pp. 79-85, Feb. 2014.

[7] W. J. Feng, W. Q. Che, and Q. Xue, "Balanced filters with wideband common mode suppression using dual-mode ring resonators," *IEEE Trans. Circuits Syst. I: Regular Papers*, vol. 62, no. 6, pp. 1499-1507, June 2015.

[8] X. Y. Zhang, Q. Y. Guo, K. X. Wang, B. J. Hu, and H. L. Zhang, "Compact filtering crossover using stub-loaded ring resonator," *IEEE Microw. Wireless Compon. Lett.*, vol. 24, no. 5, pp. 327-329, May 2014.

[9] C. Zhao, W. Feng, and W. Che, "Ultra-wideband balanced bandpass filters based on transversal signal-interference concepts," *The Applied Computational Electromagnetics Society Journal*, vol. 30, no. 10, pp. 1232-1237, Oct. 2016.

[10] X. Gao, W. Feng, and W. Che, "LTCC wideband bandpass filter based on multi-layered coupling," *The Applied Computational Electromagnetics Society Journal*, vol. 32, no. 2, pp. 158-162, Feb. 2017

[11] G. Matthaei, L. Young, and E. M. T. Jones, *Microwave Filters, Impedance Matching Networks and Coupling Structures*. Artech House Inc., Norwood, MA, Section 5, pp. 222-224, 1985.

Wanchen Yang was born in Xuzhou, Jiangsu Province, China, in 1988. She received the B. Eng. degree in Communication Engineering from the Hohai University (HHU), Nanjing, China, in 2010, and the Ph.D. degree in Electromagnetic Field and Microwave Technology from Nanjing University of Science and Technology (NUST), Nanjing, China, in 2015. From October 2013 to April 2014, she was a Research Assistant with the University of Macau. She was the recipient of the Best Paper Prize of 2014 Student Paper Competition in IEEE

HK AP/MTT Postgraduate Conference, Oct. 2014. She is currently a Teacher with Nanjing University of Science and Technology, Nanjing, China. Her main research interests include novel artificial materials, artificial material-based antennas and millimeter-wave antenna arrays.

She serves as a Reviewer of the IEEE Transactions on Microwave Theory and Techniques, IEEE Transactions on Industrial Electronics, IEEE Antennas and Wireless Propagation Letters and IET Microwaves Antennas and Propagation.

Wenjie Feng was born in Shangqiu, Henan Province, China, in 1985. He received the B.Sc. degree from the First Aeronautic College of the Airforce, Xinyang, China, in 2008, the M.Sc., and Ph.D. degrees from the Nanjing University of Science and Technology (NUST), Nanjing, China, in 2010, 2013.

From November 2009 to February 2010, March 2013 to September 2013, he was a Research Assistant with the City University of Hong Kong. From October 2010 to March 2011, he was an exchange student with the Institute of High-Frequency Engineering, Technische Universität München, Munich, Germany. He is currently a Professor with the Nanjing University of Science and Technology, Nanjing, China. He has authored or coauthored over 70 internationally referred journal and 50 conference papers. His research interests include wideband circuits and technologies, substrate integrated components and systems, multi-function circuits and systems, balanced circuits, LTCC circuits.

Feng is a Reviewer for over twenty internationally referred journal and conference papers, including five IEEE Transactions and five Letters. He now serves as an Associate Editor for *IET Electronics Letters, IEEE Access and International Journal of Electronics.*

Wenquan Che received the B.Sc. degree from the East China Institute of Science and Technology, Nanjing, China, in 1990, the M.Sc. degree from the Nanjing University of Science and Technology (NUST), Nanjing, China, in 1995, and the Ph.D. degree from the City University of Hong Kong (CITYU), Kowloon, Hong Kong, in 2003.

In 1999, she was a Research Assistant with the City University of Hong Kong. From March 2002 to September 2002, she was a Visiting Scholar with the Polytechnique de Montréal, Montréal, QC, Canada. She is currently a Professor with the Nanjing University of Science and Technology, Nanjing, China. From 2007 to 2008, she conducted academic research with the Institute of High Frequency Technology, Technische Universität München. During the summers of 2005–2006 and 2009–2012, she was with the City University of Hog Kong, as Research Fellow and Visiting Professor. She has authored or coauthored over 180 internationally referred journal papers and over 120 international conference papers. She has been a Reviewer for *IET Microwaves, Antennas and Propagation*. Her research interests include electromagnetic computation, planar/coplanar circuits and subsystems in RF/microwave frequency, microwave monolithic integrated circuits (MMICs) and medical application of microwave technology.

Che is a Reviewer for the IEEE Transactions on Microwave Theory and Techniques, IEEE Transactions on Antennas and Propagation, IEEE Transactions on Industrial Electronics, and IEEE Microwave and Wireless Components Letters. She was the recipient of the 2007 Humboldt Research Fellowship presented by the Alexander von Humboldt Foundation of Germany, the 5th China Young Female Scientists Award in 2008 and the recipient of Distinguished Young Scientist awarded by the National Natural Science Foundation Committee (NSFC) of China in 2012.

A Band-Notched Square Monopole Antenna designed for Bandwidth Enhancement in UWB Applications

B. Azarm, C. Ghobadi, J. Nourinia, M. Abbasilayegh, and M. Karamirad

Department of Electrical Engineering, University of Urmia, Urmia, Iran
st_b.azarm@urmia.ac.ir, changiz.ghobadi@urmia.ac.ir, javad.nourinia@urmia.ac.ir,
m.abbasilayegh@urmia.ac.ir, m.karamirad@urmia.ac.ir

Abstract ─ In this letter, a square monopole antenna has been designed for ultrawideband (UWB) applications having variable notch frequency characteristic. The proposed antenna consists of the small square radiating patch with two rectangular slots, which provides a wide usable fractional bandwidth from 3.1 to 14.4 GHz. The proposed antenna is simple and has a very small size of 10×15 mm^2. The bandwidth of the proposed antenna is wider than that of the antenna that has already been introduced in references. Experimental results show that the proposed antenna could be a good candidate for ultrawideband (UWB) applications.

Index Terms ─ Small square monopole antenna, ultrawideband (UWB).

I. INTRODUCTION

Recently, the ultrawideband (UWB) technology has been prominently developed and used. UWB systems for commercial purposes require small antennas that are not costly and also have omnidirectional radiation patterns as well as a large bandwidth [1]. Obviously simple structure, small size and low cost fabrication process are desired features of a planar monopole antennas which make it utilize in promising applications such as satellite communications. Taking into account all the aforementioned interesting characteristics, planar monopoles are extremely appropriate to be used in modern UWB applications and hence, so many activities focus on them. In UWB communication systems, designing compact antennas that can provide wideband characteristic in the whole operating frequency band is one of the state-of-the art concerns [2]. Utilizing UWB antennas with high gain characteristic is necessary for both military and commercial applications. Such applications require an antenna with compact and thin antenna configuration. Consequently, a multitude of planar monopoles with different geometries has been experimentally characterized [3–4] and in order to obtain the optimum planar shapes numerous automatic design methods have been developed [5, 6].

The frequency range for UWB systems between 3.1 and 10.6 GHz may interfere with the existing wireless communication systems, for example the wireless local area network (WLAN) for IEEE 802.11a operating in 5.15–5.35 GHz and 5.725–5.825 GHz bands, so the UWB antenna with a band-stop performance is required. Recently, to generate the frequency band-notch function, a novel UWB monopole antenna with controllable band notch Characteristics [6] and a compact design and new structure of monopole antenna with dual band notch characteristics [7] have been used. In this letter, a novel band-notch monopole antenna is presented that can be used for ultrawideband (UWB) applications. The size of the designed antenna is smaller than that of the antennas reported recently [6], [7].

In this work, a simple notch band antenna is presented. Basically, effects of printed square radiation surface parameters have been studied, comprehensively. Also, investigation on the defective ground has been performed in order to improve the impedance bandwidth and notch frequency. Indeed, the antenna has an impedance bandwidth of 13 GHz across an appropriate average gain of 5 dB. An experimental effort has been made in order to confirm the simulation results. Accordingly, the VSWR>2 bandwidth of the notch frequency is almost 1 GHz from 5 GHz to 6 GHz with the gain of nearly -7 dB.

II. ANTENNA DESIGN AND CONFIGURATION

Figure 1 shows the configuration of the proposed monopole antenna with tunable notch frequency. The antenna consists of a simple square patch with two rectangular slots on sides and a defective ground plate. The proposed antenna is fed by a 50 Ω feed-line printed on FR-4 substrate with the thickness of 1.6 mm, permittivity 4.4, and loss tangent 0.0018. The width of the microstrip feed line is fixed at 1.5 mm. To explain the performance of the antenna, the design has been improved evolutionary, as depicted in Fig. 3. The primary structure is displayed in step 1. Thereafter, the ground has defected in step 2 in order to improve impedance matching. Indeed, the electrical charges

Submitted On: June 8, 2017
Accepted On: September 6, 2017

1054-4887 © ACES

on ground plane distribute uniformly and a great enhancement capacitance between the feed line and ground will be achieved at high frequencies. Accordingly, due to the current distribution on ground and feed line, an improvement in high frequency bandwidth is yielded. As can be found in Fig. 4, the advancement makes the bandwidth be broadened from 5 GHz to 13 GHz. In the last step, to obtain significant notch frequency bandwidth, the proposed antenna is attained by etching two slots on sides of radiation surface. In fact, in order to achieve the desired notch, the current distribution on radiation surface should be adjusted. Consequently, the parameters of the antenna have prepared the main objective of the study.

The truncated ground plane plays an important role in the broadband characteristics of this antenna because it helps the patch be matched with the feed line in a wide range of frequencies. This is mainly because of neutralization of the inductive nature of the patch by the capacitive load created by the truncation in order to produce nearly pure resistive input impedance [8]. The two rectangular notches are used to control the impedance bandwidth and VSWR level by modifying the capacitance between the patch and the ground plane. The optimal dimensions of the designed antenna are specified in Table 1.

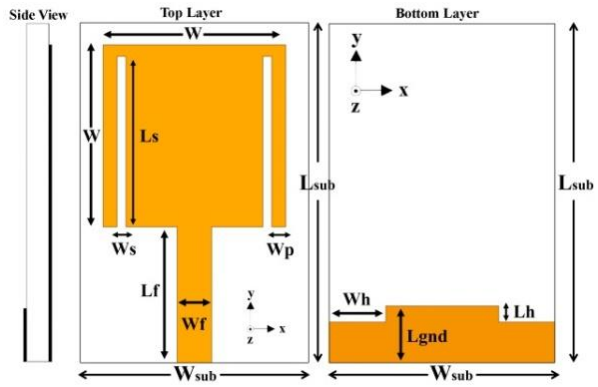

Fig. 1. Geometry of proposed antenna.

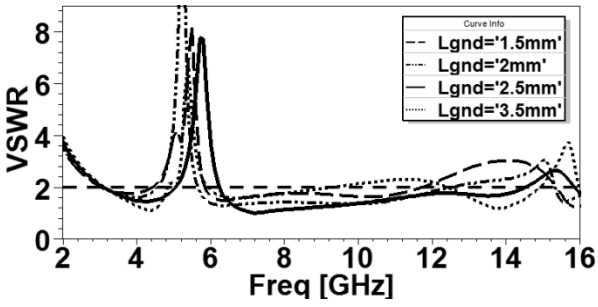

Fig. 2. Simulated VSWR characteristics of proposed antenna with different values of Lgnd length.

Table 1: Optimized parameters of the antenna (Unit: mm)

Wsub	10	Ws	0.4	Ls	7.5
Lsub	15	Lgnd	2.5	Lf	6
W	8	Wp	0.6	Lh	0.7
Wf	1.5	Wh	2.5		

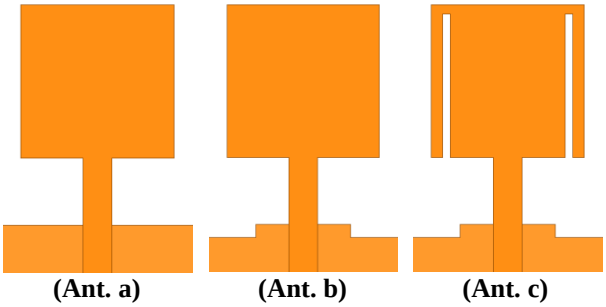

Fig. 3. Different antenna structures: (Ant. a) basic structure (ordinary square antenna); (Ant. b) the antenna with two rectangular notches in the ground plane; (Ant. c) the proposed antenna.

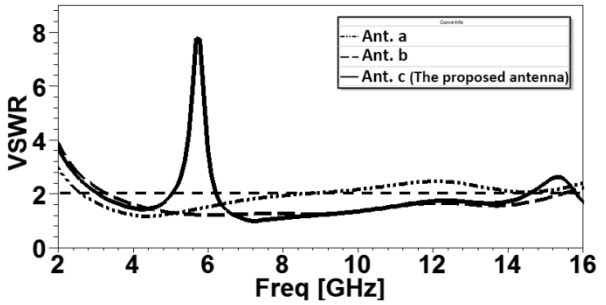

Fig. 4. Simulated VSWR characteristics for antennas shown in Fig. 3.

III. RESULTS AND DISCUSSIONS

Through the result investigation in previous works, attaining high performance in variable notch frequency leads us to study the configuration parameters. The parameters of the proposed antenna have been studied by varying one parameter while the rests are fixed. The procedures of the investigation have totally been carried out through HFSS (High Frequency Simulation Structure) [9].

In order to modify the antenna design, a parametric study is performed. Figure 2 demonstrates the effect of the Lgnd variation on impedance bandwidth. As Lgnd increases, the upper bound of the impedance bandwidth increases as well. Indeed, the capacitance property between the ground and the patch amplifies as Lgnd increases. However, the Lgnd=2.5 mm intensifies the capacitor among the ground and gaps at sides of the patch. Therefore, this phenomenon interference the main

capacitance and consequently the resonant frequency decrease to 14 GHz. It has been worth noting that the noticeable performance of the antenna is varying the notch frequency. Accordingly, two parameters (Wh and Lh) have been studied in order to attain the objective. As shown in Fig. 6 (a), the notch frequency increases as Wh raises to 3.5 mm. Also, the increment of Lh increases the frequency notch as well. In spite of notch frequency variations, other frequencies in bandwidth are extremely stable. Besides, one should be noted that the notch frequency has been altered through ground parameters. This feature leads us to design antenna leaning on just ground defection. Nevertheless, owing to the intact radiation surface, the gain will not change at all.

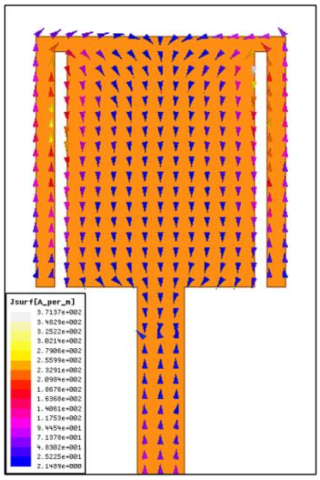

Fig. 5. Simulated surface current distributions on the radiating patch for the proposed antenna at 5.5 GHz.

Although the variation of prior parameters effects on notch frequency, the influences of other parameters should be studied as well. Notch frequency is significantly altered as the Ls varies from 6 mm to 7.8 mm. Since the frequency is proportional to the inverse of length ($f \propto \frac{1}{Ls}$), the frequency variation is rather considerable. According to the Fig. 7 (b), the frequency shift is approximately 1 GHz. As can be seen in Figs. 7 (b), 7 (c), the slight increase in notch frequency caused by Ws and Wp is almost none-uniform. The variations are almost 0.25 GHz for both Ws and Wp. As illustrated in Fig. 4, the additional two rectangular slots in the radiating patch are playing an important role in the band-stop characteristics of this antenna. Consequently, the band-stop performance is improved, especially at the central band-notch frequency. The simulated current distributions on the radiating patch for the proposed antenna at 5.5 GHz are presented in Fig. 5. It can be observed in Fig. 5 that the current is mainly concentrated on the edges of the interior and exterior of the two rectangular slots at 5.5 GHz. It is obvious that the current distributions direction on slot edges is opposite. Therefore, the inductance decreases and the resonance frequency known as notch frequency are obtained. Worth noting that signal which is transmitted through the feed line cannot reflect the main source.

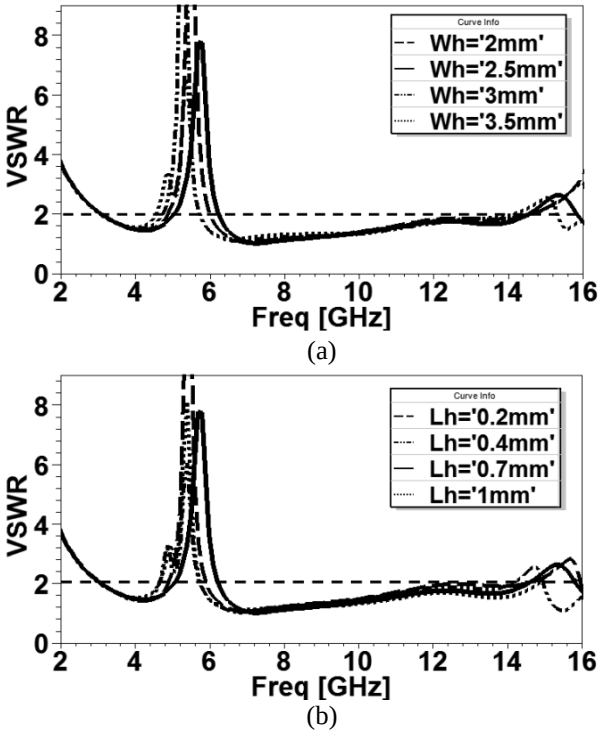

Fig. 6. Simulated VSWR characteristics of the proposed antenna: (a) with different values of Wh (Lh is fixed at 0.7 mm); (b) with different values of Lh (Wh is fixed at 2.5 mm).

The simulated VSWR curves with different values of Wh and Lh length in the ground plane are plotted in Fig. 6. Figure 7 shows the effect of varying the Ws, Ls, and Wp length in the radiating patch on the impedance bandwidth. The simulated VSWR curves with different values of Ws are plotted in Fig. 7 (a). The optimized length is selected to be 0.4 mm. Figure 7 (b) shows the effects of Ls on the impedance matching. The simulated VSWR curves with the optimal Ws and Ls for various Wp are plotted in Fig. 7 (c). In order to confirm the simulation results, a prototype of the antenna has been fabricated, as displayed in Fig. 8. Figure 8 presents the photograph of a prototype printed monopole antenna on an FR-4 substrate with the SMA connector. Figure 9 shows the simulated and measured radiation pattern in frequencies 4, 7, 10, and 14 GHz in H-plane (xz plane) and E-plane (yz plane). The half power bandwidths (HPBWs) of the antenna are almost 23° and 26° in E- and H-plane for 4 GHz, respectively, as shown in Fig. 9 (a). Also, it can be seen that the HPBWs are 21° and 25° for

10 GHz. Obviously, since the antenna is printed on a defective ground, the broadside pattern will be deflected forward slightly. VSWR characteristics of the proposed antenna are shown in Fig. 10. As shown in Fig. 10, the fabricated antenna has the frequency band of 3.1 extending to more than 14.4 GHz with a rejection band around 5–6 GHz. Figure 11 shows the effects of two rectangular slots, on the maximum gain in comparison to the antenna without the aforementioned slots.

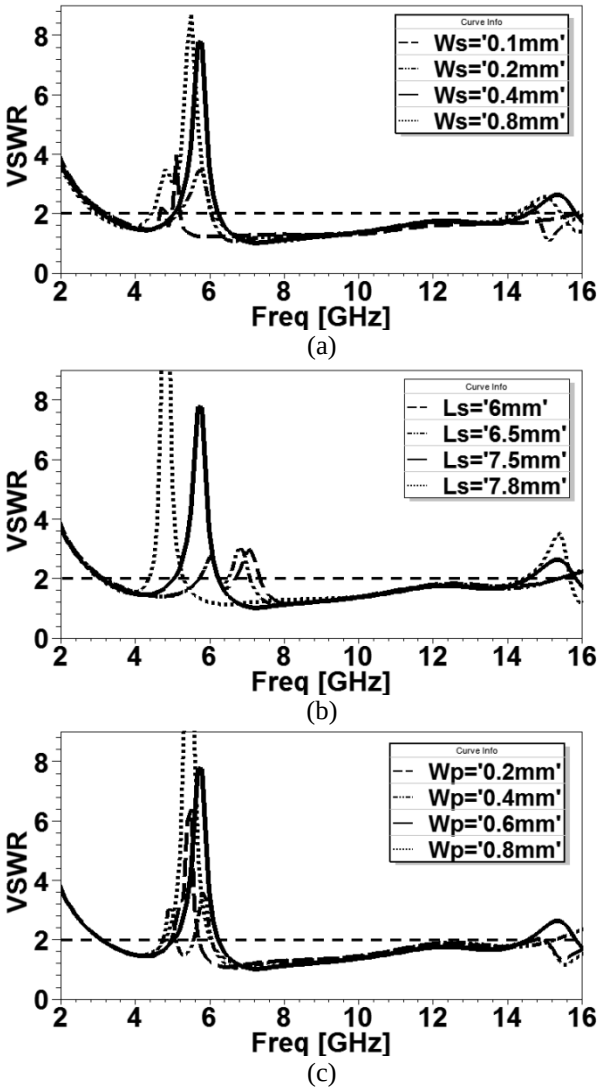

Fig. 7. Simulated VSWR characteristics of the proposed antenna: (a) with different values of Ws (Ls is fixed at 7.5 mm); (b) with different values of Ls (Ws is fixed at 0.4 mm); (c) with different values of Wp (Ws is fixed at 0.4 mm and Ls is fixed at 7.5 mm).

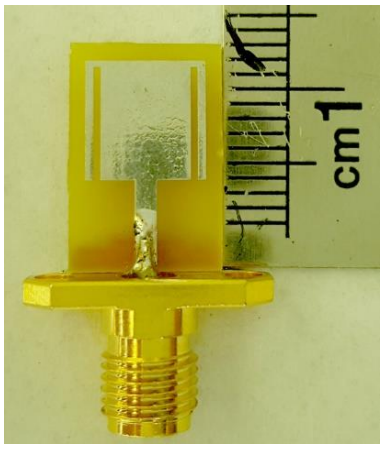

Fig. 8. Photograph of the realized antenna.

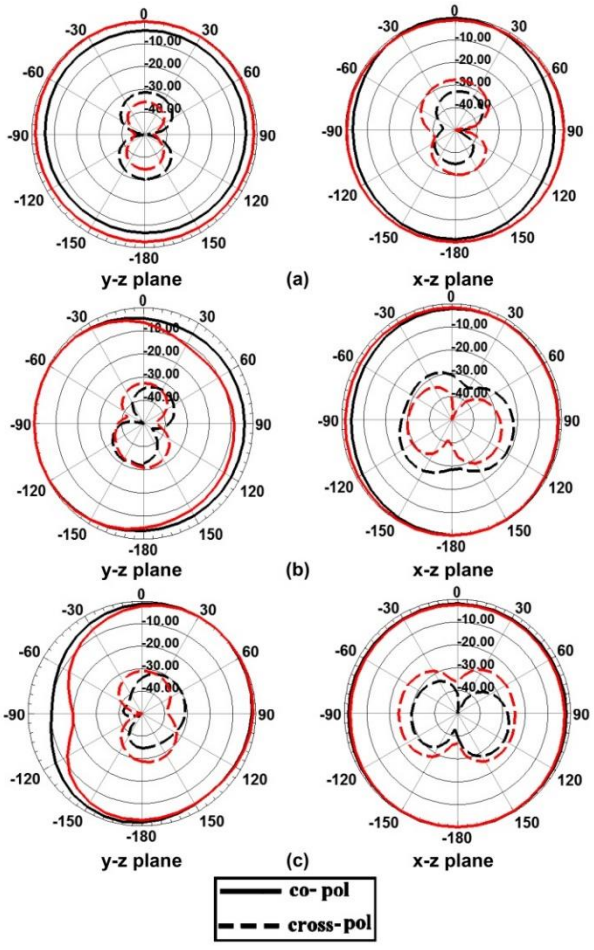

Fig. 9. Simulated and measured radiation patterns in: (a) 4, (b) 7, and (c) 10 GHz frequencies.

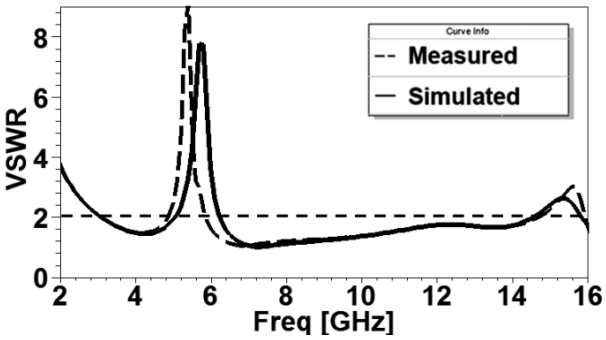

Fig. 10. Measured and simulated VSWR for the proposed antenna.

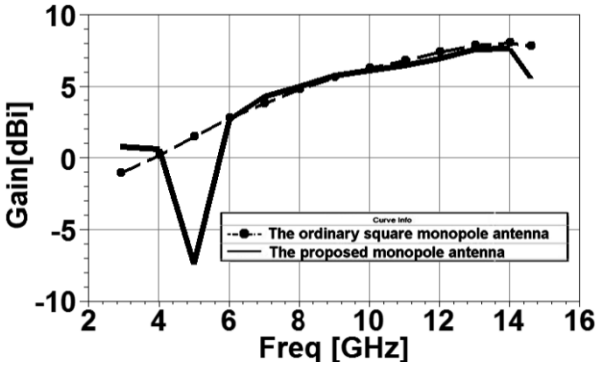

Fig. 11. Measured antenna gain of the proposed antenna.

In this study, bandwidth could be enhanced after inserting two slots in the ground plane of the proposed antenna as displayed in the figure. The main function of the slots here is to create a new path for the surface current that is able to make another resonance and hence, the bandwidth can be increased [10], [11].

In order to confirm the accurate VSWR characteristics for the designed antenna, it is recommended that the measurement process be performed carefully.

IV. CONCLUSION

In this letter, a newly-designed band-notched square monopole antenna is proposed for UWB applications. The proposed antenna has a simple configuration and it is easy to fabricate. The proposed antenna is small in size (10x15 mm^2) and the bandwidth of the proposed antenna is wider than that of the antennas reported in references. The proposed antenna has the frequency band of 3.1 to over 14.4 GHz with a rejection band around 5–6 GHz. The sizes of two rectangular slots for obtaining the wide bandwidth have been optimized by parametric analysis. Experimental results show that the proposed antenna could be a good choice for UWB application.

REFERENCES

[1] H. Schantz, *The Art and Science of Ultra Wideband Antennas*. Norwood, MA: Artech House, 2005.

[2] Z. N. Chen, "Impedance characteristics of planar bow-tie-like monopole antennas," *Electron. Lett.*, vol. 36, no. 13, pp. 1100-1101, 2000.

[3] M. J. Ammann, "Impedance bandwidth of the square planar monopole," *Microw. Opt. Technol. Lett.*, vol. 24, no. 3, pp. 185-187, 2000.

[4] M. Ojaroudi, H. Ebrahimian, C. Ghobadi, and J. Nourinia, "Small microstrip-fed printed monopole antenna for UWB application," *Microw. Opt. Technol. Lett.*, vol. 52, no. 8, pp. 1756-1761, 2010.

[5] M. Mirmozafari, C. Ghobadi, H. Mirhedayati, and A. Rezaee, "A planar UWB monopole antenna with on-ground slot band-notch performance," *Appl. Comp. Electro. Society (ACES) Journal*, vol. 28, no. 8, pp. 719-724, 2013.

[6] N. Tasouji, J. Nourinia, C. Ghobadi, and F. Mirzamohammadi, "A novel UWB monopole antenna with controllable band-notch characteristics," *Appl. Comp. Electro. Society (ACES) Journal*, vol. 32, no. 1, pp. 68-73, 2017.

[7] S. Hoseyni, J. Nourinia, C. Ghobadi, S. Masumina, and B. Mohammadi, "A compact design and new structure of monopole antenna with dual band notch characteristic for UWB applications," *Appl. Comp. Electro. Society (ACES) Journal*, vol. 31, no. 7, pp. 797-805, 2016.

[8] J. Jung, W. Choi, and J. Choi, "A small wideband microstrip-fed monopole antenna," *IEEE Microw. Wireless Compon. Lett.*, vol. 15, no. 10, pp. 703-705, 2005.

[9] Ansoft High Frequency Structure Simulation (HFSS). ver. 15, Ansoft Corporation, 2013.

[10] S. Maci and P. Piazzesi, "Dual-band slot-loaded patch antenna," *Proc. Antenna Propag.*, vol. 142, no. 3, pp. 225-232, 1995.

[11] S. Maci and G. B. Gentili, "Dual frequency patch antennas," *IEEE Antennas Propag. Mag.*, vol. 39, no. 6, pp. 13-20, 1997.

Burhan Azarm was born on 1992 in Iran. He received the B.Sc. degree in Power Engineering from Islamic Azad University, Urmia, Iran. He is currently working toward the M.Sc. degree in RF and Microwave Engineering at Urmia University. His research interests include Antennas, Microwave and Electromagnetics.

Changiz Ghobadi was born on June 1, 1960 in Iran. He received the B.Sc. degree in Electrical and Electronic Engineering and M.Sc. degree in Electrical and Telecommunication Engineering from Isfahan University of Technology, Isfahan, Iran and Ph.D. degree in Electrical-Telecommunication from University of Bath, Bath, UK in1998. From 1998 he was an Assistant Professor and now is Full Professor in the Department of Electrical Engineering, of Urmia University, Urmia, Iran. His primary research interests are in Antenna, Microwave and Electromagnetics.

Javad Nourinia was born in 1969 in Iran. He received the B.Sc. degree in Electrical and Electronic Engineering from Shiraz University and M.Sc. degree in Electrical and Telecommunication Engineering from Iran University of Science and Technology, and Ph.D. degree in Electrical and Telecommunication from University of Science and Technology, Tehran, Iran in 2000. From 2000 he was an Assistant Professor and now is Full Professor in the Department of Electrical Engineering, of Urmia University, Urmia, Iran. His primary research interests are in Antenna, Microwave and Electromagnetics.

Compact Design of Wide Bandpass, Symmetric and Asymmetric Dual Bandpass Filters with Finline and Split Ring Resonators

V. Madhusudana Rao [1] and B. Prabhakara Rao [2]

[1] Department of Electronics and Communication Engineering
Jawaharlal Technological University, Kakinada, INDIA-532003
vepakayala@gmail.com

[2] Rector of Jawaharlal Nehru Technological University, Kakinada, INDIA-532003
drbpr@rediffmail.com

Abstract ─ The finline based transmission line is used for realization of wide band pass filter. In this paper designing a bandpass filter for wide bandwidth, based on parallel coupled unilateral three finline structures. A design graph for symmetric three unilateral finline structures is presented for the design of bandpass filter. A bandpass filter of order 3 having center frequency of 10 GHz with fractional bandwidth of 20% is designed fabricated and measured. This wide bandpass filter is converted into symmetric and asymmetric dual band pass filters with the help of metamaterials (Split Ring Resonators SRR) on the other side of the finline structure is simulated with High Frequency Structure Simulator (HFSS) and fabricated. Transmission (S_{21}) and reflection (S_{11}) parameters of measured results compared with simulated results.

Index Terms ─ Asymmetric dual bandpass filters, metamaterials, split ring resonator (SRR), unilateral finline, wide band pass filter.

I. INTRODUCTION

The metamaterials or artificial electromagnetic (EM) materials are those materials that do not have any natural occurrence in nature. They are synthesized artificially through man-made processes. Their structures exhibit strange and uncommon electromagnetic properties. Metamaterial is a material which gains its properties from its structure rather than directly from its composition. These materials are often recorded as left handed materials or double negative materials as they have simultaneous negative permittivity ($\varepsilon < 0$) and permeability ($\mu < 0$). Due to the fact that both ε and μ are negative, these materials show negative index of refraction. In 1968, Victor Veselago studied and theoretically suggested these materials [1]. As the name suggests, left-handed materials obey left hand rule which is in complete contrast to the right-hand rule followed for usual materials. The electric field, magnetic field and wave vector of electromagnetic wave propagation in left-handed (LH) materials are opposite to those in right-handed materials. It has also been demonstrated that many other resonator topologies, derived from the basic SRR proposed by Pendry *et al.* [2], are appropriate to achieve effective (continuous) media with negative permeability. With the rapid development of microwave and millimeter wave communication systems, it greatly stimulates the demand on high performance bandpass filters with compact dimensions, low insertion loss, high attenuation in stopband and low cost [3, 4]. The finline transmission line is a wave guiding structure which is increasingly used as millimeter wave component due to various advantages such as high transmission level, reducing size, and weight. The wide bandpass filter structure based on finline topology which offer the benefit to concentrate the fields near the slot of planner transmission line embedded in side a hallow wave guide to prevent any radiation losses [5, 6]. With the help of these SRRs, this wide bandpass filter has been converted into symmetric and asymmetric dual bandpass filters presented in this paper.

II. ANALYSIS OF THREE COUPLED UNILATERAL FINLINES

The dispersion characteristics of multiple coupled unilateral finlines on isotropic substrate have been evaluated by using full wave modal analysis as shown in Fig. 1. In this modal analysis, all the field components are constructed in terms of x-components of electric and magnetic fields in each region, which are expanded in terms of modal fields with unknown coefficients, are given below.

The Maxwell equation is:

$$\begin{bmatrix} E_t \\ H_t \end{bmatrix} = \frac{1}{\left(k_o^2 \varepsilon_r - k_x^2\right)} \begin{bmatrix} \partial/\partial x & j\omega\mu_o x \\ -j\omega\varepsilon_o\varepsilon_r x & \partial/\partial x \end{bmatrix} \begin{bmatrix} \nabla_t E_x \\ \nabla_t H_x \end{bmatrix}. \quad (1)$$

The x-component of the electric and magnetic fields

Submitted On: February 26, 2017
Accepted On: August 16, 2017

1054-4887 © ACES

satisfy the Helmholtz equation:

$$\left[\frac{\partial^2}{\partial x^2}+\frac{\partial^2}{\partial y^2}+\left(k_o^2\varepsilon_r-\beta^2\right)\right]\begin{bmatrix}E_x\\H_x\end{bmatrix}=0. \quad (2)$$

Here side walls are considered to be electric walls. Solutions of the equations in the three regions are:

$$E_x^{(1)}=\sum_{n=1}^{\infty}A_{n1}Cos\left[\Gamma_{n1}(x-h_1)\right]Sin(\alpha_n y)e^{-j\beta z}, \quad (3)$$

$$H_x^{(1)}=\sum_{n=0}^{\infty}B_{n1}Sin\left[\Gamma_{n1}(x-h_1)\right]Cos(\alpha_n y)e^{-j\beta z}, \quad (4)$$

$$E_x^{(2)}=\sum_{n=1}^{\infty}\left[A_{n2}Sin(\Gamma_{n2}x)+A'_{n2}Cos(\Gamma_{n2}x)\right]Sin(\alpha_n y)e^{-j\beta z}, \quad (5)$$

$$H_x^{(2)}=\sum_{n=0}^{\infty}\left[B_{n2}Cos(\Gamma_{n2}x)+B'_{n2}Sin(\Gamma_{n2}x)\right]Cos(\alpha_n y)e^{-j\beta z}, \quad (6)$$

$$E_x^{(3)}=\sum_{n=1}^{\infty}A_{n3}Cos\left[\Gamma_{n3}(x+d+h2)\right]Sin(\alpha_n y)e^{-j\beta z}, \quad (7)$$

$$H_x^{(3)}=\sum_{n=0}^{\infty}B_{n3}Sin\left[\Gamma_{n3}(x+d+h2)\right]Cos(\alpha_n y)e^{-j\beta z}, \quad (8)$$

where k_0 is propagation constant, A_{n1}, B_{n1}, A_{n2}, B_{n2}, A'_{n2}, B'_{n2}, A_{n3} and B_{n3} are amplitude constants;

$$\Gamma_{n1}=\sqrt{k_0^2-\alpha_n^2-\beta^2},$$

$$\Gamma_{n2}=\sqrt{k_0^2\varepsilon_{r2}-\alpha_n^2-\beta^2},$$

$$\Gamma_{n3}=\sqrt{k_0^2\varepsilon_{r3}-\alpha_n^2-\beta^2},$$

$$\alpha_n=\frac{(2n+1)\pi}{b},\ \beta = 2\Pi/\text{wavelength}.$$

The boundary conditions at x = h1, (-h2+d) and y = ± b/2 have been incorporated. Using these boundary conditions in Eq. (1), the other field components (3)-(8) can be derived.

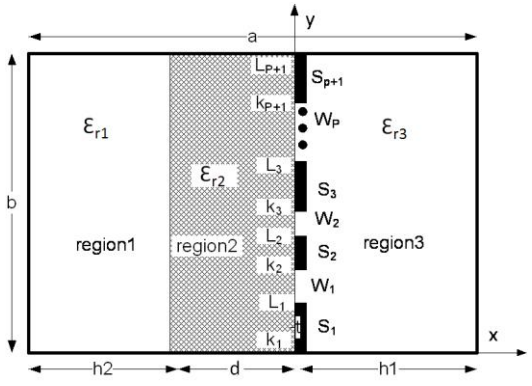

Fig. 1. Cross-section view of multiple edge coupled unilateral fin-line on isotropic substrate.

A. Normal mode parameters

The propagation constants are evaluated by applying the Galerkin's method to the transformed Green's function matrix relating the voltage and electric fields at various boundaries of the structure and solving for the roots of the determinant of the Eq. (1):

$$\sum_{k=1}^{\infty}c_k\sum_{n=0}^{\infty}p_nG_{11}L_{2n}^kL_{2n}^m+\sum_{k=1}^{\infty}d_k\sum_{n=0}^{\infty}q_nG_{12}L_{1n}^kL_{2n}^m=0.$$

$$\sum_{k=1}^{\infty}c_k\sum_{n=1}^{\infty}p_nG_{21}L_{2n}^kL_{1n}^m+\sum_{k=1}^{\infty}d_k\sum_{n=1}^{\infty}q_nG_{22}L_{1n}^kL_{1n}^m=0. \quad (9)$$

The set of basis functions used in this analysis are sinusoidal and expressed as follows:

$$V_z(y)=\frac{\cos\left[2(n-1)\pi\frac{(y-y_i)}{w_i}\right]}{\sqrt{1-\left[\frac{2(y-y_i)}{w_i}\right]^2}},\qquad V_y(y)=\frac{\sin\left[2n\pi\frac{(y-y_i)}{w_i}\right]}{\sqrt{1-\left[\frac{2(y-y_i)}{w_i}\right]^2}}, \quad (10)$$

where w_i being the width of the i^{th} fin, y_i is the distance from origin to the center of i^{th} fin.

B. Characteristics impedances

Mode characteristics impedance of the coupled unilateral finlines lines are evaluated for all hybrid modes in a straight forward manner by calculating the power associated with a given finline for a given mode. The finline mode impedance is given by:

$$Z_{lm}=\frac{(V_{lm})^2}{P_{lm}}, \quad (11)$$

where V_{lm} is the modal voltage of the l^{th} slot given by the integral of the electric field across the slot and P_{lm} is the partial modal power associated with the same slot when the m^{th} normal mode is excited.

III. FILTER DESIGNAND FABRICATION

The Fig. 2 shows the simulated structure of a resonator used to realize the wideband pass filter structure. The resonator consists of three parallel-coupled unilateral finlines approximately quarter wavelength long. In this paper multi resonators are cascaded to achieve high rejections. H field is perpendicular to the SRR plane (i.e., in the direction of X-axis) and the incident E field is in the same direction of the SRR rings (i.e., in the direction of Z-axis). The PEC type boundary conditions are applied at the boundary surfaces perpendicular to the E field, while the PMC type boundary conditions are applied at the boundary surfaces perpendicular to the H field. Remaining boundaries are defined as the input and output ports.

The six port impedance matrix parameters for a section of three coupled finlines of length *l* are found from mode characteristic impedances, phase velocities and voltage ratios [7-10]. This three-coupled finline

structure supports three dominant modes as OE, EE, and OO, which correspond to 1, 2 and 3, respectively. Each mode has its own modal phase constant, eigen voltage vector and characteristic impedance. The eigen voltage matrix for symmetrical three line which have equal fin-width and spacing are given by:

$$[\mathrm{Mv}] = \begin{bmatrix} 1 & 1 & 1 \\ \mathrm{m}_1 & 0 & \mathrm{m}_3 \\ 1 & -1 & 1 \end{bmatrix}.$$

Each vector of $[\mathrm{M_V}]$ is the eigen voltage vector of the matrix product [L] [C]. The matrix $[\mathrm{M_V}]$ can be used to derive the relation between port voltages and port currents:

$$\begin{bmatrix} V_A \\ V_B \end{bmatrix} = \begin{bmatrix} Z_A & Z_B \\ Z_B & Z_A \end{bmatrix} \begin{bmatrix} I_A \\ I_B \end{bmatrix}, \tag{12}$$

where

$$[V_A] = [V_1, V_2, V_3]^T,\ [V_B] = [V_4, V_5, V_6]^T,$$
$$[I_A] = [I_1, I_2, I_3]^T,\ [I_B] = [I_4, I_5, I_6]^T. \tag{13}$$

The impedance matrix $[Z_A]$ and $[Z_B]$ can be derived as:

$$[Z_A] = [M_V]\ \ diag[-jZ_{mi}\ cot\theta_i\ ][M_V]^T. \tag{14}$$

Now $\theta_i = \beta_i l$ with β_i is the phase constant of the i^{th} mode, l the length of the coupled section, and Z_{mi} given by:

$$Z_{mi} = \frac{Z_{oi}}{m_i^2 + 2}, \tag{15}$$

where Z_{oi} is the characteristic impedance of i^{th} mode. In Eq. (15), m_2=0. Comparing the two port Z-Parameters of the circuit in Fig. 3 (b) with Fig. 3 (c), we obtain Eqs. (16), (17), (18):

$$m_1 Z_{m1} - m_3 Z_{m3} = JZ_A Z_B, \tag{16}$$
$$m_1^2 Z_{m1} - m_3^2 Z_{m3} = Z_A(J^2 Z_A Z_B + 1), \tag{17}$$
$$Z_{m1} + Z_{m3} = Z_B(J^2 Z_A Z_B + 1), \tag{18}$$
$$m_1 Z_{m1} \approx \left[\frac{2+\mu^2}{2\mu}\right](Z_0/2)(J^2 Z_0^2 + JZ_0 + 1), \tag{19}$$
$$m_3 Z_{m3} \approx \left[\frac{2+\mu^2}{2\mu}\right](Z_0/2)(J^2 Z_0^2 - JZ_0 + 1), \tag{20}$$

where

$$\mu = \frac{\sqrt{2\left[2(Z_{ee}-Z_{oo})^2 - Z_{oe}(Z_{oe}-Z_{ee}-Z_{oo}) - Z_{ee}Z_{oo}\right]}}{2Z_{ee} - Z_{oe} - Z_{oo}}.$$

The value of JZ_O for each admittance inverter can be determined from the values of lumped circuit elements of the low pass prototype:

$$J_1 = \frac{1}{Z_0}\sqrt{\frac{\pi\Delta}{2g_1}}, \tag{21}$$
$$J_n = \frac{1}{Z_0}\sqrt{\frac{\pi\Delta}{2g_{n-1}g_n}},\ for\ n = 2, 3.....N, \tag{22}$$
$$J_{N+1} = \frac{1}{Z_0}\sqrt{\frac{\pi\Delta}{2g_N g_{N+1}}}, \tag{23}$$

where $\Delta = \frac{\omega_2 - \omega_1}{\omega_0}$.

For N = 3, characteristic impedance (Z_0) = 100 Ω, the values of g_1 to g_{N+1} are given below using [11]. g_1 = 1.5963, g_2 = 1.0967, g_3 = 1.5963, g_4 = 1.0000. Once JZ_O is known, the values of $m_1 Z_{m1}$ and $m_3 Z_{m3}$ for each coupled section can be known. The values of $m_1 Z_{m1}$ and $m_3 Z_{m3}$, for Section I are 82.02 Ω and 64.69 Ω respectively, and for the Section II are 37.65 Ω and 40.94 Ω respectively. The designed filter dimension has been simulated with HFSS. The optimized filter dimension has been shown in Table 1.

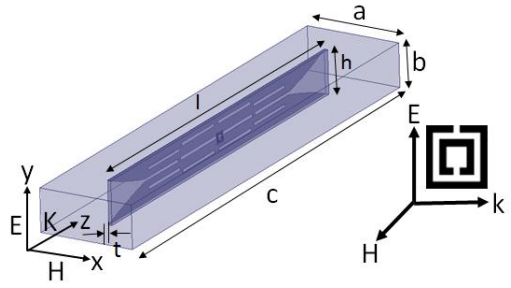

Fig. 2. Simulated structure of parallel coupled three finline wide bandpass filter housed in X-band wave guide (dimensions are a = 22.86 mm, b = 10.16 mm, c = 111 mm) and RT-Duriod 5880™ dielectric substrate parameters (dielectric constant (ε_r) = 2.2, substrate thickness (t) = 0.8 mm, length (l) = 90 mm, height (h) = 10.16 mm, loss tangent is 0.0009, frequency = 10 GHz).

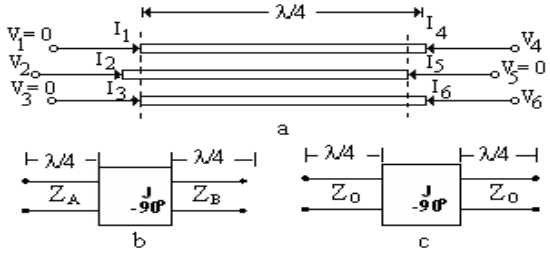

Fig. 3. Reduction of a coupled three-finline section to a two-port network: (a) coupled three-line section as a six-port network, (b) equivalent admittance inverter, and (c) further approximated admittance inverter.

Table 1: Three finline coupled wide bandpass filter (resonator parameters), dimensions are in mm

Dimensions	Designed Data		Optimized Data	
	Section 1	Section 2	Section 1	Section 2
W	0.650	0.68	0.750	0.750
S	1.320	2.370	1.400	2.400
L	9.592	10.164	12.970	13.413
G	1.975	2.033	1.076	1.633

The design graph of Fig. 4 for $\varepsilon_r = 2.2$ is used to determine the line width (W) and line spacing (S) of three coupled unilateral finlines at 10 GHz. Due to symmetry of filter, half part of the filter dimensions (width, spacing and length (L)) from center structure is designated in two sections have been mentioned in Table 1. With this data, the three coupled finline structure have been simulated with HFSS and fabricated. The pattern of the fabricated filter has been shown in Fig. 5.

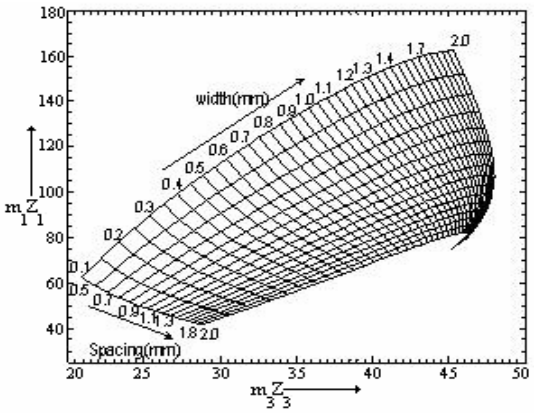

Fig. 4. The bandpass filter design graph for a symmetric three unilateral finline structure.

The return loss S11 and insertion loss S21 over the frequency band have been given in Fig. 6. The insertion loss in passband is 0.5 dB and return loss is less than -10 dB, and stop band attenuation is 20 dB at 11.5 GHz frequency. The transmission (S21), reflection (S11) coefficients of simulated and measured wide bandpass filter is compared and found reasonably matched. This wide bandpass filter has been converted into dual bandpass filters by using metamaterial (SRR) concept.

IV. METAMATERIAL (SRR) CONCEPT

Pendry et al. in 1999, proposed split-ring resonators (SRRs), which is a set of two concentric planar rings with splits in them at opposite ends as depicted in Fig. 4 (a), printed on a thin dielectric substrate (ε_r = 2.2) RT-Duriod 5880™.

The rings are made of nonmagnetic metal like copper and have a small gap between them. The splits in the rings cause the structure to support resonant wavelengths much larger than the diameter of the rings, which cannot occur in closed rings. Thus, SRRs that have a negative index of refraction are capable of high-frequency magnetic response. Below the resonant frequency the magnetic permeability of a SRR is positive, and above resonance frequency is negative. SRRs demonstrate a quasi-static resonance by virtue of the distributed capacitance between concentric rings and overall rings inductance. Topology of the SRR and its equivalent-circuit models has been depicted in Fig. 7. They act as LC resonators and their equivalent-circuit model as depicted in Fig. 7 (c). Where Co is the total capacitance between the rings, and Cs = Co/4 where Cs is the series capacitance of the upper and lower halves of the SRR. Now we introduced double SRR on the other side of substrate at center as shown in Fig. 7. This double SRR creates negative effective permeability μ_{eff} (ω) at desired frequency. It creates a notch at resonance frequency. This is the useful characteristics for converting the wideband filter in to dual bandpass filters. The notch can be controlled by number of SRR for desired frequency. With this technique we can create symmetric and asymmetric dual bandpass filters for different band widths [13-18].

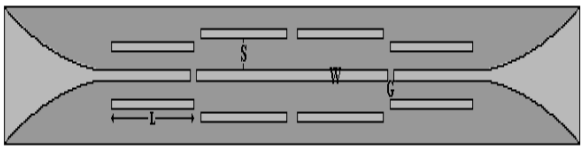

(a)

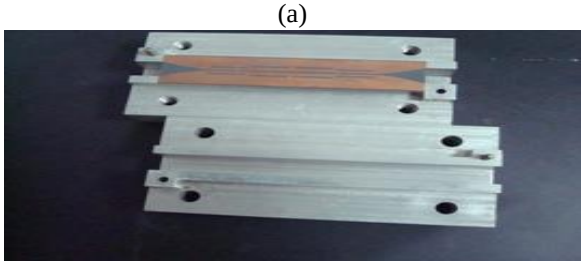

(b)

(c)

Fig. 5. (a) Simulated structure of parallel coupled three finline wide band pass filter of order 3, (where L = length of the resonators, S = spacing between resonators, W = width of resonators, G = gap between adjacent resonators). (b) Photo of X-band wave guide housing to keep this filter. (c) Photo of measurements setup of dual bandpass filters.

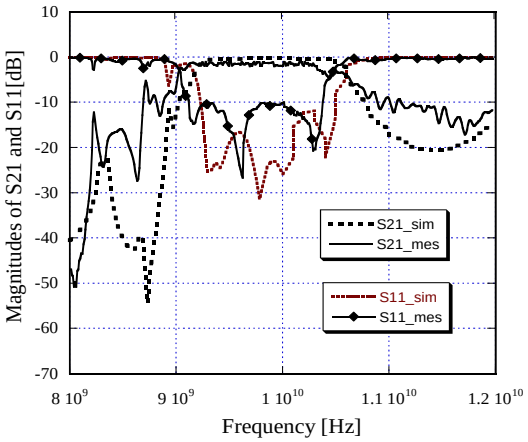

Fig. 6. Simulated and measured responses s-parameters of three finline wide bandpass filter.

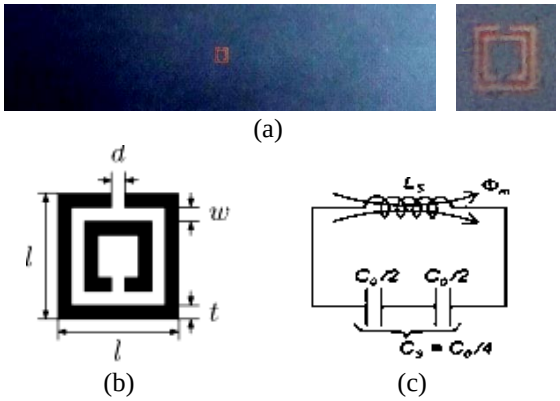

Fig. 7. (a) Photographic view of SRR fabricated on the back side of the substrate of three coupled finline wide bandpass filter and magnified view of this SRR besides this structure. (b) Copper SRR dimensions: l = 2.54 mm, t = 0.254 mm, w = 0.1252 mm, d = 0.254 mm, thickness = 0.038 mm and the conductivity = $5.8*10^7$ S/m. (c) Electrical equivalent circuit diagram of SRR.

Comparisons of measured and simulated S-parameters of asymmetric dual bandpass are shown in Fig. 8. We further simulated for different combinations of SRRs as shown in Table 2.

Table 2: Band width variations with number of SRRs

No of SRRs	Notch at Frequency
1 Cell	9.75 GHz
3 Cells	10.25 GHz
5 Cells	10.75 GHz
7 Cells	11.25 GHz
9 Cell	11.75 GHz

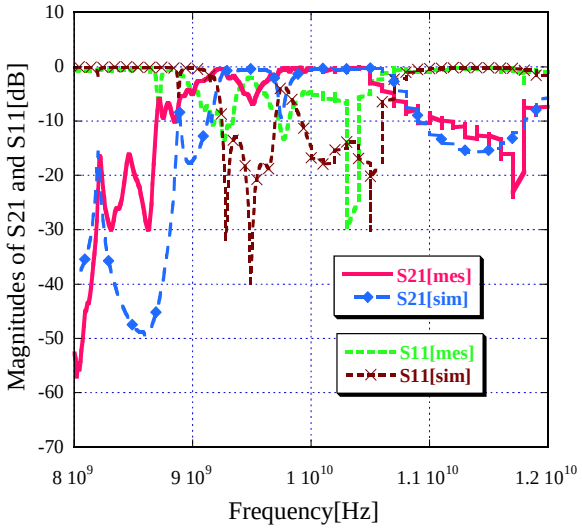

Fig. 8. Comparison plot of simulated and measured S-parameters of asymmetric dual bandpass filter.

V. CONCLUSION

This paper presents, asymmetric and symmetric dual bandpass filters that can be realized with these SRR in three coupled finline structure, to meet the transmission for particular frequency band which is possible for non-continuous channel. Modern communication transceivers require high performance microwave filters with low insertion loss, high frequency selectivity and small group delay variations. Most of the above said parameters will be obtained with these filters. Some of the most important advantages of these filters can be widely used in microwave and millimeter wave applications, exclusively in radar and satellite applications. These results have been compared with existing publications as shown in Table 3.

Table 3: Comparison with other proposed dual band-pass filters

Parameters	Ref. [17]	Ref. [18]	Ref. [13]	Proposed
Substrate	Roger 588 oLZ	Roger O3003	RT-Duriod	RT-Duriod
ε_r	1.96	3	10.2	2.2
1st and 2nd pass band frequencies [GHz]	4.1, 5.6	5.8, 8.7	0.9, 2.4	9.5, 10.3
Return loss S11 [dB]	<-15	<-22	<-15	<-15
Insertion loss S21 [dB]	<-0.1	<-2	<-2	<-0.5

REFERENCES

[1] V. G. Veselago, "The electrodynamics of substances with simultaneously negative values of permittivity and permeability," *Sov. Phys. USPEKHI*, vol. 10, p. 509, 1968.

[2] J. B. Pendry, A. J. Holden, D. J. Robbins, and W. J. Stewart, "Magnetism from conductors and enhanced nonlinear phenomena," *IEEE Trans. Microwave Theory Tech*., vol. 47, p. 2075, 1999.

[3] R. Marques, J. Martel, F. Mesa, and F. Medina, "Left handed–media simulation and transmission of EM waves in subwavelength split ring resonators-loaded metallic saveguides," *Physical Review Letters*, vol. 89, no. 18, Oct. 2002.

[4] R. W. Zoilkowski, "Design, fabrication, and testing of double negative metamaterials," *IEEE Trans. Antennas Propagate.*, vol. 51, no. 7, July 2003.

[5] B. Bhat and S. K. Koul, *Analysis, Design and Application of Finlines*. Artech House, 1987.

[6] P. J. Meier, "Integrated finline millimeter components," *IEEE Trans. Microwave Theory & Tech*., vol. MTT-22, no. 12, pp. 1209-1216, Dec. 1974.

[7] D. M. Syahkal and J. B. Davies, "An accurate, unified solution to various finline structures, of phase constant, characteristic impedance and attenuation," *IEEE Trans. Microwave Theory & Tech*., vol. MTT-30, no. 11, pp. 1854-1861, Nov. 1982.

[8] S. Luo, A. Biswas, and V. K. Tripathi, "Finline multiport couplers," *IEEE Trans. Microwave Theory & Tech*., vol. MTT-42, no. 12, pp. 2208-2215, Dec. 1994.

[9] A. Biswas and V. K. Tripathi, "Analysis and design of symmetric and multiple coupled finline couplers and filters," *in IEEE MTT-S Int. Microwave Symp. Dig*., pp. 403-406, 1990.

[10] J.-T. Kuo and E. Shih, "Wideband band-pass filter design with three line microstrip structures," *in IEEE MTT-S Int. Microwave Symp. Dig.*, pp. 1593-1596, 2001.

[11] D. M. Pozar, *Microwave Engineering*. John Wiley & Sons, Inc.

[12] T. Decoopman, A. Marteau, E. Lheurette, O. Vanbésien, and D. Lippens, "Left-handed electromagnetic properties of split-ring resonator and wire loaded transmission line in a fin-line technology," *IEEE Transactions on Microwave Theory and Techniques*, vol. 54, no. 4, Apr. 2006.

[13] G. Jang and S. Kahng, "Design of a dual-band metamaterial bandpass filters using Zeroth order resonance," *Progress In Electromagnetics Research C*, vol. 12, pp. 49-162, 2010.

[14] S. Chaimool and P. Akkaraekthalin, "Miniaturized wideband bandpass filter with wide stopband using metamaterial based resonator and defected ground structure," *Radio Engineering*, vol. 21, no. 2, June 2012.

[15] X. Q Lin, J. Y. Jin, Y. Jiang, and Y. Fan, "Metamaterial-inspired waveguide filters with compact size and sharp skirt selectivity," *Journal of Electromagnetic Waves and Applications*, vol. 27, no. 2, pp. 224-232, 2013.

[16] N. Benmostefa, M. Meliani, and H. Ouslimani, "Metamaterial tunable filter design," *Journal of Electromagnetic Analysis and Applications*, no. 5, pp. 250-254, June 2013.

[17] M. Duran Sindreu, J. Bonache, F. Martin, and T. Itoh, "Single–layer fully-planar extended-composite right-/left handed transmission lines based on substrate integrated waveguides for dual-band and quad- band applications," *International Journal of Microwave and Wireless Technologies*, vol. 3, no. 5, pp. 213-220, May 2013.

[18] A. Boubraki, F. Choubani, T. H. Vuong, and J. David, "A compact dual band band pass filter using a new topology of transmission line metamaterial," *PIERS Proceeding*, Guangzhou, China, Aug. 25-28, 2014.

An Experimental Study on Microwave Imaging of Breast Cancer with the use of Tumor Phantom

Mustafa B. Bicer and Ali Akdagli

Department of Electrical and Electronics Engineering
Mersin University, Mersin, 33343, Turkey
mbbicer@mersin.edu.tr, akdagli@mersin.edu.tr

Abstract ─ Nowadays, breast cancer is the most common type of the cancer among women's diseases. It is the leading cause of death after cardiovascular diseases. Due to risk of uncontrolled reproduction and propagation of the cancer cells, early diagnosis has a crucial importance. Microwave imaging (MWI) is an evolving method and has a variety of advantages such as operating at lower frequencies with a lower power, cost-effectiveness, and providing comfortable measurements without contact. In this paper, an experimental study on microwave imaging of breast cancer with the use of tumor phantom is presented. For this purpose, an experimental setup containing sand, screw and tumor phantom is prepared as replacement of real tissue. Two-dimensional inverse synthetic aperture radar (ISAR) method is used in handling the scattered electric field data from the measurement setup. Inverse radon transform (IRT) method is then utilized to extract the image of the measured scattering electric field data. The resultant images show that the microwave imaging method can be successfully used together with IRT for the breast cancer problem.

Index Terms ─ Breast cancer, breast phantom, imaging algorithm, microwave imaging, radar-based imaging.

I. INTRODUCTION

At present, cancer is the disease having the highest mortality rate after cardiovascular diseases and the breast cancer is the leading one among the female population. Early detection and diagnosis of the breast cancer is a key factor due to having 95% survival rate in its early stages. There are various primary modalities for breast cancer imaging and diagnosis such as x-ray mammography, magnetic resonance imaging (MRI) and ultrasound imaging (USI) [1,2]. However, there are significant disadvantages of these methods such as the use of x-rays and compression requirements of the breast for x-ray mammography; expensiveness and low specificity of MRI and the need of pressurizing the breast while applying USI. On the other hand, microwave imaging having advantages such as providing independent information about tumor tissue, having a wide application area, and high sensitivity and specificity is gaining a high interest by the researchers and pharmaceutical companies. The use of microwaves in breast cancer imaging is attracting researcher's attention and consequently many related studies are reported in the literature [2–20]. Microwave imaging (MWI) is a promising alternative to x-ray mammography since it has many advantages such as low-cost, using non-ionizing microwave, no need to compress the breast, portable fabrication and safety of using low power levels [3]. Microwave tomography and radar-based microwave imaging are two main methods that illuminate the breast with signals in microwave band and measure the backscattered or transmitted signals. The radar-based MWI (RBMWI) is especially widely researched method that provides simple and powerful image reconstruction algorithms [11–24]. The microwave signals scatter from each different dielectric interface because of the contrast in the dielectric constants and the scattered signals contain physical information such as size and distance of the scattering object. RBMWI technique uses the difference of permittivities between healthy and malignant tissues over the microwave frequency range to reconstruct the breast image map from scattering signals [2–20]. In the literature, there are several theoretical and experimental studies on radar-based imaging methods such as confocal microwave imaging [7,11], statistical microwave imaging [8], multistatic adaptive microwave imaging [9], field mapping algorithm [10], dynamic microwave imaging [17], hybrid reconstruction [18], multistatic delay-and-sum [19], microwave imaging with stochastic optimization [20]. In [22], a compact bowtie antenna with cavity operating in the range between 2 – 4 GHz is designed for microwave breast cancer imaging and two-dimensional tumor scattering map was obtained. Fear *et al*. [11] used the method of confocal microwave imaging with the help of data acquired from the numerically modelled breast, and the breast tumor of 6 mm in size was imaged in three-dimensional while Li *et al*. [7] imaged the tumor of 4 mm in size in two-dimensional. In [13], experimental studies were carried out with the use of coupling liquid to

Submitted On: April 12, 2017
Accepted On: September 10, 2017

1054-4887 © ACES

provide the matching between the breast skin and the antenna array. References [8] and [10] present the methods of statistical microwave imaging and field mapping algorithm to obtain the two-dimensional screening map with several experimental results, respectively. In order to exploit the advantages of array of antennas, a monopole antenna array of 16-elements in the liquid coupling with the breast skin was proposed in [14]. Although there are many methods given above for imaging, they have been used with their own benefits and limitations but none of them fulfill all of the requirements. Therefore, microwave imaging methods based on theoretical, experimental and also simulation have been continuously developed by using the antenna systems including monostatic, bi-static and array configurations. The theoretical and simulation approaches are numerically handled by ignoring the effects of physical conditions such as noise, multipath effects, antenna and cable losses and intrinsic errors. Suggestion of liquid usage for coupling between the breast and the antenna results in uncomfortable measurement for the patient. Antenna arrays provide fast data acquirement at the expense of system complexity.

In this work, microwave imaging for breast cancer detection is carried out experimentally by using the monostatic antenna without coupling liquid. The reconstruction method of inverse radon transform (IRT) [25] is merged with the inverse synthetic aperture radar (ISAR) [26] principle without introducing the antenna array. IRT, as an imaging method, is simple and easy to use and implement. With the use of ISAR principle, an individual antenna acts as if it were an array of antennas. In this work, to take advantages of both IRT and ISAR, electrical field scattering data from the phantom were experimentally acquired by ISAR and the resultant image including the representative tumors was successfully reconstructed with IRT method.

The paper is organized as follows: at first, fundamentals of monostatic ISAR principle are explained. The reconstructed images are then given for four different scenarios in the section of experimental results. In conclusion section, the achieved results are briefly described.

II. INVERSE SYNTHETIC APERTURE RADAR (ISAR) PRINCIPLE

According to the monostatic ISAR principle, the phantom is illuminated with electromagnetic waves and rotated on its axis in such a way that it is concentric with the illuminating antenna. The reflected electromagnetic waves are measured with an antenna [26]. Principle of two dimensional monostatic ISAR imaging is shown in Fig. 1.

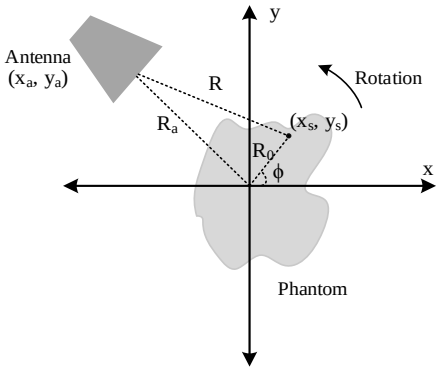

Fig. 1. Two dimensional monostatic ISAR imaging principle.

The scattering field vector in frequency domain $E_s[f,\phi]$ is calculated as [26]:

$$E_s[f,\phi] = A_0 e^{-j\left(\frac{4\pi f}{v}\right)R(\phi)}, \quad (1)$$

where f, A_0, R and ϕ terms represent a frequency vector, the amplitude of the electric field, the Euclidean distance between the antenna and the phantom and the cylindrical angle, respectively. The phase velocity of the wave in the medium $v = \frac{c}{\sqrt{\varepsilon_r}}$ and ε_r denotes the dielectric constant of the medium. The Euclidean distances are calculated as in [26]:

$$R = \sqrt{\left(\left|x_a - R_0\cos(\phi)\right|\right)^2 + \left(\left|y_a - R_0\sin(\phi)\right|\right)^2}, \quad (2)$$

while R_0 denote the tumor distance relative to the origin of the breast, (x_a, y_a) represents the position of the antenna. For the sake of simplicity, the whole experimental setup is assumed to be homogeneous and the phantom consists of discrete points. The values of the parameters are given in Table 1 and the experimental setup is illustrated in Fig. 2.

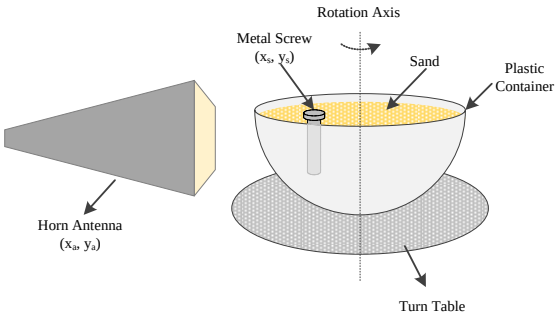

Fig. 2. Measurement setup.

Table 1: Values for measurement parameters

Parameter	Value			
Power (mW)	1			
Start frequency (GHz)	2			
Stop frequency (GHz)	8			
Frequency count	601			
Foam container radius (cm)	7			
Antenna distance (cm)	12			
Rotation angle increment (degree)	1			
Screw dimension (cm x cm)*	1 x 5			
	Locations (r, ϕ) for Scenarios			
	#1	#2	#3	#4
Screw	(0,0°)	(4,180°)	(5,190°)	–
Phantom	–	–	–	(3,170°)

**Screw dimension (Diameter x Width)*

The antenna is located R_a distance from the center of the foam container. The container is rotated around the z-axis and at each angle, the scattered field from each discrete point of the phantom is summed according to:

$$E_{total}(r,\phi)=\int_0^{2\pi}\int_0^{R} A_0 e^{-j\left(\frac{4\pi f}{v}\right)r}\,dr d\phi, \qquad (3)$$

where ϕ and r represent the angle difference between the actual and the range between the antenna and the scattering object, respectively. The electric field matrix obtained with the use of Eq. (3) contains information about the skin and tumor points. When the measured data are analyzed, it is understood that there are strong radiations from the tumor tissue(s) and skin. In addition, background subtraction was applied to highlight the effect of the radiations. Background subtraction is defined as:

$$E=E_{total}-E_{calibration}, \qquad (4)$$

where $E_{calibration}$ represents the electric field data in the stage of only sand filled container. Then, the size of data is increased by applying zero-padding method so as to obtain the better quality for images, as follows:

$$E(r,\phi)=\begin{cases} E(r,\phi), & r=0,...,N-1 \\ 0, & r=N,...,M-1 \end{cases}, \qquad (5)$$

where N and M represent the lengths of the measured electric field data and the target data, respectively. The resultant data is filtered by using Binomial filter. The coefficients of the Binomial filter are calculated by:

$$h=\sum_{j=1}^{J}(h*cc), \qquad (6)$$

where h, J and cc denote filter coefficients of the filter, limit of the iteration and a constant coefficient, respectively. In this study, cc is selected as [0.5 0.5] and the initial value of the h is selected as same as cc while J is set to 571. The IRT method is then utilized on the resultant data to reconstruct the resultant image [25]. The pixel value of image G using inverse radon transform is defined as,

$$G(x,y)=\int_0^{2\pi} E(x\cos(\phi)+y\sin(\phi),\phi)d\phi, \qquad (7)$$

where x and y define the location of the image and ϕ is the cylindrical angle aforementioned in Eq. (2). E in Eq. (7) is an array consist of electric field data depending on frequency values in start and stop frequencies accordingly. Since the measurement setup is based on the monostatic imaging, the upper limit of ϕ is 2π rather than π. The flowchart summarizing the applied procedures carried out in this work is given in Fig. 3.

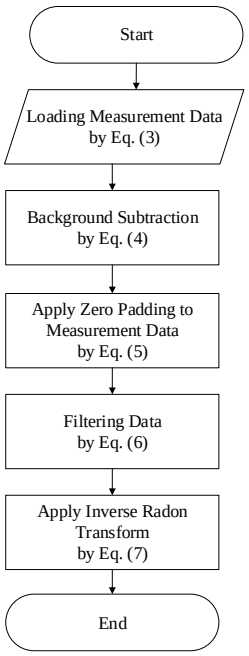

Fig. 3. Flowchart of the microwave imaging procedure used in this work.

III. EXPERIMENTAL RESULTS

In this study, breast tumor tissue phantom proposed by Ortega-Palacios *et al*. [27] is formed to be used in measurements for microwave imaging. For measurements, the phantom is placed in a container filled with sand. Results of the measured permittivity for the sand and phantom from 2 to 8 GHz frequency range are given in Fig. 4.

In medical applications, biological tissues show lossy medium properties because of their conductivity. With the rise of frequency, the penetration depth of the electromagnetic wave begins to decrease. For this reason, the optimal frequency range should be chosen so that the waveguide can penetrate to achieve an optimal imaging. The UWB band is acceptable to ensure optimal imaging.

It can be seen from the Fig. 4 that the permittivity of sand is remained constant at almost 2 while the permittivity of the tumor phantom is decreasing monotonously from 70 to 59 in the range of 2 to 8 GHz. The dielectric constant values of the tumor and healthy breast tissue are given in Table 2. These values are computed by using the 4-Cole-Cole Model [28].

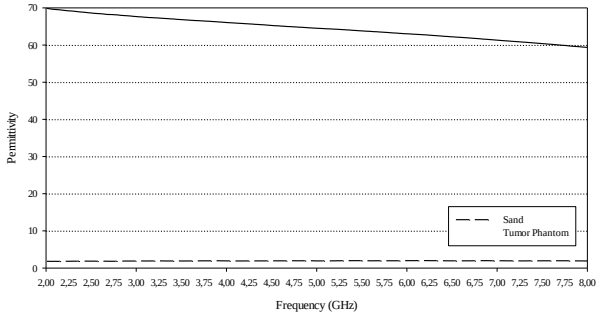

Fig. 4. Measured permittivity data of the sand (dashed) and the tumor (solid) phantom.

Table 2: Computed dielectric constant values of real human tissues at different frequencies [26]

Tissue	Frequencies for Dielectric Constants (ε)		
	2 GHz	4 GHz	6 GHz
Breast Fat	5.232	4.839	4.462
Skin (Dry)	38.567	36.587	34.945
Skin (Wet)	43.520	40.847	38.377

In this study, the effect of skin is disregarded. As it can be seen from the Fig. 4 and Table 2, the dielectric constant value of the sand and real breast tissue is close enough, thus, sand is eligible to use in the measurement setup. Microwave imaging is based on the contrast difference between the dielectric constant value of healthy and tumor tissues. The constant difference between sand and tumor phantom is appropriate. The frequency domain measurements are performed by the help of Agilent ENA E5071B Series RF Network Analyzer at the anechoic chamber, a double-ridged horn antenna and a turntable for rotation. The return loss data of 601 frequency points from 2 GHz to 8 GHz are acquired by using the double-ridged horn antenna. The gain values of the antenna are specified as 5 dBi, 13 dBi, 15 dBi, and 16 dBi for 2 GHz, 4 GHz, 6 GHz, and 8 GHz frequencies, respectively. The use of the double-ridged horn antenna eliminates the disadvantages such as low gain and omnidirectional radiation pattern of the microstrip antennas. A foam container filled with sand is placed on a plate of a computer-controlled turntable that rotates with a precision of 1 degree. The double ridged horn antenna, operating at 2 – 26 GHz frequency band, is placed 12 cm away from the container. For the scenarios #1 – 3, a metallic screw is placed in the sand at different positions. Then, a malignant tumor phantom is placed at 3 cm away from the center of the container for scenario #4. Before beginning the scenario-related measurements, sand only filled container without screw or phantom is measured. The measurement was used in the calibration process by background subtraction method to remove ambient effects. Background subtraction process is performed by subtracting the data acquired from screwless scenario from other scenarios. After the calibration, one screw is positioned at different locations in the sand filled foam container for the next three scenarios as shown in Fig. 5.

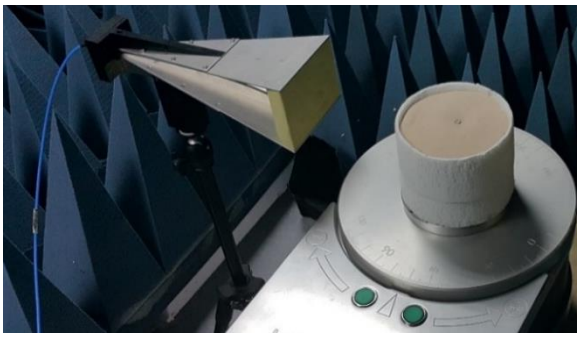

Fig. 5. Screw in sand filled foam container on the turntable.

Figure 6 (a) shows the sand filled foam container without screw or tumor phantom. The blue circle refers to the foam container. The return loss data is measured in the frequency domain. For image generation, the resultant data obtained by applying Inverse Fast Fourier Transform (IFFT) to the measured ones is used. Physical circumstances such as losses related to multiple reflections inside the foam container and the interactions between antenna and the container, and the conditions depending on filtering and other preprocessing procedures applied to can be considered as the reason for the artifacts. Some of the mentioned artifact sources can be eliminated with background subtraction procedure.

Figure 6 (b) shows the image of the screw placed in the origin of the foam container obtained after the background subtraction procedure. As it is seen from Fig. 6 (c) and Fig. 6 (d), when the screw was moved towards the edge of the container, distortions occurred in the obtained image. A sharper image could be obtained by lowering the value of the dynamic range based on logarithmic scaling, but in this study, the dynamic range is taken large enough to show possible artifacts. In addition, the larger value of the dynamic range causes the smaller objects to appear larger than their actual size. Therefore, the dynamic range value should be selected optimally. By decreasing the dynamic range value, the detection and imaging of the object can be simplified and artifacts with low amplitudes can be eliminated. Also,

postprocessing methods can be applied to remove the artifacts from the obtained image. It is assumed that the region with the highest peak value of the amplitudes is related to the scatterer. Therefore, the calculated positions are chosen to be the point at which the highest peak value is found. The more precise detection of the location can be performed by reducing the dynamic range value.

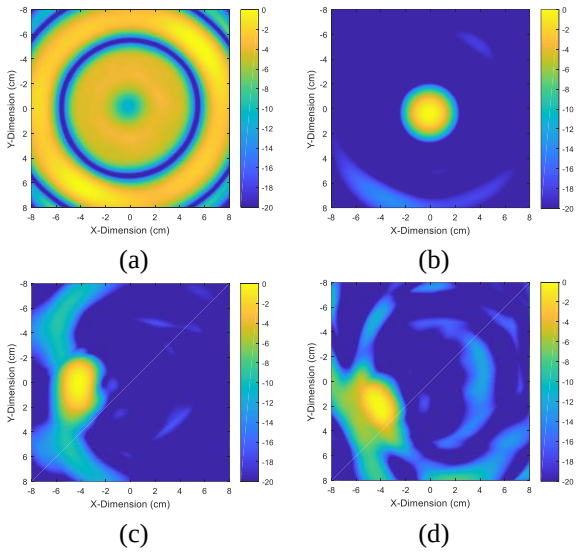

Fig. 6. (a) Sand filled foam container without screw or phantom, (b) screw positioned in the center of the foam container, (c) screw positioned 4 cm, and (d) 5 cm away from the center of the foam container.

In next scenarios, a screw is placed in various positions in the sand. As seen in Fig. 6 (b), screw is located in the center of the foam container. Then, screw is placed 4 and 5 cm away from the center, respectively, as seen from Fig. 6 (c) and Fig. 6 (d). When the screw is moved away from the center of the container, the screw resembles an ellipse-like shape. The maximum peaks are calculated as placed 4.15 cm and 4.63 cm away from the center for scenario 2 and scenario 3, respectively. Finally, the 2-cm diameter of tumor phantom is placed at the distance of 3 cm from the center of the sand filled foam container. The generated image with the use of IRT method is given in Fig. 7. The position of the tumor phantom is calculated as 3.31 cm away from the center using the Fig. 7.

Since the phantom lost water during the measurement, only one measurement could be made. The numerical results for the physical and calculated positions from the generated image are given in Table 3.

According to Table 3, the screw positions in the sand filled foam container for three scenarios are, respectively, calculated as 0.42 cm, 0.15 cm and 0.36 cm away from the initial screw positions and the phantom position is 0.31 cm different from the actual position. These deviations in approximately calculated positions on the resultant image are within acceptable ranges. The noises and position deviations shown in Fig. 6 and Fig. 7 are due to algorithm-dependent parameters, water loss of the tumor phantom during the measurement, crosstalk of the antenna, and reflections from the gap between the antenna and the container.

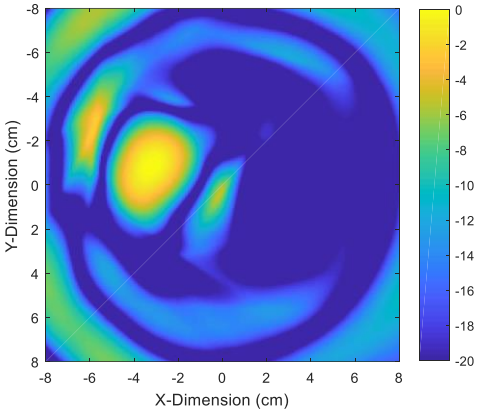

Fig. 7. Phantom positioned 3 cm away from the center of the foam container.

Table 3: The initial positions and calculated positions from the generated image

	Physical Position (r, ϕ)	Calculated Position (r, ϕ)
Screw	(0 cm, 0˚)	(0.42 cm, 0˚)
	(4 cm, 180˚)	(4.15 cm, 184˚)
	(5 cm, 205˚)	(4.63 cm, 208˚)
Tumor Phantom	(3 cm, 175˚)	(3.31 cm, 173˚)

IV. CONCLUSION

In this study, the method of IRT was utilized to reconstruct the image of the emulated breast with a malignant tumor by using the data acquired by ISAR principle. The experimental studies were carried out with four scenarios containing screw and tumor phantom at different locations. Sand and a screw were chosen in the first three scenarios because of having highly contrasted permittivity values. In the last scenario, a realistic tumor phantom was created and placed in the sand. For all scenarios, the container was illuminated by electromagnetic waves from various angles by rotating the container with turntable. Experimental measurements were taken with the use of network analyzer in frequency domain. By increasing the sample points, the image with higher resolution relatively can be reconstructed at the expense of much more elapsed measurement and processing time. The IRT algorithm was utilized to generate the radar-based microwave image of the experimental setup for the four scenarios. The resultant

images were obtained with a success and the IRT algorithm showed a good performance on breast cancer imaging with microwaves.

ACKNOWLEDGMENT

This study was supported by the Research Fund of Mersin University in Turkey with Project Number: 2017-1-TP3-2190. The authors are thankful to the Electrical and Electronics Engineering of Iskenderun Technical University for their help in the dielectric constant measurement of the tumor phantom.

REFERENCES

[1] M. Patlak, S. J. Nass, I. C. Henderson, and J. C. Lashof, Mammography and Beyond: Developing Technologies for the Early Detection of Breast Cancer, Washington, DC: National Academy Press, 2001.

[2] M. B. Bicer, A. Akdagli, and C. Ozdemir, "Breast cancer detection using inverse radon transform with microwave image technique," *23th Signal Processing and Communications Applications Conference (SIU)*, Malatya, TR, pp. 2182-2185, 2015.

[3] E. C. Fear, P. M. Meaney, and M. A. Stuchly, "Microwaves for breast cancer detection?," *IEEE Potentials*, vol. 22, no. 1, pp. 12, 2003.

[4] D. J. Kurrant, E. C. Fear, and D. T. Westwick, "Tumor response estimation in radar-based microwave breast cancer detection," *IEEE Transactions on Biomedical Engineering*, vol. 55, no. 12, pp. 2801-2811, 2008.

[5] S. K. Davis, B. D. Van Veen, S. C. Hagness, and F. Kelcz, "Breast tumor characterization based on ultrawideband microwave backscatter," *IEEE Trans. Biomed. Eng.*, vol. 55, no. 1, pp. 237-246, 2008.

[6] Y. Chen and P. Kosmas, "Detection and localization of tissue malignancy using contrast-enhanced microwave imaging: Exploring information theoretic criteria," *IEEE Trans. Biomed. Eng.*, vol. 59, no. 3, pp. 766-776, 2012.

[7] X. Li, E. J. Bond, B. D. Van Veen, and S. C. Hagness, "An overview of ultra-wideband microwave imaging via space-time beamforming for early-stage breast-cancer detection," *IEEE Antennas Propag. Mag.*, vol. 47, no. 1, pp. 19-34, 2005.

[8] S. K. Davis, H. Tandradinata, S. C. Hagness, and B. D. Van Veen, "Ultrawideband microwave breast cancer detection: A detection-theoretic approach using the generalized likelihood ratio test," *IEEE Trans. Biomed. Eng.*, vol. 52, no. 7, pp. 1237-1250, 2005.

[9] Y. Xie, B. Guo, L. Xu, J. Li, and P. Stoica, "Multistatic adaptive microwave imaging for early breast cancer detection," *IEEE Trans. Biomed. Eng.*, vol. 53, no. 8, pp. 1647-1657, 2006.

[10] G. Cheng, Y. Zhu, and J. Grzesik, "3-D microwave imaging for breast cancer," *6th European Conference on Antennas and Propagation (EUCAP)*, Prague, pp. 3672-3676, 2011.

[11] E. C. Fear, X. Li, S. C. Hagness, and M. A. Stuchly, "Confocal microwave imaging for breast cancer detection: Localization of tumors in three dimensions," *IEEE Trans. Biomed. Eng.*, vol. 49, no. 8, pp. 812-822, 2002.

[12] E. J. Bond, X. Li, S. C. Hagness, and B. D. Van Veen, "Microwave imaging via space-time beamforming for early detection of breast cancer," *IEEE Transactions on Antennas and Propagation*, vol. 51, no. 8, pp. 1690-1705, 2003.

[13] M. Klemm, I. Craddock, J. Leendertz, A. Preece, and R. Benjamin, "Experimental and clinical results of breast cancer detection using UWB microwave radar," *IEEE Antennas and Propagation Society International Symposium*, no. 1, pp. 1-4, 2008.

[14] P. M. Meaney, M. W. Fanning, T. Zhou, A. Golnabi, S. D. Geimer, and K. D. Paulsen, "Clinical microwave breast imaging - 2D results and the evolution to 3D," *Proceedings of the 2009 International Conference on Electromagnetics in Advanced Applications*, ICEAA'09, pp. 881-884, 2009.

[15] N. Irishina, M. Moscoso, and O. Dorn, "Microwave imaging for early breast cancer detection using a shape-based strategy," *IEEE Trans. Biomed. Eng.*, vol. 56, no. 4, pp. 1143-1153, 2009.

[16] H. B. Lim, N. T. T. Nhung, E.-P. Li, and N. D. Thang, "Confocal microwave imaging for breast cancer detection: Delay-multiply-and-sum image reconstruction algorithm," *IEEE Transactions on Biomedical Engineering*, vol. 55, no. 6. pp. 1697-1704, 2008.

[17] M. Klemm, I. J. Craddock, and A. Preece, "Contrast-enhanced breast cancer detection using dynamic microwave imaging," *Proceedings of the 2012 IEEE International Symposium on Antennas and Propagation*, pp. 1-2, 2012.

[18] M. Pastorino, "Hybrid reconstruction techniques for microwave imaging systems," *2010 IEEE International Conference on Imaging Systems and Techniques*, pp. 198-203, 2010.

[19] I. Ünal, B. Türetken, and Y. Çotur, "Microwave imaging of breast cancer tumor inside voxel-based breast phantom using conformal antennas," *31st URSI General Assembly and Scientific Symposium*, pp. 1-4, 2014.

[20] A. Jeremic and E. Khoshrowshahli, "Detecting breast cancer using microwave imaging and stochastic optimization," *Engineering in Medicine and Biology Society (EMBC), 2015 37th Annual International Conference of the IEEE*, pp. 89-92,

2015.
[21] R. Benjamin, I. J. Craddock, G. S. Hilton, S. Litobarski, E. McCutheon, R. Nilavalan, and G. N. Crisp, "Microwave detection of buried mines using non-contact, synthetic near-field focusing," *Radar, Sonar Navig. IEE Proc.*, vol. 148, no. 4, pp. 233-240, 2001.
[22] X. Yun, E. C. Fear, and R. H. Johnston, "Compact antenna for radar-based breast cancer detection," *IEEE Trans. Antennas Propag.*, vol. 53, no. 8, pp. 2374-2380, 2005.
[23] A. K. Alqallaf, R. K. Dib, and S. F. Mahmoud, "Microwave imaging using synthetic radar scheme processing for the detection of breast tumors," *The Applied Computational Electromagnetics Society Journal (ACES Journal)*, vol. 31, no. 2, pp. 98-105, 2016.
[24] İ. Ünal, B. Türetken, and C. Canbay, "Spherical conformal bow-tie antenna for ultra-wide band microwave imaging of breast cancer tumor," *The Applied Computational Electromagnetics Society Journal (ACES Journal)*, vol. 29, no. 2, pp. 124-133, 2014.
[25] W. M. Boerner, C. M. Ho, and B. Y. Foo, "Use of Radon's projection theory in electromagnetic inverse scattering," *IEEE Trans. Antennas Propag.*, vol. 29, no. 2, pp. 336-341, 1981.
[26] C. Ozdemir, *Inverse Synthetic Aperture Radar Imaging*. NJ: Wiley & Sons, Inc., 2012.
[27] R. Ortega-Palacios, L. Leija, A. Vera, and M. F. J. Cepeda, "Measurement of breast - Tumor phantom dielectric properties for microwave breast cancer treatment evaluation," *Program and Abstract Book - 2010 7th International Conference on Electrical Engineering, Computing Science and Automatic Control*, pp. 216-219, 2010.
[28] C. Gabriel, *Compilation of the Dielectric Properties of Body Tissues at RF and Microwave Frequencies.* U.S. Air Force Report, 1996.

Mustafa Berkan Bicer was born in 1988. In 2009, he received B.S. degree in Electrical and Electronics Engineering from Firat Universiy, Turkey. In 2012, he received M.S. degree in Electrical and Electronics Engineering from Mersin University, Turkey. He has been working as Research Engineer at Electrical and Electronics Engineering Department of Mersin University since 2009. He has been studying towards the Ph.D. degree at the same department. His current research interests include microwave imaging, antennas, microstrip antennas, computational electromagnetic, artificial intelligent and applications of optimization algorithms to electromagnetic problem such as radiation, resonance and bandwidth.

Ali Akdagli obtained the B.S., M.S. and Ph.D. degrees from Erciyes University, Kayseri, in 1995, 1997 and 2002 respectively, all in Electronic Engineering. From 2003 to 2006 he was an Assistant Professor in the Electronic Engineering Department at Erciyes University. He joined the same department at Mersin University, where he currently works as an Associate Professor. He has published more than 100 papers in journals and conference proceedings. His current research interests include evolutionary optimization techniques (genetic algorithm, ant colony optimization, differential evolution, particle swarm optimization, and artificial bee colony algorithms), artificial neural networks and their applications to electromagnetic, microwave circuits, microstrip antennas and antenna pattern synthesis problems.

The Optimal Design of Real Time Control Precision of Planar Motor

Guangdou Liu [1], Yanzhe Wang [1], Xingping Xu [1], Wuyi Ming [2], and Xin Zhang [1]

[1] College of Mechanical and Electronic Engineering
China University of Petroleum, Qingdao 266580, China
gdliu@upc.edu.cn, shidajizi212@ 163.com, xuxp@upc.edu.cn, zxin0927@163.com

[2] Department of Electromechanical Science and Engineering
Zhengzhou University of Light Industry, Zhengzhou, 450002, China
mingwuyi81@gmail.com

Abstract ─ In this paper, the Halbach permanent magnet array with 2 segments per pole is selected for analysis. The harmonics that the harmonic numbers for the ^{l}x- and ^{l}y-direction in local coordinate system are equal to each other are set as a pair for transformation. Then the expressions of the magnetic flux density distribution of the Halbach array in global coordinate system are derived. The dimensions of the coil are parameterized. The force and torque exerted on the Halbach array by a coil are calculated by Lorentz force law. The first three harmonics are chosen for real time control by analyzing the ratio of each harmonic in the total harmonics. The harmonic model has good performance on torque by comparing with the models used before. As for the force, the errors can be significantly reduced by optimizing the parameterized dimensions of coil because of the cosine or sine form error figures. The optimized model has good precision on both force and torque. The same method can be applied on the Halbach permanent magnet array with different segments per pole.

Index Terms ─ Force ripple, genetic algorithm, Halbach array, harmonic model, planar motor.

I. INTRODUCTION

The planar motor has an advantage in that the motor occupies a small area and the system can be compact in contrast to systems using two linear motors, and the planar motor is gradually applied in pick-and-place machines, lithography and inspection systems and objects which are positioned and moved in a horizontal plane [1-10]. In the planar motors, the synchronous permanent magnet planar motors with Halbach array are discussed in this paper. This type of planar motor has the advantages such as large motion, high response speed and high position precision.

Compter [6] described an electro-dynamic planar motor with moving coils and Halbach permanent array. The coils are positioned 45° relative to the Halbach permanent magnet array in this proposed planar motor. Then the arrangement of coils and Halbach array is used in the force and torque calculation. There are three models of Halbach array as follows, surface charge model, harmonic model and analytical model used in [7,8] by Jansen. To satisfy the real time control, the analytical model is applied to calculate the force and torque. There are three models of coil are presented in [7, 9]. For the calculation accuracy of the force and torque, the coil model with filaments is not taken into account. Jansen *et al*. [7] obtained the force and torque by Lorentz force law with the analytical model and coil model with surfaces. Peng *et al*. [9] calculated by the composite numerical integration and the Newton-Leibniz formula with the analytical model and coil model with surfaces and corners.

In this paper, to obtain high accuracy of force and torque exerted on the Halbach array by coil in the real time control, the harmonic model and coil model with volumes are introduced to the force and torque calculation. The coil model with volumes is optimized by Matlab with genetic algorithm toolbox [11]. The high accuracy of force and torque can be obtained when the force and torque expressions are associated with the different dimensions of coil model with volumes.

The Halbach array with 2 segments per pole shown in Fig. 1 is used in this paper. The force and torque expressions can be also applied in the Halbach array with different segments per pole, such as the Halbach array with 4 segments per pole proposed by Min *et al*. [10].

II. MODELING OF THE HALBACH ARRAY AND COIL

A. Magnetic flux density distribution in global coordinate system

Figure 1 shows the front and top view of the Halbach array with 2 segments per pole and a rectangular coil in global coordinate system. The planar motor

Submitted On: June 5, 2017
Accepted On: August 12, 2017

1054-4887 © ACES

system is simplified by leaving out other appurtenance except for the Halbach array and a rectangular coil. The local and global coordinate systems shown in Fig. 1 are located at the center of the Halbach array. The local coordinate system is denoted with superscript ^{l} and rotates 45° clockwise about the ^{l}z-axes to get the global coordinate system. The arrows mean the magnetization direction of magnets from *s*-pole to *n*-pole, in which *N* shows the direction outward the paper and *S* toward the paper.

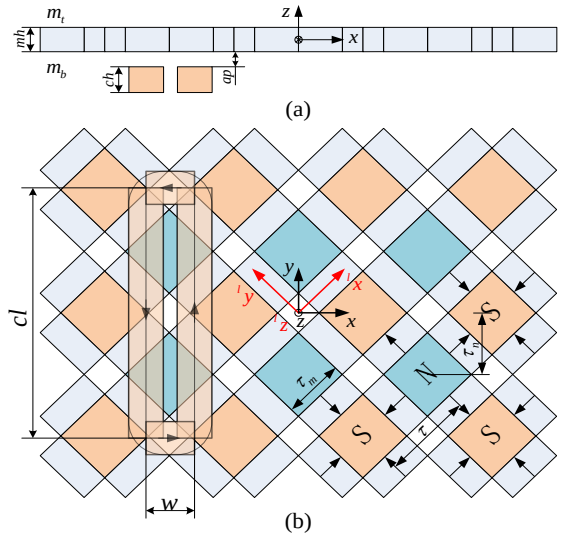

Fig. 1. The Halbach array and a rectangular coil in global coordinate system: (a) front view and (b) top view.

The expressions of the magnetic flux density distribution of the Halbach array for calculation in the local coordinate system are given by [7]:

$$ {}^{l}\vec{B} = -\sum_{m=1}^{\infty}\sum_{n=1}^{\infty} A \begin{bmatrix} m\omega\cos\left(m\omega\,{}^{l}x\right)\sin\left(n\omega\,{}^{l}y\right) \\ n\omega\sin\left(m\omega\,{}^{l}x\right)\cos\left(n\omega\,{}^{l}y\right) \\ \lambda\sin\left(m\omega\,{}^{l}x\right)\sin\left(n\omega\,{}^{l}y\right) \end{bmatrix}, \quad (1) $$

where *m* and *n* are the harmonic numbers for the ^{l}x- and ^{l}y-direction, respectively, μ_0 is the permeability, and,

$$ A = \mu_0 K_3 e^{\lambda z}, \quad (2) $$

$$ \omega = \pi/\tau, \quad (3) $$

$$ a(m) = \frac{4}{m\pi}\cos\frac{m\omega\tau_m}{2}\sin\frac{m\pi}{2}, \quad (4) $$

$$ b(m) = \frac{4}{m\pi}\sin\frac{m\omega\tau_m}{2}\sin\frac{m\pi}{2}, \quad (5) $$

$$ \lambda = \omega\sqrt{m^2+n^2}, \quad (6) $$

$$ K_3(\mu_r=1) = \frac{B_r}{2\lambda^2\mu_0}\left(e^{-m_t\lambda}-e^{-m_b\lambda}\right)\times \left(b(m)b(n)\lambda + a(m)b(n)m\omega + a(n)b(m)n\omega\right), \quad (7) $$

where τ is the pole pitch, τ_m is the length of the side of the magnets which are magnetized in ^{l}z-direction, μ_r is the relative permeability, B_r is the residual magnetization of the permanent magnet, m_t and m_b are the upper and bottom boundaries of the Halbach array, respectively.

For the expressions derived by Fourier series of magnetic flux density distribution of the Halbach array with different segments per pole, only the amplitude constant K_3 is different according the reference [15], so are the force and torque expressions derived by the magnetic flux density distribution.

The $a(m)$ and $b(m)$ are equal to zero when the *m* is even, the items only remain when *m* is an odd number. The harmonics which the harmonic numbers for the ^{l}x- and ^{l}y-direction in local coordinate system are equal to each other are set as a pair for transformation, and divided into two parts, such as m=n and m=1, n=3 (m=3, n=1). The expressions of magnetic flux density distribution of the Halbach array in the global coordinate system results in:

$$ B_x = -\frac{1}{2}\sum_{m=n=1}^{\infty} A\omega_1\sin(\omega_1 x) - \sum_{m=1}^{m<n}\sum_{n=3}^{\infty} A\sum_{i=1}^{2}(-1)^{i-1}\omega_i\sin(\omega_i x)\cos(\omega_{3-i}y), \quad (8) $$

$$ B_y = \frac{1}{2}\sum_{m=n=1}^{\infty} A\omega_1\sin(\omega_1 y) + \sum_{m=1}^{m<n}\sum_{n=3}^{\infty} A\sum_{i=1}^{2}(-1)^{i-1}\omega_i\sin(\omega_{3-i}x)\cos(\omega_3 y), \quad (9) $$

$$ B_z = \frac{1}{2}\sum_{m=n=1}^{\infty} A\lambda\left(\cos(\omega_1 x)-\cos(\omega_1 y)\right) + \sum_{m=1}^{m<n}\sum_{n=3}^{\infty} A\lambda\sum_{i=1}^{2}(-1)^{i-1}\cos(\omega_i x)\cos(\omega_{3-i}y), \quad (10) $$

where

$$ \omega_1 = \omega(m+n)/\sqrt{2}, \quad (11) $$

$$ \omega_2 = \omega(m-n)/\sqrt{2}. \quad (12) $$

B. Parameterized coil model

Figure 2 shows the coil models with volumes and the parameterized dimensions definition. There are four straight segments in coil model with volumes.

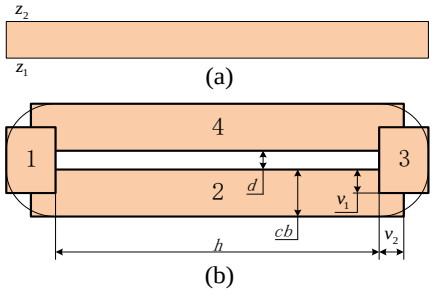

Fig. 2. The parameterized dimensions of coil with volumes: (a) front view and (b) top view.

The variables v_1 and v_2 are introduced for denoting the straight segments of coil. So the dimensions of the straight segments of the coil are not constant and can be variable for the force and torque optimization.

III. CALCULATION OF FORCE AND TORQUE

The Lorentz force and torque volume integral is applied in the force and torque calculation. The current is constant in each straight segment. The integral for the force and torque exerted on the Halbach array by one coil are equal to [14]:

$$\begin{aligned}\vec{F} &= -\int_{Vcoil} \vec{j}\times\vec{B}dV = \\ &-\int_{z_1}^{z_2}\int_{y_c-y_2}^{y_c-y_3}\int_{x_c-x_1}^{x_c+x_1}\begin{bmatrix} j & 0 & 0\end{bmatrix}^{\mathrm{T}}\times\vec{B}dxdydz \\ &-\int_{z_1}^{z_2}\int_{y_c-y_1}^{y_c+y_1}\int_{x_c+x_3}^{x_c+x_2}\begin{bmatrix} 0 & j & 0\end{bmatrix}^{\mathrm{T}}\times\vec{B}dxdydz \\ &-\int_{z_1}^{z_2}\int_{y_c+y_3}^{y_c+y_2}\int_{x_c-x_1}^{x_c+x_1}\begin{bmatrix} -j & 0 & 0\end{bmatrix}^{\mathrm{T}}\times\vec{B}dxdydz \\ &-\int_{z_1}^{z_2}\int_{y_c-y_1}^{y_c+y_1}\int_{x_c-x_2}^{x_c-x_3}\begin{bmatrix} 0 & -j & 0\end{bmatrix}^{\mathrm{T}}\times\vec{B}dxdydz\end{aligned} \quad (13)$$

$$\begin{aligned}\vec{T} &= -\int_{Vcoil} \vec{x}\times\left(\vec{j}\times\vec{B}\right)dV = \\ &-\int_{z_1}^{z_2}\int_{y_c-y_2}^{y_c-y_3}\int_{x_c-x_1}^{x_c+x_1}\vec{x}\times\left(\begin{bmatrix} j & 0 & 0\end{bmatrix}^{\mathrm{T}}\times\vec{B}\right)dxdydz \\ &-\int_{z_1}^{z_2}\int_{y_c-y_1}^{y_c+y_1}\int_{x_c+x_3}^{x_c+x_2}\vec{x}\times\left(\begin{bmatrix} 0 & j & 0\end{bmatrix}^{\mathrm{T}}\times\vec{B}\right)dxdydz \\ &-\int_{z_1}^{z_2}\int_{y_c+y_3}^{y_c+y_2}\int_{x_c-x_1}^{x_c+x_1}\vec{x}\times\left(\begin{bmatrix} -j & 0 & 0\end{bmatrix}^{\mathrm{T}}\times\vec{B}\right)dxdydz \\ &-\int_{z_1}^{z_2}\int_{y_c-y_1}^{y_c+y_1}\int_{x_c-x_2}^{x_c-x_3}\vec{x}\times\left(\begin{bmatrix} 0 & -j & 0\end{bmatrix}^{\mathrm{T}}\times\vec{B}\right)dxdydz\end{aligned} \quad (14)$$

where x_c and y_c are the x- and y-positions of the coil geometric center, respectively, and,

$$x_1 = d/2 + v_1, \quad (15)$$

$$x_2 = d/2 + cb, \quad (16)$$

$$x_3 = d/2, \quad (17)$$

$$y_1 = h/2 + v_2, \quad (18)$$

$$y_2 = h/2 + cb, \quad (19)$$

$$y_3 = h/2, \quad (20)$$

$$z_1 = m_b - ap - ch, \quad (21)$$

$$z_2 = m_b - ap, \quad (22)$$

where d and h are the width and the length of center space in the coil, respectively, ch is the height of the magnet and coil, ap is the clearance between the Halbach array and coil, cb is the bundle width of the conductor.

For the accuracy and theoretical analysis, the harmonic model and the coil model with volumes is applied to the calculation of the force and torque exerted on the Halbach array by a coil. The force and torque expressions of the coil are described as:

$$\begin{aligned}F_x &= -y_1\sum_{m=n=1}^{\infty} R_0 g(\omega_1, w)\sin(\omega_1 x) \\ &+\sum_{m=1}^{m<n}\sum_{n=3}^{\infty} R_1\sum_{i=1}^{2}\begin{pmatrix}(-1)^i g(\omega_i, w)\sin(\omega_{3-i} y_1) \\ \sin(\omega_i x)\cos(\omega_{3-i} y)\end{pmatrix},\end{aligned} \quad (23)$$

$$\begin{aligned}F_y &= x_1\sum_{m=n=1}^{\infty} R_0 g(\omega_1, cl)\sin(\omega_1 y) \\ &+\sum_{m=1}^{m<n}\sum_{n=3}^{\infty} R_1\sum_{i=1}^{2}\begin{pmatrix}(-1)^i g(\omega_{3-i}, cl)\sin(\omega_i x_1) \\ \cos(\omega_i x)\sin(\omega_{3-i} y)\end{pmatrix},\end{aligned} \quad (24)$$

$$\begin{aligned}F_z &= \sum_{m=n=1}^{\infty} R_0\begin{pmatrix}y_1 g(\omega_1, w)\cos(\omega_1 x) \\ -x_1 g(\omega_1, cl)\cos(\omega_1 y)\end{pmatrix} \\ &+\sum_{m=1}^{m<n}\sum_{n=3}^{\infty}\frac{R_1}{\lambda}\sum_{i=1}^{2}\begin{pmatrix}(-1)^i\begin{pmatrix}\omega_{3-i} g(\omega_{3-i}, w)\sin(\omega_i y_1) \\ +\omega_i g(\omega_i, cl)\sin(\omega_{3-i} x_1)\end{pmatrix} \\ \cos(\omega_{3-i} x)\cos(\omega_i y)\end{pmatrix},\end{aligned} \quad (25)$$

$$\begin{aligned}T_x &= F_y(C_2) - yF_z - x_1\sum_{m=n=1}^{\infty}\frac{R_0}{2}h(\omega_1, cl)\sin(\omega_1 y) \\ &+\sum_{m=1}^{m<n}\sum_{n=3}^{\infty}\frac{R_1}{2\lambda}\sum_{i=1}^{2}\begin{pmatrix}\frac{(-1)^i}{\omega_i}\begin{pmatrix}2\omega_{3-i} g(\omega_{3-i}, w)u(\omega_i, y_1) \\ +\omega_i^2 h(\omega_i, cl)\sin(\omega_{3-i} x_1)\end{pmatrix} \\ \cos(\omega_{3-i} x)\sin(\omega_i y)\end{pmatrix},\end{aligned} \quad (26)$$

$$\begin{aligned}T_y &= xF_z - F_x(C_2) - y_1\sum_{m=1}^{\infty}\frac{R_0}{2}h(\omega_1, w)\sin(\omega_1 x) + \\ &\sum_{m=1}^{m<n}\sum_{n=3}^{\infty}\frac{R_1}{2\lambda}\sum_{i=1}^{2}\begin{pmatrix}\frac{(-1)^i}{\omega_i}\begin{pmatrix}2\omega_{3-i} g(\omega_{3-i}, cl)u(\omega_i, x_1) \\ +\omega_i^2 h(\omega_i, w)\sin(\omega_{3-i} y_1)\end{pmatrix} \\ \sin(\omega_i x)\cos(\omega_{3-i} y)\end{pmatrix},\end{aligned} \quad (27)$$

$$\begin{aligned}T_z &= -xF_y + yF_x + \\ &\sum_{m=1}^{m<n}\sum_{n=3}^{\infty}\frac{R_1}{\omega_1\omega_2}\sum_{i=1}^{2}\begin{pmatrix}(-1)^i\begin{pmatrix}\omega_{3-i} g(\omega_{3-i}, cl)u(\omega_i, x_1) \\ -\omega_i g(\omega_i, w)u(\omega_{3-i}, y_1)\end{pmatrix} \\ \sin(\omega_i x)\sin(\omega_{3-i} y)\end{pmatrix},\end{aligned} \quad (28)$$

where

$$g(\omega_i, cl) = \sin\frac{\omega_i w}{2}\sin\frac{\omega_i cb}{2}, \quad (29)$$

$$\begin{aligned}h(\omega_i, cl) &= \frac{cl}{2}\cos\frac{\omega_i cl}{2}\sin\frac{\omega_i cb}{2} + \\ &\frac{cb}{2}\sin\frac{\omega_i cl}{2}\cos\frac{\omega_i cb}{2} - \frac{2}{\omega_i}\sin\frac{\omega_i cl}{2}\sin\frac{\omega_i cb}{2}\end{aligned}, \quad (30)$$

$$u(\omega_i, y_1) = \omega_i y_1\cos(\omega_i y_1) - \sin(\omega_i y_1), \quad (31)$$

$$C_1 = \left(e^{\lambda z_2} - e^{\lambda z_1}\right)/\lambda, \quad (32)$$

$$C_2 = \left(e^{\lambda z_1} - e^{\lambda z_2} + \lambda z_2 e^{\lambda z_2} - \lambda z_1 e^{\lambda z_1}\right)/\lambda^2, \quad (33)$$

$$R_0 = 4 j\mu_0 K_3 C_1, \quad (34)$$

$$R_1 = 8 j\mu_0 K_3\lambda C_1/(\omega_1\omega_2), \quad (35)$$

and *w* and *cl* are the sizes of the filament coil along the *x*- and *y*-directions, respectively, $F_y(C_2)$ and $F_x(C_2)$ mean the C_1 is only replaced by C_2 in the F_x and F_y expressions without changing the others, respectively.

IV. COMPARISON OF FORCE AND TORQUE

The force and torque expressions of the harmonic model and coil model with volumes are too complicated to be used in real time control and can be simplified by analyzing the ratio of each harmonic. Figure 3 shows the ratio of each harmonic in the total harmonics. It is found that the ratios of each higher harmonic decrease along the air-gap length in *z*-direction. The majority harmonics are composed of *m*=1, *n*=1, *m*=1, *n*=3 and *m*=3, *n*=1. The maximum ratio magnitudes of m=1, n=5 and m=5, n=1 along the air-gap length in *z*-direction are 0.627%. So the force and torque expressions are simplified by taking the first three harmonics in the real time control and the others can be ignored due to the ratio magnitudes.

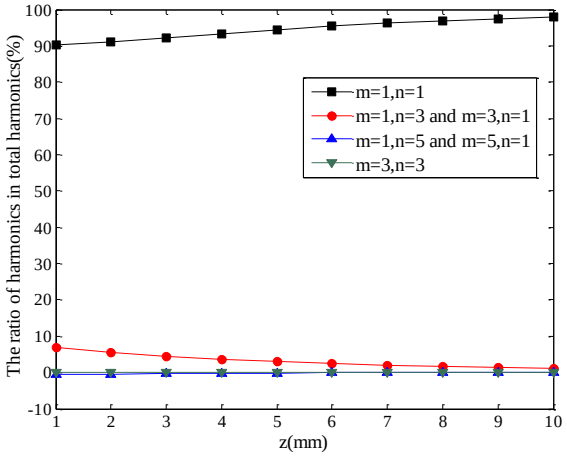

Fig. 3. Ratio of harmonic in total harmonics along the air-gap length in *z*-direction.

In the real time control, the calculation time is an important item to be inspected. Take the force F_x for example, the simplified expression is list as follow:

$$F_x = C_{x1}\sin\left(\sqrt{2}\omega x\right) + C_{x2}\sin\left(2\sqrt{2}\omega x\right)\cdot \cos\left(\sqrt{2}\omega y\right) + C_{x3}\sin\left(\sqrt{2}\omega x\right)\cos\left(2\sqrt{2}\omega y\right), \quad (36)$$

where

$$C_{x1} = -y_1\left(R_0 g\left(\omega_1, w\right)\right)_{(1,1)}, \quad (37)$$

$$C_{x2} = \sin\left(\sqrt{2}\omega y_1\right)\left(R_1 g\left(\omega_1, w\right)\right)_{(1,3)}, \quad (38)$$

$$C_{x3} = -\sin\left(2\sqrt{2}\omega y_1\right)\left(R_1 g\left(\omega_2, w\right)\right)_{(1,3)}, \quad (39)$$

and the coefficient C_{x1} is calculated with the subscript (1,1) denoting *m*=1 and *n*=1, so do the C_{x2} and C_{x3}.

The other force and torque expressions are similar to F_x and not list. The calculation time is determined on the DSP system. The simplified force and torque also have simple expressions to get short calculation time.

The same dimensions of coil and Halbach array to the planar motor used by Jansen are adopted. The variables v_1 and v_2 take 4.75 mm and 4.75 mm for the consistency with the model used by Jansen, respectively. Then the x_1 and y_1 are equal to 6.65 mm and 35.95 mm, respectively. The parameters of coil and Halbach array are shown in Table 1.

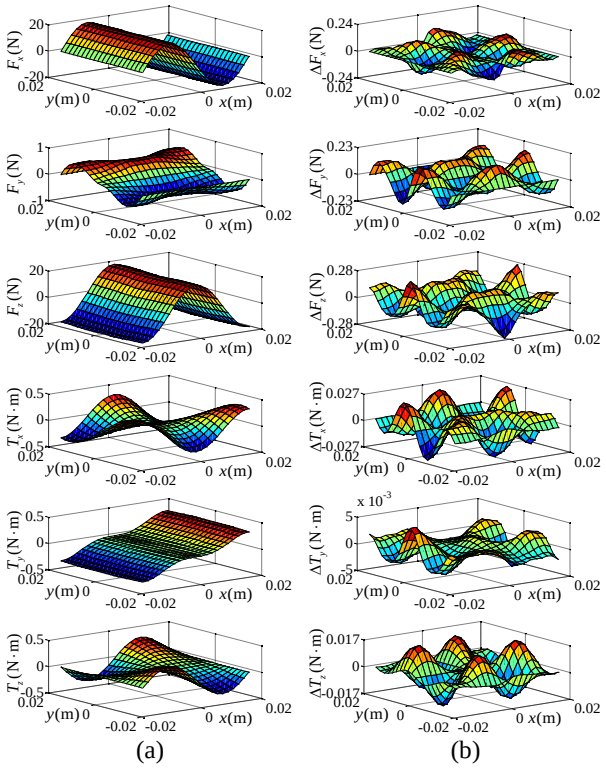

Fig. 4. (a) The force and torque predictions by Ansoft Maxwell, and (b) the force and torque error predictions between the model used by Peng and Ansoft Maxwell.

Table 1: Parameters of coil and Halbach array

Parameters	Value	Unit
Pole pitch (τ)	25	mm
Position of the top of the array (m_t)	3.5	mm
Position of the bottom of the array (m_b)	-3.5	mm
Clearance (*ap*)	1	mm
Coil length (*cl*)	71.9	mm
Coil width (*w*)	13.3	mm
Conductor bundle width (*cb*)	9.5	mm
Magnet size ratio (τ_m/τ)	0.68	-
Remanence of the magnets (B_r)	1.24	T
Current density (*j*)	10	A/mm^2

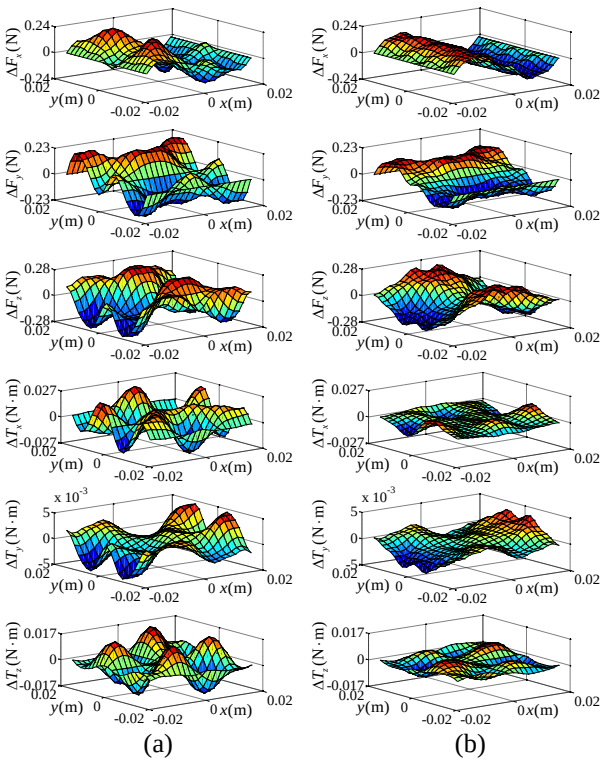

Fig. 5. The force and torque error predictions: (c) between the model used by Jansen and Ansoft Maxwell, and (d) between the model proposed by this paper and Ansoft Maxwell.

To validate the accuracy, the force and torque calculated by Ansoft Maxwell [12], Jansen, Peng and this paper are compared. Jansen used the analytical model and coil model with surfaces, Peng used the analytical model and coil model with surfaces and corners. The force and torque predictions are compared for the positions of the center of coil in a square region, which is located at z = -7.5 mm, with x from -17.7 mm to 17.7 mm and y from -17.7 mm to 17.7 mm. The square region shows a period in Halbach array and is split into 21×21 points, each of which is the coordinate values of the center of coil.

The force and torque predictions by Ansoft Maxwell and the force and torque error predictions between the model used by Peng and Ansoft Maxwell are shown in Fig. 4. The force and torque error predictions between the model used by Jansen and Ansoft Maxwell and between the model proposed by this paper and Ansoft Maxwell are shown in Fig. 5.

From Fig. 4 and Fig. 5, it is difficult to distinguish which is best in the force and torque calculation. The root mean square (rms) value which represents the ripples of the force and torque is introduced to predict the performance of the error predictions for each model. The smaller of the rms value, the better of the model. The rms values of the errors of the model used by Peng, the model used by Jansen and the model proposed by this paper are shown in Table 2.

Table 2: Parameters of each model

Parameters	Model used by Peng	Model used by Jansen	Model Proposed by this Paper	Unit
rms (ΔF_x)	0.0506	0.1022	0.0928	N
rms (ΔF_y)	0.0803	0.116	0.0884	N
rms (ΔF_z)	0.0990	0.159	0.1316	N
rms (ΔT_x)	0.0107	0.0111	0.0037	Nm
rms (ΔT_y)	0.0015	0.0019	0.0014	Nm
rms (ΔT_z)	0.0071	0.0073	0.0030	Nm

It can be seen in Table 2, the accuracy of the model used by Peng is best in the rms values of the force components and the accuracy of the model used by this paper is best in the rms values of the torque components. From the Fig. 5 (b), the three components of the force error predictions are close to cosine or sine form. According to the force predictions of Ansoft Maxwell and the error predictions between the model proposed by this paper and Ansoft Maxwell, the force error can be significantly reduced by optimizing the parameterized dimensions of coil.

V. OPTIMIZATION OF FORCE AND TORQUE

In order to reduce the force and torque error, the model proposed by this paper is optimized by genetic algorithm (GA).

The objective function is the maximum error of each force and torque components between the model proposed by this paper and Ansoft Maxwell on coil center coordinates in the square region mentioned above. The function is given by:

$$f(x_1, y_1) = \max\left|R_1(S_{mn}) - R_2(S_{mn})\right|, \quad (40)$$

where R_1 and R_2 are the force and torque obtained by Ansoft Maxwell and the model proposed by this paper, respectively, the function R represents F_x, F_y, F_z, T_x, T_y and T_z, respectively, S_{mn} is the coordinate values of coil center, in which the values are in millimeters, and,

$$S_{mn} = (-17.7 + 1.77m, -17.7 + 1.77n, -7.5). \quad (41)$$

There are two parameters x_1 and y_1 by observing the force and torque expressions, which are related to the v_1 and v_2, respectively. In this part, the parameters x_1 and y_1 are set as variables for optimizing the force and torque. The optimization variables are shown in Table 3.

In the optimization of torque, the values of the F_x, F_y and F_z in the torque expressions are considered as constant obtained by the force optimization before. So the dimensions of x_1 and y_1 used in force and torque are different. The flowchart of the parameter optimizing

procedure using genetic algorithm (GA) [13] is shown in Fig. 6. The genetic algorithm of optimization tool of MATLAB is used. Firstly, the elite are selected by fitness evaluation. Then the new elite are selected from the new population generated by the crossover and mutation. Finally, the stopping criterion is the stall generations reach one hundred. The selection function, crossover function and mutation function use stochastic uniform, scattered and use constraint dependent, respectively.

Table 3: Optimization variables

Variables	Constraints	Unit
The dimension of the coil straight segments in x-direction (x_1)	$\left[\frac{d}{2}, \frac{d}{2}+cb\right]$	mm
The dimension of the coil straight segments in y-direction (y_1)	$\left[\frac{h}{2}, \frac{h}{2}+cb\right]$	mm

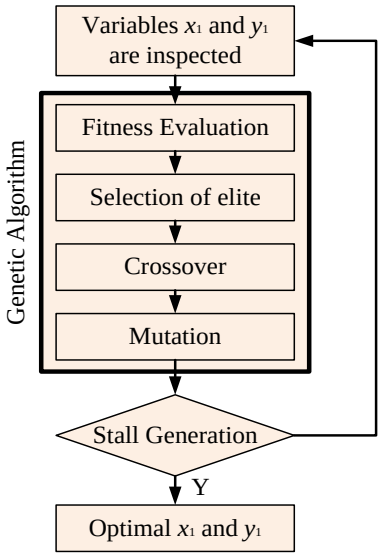

Fig. 6. The optimization process.

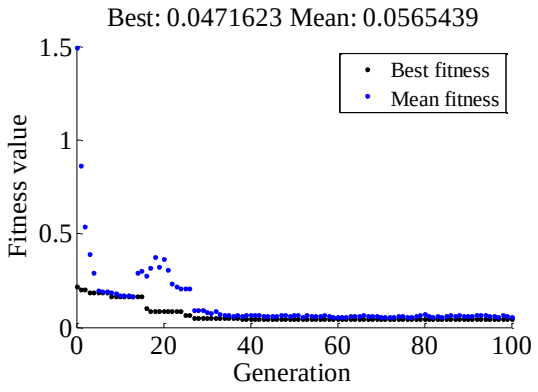

Fig. 7. Iteration accomplished by GA to obtain the best fitness for *Fz*.

The fitness values of F_z shown in Fig. 7, illustrate that after 40 number of iteration the error reaches to an acceptable value. The other force and torque are similar and not listed. The results of the optimization variables are shown in Table 4.

Table 4: The results of the optimization variables

Force and Torque	x_1 (mm)	y_1 (mm)	$f(x_1, y_1)$
F_x (N)	-	36.2	0.1761
F_y (N)	8.69	-	0.0093
F_z (N)	8.34	36.2	1.4763
T_x (Nm)	6.84	31.53	0.0440
T_y (Nm)	7.14	36.9	0.0195
T_z (Nm)	11.4	38.12	0.0019

The error predictions between the optimized model and Ansoft Maxwell are shown in Fig. 8. Each error prediction is obtained by using the different optimization results. The rms values of the error between the optimized model and Ansoft Maxwell are shown in Table 5.

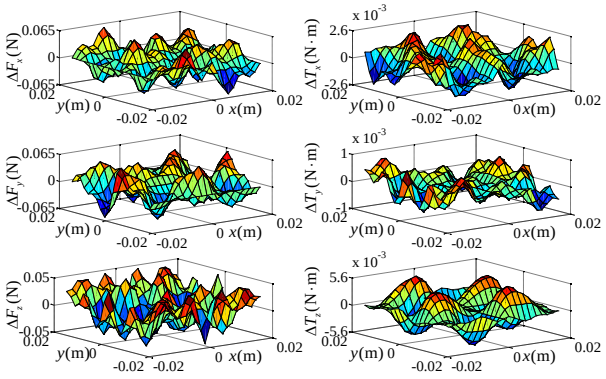

Fig. 8. Error predictions after optimization of the force exerted by a coil.

Table 5: The rms values of the error between the optimized model and Ansoft Maxwell

Parameters	Optimized	Unit
rms (ΔF_x)	0.0228	N
rms (ΔF_y)	0.0254	N
rms (ΔF_z)	0.0249	N
rms (ΔT_x)	0.0011	Nm
rms (ΔT_y)	0.0003	Nm
rms (ΔT_z)	0.0006	Nm

Comparing the force rms values of the optimized model with the model used by Peng, the rms values are much lower. The rms (ΔF_x), rms (ΔF_y) and rms (ΔF_z) are 45.06%, 31.63% and 25.15% of the model used by Peng, respectively. Comparing the torque rms values of the optimized model with the model proposed by this paper, the lower rms values are obtained. The rms (ΔT_x),

rms (ΔT_y) and rms (ΔT_z) are 29.73%, 21.43% and 20% of the model proposed by this paper, respectively. The only change between the optimized model and the model proposed by this paper is that different dimensions of coil segments are adopted for force and torque calculation. The optimized model can achieve good accuracy.

VI. CONCLUSION

The magnetic flux density distribution of the Halbach array is expressed in global coordinate system after transformation. The dimensions of coil are parameterized for modeling.

The analytical expressions of force and torque exerted on the Halbach array by a coil with the harmonic model and the coil model with volumes are obtained. The model proposed by this paper is simplified by taking the first three harmonics to be used in real time control.

The rms for force and torque of the optimized model are very low comparing with the previous models. The optimized model can be applied to the force and torque calculation to improve control precision. The same method can be applied on the Halbach permanent magnet array with different segments per pole.

ACKNOWLEDGMENT

Research was supported by the Natural Foundation of Shandong Province (ZR2015EQ015) and the Fundamental Research Funds for the Central Universities (15CX02031A, 15CX02123A).

REFERENCES

[1] H. S. Cho and H. K. Jung, "Analysis and design of synchronous permanent-magnet planar motors," *IEEE Trans. Energy Conver.*, vol. 17, no. 4, pp. 492-499, 2002.

[2] A. Shiri and A. Shoulaie, "Investigation of frequency effects on the performance of single-sided linear induction motor," *Applied Computational Electromagnetics Society (ACES) Journal*, vol. 27, no. 6, pp. 497-504, June 2012.

[3] J. F. Pan, N. C. Cheung, and J. M. Yang, "High-precision position control of a novel planar switched reluctance motor," *IEEE Trans. Ind. Electron.*, vol. 52, no. 6, pp. 1644-1652, Dec. 2005.

[4] H.-S. Cho and H.-K. Jung, "Analysis and design of synchronous permanent-magnet planar motors," *IEEE Trans. Energy Convers.*, vol. 17, no. 4, pp. 492-499, Dec. 2002.

[5] L. Huang, X. Huang, H. Jiang, and G. Zhou, "Comparative study of magnetic fields due to types of planar permanent magnet array," *International Conference on Electrical and Control Engineering*, DOI 10. 1109/Icece. 844, 2010.

[6] J. C. Compter, "Electro-dynamic planar motor," *Precision Eng.*, vol. 28, pp. 171-180, 2004.

[7] J. W. Jansen, C. M. M. van Lierop, E. A. Lomonova, and A. J. A. Vandenput, "Modeling of magnetically levitated planar actuators with moving magnets," *IEEE Trans. Magn.*, vol. 43, no. 1, pp. 15-25, Jan. 2007.

[8] J. W. Jansen, C. M. M. van Lierop, E. A. Lomonova, and A. J. A. Van-denput, "Magnetically levitated planar actuator with moving magnets," *in Proc. IEEE Int. Electric Machines & Drives Conf.* (IEMDC '07), vol. 1, pp. 272-278, May 2007.

[9] J. Peng, Y. Zhou, and G. Lin, "Calculation of a new real-time control model for the magnetically levitated ironless planar motor," *IEEE Trans. Magn.*, vol. 49, no. 4, pp. 1416-1422, Jan. 2013.

[10] W. Min, M. Zhang, Y. Zhu, B. Chen, G. Duan, J. Hu, and W. Yin, "Analysis and optimization of a new 2-D magnet array for planar motor," *IEEE Trans. Magn.*, vol. 46, no. 5, May 2010.

[11] Numerical Integration and Differentiation Users Guide [M]. Mathworks Inc., 2009.

[12] E. Schmidt and M. Hofer, "Application of the sliding surface method with 3D finite element analyses of a hybrid magnetic bearing," *25th Annual Review of Progress in Applied Computational Electromagnetics (ACES)*, Monterey, California, pp. 440-445, Mar. 2009.

[13] A. Nejadpak, M. R. Barzegaran, and O. A. Mohammed, "Evaluation of high frequency electromagnetic behavior of planar inductor designs for resonant circuits in switching power converters," *Applied Computational Electromagnetics Society Journal*, vol. 26, no. 9, pp. 737-748, 2011.

[14] K. J. Binns, P. J. Lawrenson, and C. W. Towbridge, *The Analytical and Numerical Solutions of Electrical and Magnetic Fields*. Chichester, England: *John Wiley & Sons*, 1994.

[15] Y. Zhou, G. Liu, R. Zhou, L. Huo, and W. Ming, "Modeling and comparison of the Halbach array with different segments per pole," *International Journal of Applied Electromagnetics and Mechanics*, vol. 47, no. 3, pp. 629-641, 2015.